Measurement and Modelling of Soft Solid Layers in Cleaning Applications

Jheng-Han Tsai

Department of Chemical Engineering and Biotechnology

University of Cambridge

This thesis is submitted for the degree of

Doctor of Philosophy

Jesus College   May 2020

Declaration

This thesis is the result of my own work and includes nothing which is the outcome of work done in collaboration except as specified in the text. It is not substantially the same as any that I have submitted, or, is being concurrently submitted for a degree or diploma or other qualification at the University of Cambridge or any other University or similar institution except as specified in the text. I further state that no substantial part of my thesis has already been submitted, or, is being concurrently submitted for any such degree, diploma or other qualification at the University of Cambridge or any other University or similar institution except as specified in the text. It does not exceed the prescribed word limit for the Engineering Degree Committee.

<div align="right">

Jheng-Han Tsai

May 2020

</div>

Abstract

Measurement and Modelling of Soft Solid Layers in Cleaning Applications

Fouling and effective cleaning are important operating issues in the food and pharmaceutical industries, which need to be managed well to ensure process hygiene and productivity. In order to understand fouling and cleaning mechanisms, methods are required to quantify soft solid soil or deposit characteristics by measuring these *in situ*. This dissertation describes the development of millimanipulation and two new fluid dynamic gauging (FDG) devices, namely sideways FDG (SiDG) and integrated FDG (iFDG), and demonstrates their application for *in situ* measurement. Computational fluid dynamic (CFD) simulations of the flow patterns using the volume of fluid method were performed which enables previously inaccessible information to be extracted from the experimental data.

The millimanipulation device reported by Magens *et al.*, *J Food Eng*, **197** (2017) 48-59 measures the force experienced by a blade as it is pushed through a soil layer. The deformation of layers of viscoplastic petroleum jelly, soft white paraffin and toothpaste were studied and simulated using the regularized Bingham and the bi-viscosity models. The simulations gave good agreement with experimental results: combining visualisation and an interrupted testing mode allowed the material's yield stress to be estimated.

The SiDG device allows one to study the initial and long-term swelling of soft solid layers. The concept was implemented, commissioned and demonstrated by monitoring the swelling of gelatin, poly(vinyl acetate) (PVAc) and complex model soil layers at different pH and temperatures. All these materials underwent rapid initial hydration, followed by different longer term behaviour: gelatin and PVAc layers at pH < 11 exhibited Fickian diffusion control while at pH ≥ 11, PVAc exhibited relaxation control associated with hydrolysis.

In the iFDG system the distances between the nozzle head and the soil layer, and the metallic substrate, are measured simultaneously by incorporating an inductive sensor in the gauging nozzle. The iFDG device was taken from concept to demonstration with a range of gauging liquids: water, UHT milk (opaque), a more viscous Newtonian fluid (washing-up liquid) and non-Newtonian aqueous solutions of 1 wt% and 3 wt% carboxymethyl cellulose (CMC). The CFD simulations gave good agreement with the experimental data. An ice growth experiment was performed using the iFDG device to demonstrate its application to monitoring growth of fouling layers.

The CFD simulations were extended to consider the coupled flows which can arise in FDG measurements, where the stressed imposed by the gauging liquid flow can deform the soft solid soil layer. Two-fluid simulations were performed to estimate the change of topography of a petroleum jelly layer subject to FDG testing at different clearances. Acceptable agreement between the simulation results and measurements was obtained, and the observed differences were attributed to tubing-induced artefacts. A short feasibility study considered extending the approach to the three-fluid problem when a coherent liquid jet impinges horizontally on a horizontal plane coated with a soft solid soil layer. The results showed promising agreement with experiments on water jet cleaning of petroleum jelly layers.

<div align="right">Jheng-Han Tsai</div>

Acknowledgements

List of Publications

Some of the work in this thesis has been published in journal and conference papers, which are listed as follows.

J.-H. Tsai, G.L. Cuckston, L. Schnöing, W. Augustin, S. Scholl, B. Hallmark and D.I. Wilson, Fluid dynamic gauging for studying early stages of swelling of fouling deposits, *Heat Transf Eng* (2020) – Under review.

R. Wang, J.-H. Tsai, M. Snead, P. Alexander and D.I. Wilson, Stability of the interface between two immiscible liquids in a model eye subject to saccadic motion, *J Biomech Eng* (2020) – Under review.

J.-H. Tsai, J.-Y. Huang, D.I. Wilson, Life cycle assessment of cleaning-in-place operations in egg yolk powder production, *J Clean Prod*, **278** (2021) 123936.

J.-H. Tsai, R.R. Fernandes, D.I. Wilson, Measurements and modelling of the 'millimanipulation' device to study the removal of soft solid layers from solid substrates, *J Food Eng*, (2020) 110086.

J.-H. Tsai, B. Hallmark, D.I. Wilson, Integrated fluid dynamic gauge for measuring the thickness of soft solid layers immersed in opaque, viscous, and/or non-Newtonian liquids in situ, *Ind Eng Chem Res*, **58** (2019) 23124-23134.

J.-H. Tsai, G.L. Cuckston, B. Hallmark, D.I. Wilson, Fluid-dynamic gauging for studying the initial swelling of soft solid layers, *AlChE J*, **65** (2019) e16664.

G.L. Cuckston, J.-H. Tsai, D.I. Wilson, Dynamic gauging for studying rapidly swelling or shrinking layers, 13th International Congress on Engineering and Food (ICEF13), Australia, Sep. 23-26, 2019

J.-H. Tsai, G.L. Cuckston, L. Schnöing, W. Augustin, S. Scholl, B. Hallmark and D.I. Wilson, Fluid dynamic gauging for studying early stages of swelling of fouling deposits, 13th Heat Exchanger Fouling and Cleaning Conference, Poland, Jun. 2-7, 2019

J.-H. Tsai, B. Hallmark and D.I. Wilson, Modelling of coupled deformation of viscoplastic layers and fluid dynamic gauging flows using two-phase CFD, UK Fluids Network Special Interest Group 10 (SIG10), Fluid Mechanics of Cleaning and Decontamination, Cambridge, Aug. 29-30, 2018

Contents

List of Figures

List of Tables

Nomenclature

Latin

A	Oscillation amplitude	°
a	Radius of cleaned area	m
a_0	Radius when cleaning front is first seen	m
Bn	Bingham number	-
b	Length of berm of sample layer	m
b_0	Original length of berm of sample layer	m
C_{NaOH}	Concentration of sodium hydroxide solution	kg/m^3
C_c	Cable capacitance	F
C_d	Discharge coefficient	-
C_r	Resonance capacitor	F
D	Dryer diameter	m
D_i	Internal diameter of silicon rubber tube	m
D_o	External diameter of silicon rubber tube	m
ΔD_i	Change of internal diameter of silicon rubber tube	m
$\mathbf{D}$	Rate of deformation tensor ($\mathbf{D} = \frac{1}{2}(\nabla\mathbf{v} + (\nabla\mathbf{v})^T)$)	1/s
d_i	Inner diameter of nozzle tube	m
d_j	Jet diameter	m
d_t	Diameter of nozzle throat	m
E	Elasticity modulus	Pa

F_C	Removal force at point C	N/m
$F_{C'}$	Removal force at point C'	N/m
F_D	Removal force at point D	N/m
F_w	Removal force	N/m
$\bar{F}_w$	Average removal force	N/m
G'	Elastic modulus	Pa
G''	Viscous modulus	Pa
g	Gravity vector	m/s^2
g_i	Elastic constant of Maxwell model	Pa
h	Nozzle-layer clearance	m
h_b	Height of berm of sample layer	m
h_f	Water film thickness	m
h_{new}	New clearance after ZFDG operation	m
h_o	Nozzle-substrate clearance	m
K	Cleaning rate parameter	$m/s^{0.2}$
k	Flow consistency index of simple power law	$1/s^n$
k'	Cleaning rate constant	m-s/kg
k_D	Kinetic constant of simple power law	$1/s^n$
k_{HB}	Flow consistency index of Herschel-Bulkley model	Pa
k_m	Kinetic constant $k(\delta_\infty - \delta_0)$	m/s^n
k_s	Kinetic constant	m^2-s/kg
L	Initial length of sample layer	m
L_c	Cable inductance	H
L_i	Inductance of inductive coil	H
L_p	Length of sample layer behind blade	m
l	Length of nozzle tube	m

M	Momentum in the liquid film per unit length	kg/s^2
M_Y	Momentum flux required to cause yield	kg/s^2
m	Amount of solvent in a polymer	kg
m_{BP}	Smoothing parameter of Bingham-Papanastasiou model	-
m_∞	Amount of solvent at swelling equilibrium	kg
$\dot{m}$	Mass flow rate	kg/s
$\dot{m}_{actual}$	Actual mass flow rate of gauging liquid	kg/s
$\dot{m}_{ideal}$	Ideal mass flow rate of gauging liquid	kg/s
$N_1 - N_2$	Difference of normal stress differences	Pa
n	Flow behaviour index of simple power law	-
$\hat{n}$	Surface normal	-
$\hat{n}_w$	Unit vector normal	-
n_D	Diffusion index of simple power law	-
n_{HB}	Flow index of Herschel-Bulkley model	-
ΔP	Differential pressure $(P - P_0)$	Pa
P	Measured pressure	Pa
P_0	Ambient pressure	Pa
P_{true}	Real pressure for pressure transducer calibration	Pa
p	Pressure	Pa
pk-pk	Peak to peak voltage	V
Q	Volumetric flow rate	m^3/s
Q_D	Viscous dissipation	W/m
R^2	Goodness of fit	-
RP	Relative productivity	-
R_c	Resistance of cable	Ω
Re	Reynolds number	-

Re_j	Reynolds number of jet based on nozzle diameter	-
Re_t	Reynolds number at FDG nozzle throat	-
R_i	Resistance of inductive coil	Ω
R_q	Roughness	m
r	Radial co-ordinate	m
r_i	Inner radius of FDG nozzle	m
r_o	Outer radius of FDG nozzle	m
r_t	Transition radius	m
s	Scrape depth	m
T	Temperature	°C
T_i	Temperature	°C
t	Time	s
Δt	Total time when cleaning front is first seen	s
Δt_i	Total time when polymer is submerged into solution	s
$\hat{t}_w$	Unit vector tangential to wall	-
t_i	Time at which immersion occurs	s
t_{sim}	Time in simulation	s
t_0	Time when cleaning front is first seen	s
U	Mean velocity	m/s
V	Scrape velocity	m/s
$\bar{V}$	Average velocity	m/s
V^*	Relative velocity	-
V_{DAQ}	Voltage collected by DAQ	V
$\mathbf{v}$	Velocity vector	m/s
$\bar{v}$	Mean velocity	m/s
$v_{ejection}$	Inlet velocity for ejection mode	m/s

v_{jet}	Jet velocity	m/s
v_r	Radial velocity	m/s
$v_{suction}$	Inlet velocity for suction mode	m/s
v_z	Axial velocity	m/s
w_e	Nozzle rim thickness	m
w_r	Nozzle rim width	m
x	Horizontal coordinate (x-axis in Cartesian coordinate system)	m
y	y-axis coordinate (Cartesian coordinate system)	m
z	Axial coordinate (z-axis in Cartesian coordinate system)	m

Greek

α	Volume fraction of sample phase	-
α_i	Volume fraction of species i	-
β	Converging angle of nozzle	°
γ	Shear strain	-
$\dot{\gamma}$	Shear rate	1/s
δ	Layer thickness; Residual thickness of sample layer	m
δ_0	Initial dry layer thickness	m
δ_i	Measured thickness at which immersion occurs	m
δ_∞	Equilibrium layer thickness	m
$\Delta\delta$	Change in thickness ($\delta - \delta_0$)	m
$\Delta\delta_i$	Initial change in thickness ($\delta_i - \delta_0$)	m
ε	Voidage	-
η	Apparent viscosity	Pa s
η^*	Complex viscosity of Cox-Merz rule	Pa s

η_0	Creeping viscosity in bi-viscosity approach	Pa s
η_p	Polymeric viscosity	Pa s
θ	Angle of topography measured	°
θ_w	Contact angle	°
κ	Coefficient of relationship between squared height and length of layer berm	m
λ	Relaxation time	s
λ_i	Relaxation time of Maxwell time	s
μ	Dynamic viscosity	Pa s
μ_0	Creeping viscosity of bi-viscosity model	Pa s
μ_A	Dynamic viscosity for species A	Pa s
μ_i	Dynamic viscosity for species i	Pa s
μ_p	Plastic viscosity of Bingham-Papanastasiou model	Pa s
ν	Poisson's ratio	-
π	Ratio of circumference to diameter	-
ρ	Density	kg/m^3
ρ_A	Density for species A	kg/m^3
ρ_i	Density for species i	kg/m^3
σ_{A-B}	Surface tension for species A and B	N/m
σ_{ij}	A term in Cauchy stress tensor	Pa
σ_v	Von Mises stress	Pa
τ	Shear stress	Pa
τ_{60}	Measured shear stress at 60 s	Pa
τ_c	Critical stress	Pa
τ_{cp}	Ratio of cleaning time to production time	-

τ_p	Polymeric extra stress tensor	Pa
τ_w	Wall shear stress	Pa
$\bar{\tau}_w$	Average wall shear stress	Pa
τ_w^*	Dimensionless wall shear stress	-
$\bar{\tau}_w^*$	Average dimensionless wall shear stress	-
τ_y	Yield stress	Pa
$\tau_\mathrm{y}^{\mathrm{e1}}$	First estimate of yield stress	Pa
$\tau_\mathrm{y}^{\mathrm{e2}}$	Second estimate of yield stress, $\tau_\mathrm{y}^{\mathrm{e2}} = \tau_\mathrm{y}^{\mathrm{e1}} \times (F_{\mathrm{C'}}/F_{\mathrm{C}})$	Pa
$\tau_\mathrm{y}^{\mathrm{e3}}$	Third estimated of yield stress, $\tau_\mathrm{y}^{\mathrm{e3}} = \tau_\mathrm{y}^{\mathrm{e1}} \times (F_{\mathrm{D}}/F_{\mathrm{C}})$	Pa
$\varPhi$	Viscous dissipation rate	W/m^3
ϕ	Cutting angle	rad
χ	Slope angle	°
ω	Angular frequency	rad/s

Acronymns

AFM	Atomic force microscopy
BLFZ	Boundary layer formation zone
BOD	Biochemical oxygen demand
BSP	Breaking, storage and pasteurisation
BVM	Bi-viscosity model
CFD	Computational fluid dynamics
CIP	Cleaning-in-place
CMC	Carboxymethyl cellulose
CMS	Complex model food soil
COD	Chemical oxygen demand

CTS	Confocal thickness sensor
DAQ	Data acquisition
E	Error
EDX	Energy dispersive X-ray spectroscopy
FDG	Fluid dynamic gauging
FEM	Finite element method
FRS	Fossil resource scarcity
FTIR	Fourier-transform infrared spectrometry
FU	Functional unit
GW	Global warming
HCT	Human carcinogenic toxicity
HNCT	Human non-carcinogenic toxicity
IC	Impact category
iFDG	Integrated FDG
IPS	Inductive proximity sensor
IR	Ionisation radiation
LCA	Life cycle assessment
LCI	Life cycle inventory
LVDT	Linear variable differential transformer
LZ	Laminar film zone
ME	Marine ecotoxicity
MRI	Magnetic resonance imaging
NMR	Nuclear magnetic resonance
PEEK	Polyethyletherketone
PIV	Particle image velocimetry
PJ	Petroleum jelly

PPFC	Parallel plate flow cell
PT	Pressure transducer
PVA	Polyvinyl alcohol
PVAc	Poly(vinyl acetate)
RBM	Regularised Bingham model
SEM	Scanning electronic microscopy
sFDG	Scanning fluid dynamic gauging
SiDG	Sideways FDG
SS	Stainless steel
SWP	Soft white paraffin
TE	Terrestrial ecotoxicity
TZ	Turbulent zone
UFO-MBR	Ultrafiltration, forward osmosis and membrane bioreactor
VOF	Volume of fluid
WC	Water consumption
XRD	X-ray diffraction
ZFDG	Zero-discharge fluid dynamic gauging

Chapter 1   Research Motivation

1.1   Introduction and Background

Fouling on surfaces has attracted growing attention in the food and biotech sectors in recent years, which results in a series of concerns, such as hygienic issues, contamination, reduction of productivity, corrosion of equipment surfaces, and increasing operating costs [1, 2]. Removing these fouling deposits on equipment surfaces often require large volumes of water and/or chemical agents at high temperature, leading to high consumption of water, materials and energy. These are also associated with large environmental impacts [3]. Müller-Steinhagen reported an estimate of production losses caused by fouling on heat exchanger surfaces, which accounted for around 0.25 % of the annual GDP in industrialised countries [4]. Moreover, USDA figures in 2019 showed that more than 500 billion tons of dairy products, double that of the 2000's, was produced that year across the world [5]. Based on this trend, annual production of 1000 billion tons can be expected in the next decade, and the consumption of water, chemicals and energy would be dramatic. Further studies of cleaning fouling deposits on equipment surfaces for mitigating the economic and environmental impacts are thus required.

Quantitative understanding of fouling mechanisms and deposit characteristics are needed to develop more effective and efficient cleaning processes. For physical cleaning methods, where removal is driven by forces generated by a flowing fluid, a range of parameters need to be known (either by measurement or prediction). These include the fluid shear, removal force, and mass transfer characteristics of the flow: the strength of adhesion between the foulant and equipment surface; the thickness and change in thickness of fouling layers; and the mechanical properties of fouling deposits (*e.g.* yield stress). Quantitative models linking the characteristics of the flow and the behaviour of the fouling layer (with and without chemical action) can then be developed or used in simulations. With these tools, the required flow rate for cleaning

devices (*e.g.* cleaning jets) and operating times can be estimated for developing cleaning protocols or refining existing ones, for example to avoid overconsumption of water and chemicals.

However, some fouling deposits have proved difficult to remove and measure. Some of these deposits are porous, and contain a large amount of liquid when immersed in a liquid environment. On being touched or removed from the liquid, they collapse readily, increasing the difficulty of studying them. Furthermore, conventional mechanical instruments, such thickness gauges, cannot be employed for measuring the thickness of such layers accurately and easily. Even through some non-contact techniques like tomography allow thicknesses to be measured with high accuracy, installation of these is often pricey or may not be viable [6]. Innovation and development of hardware for studying such challenging layers is therefore needed. These may require detailed simulation of the operation in order to extract intrinsic properties of the deposit from the measurements.

This dissertation focuses on two measurement techniques developed in the P^4G research group in the Department of Chemical Engineering and Biotechnology at Cambridge, for studying soft solid fouling layers *in situ*, namely fluid dynamic gauging (FDG) and millimanipulation.

The first FDG device was constructed by Tuladhar [7]. The FDG device considered in this work was constructed by previous PhD student Shiyao Wang [8], to demonstrate the zero discharge concept (ZFDG). FDG devices are able to measure the thickness of soft solid layers immersed in a liquid environment *in situ* and in real time. Simulations of the fluid flow pattern in the FDG device allow the stress imposed on the layer by the gauging flow, and hence its strength, to be determined by *in situ* measurements. While devices such as the ZFDG allow the thickness, growth (and shrinkage) rates and removal shear stress of fouling layers to be quantified, the initial swelling rate was not able to be monitored reliably. For layers which change shape rapidly on contact with liquids, this is a phase where information is needed in order to determine the mechanisms involved.

Millimanipulation measures the forces required to disrupt a deposit layer as a result of it being dislodged by a moving blade. This allows the forces active in the layer and at the layer/substrate interface to be measured. Unlike FDG, where a liquid flow imposes a force, in millimanipulation a known deformation is imposed. The millimanipulation device was built by previous PhD student, Ole M. Magens [9], to measure adhesion forces. Simulations are

required to estimate layer properties, such as the yield stress and rheology. Estimating these properties from *in situ* measurements, avoiding changing the properties by removing the deposit from the substrate, will allow more reliable understanding of deposit behaviour.

The dissertation present the improvement and development of these two techniques to enable the characteristics of fouling layers to be studied *in situ*. They are linked by the application field and by the type of modelling involved, namely computational fluid dynamics (CFD) simulations of flows of non-Newtonian fluids featuring a free surface.

1.2 Research Aims

The aims of this PhD project are to understand the characteristics of fouling deposits and fouling-related cleaning methods for establishing a more sustainable cleaning practice. This involves developing the apparatuses and techniques of FDG and millimanipulation, supported by experiments and computational fluid dynamics (CFD) simulations. The CFD methodology is also applied to cleaning viscoplastic soil layers using an impinging water jet. The FDG component follows builds on the Wang's work on ZFDG [8]. Two new versions of ZFDG are developed, namely sideways FDG (SiDG), which allows one to study the initial and long-term swelling of soft solid layers, and integrated FDG (iFDG), which enables the distances between the nozzle head and the soil layer, and the metallic substrate, to be determined simultaneously. The millimanipulation project builds on the Magens's work [9], to boost the capability of his millimanipulation device for tracking the deformation and slip of soft layers *in situ*.

In both cases, viscoplastic materials are studied as the model soils simulating fouling deposits which are difficult to remove.

The aims and relative objectives of the work are:

i.   To extend the applicability of Magen's millimanipulation device – studying the removal behaviour of viscoplastic layers, including the topography, flow and force distributions, using experiments and computational fluid dynamic studies.

ii. To design, construct and commission two test FDG devices – the sideways concept for measuring the initial swelling and cleaning behaviour is introduced and demonstrated via studies of a range of soil layers (*e.g.* polyvinyl acetate). The feasibility of integrating

an inductive proximity sensor into a FDG nozzle (iFDG), simplifying FDG measurements, is demonstrated for different substrates and various gauging liquids.

iii. To develop simulations of the flows in SiDG and iFDG devices – CFD models are constructed, which allows flow patterns and the stresses imposed on the soil and substrate by the flow, for different gauging solutions (*e.g.* water, viscosity and non-Newtonian fluids) to be estimated. These model are extended to simulate the coupled deformation of viscoplastic layers and FDG gauging flows using the volume-of-fluid (VOF) approach.

iv. To apply the CFD tool developed in (iii) for an initial study of the removal of a viscoplastic soil layer using an impinging water jet.

1.3 Structure of the Dissertation

This dissertation is organised in six chapters. This first chapter introduces the background of the research and its aims.

Chapter 2 reviews the fouling problem and challenges in cleaning, especially for cleaning-in-place processes (CIP). A life cycle assessment of cleaning-in-place in the production of powdered egg yolk is presented which highlights that cleaning is a sustainability hotspot in manufacturing processes. Cleaning mechanisms and methods, including the development of millimanipulation, are introduced and summarised. The techniques of measuring the characteristics of soft solid layers are compared and the evolution of FDG is presented.

Chapter 3 focuses on the development of the millimanipulation device, including visualisation, measurement of adhesive strength and interrupted testing, for a commercial petroleum jelly, a pharmaceutical soft white paraffin and a commercial toothpaste. A new estimation of yield stress of soft layers is presented and discussed. A CFD model of the millimanipulation device is presented. A test case using Carbopol® gel is presented and compared with the literature. Simulations are compared with experimental data.

Chapter 4 presents the design, construction, commission and calibration of two innovative FDG devices and an improved ZFDG apparatus as well as the software with graphical user interface (GUI) required to drive the device. The applications of the SiDG technique to measure the layer thickness and swelling of polyvinyl acetate, gelatin and a complex model soil are described.

2D and 3D computational fluid dynamics studies of SiDG are presented and the results are compared with experimental data. The flow patterns and induced shear stress are analysed. The tests for the concept of iFDG using substrates of copper and mild and stainless steel as well as different gauging liquids, including water, whole ultrahigh-temperature milk, commercial washing-up liquid and 1 and 3 wt % carboxymethylcellulose (Non-Newtonian) solutions are demonstrated. CFD models of iFDG for these fluids is presented.

Chapter 5 describes the experiments of coupled deformation of a viscoplastic layer (a commercial petroleum jelly) and FDG flows. The evolutions of pressure drop and topography of the sample layer in both ejection and suction modes and at different clearances are discussed. The experimental results are compared with CFD simulations. A further application of the CFD model for cleaning the viscoplastic layer using an impinging water jet is presented, and the results compared with experimental measurements.

Chapter 6 presents the conclusions of the investigations and topics for future work.

Chapter 2   Literature Review

2.1   Fouling Problems and Cleaning Processes

Fouling is the deposition of unwanted material on a surface during processing. It is a widespread issue, especially in the food and biotechnology sectors, and often results in reduced operating efficiency, unhygienic conditions, and increase in energy consumption. Fouling creates a need for cleaning, requiring downtime and lost production, cleaning agents and energy. The mechanisms causing fouling have been classified as (1) precipitation/crystallisation, (2) sedimentation, (3) corrosion, (4) chemical reaction, (5) solidification and (6) biofouling. Deposition often involves a combination of these mechanisms [10].

Crystallisation is often observed in membrane and heat transfer operations. Taking membrane distillation as an example, solutes accumulate adjacent to the membrane surface due to water vapour going through the membrane, resulting in supersaturated conditions there. The solutes then crystallise on the membrane surface. This phenomenon is called scaling, and is widely observed in heating hard water (containing calcium sulphate and calcium carbonate) [11]) as well as milk stone (calcium phosphate and proteins) deposited on heat exchanger surfaces in dairy industry [12].

Sedimentation means that the particulate material falls or rises under gravity and collects on a surface.

Corrosion fouling is where the surface itself undergoes a change or reaction to form a fouling layer [13].

Generally, chemical reaction fouling involves a multistep mechanism, presented in Fig. 2.1(a) [14]. Precursor A (soluble) flows through a heat exchanger with the fluid, and can react to form insoluble species B on the equipment surface. Alternatively, A reacts to become B in the bulk,

which then moves to a surface and deposits there. Chemical reaction fouling often occurs in organic fluids, such as are found in oil refining and the petrochemical sectors. This is mainly attributed to autoxidation, polymerisation and thermal decomposition [15]. In the dairy sector, some of the whey proteins present in milk react at the conditions used for pasteurisation and sterilisation to form proteinaceous deposits [16].

Solidification refers to freezing components generating on a coolant side surface, such as ice.

The formation of biofilms comprises a series of steps. The macromolecules presenting in a bulk solution transport to a surface, and then attach on the surface. The attaching microbial grow (cell-to-cell) to form a biofilm. This mechanism is shown in Fig. 2.1(b) [17]. Biofilms often develop on equipment surfaces in the food and biotechnology sectors [18] and in water treatment plants [19]. In addition, the presence of fouling deposits such as scaling facilitates nutrients to be adsorbed on equipment surfaces and promotes the growth of microorganisms.
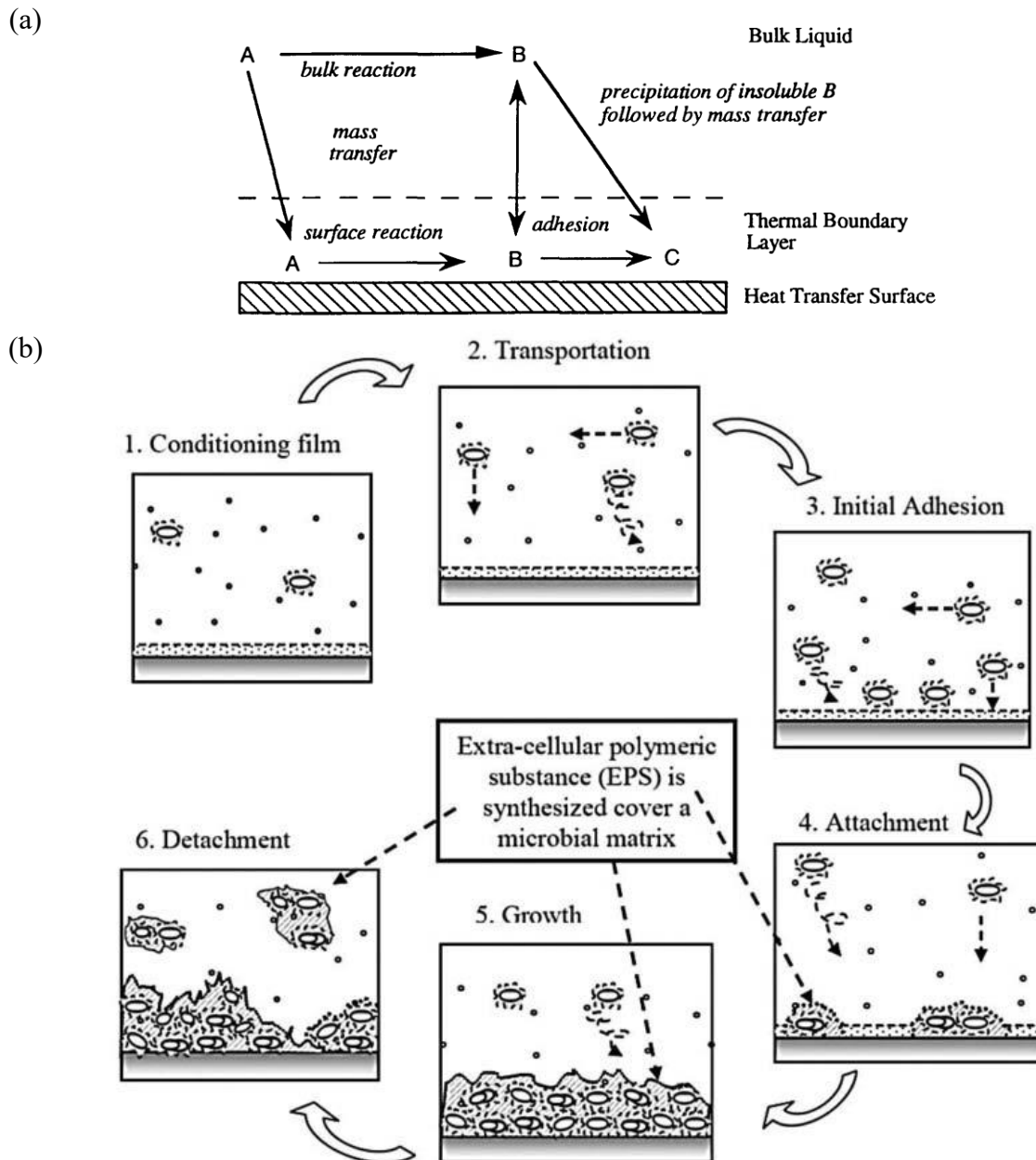
Fig. 2.1. (a) General multistep chemical reaction fouling mechanism published by Watkinson and Wilson [14]. (b) Sequential stages in biofilm formation, presented by Nonjabulo *et al*. [20] and Tiranuntakul [21].

These fouling mechanisms are complex and controlled by various factors, such as temperature, pressure, pH, fluid composition, fluid velocity, and surface properties. In order to mitigate fouling, understanding of the fouling mechanisms is needed.

Cleaning is the removal of fouling deposits from equipment surfaces, and the nature of the fouling deposit determines the most appropriate cleaning method [22]. Wilson [22] proposed a procedure for identifying factors in developing cleaning methods. Firstly, the characteristics of

the deposit need to be established. Specification of cleaning techniques, acceptable cleaning criteria, variability for current processes, and the worst case scenarios also need to be considered. A cleaning protocol subsequently needs to be validated. In addition, ageing is a critical stage in the fouling growth, as it often increases the difficulty of cleaning. Examples included the ageing of deposits on heat exchanger surfaces in crude oil preheat trans [23] and in dairies [24]. In order to alleviate the consequences caused by ageing and find the optimal cleaning cycle, monitoring and modelling can be used. For example, computational fluid dynamics (CFD) has been used to simulate the crystal growth on a heat exchanger surface [25].

Industrial cleaning methods are often categorised into *physical* and *chemical* techniques. Physical methods rely on mechanical action/forces to break attachment to the surface; chemical methods reduce the force needed to remove the layer. High pressure jets and brushing are physical methods used for cleaning in the food and biotech sectors. Pigging techniques, in which a 'pig' (a scraper) is inserted in a pipeline and driven by pressure to scrape deposits off the pipeline surface, are widely used to clear petroleum pipelines. The 'ice pigging' method, presented by Quarini *et al.*[26], sweeps deposits off the internals of process equipment by pumping a concentrated ice suspension through the item. The 'ice pig' has one noteworthy advantage: if gets stuck, it can be left to melt in place.

Chemical methods often employ multiple-agent formulations. Dosage chemicals react with the foulants, and make them weaker and easier to be removed by the available forces. Acidic agents are widely used to remove mineral scale, such as calcium carbonate scales in desalination units [27]. Alkaline-based agents are employed to clean proteinaceous deposits, making the deposits swell due to increased (antagonistic) interactions. The swelled foulants form a gel-type matrix, which is easier to be eroded by shear [28]. In general, cleaning processes combine chemical and mechanical force to achieve the removal within a desired timescale. .

For a plant which produces the same product regularly, the above fouling and cleaning processes can be considered as a fouling-cleaning cycle, reported by Wilson [29] (Fig. 2.2). The cycle starts from a pristine surface without any fouling deposition. After operating for some time, deposits attach and grow on the surface, which lowers the production efficiency and causes hygiene issues. A cleaning step is thus required to solve the problem. In order to recover the performance of the surface, several treatments need to be conducted, such as disinfection. The process also involves two different fouling components: one reversible and

one irreversible. Taking membrane filtration as an example, reversible fouling means loosely bound foulants on the membrane surface, such as cake layers. These can be removed readily by conventional physical methods. By contrast, irreversible fouling refers to deposit which forms and attaches to the membrane through strong adhesive forces. Examples are biofilm and pore-blocking. The foulant cannot be removed using physical means alone, and chemical agents are usually required [30]. However, after chemical cleaning, the performance of surface will degrade and is not the same as the pristine material. After cleaning, the surface then enters the cycle again.
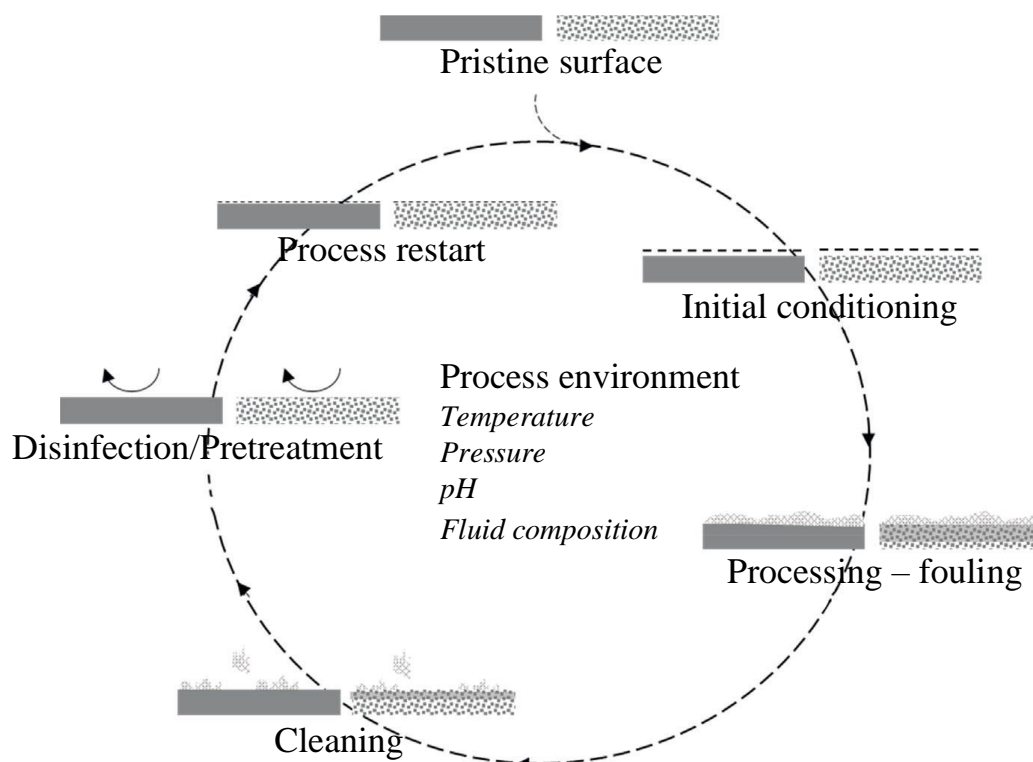
Fig. 2.2. Fouling-cleaning cycle reported by Wilson [29]. Symbols: solid bar – heat transfer surface; dotted bar – membrane surface.

In the food manufacturing sectors (*e.g.* breweries and dairies), cleaning of vessels and pipelines consumes a large amount of water and/or chemical solutions and increases downtime, resulting in a significant increase in total costs. Automated cleaning-in-place (CIP) systems are now common in modern manufacturing plants. CIP is a method for cleaning process equipment, pipelines and tanks without disassembly. The techniques used are determined by the nature of the deposit or *soil*. CIP brings several benefits, such as maintaining product quality, safety, and

reduced downtime [31]. In cases where CIP involves recirculation of water or chemical agents, it can reduce water and chemical consumptions.

The demand for food is expected to increase significantly due to the fast growing global population; however, the natural resources available are approaching their limits. In order to be able to supply sufficient food for future generations, the food sector has paid more attention to sustainability, meaning that not only the economic viability but also the environmental impact has to take into consideration. Sustainable production usually balances productivity, use of resources (*e.g.* land, water and chemicals), and pollutant emissions. In a food manufacturing process, a large volume of water is often consumed in the cleaning step, and this can be a hotspot in the food production life cycle. For example, Blondin *et al.* [32] reported that approximately 430 billion litres of wastewater were discharged in the fruit and vegetable industry in the US per year. Further studies of cleaning to promote the sustainability are thus required.

One of the methods used to quantify sustainability is life cycle assessment (LCA). As part of this work, a LCA study of cleaning-in-place operations in the production of egg yolk powder was conducted by the author in order to estimate the impact of cleaning. The assessment is presented in Appendix A. The environmental impact scores arising from the consumption of water, energy and chemicals in the cleaning process were calculated and a series of potential improvement methods were analysed. The results demonstrate that the CIP processes are hotspots in powdered egg yolk manufacturing, as in dairy processing. Both are cases where fouling and cleaning involves soft solid deposits which are difficult to clean and need to be studied *in situ*, *i.e.* examples of the materials that the FDG and millimanipulation techniques were developed to study.

2.2   *Understanding of Cleaning Mechanisms*

2.2.1 *Techniques to study cleaning mechanisms*

Cleaning mechanisms in industrial cleaning processes have been categorised into 4 groups, namely diffusive dissolution, cohesive separation, viscous shifting and adhesive detachment

(or peeling), by Joppa *et al.* [33] (see Fig. 2.3). In diffusive dissolution, the soil at the surface dissolves and is then removed from the surface by mass transfer. Examples include mineral salts in acid and sugars in water [34]. Cohesive separation and adhesive detachment happen when the force imposed on the soil layer overcomes cohesive and adhesive forces, respectively. Viscous shifting is similar to a case of two immiscible fluids (*e.g.* removal of petroleum jelly by a water jet, discussed in 2.2.4), where the soil is mobile and can be pushed out by the cleaning fluid [35].

Diffusive dissolution

Cohesive separation

Viscous shifting

Adhesive detachment (Peeling)
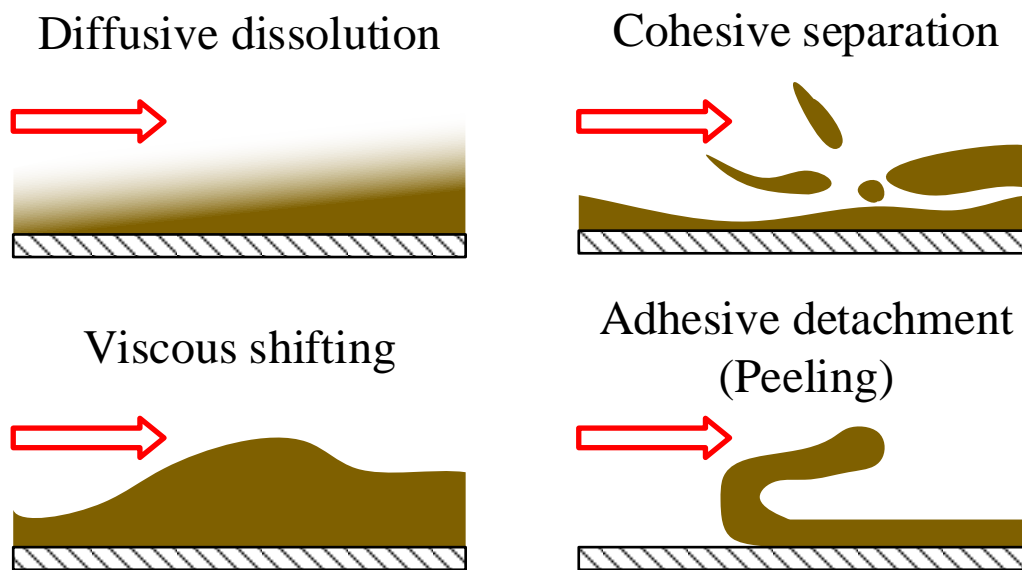
Fig. 2.3. Schematic of the modes in cleaning mechanisms (Adapted from Joppa *et al.* [33]).

These mechanisms often do not occur alone. In order to establish the most appropriate cleaning method, understanding the soil removal characteristics is required. This thesis focuses on physical cleaning methods, so measurements of fluid shear, mechanical friction, mechanical properties of fouling materials, and thickness of soil layers are necessary. In addition to these characteristics, the initial swelling of fouling layers has been reported to be an important feature when studying cleaning mechanisms [36], especially in the removal of proteinaceous fouling deposits. Xin *et al.* [37] proposed a cleaning model including this parameter for the removal of a model milk foulant from a stainless steel substrate. The initial swelling stage of proteinaceous deposits is mainly controlled by the interaction between protein and sodim hydroxide; however, the swelling rate can be very fast and difficult to monitor [38]. Saikhwan *et al.* [39] studied alkaline cleaning of a number of model proteinaceous dairy soils using FDG and reported that

the device they used could not measure the initial thickness and early swelling behaviour due to the time taken to establish gauging flow at the start of their cleaning experiments (up to 3 mins).

In addition, most fouling deposits cannot be loaded into conventional measurement devices, (*e.g.* standard rheometers or thickness gauges), so alternative methods for measuring the deposits *in situ* are desired. Some hydrodynamic devices have been used to study the mechanical properties of soils, such as the parallel plate flow cell (PPFC), radial-flow cell, rotating disc, plynometer, impinging jet and fluid dynamic gauging (FDG), as well as non-hydrodynamic devices such as millimanipulation.

The radial-flow cell consists of two parallel discs separated by a narrow gap. A liquid is pumped through a hole at the centre of the upper disk outwards through the gap, so a controlled shear stress can be generated and the adhesion forces of soil on the disc surfaces can be assessed [40]. The configuration of the rotating disk is usually a one plate system (sometimes two parallel plates). A holder filled with a sample is mounted on the disc and spun at a constant rotational speed. Cell adhesion can be quantified by measuring the number of cells before and after spinning [41]. The millimanipulation, PPFC, impinging jet, and FDG techniques are discussed in later sections.

2.2.2 Evolution of millimanipulation

In the past decade, techniques for studying the deformation of soft soils at different length scales have been developed. Zhang *et al.* [42] demonstrated a 'micromanipulation' device for investigating the bursting strength of mammalian cells. In this, a single cell was squeezed between two parallel flat surfaces, with one of the probes connected to a force transducer to monitor the force involved. Liu *et al.* [43] presented a variant of the micromanipulation technique which used a T-shaped stainless steel probe to pull a fouling deposit away from a surface, again measuring the required force. The effect of different scraping depths was studied. A modified micromanipulation tool was subsequently reported by Akhtar *et al.* [44]. The results obtained from micromanipulation were compared with results from atomic force microscopy (AFM) for deposit-surface interactions, and similar trends were observed.

14

Ashokkumar and Adler-Nissen [45] reported a scraping device which measured the force required to remove pancake cooked in place from different surface materials. Ali *et al.* [46] developed a similar mm-scale scraping device, which they called 'millimanipulation', to study the forces generated as viscoplastic layers were removed from solid surfaces. With this device, a force transducer was mounted above a platform, and the force generated on the scraping blade was measured when the platform moved and the sample contacted the blade. Magens *et al.* [9] reported an improved version of this device described for evaluating different surface coatings. Fuchs *et al.* [47] used an apparatus similar to these [9, 43, 46] to measure the binding forces of soils and their cleaning behaviour. Cuckston *et al.* [48] modified the Magens *et al.* device to include a flow system, which allowed the sample to be immersed or removed from solution before or during testing. A video camera allowed the removal behaviour of the layers to be visualised.

Millard *et al.* [49] reported a blade-coating study, whose apparatus was similar to the Magens *et al.* device [9], but at a different length scale (cm). A yield stress fluid, a Carbopol 980 gel, with different concentrations was used as the soil and occupied a 140 cm-long and 12 cm-wide channel. A vertical plate (12 cm square) was used to scrape the sample at speeds ranging between 1 and 500 mm/s. The influence of the initial liquid thickness, scrape depth, scrape speed and fluid yield stress were studied.

The working action of millimanipulation is depicted in Fig. 2.4. The vertical blade moves horizontally through the sample layer of initial thickness δ_0 at a constant velocity, V and scrape depth, s. The sample is dislodged and the blade leaves a layer with residual thickness δ. The force required to deform and move the sample is composed of three components: (i) the force to deform undisturbed material ahead of the blade (Region I), (ii) the force required to move the deformed material in I, upwards and forming a berm of height h (Region II), and (iii) the force to overcome the shear resistance acting on the blade edge (Region III) [50]. Ali *et al.* [46] showed a method to record the deformation of their test soil, Vaseline™, by marking the sample with black lines as reference points. Millard *et al.* [49] presented particle image velocimetry (PIV) measurements based on tracking bubbles present inside the sample to estimate the local velocity.
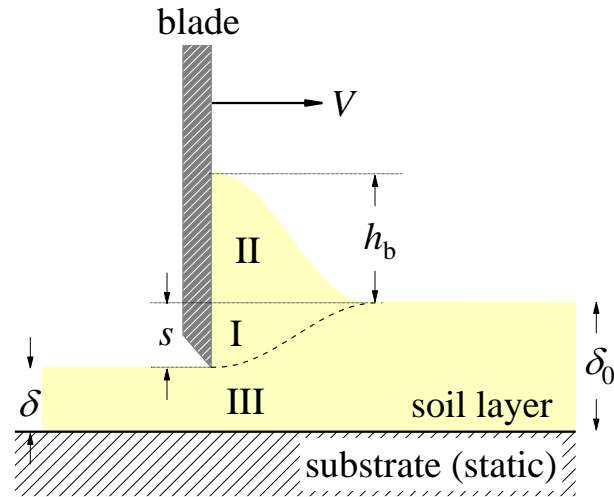
Fig. 2.4. Schematic of millimanipulation action, adapted from Ali *et al.* [46].

Numerical simulations have been used to predict the behaviour of samples during micromanipulation. Mercade-Prieto *et al.* [46, 51] utilised the finite element method (FEM) code ABAQUS to simulate the compression of core-shell capsules between two parallel plates. However, they did not extend the model to the mode reported by Liu *et al.* [43]. Simulations of the millimanipulation geometry have yet not been reported. Although the Ali *et al.* millimanipulation device could measure the removal force for soft solid layers, the information is limited in terms of applicability (*e.g.* scale up). The distributions of velocity and shear stresses generated during testing are important for cleaning. A model to predict and provide this information thus needs to be developed.

2.2.3 Techniques and modelling of duct and pipeline cleaning

The PPFC is the most common device used for studying microbial adhesion to surfaces immersed in an aqueous environment, in which the rate of adhesion is determined by calculating the number of microorganisms transported to the surface at a controlled mass flow rate [52]. Bakker *et al.* [53] employed CFD simulations to establish the velocity profiles for four different PPFCs, and the numerical results were validated by the profiles measured by particle image velocimetry.

16

CIP cleaning of a pipeline is also popular. A number of studies of interactions between immiscible fluids in pipe cleaning applications have been conducted. Cole *et al.* [54] investigated the cleaning of toothpaste in a pipe by passage of a second fluid (water) to flush the soil out. Experiments at both lab and pilot scales were conducted. Three removal steps were identified, namely core removal, thin film removal and patch removal. In the core removal step, the bulk of the soil was removed from the pipe. The residual layer near the wall was then sheared away by the cleaning fluid (thin film removal). In the final stage, called patch removal, residual patches was removed. Alba and Frigaard [55] studied cleaning of viscoplastic fluids from an inclined pipe. An integrated experimental-theoretical approach (control volume analysis) was created for estimating the interfacial and shear stresses. The solutions were compared with the results measured by Ultrasonic Doppler Velocimetry, which showed that the model could predict the interaction between Newtonian and shear-thinning fluids well. However, the approach overestimated the cleaning velocity due to the fact that the inertial stresses at the soil front was not considered.

In addition to the integrated experimental-theoretical approach, CFD modelling has also employed. de Sousa *et al.* [56] used Galerkin FEM approaches to simulate the displacement of fluids by gas in capillary tubes. Two materials were tested, including a power-law shear-thinning liquid and a viscoplastic fluid simulated by the Bingham-Papanastasiou model [57]. Experimental data from the literature were reproduced by the simulations with good agreement. A decrease of residual layer thickness caused by increasing the viscosity was observed. Thompson *et al.* [58] subsequently improved the de Sousa *et al.* model and found that the mass fraction of layers on the wall depended on the power-law index, so the efficiency of gas-displacement for shear-thickening fluids was lower than that of Newtonian and shear-thinning fluids. Subsequently, Freitas *et al.* [59] numerically analysed the interactions between two viscoplastic fluids in a plane channel using FEM. Both fluids were simulated by the Bingham-Papanastasiou model [57], and the interfacial capillary forces between them were considered The results showed that compared to changing the yield stress of the displacing fluid, changing the yield stress of the displaced fluid had greater more impacts on removal.

2.2.4 Techniques and modelling of impinging jet

Impinging liquid jets, emitted by moving nozzles and static or rotating spray balls, are commonly used for cleaning industrial tanks and vessels. The soil is removed directly by the jet hitting the deposit surface or by the radial thin film flowing away from the point of impingement. The film generates a high shear stress which erodes or peels the deposit away. Currently, automated CIP systems are designed and constructed based on a series of empirical studies. To aid of the development of impinging jets and minimising the risks and costs, a model of impinging jet cleaning is required.

A number of experimental studies and analytical models for impinging jets have been reported. Yeckel and Middleman [60] considered the case where the radial film generated by an impinging water jet removed a viscous oil film on a horizontal substrate. The oil was removed by the radial shear flow induced by the jet [60]. Buoyancy effects, and the effect of the oil motion on the water flow, were not considered. The model for the oil flow was based on the Reynolds lubrication approximation. Hsu *et al.* [61] investigated impinging jet rinsing flows on both Newtonian and elastic fluid layers. For Newtonian fluids, the growth of cleaning circle was nearly linear, but the elasticity of the viscoelastic fluids caused 'recoil' of the circle. Walker *et al.* [62] extended the Hsu *et al.* work to study the free surface of non-Newtonian coating fluids by a rinsing water jet. The results demonstrated that the flow structure depends on the viscosity ratio between the jet and the soil.

Wilson *et al.* [63] presented an analytical model for the flow of a liquid film generated by a liquid jet impinging on a vertical wall. The momentum in the liquid film per unit length, *M*, was given by

$$M = \frac{6}{5}\rho U^2 h_f \qquad (2.1)$$

where ρ is the liquid density, U is the average velocity in the film and h_f the film thickness. Wilson *et al.* [64] subsequently presented results for cleaning of petroleum jelly from vertical and horizontal plates by water jets impinging normally on a flat substrate. The rate of growth the circular cleaned area (radius: *a*) was proportional to *M* :

$$\frac{da}{dt} = k'M \qquad (2.2)$$

18

The key part of this work was the assertion that some soft solids are removed by a peeling mechanism. Glover *et al.* [65] proposed a model for the cleaning of two soil layers, polyvinyl acetate (PVA) and petroleum jelly, by an impinging water jet. The model of cleaning by jets was created by fixed and moving nozzles in batch processes (fixed jet).

Bhagat and Wilson [66] developed the Wilson *et al.* model [63], describing the hydrodynamics in the thin film as involving three flow regions, namely a boundary layer formation zone (BLFZ), laminar film zone (LZ) and turbulent zone (TZ). Bhagat *et al.* [67] identified scenarios of 'strong' and 'weak' soils. The strong soil is one which is difficult to remove so *a* is close to the jet radius, and vice versa. Fernandes *et al.* [68] subsequently modified the Bhagat *et al.* models to describe cleaning of viscoplastic layers (a commercial petroleum jelly) from Perspex and glass surfaces using impinging water jets. They measured the shape of the berm of removed material: it depended on the ratio of the water film thickness to the initial thickness of the layer.

Although these analytical models can give exact solutions, they are based on some assumptions and cannot be applied to more complex problems and geometries. For complex cases, numerical methods (*e.g.* computational fluid dynamics, CFD), are required. CFD is a numerical method for predicting fluid flow behaviour by solving the equations of fluid motion. In CFD analysis, the spatial domain is divided to a number of mesh points or elements, and numerical solutions are matched to these points [69]. Thus, CFD can deal with very complex geometries. Numerical simulations for estimating soil cleaning using an impinging liquid jet are limited. Joppa *et al.* [33] presented a CFD simulation of jet cleaning of a swellable starch-based model soil introducing diffusive dissolution. A transient Dirichlet boundary condition [70] was employed for calculating the volume fraction of soil, based on two assumptions: the effect of the layer thickness on the flow was negligible and the layer remained smooth during cleaning. The results were validated successfully and could be applied for more complex geometries and conditions.

Although the Joppa *et al.* [33] case simulated deformation of the layer surface, the effect of the layer thickness on the impinging flow was neglected. Numerical simulations for the interactions between the soft film surface and jet flow are still limited, and more studies are required.

2.3   Techniques for Measuring Layer Characteristics

2.3.1 Introduction

Knowledge of the characteristics of fouling deposits are critical for cleaning, but studies and analysis of deposit characteristics are challenging because the soil layers are often immersed in aqueous environments and some (*e.g.* foods and biofilms) collapse when touched. Not only availability, but also affordability of the measurement techniques are important. Current methods for monitoring the characteristics of fouling layers are summarised and compared in Table 2.1.

Table 2.1. Research techniques for studying characteristics of fouling layers

Technique	Properties of soils	*in situ*	Spatial resolution	Reference
Energy dispersive X-ray spectroscopy (EDX)	Chemical composition and metallic coating thickness	No	10 nm	[71-73]
X-ray diffraction	Crystallographic structure and chemical composition	No	NA	[73, 74]
Atomic force microscopy (AFM)	Adhesion force and surface roughness	No	nm	[72, 75, 76]
Confocal microscopy	Surface roughness	Yes	μm	[77, 78]
Fluid dynamic gauging (FDG)	Surface topography and strengthens	Yes	~5 μm	[79]
Magnetic resonance imaging (MRI)	Spatial information	Yes	~100 μm/pixel	[80-82]
Scanning electronic microscopy (SEM)	Surface topography and composition	No	20 nm	[72, 83]
Ultrasound	Element thickness	Yes	10 μm	[84, 85]
White light interferometry	Surface morphology, roughness and thickness	Yes	~5 μm	[86, 87]

Atomic force microscopy (AFM) is a type of scanning probe microscopy with a very high resolution of about nanometre using a sharp tip (probe) to scan the sample surface. The measured deflection force between the tip and surface can be used to describe the surface properties, such as Young's modulus and stiffness [76]. Goode *et al.* [75] used AFM to measure the adhesion forces between different substrates (stainless steel and fluoro-coated glass) and soils (whey protein, condensed milk and caramel). However, the AFM tip was easier to be functionalised by the substrate surfaces than the deposits, so the tip was modified before tests using SS and glass microparticles.

Confocal microscopy is an optical microscopy technique using a spatial pinhole to eliminate out-of-focus light for enhancing resolution, to micrometre scales [78]. The technique was used

by Piepiórka-Stepuk *et al.* [77] to study milk fouling on stainless steel substrates with different roughnesses.

Ultrasound thickness sensing is a non-destructive method for measuring the thickness of a solid object by calculating the time period between emission and return of the ultrasound wave. Ubeda *et al.* [84] developed a low-power ultrasound gauging system to measure the removal of milk foulant inside a heat exchanger with a detection accuracy of more than 80%.

X-ray diffraction (XRD) is used to determine chemical composition and crystallographic structure by analysing elastic scattering of X-ray photons by atoms in a periodic lattice, using Bragg's law [74]. Hagsten *et al.* [73] used XRD to study the crystalline structure of high temperature milk fouling deposits.

Energy dispersive X-ray spectroscopy (EDX) is an analytical technique for measuring composition distributions of samples by analysing the interaction between the source X-ray and the sample. Li *et al.* [72] analysed the fouling properties including composition and surface topographies on zirconia ceramic ultrafiltration membranes for filtering limed sugarcane juice using AFM, EDX, scanning electronic microscopy (SEM), and Fourier-transform infrared spectrometry (FTIR). SEM utilises a focused electron beam to scan the sample surface, and the signals generated by the interaction between the beam and sample are used to detect the surface topography and composition [83].

Magnetic resonance imaging (MRI) is a non-invasive technology which can produce 3-dimensional images of non-ferric samples and has been widely used for disease diagnosis. The principle of MRI is to use a strong static magnetic field to align protons in the sample, and radiofrequency pulses are then applied to excite these protons. The energy subsequently released from the protons can be detected and the phenomenon is called nuclear magnetic resonance (NMR). Electric signals do not include spatial information, so a gradient magnetic field is employed to generate a 3D image [82]. Creber *et al.* [80] reported a MRI study of biofilm accumulation and shrinkage during cleaning of reverse osmosis membranes. The distributions of both water flow and biofilm inside a membrane module was captured by MRI and good agreement was obtained between experimental and lattice Boltzmann simulations.

White light interferometry is a non-destructive measurement method in which light traveling from the target surface to a certain point is detected for estimating the surface roughness of a

sample [87]. Larimer *et al.* [86] utilised an interferometric optical microscope to monitor the thickness and surface morphology of *P. putida* biofilms over time, and the measured thickness of bacterial growth showed good agreement with a theoretical prediction.

Although these existing techniques can help to understand the characteristics of soils, not all can measure the material's properties *in situ*. Even though measurements *in situ* are feasible, the installation is often expensive, such as ultrasound and MRI. An affordable technique is still desired.

2.3.2 Fluid Dynamic Gauging (FDG)

In the food and biotechnology sectors, some fouling deposits have proved difficult to remove and measure, since these layers are often weak and contain a large amount of liquid, and collapse when removed from their immersed environment. Conventional mechanical instruments such as thickness gauges cannot measure the thickness of this type of soil layer accurately and easily. While the accuracy of measurement by some non-contact methods discussed above (*e.g.* ultrasonic) is high, installation of these is often expensive or may not be feasible [6].

The technique of fluid dynamic gauging (FDG), firstly proposed by Tuladhar *et al.* [7], was developed to deal with this problem. The concept built on the existing method of pneumatic proximity gauging, reported by Macleod *et al.* [88], but using a liquid as the fluid rather than a gas. FDG allows measurement of the thickness of soft solid layers *in situ* in real time. A schematic of a typical FDG nozzle and the principle of FDG operation are shown in Fig. 2.5. Liquid is ejected or withdrawn from a nozzle located near the deposit surface. The thickness of the layer is estimated in three steps. (i) Firstly, an alternative method is used to determine the clearance, h_o (the nozzle relative to the substrate). (ii) The clearance, h, between the nozzle and layer is determined thus: when liquid is withdrawn and/or ejected through the nozzle at a set mass flow rate, $\dot{m}$, the pressure drop across the nozzle, $\Delta P = P - P_0$, will be a function of $\dot{m}$ and the nozzle geometry.

$$\Delta P = f(\dot{m}, h/d_t) \tag{2.3}$$

23

where d_t is the diameter of nozzle throat. The measured pressure drop at a controlled mass flow rate can thus be used to determine h, and (iii) thereby to establish the thickness of the soft layer, from $\delta = h_o - h$. In general, ΔP is expressed as a discharge coefficient, C_d, which is a normalised energy loss across the nozzle [89]:

$$C_d = \frac{\dot{m}_{actual}}{\dot{m}_{ideal}} = \frac{4\dot{m}}{\pi d_t^2 \sqrt{2\rho\Delta P}} \qquad (2.4)$$

The development and applications of the FDG technique are summarised in Table 2.2. The first FDG device, reported by Tuladhar *et al.* [7], consisted of a siphon tube, one end of which was a nozzle positioned near to the surface being gauged by a micrometre screw gauge and immersed in a reservoir, and the other end was connected to a flow rate measuring device. Fig. 2.6 is a schematic of their device. When the liquid level was fixed, the suction pressure would be equivalent to the hydrostatic head under siphon action. The volume of liquid flowing out of the tank through the siphon tube was measured over time, and the thickness measurement could be calculated using Eq. (2.3). Measuring the mass flow rate to estimate the thickness is denoted 'mass mode' or 'flowing mode'. In this setup, only suction mode measurements can be made. The technique was employed for measuring the thickness change of whey protein deposits, supermarket butter and sticky foam on SS substrates in water and NaOH solution. Tuladhar *et al.*[90] subsequently monitored the growth of ice films in a duct flow of 10% sucrose solution with a flow velocity of $400 < Re$ (Reynolds number) < 2000, and the results proved that FDG could perform measurements in a high Re duct flow (up to 10,000).
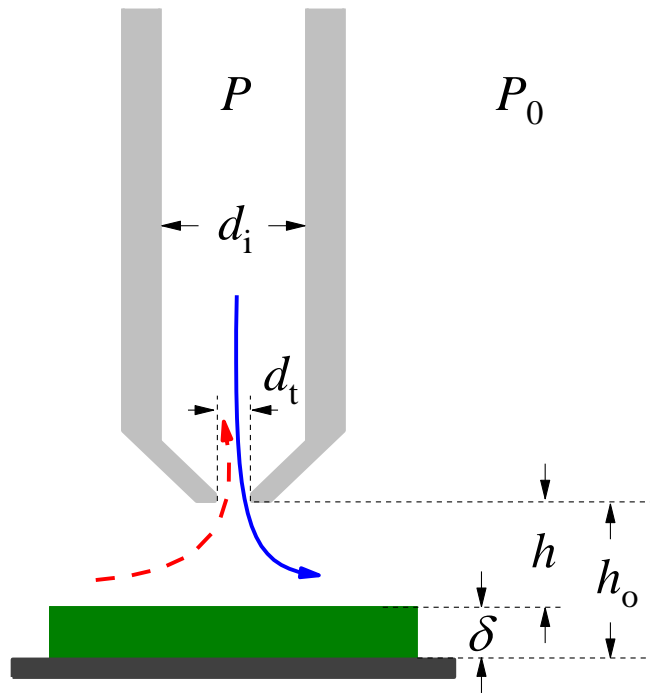
Fig. 2.5. Schematic of FDG operation. Solid and dashed streamlines indicate ejection and suction modes, respectively.

Chew *et al.* [79] extended the FDG technique to quantify the strength of tomato paste fouling deposits and its removal characteristics. A CFD model was created to predict the shear stress exerted on the layer surface induced by the FDG flow. Changes in thickness, measured by FDG, could then be used to estimate the deposit strength. The estimated shear stress for removing the tomato paste could be extended to predict the required velocity for cleaning the paste in a pipeline. Chew *et al.* [91] subsequently used an FDG device to measure the swelling of two polystyrene co-polymers in various commercial solvents for cleaning of emulsion polymerisation reactors. The removal behaviour of the materials was related to the swelling rate and dissolution of the layers, and could be extended to find the optimal cleaning strategies and schedule batch production.

In a further application of FDG reported by Chew *et al.* [92], filter papers and suspensions of glass ballotini suspensions were employed to mimic dead end microfiltration. The FDG nozzle was located above the paper to monitor the growth of fouling layers. This study confirmed that FDG could be used to gauge layers on porous surfaces such as filters and membranes *in situ*, in real-time.
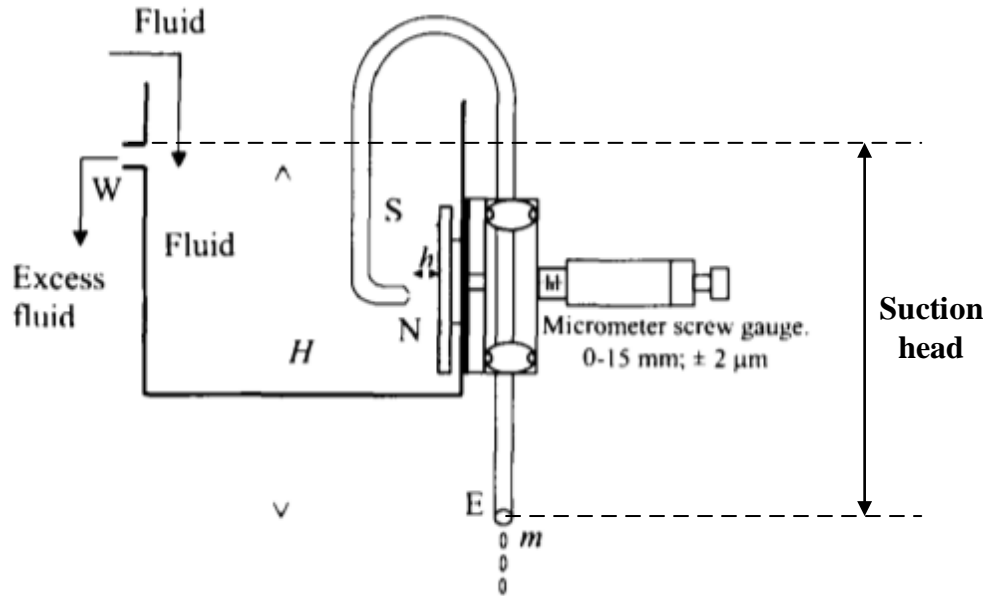
Fig. 2.6. Schematic diagram of the first FDG apparatus, reproduced from Tuladhar *et al.* [7].

Gu *et al.* [89] employed the FDG technique to measure the thickness of layers on a curved surface. A cylindrical SS rod positioned inside an acrylic tube served as the gauging surface, and the FDG gauge was mounted in the outer wall of the annular channel to make measurements on the rod. Cases with slower and with turbulent annular flows ($14000 < Re < 32000$) were investigated. In general, the measured mass flow rate depends on the clearance, but one exception was observed in their experiments. The mass flow rate was independent of the clearance at small clearance ($h/d_t < 0.1$) due to leakage from the small gap between the nozzle rim and curved surface.

Gordon *et al.* [93] constructed an automated, scanning FDG (sFDG) for measuring the thickness of soil layers at several points on the same sample by installing two perpendicular linear slides under the water tank, which allowed the nozzle to move to different points on the sample. Gelatine, polyvinyl alcohol (PVA) and baked tomato purée deposits were gauged with a resolution of ±5 μm, and the feasibility of using sFDG as an imaging device was demonstrated.

Jones *et al.* [94] proposed 'pressure mode' operation by fixing the flow rate of liquid withdrawn through the nozzle and recording the pressure drop, for measuring the thickness of fouling deposits in dead-end and cross-flow microfiltration. Lewis *et al.* [95] studied the thickness and strength of cake foulants during microfiltration of suspended *Saccharomyces cerevisiae* yeast

using FDG. Ali *et al.* [96] measured the thickness of fouling deposits on a curved surface in opaque and viscous mineral oil with a viscosity of 44 mPa s at elevated temperature and pressure. The results showed that the practical working range of h/d_t from 0.05 to 0.25 was not affected by pressure and temperature.

Yang *et al.* [97] subsequently presented a different operating mode for FDG, namely zero-discharge fluid dynamic gauging (ZFDG), wherein a fixed volume of gauging liquid was withdrawn and then ejected through the nozzle using a syringe pump, so that the net flow of liquid was zero with advantages for hazardous, sterile and aseptic operations. Wang and Wilson [98] subsequently used an automated ZFDG device to monitor swelling of PVA and gelatin layers over time at different pH, and the measurements showed good agreement with gravimetric methods. Lemos *et al.* [99] subsequently reported a ZFDG device for measuring the thickness of biofilms and the shear stress required to remove these from a cylindrical surface. Tests for *Pseudomonas fluorescens* biofilms on both high density polyethylene and SS cylinders were conducted.

Lewis *et al.* [100] reported an investigation in the development of an automatic and more accurate FDG system for measuring the growth rate of cake foulants in cross-flow filtration. A linear variable differential transformer (LVDT) with a resolution of ±0.5 µm was installed on the gauging nozzle to indicate its position and enhance accuracy. A resolution of the clearance relative to the layer surface, from −6 µm to +7 µm, was achieved. Wang *et al.* [6] then introduced an extended application of ZFDG to measure the thickness of soft solid layers immersed in a series of Newtonian liquids with a range of viscosities, from water to paraffin oil, under aseptic (closed system) conditions. The aseptic condition was achieved by fitting a flexible polypropylene film over the top of the tank.

A study of cake growth during microfiltration of Kraft lignin suspensions using FDG was carried out by Lewis *et al.* [101]. The transition points for pore blocking were identified, and a significant flux decline of approximately 75 %, resulted from pore fouling, was observed. An approach for diagnosing membrane fouling was presented. This experiment showed good agreement with the critical flux model, indicating that it was available to be applied for improvements of microfiltration. Wang *et al.* [8] subsequently applied the ZFDG system for quantifying the shear stress of bacterial spore removal from different substrates and monitoring

27

the erosion rate of *Rhodopseudomonas plaustris* biofilms from with and w/o graphene-coated carbon papers.

However, so far, two major challenges for operating FDG devices remain to be solved. One is that measurements require a second method to determine the clearance between the nozzle and the substrate. For example, in the operation of the current ZFDG device reported by Wang *et al.* [8], feeler gauges were employed to determine the initial clearance, which introduces some inaccuracy to measurements of thicknesses of soil layers. It is also a very time-consuming process. A second issue is that several minutes can elapse after the sample is initially immersed, before reliable measurements can be made. Soft solid layers can change their properties noticeably over these time periods, so it would be advantageous to eliminate this delay.

Table 2.2. Evolution and applications of the FDG technique (E – experimental-based; CFD – computational fluid dynamics simulations)

Year	Applications	Gauging liquid	Gauging materials	E/CFD	Ref.
2000	Thickness measurement in fouling studies	Water and alkali (NaOH) solution	Whey protein deposit, supermarket butter and sticky foam	E	[7]
2002	Swelling and removal of whey protein to CIP of dairy heat exchanger fouling deposits	NaOH solution	Whey protein films	E	[28]
2003	Monitoring the swelling of soft films in flowing systems	Water and sucrose solution	SS plates and ice deposits	E	[90]
2004	Measurement of the strength of soft deposits	Water and sucrose solution	Tomato paste	E/CFD	[79]
2004	Validation of FDG simulation	Water and CMC solution	316 SS plates	E/CFD	[102]
2006	Study of cleaning kinetics	NaOH and sodium metasilicate solution/ cleaning agent (TPU) and organic solvent MEK	Polystyrene co-polymers	E	[91]
2006	Study of removal of food soils for surface treatment	Water	Baked tomato paste	E	[103]
2006	Study of cleaning of milk fouling deposits	NaOH solution	Whey protein foulants	E	[104]
2007	Study of fouling layers on porous surface (micro- and macro-filtration)	Ballotini suspension in water	Ballotini fouling on filter papers	E/CFD	[92]
2009	Thickness and strength measurement on curved surface	Water	316 SS and acrylic curved surfaces	E/CFD	[89]
2009	Operation in duct flows	Water	Perspex surface	E/CFD	[105]
2010	Investigation in fouling deposition of microfiltration	Ballotini suspensions in dodecane and water	Ballotini fouling on membranes	E	[94]
2010	Studies of swelling kinetics and deformation behaviour	Water	Layers of gelatine, polyvinyl alcohol (PVA) and baked tomato deposits	E	[93]
2011	Thickness measurement for fouling and cleaning in annular devices	Water and water with whey protein	316 SS rod and whey protein fouling	E/CFD	[106]
2011	Study of cake build-up in cross-flow microfiltration	Ballotini suspensions in water	Ballotini cakes	E/CFD	[107]

2011	Optimisation of FDG nozzle (CFD modelling)	Water		CFD	[108]
2012	Investigation in enzyme-based cleaning	Protease and buffer solutions	Gelatin and egg yolk films	E	[109]
2012	Study of cake fouling in cross-flow microfiltration	Yeast suspension in water	Yeast cakes on membranes	E	[95]
2013	Thickness measurement of fouling deposits in opaque liquids	Mineral oil	Oil deposits	E/CFD	[96]
2014	Study of removal of cohesive fouling layers	NaOH solution	Waxy maize starch layers	E	[110]
2014	Thickness measurement of soft solid layers	Water	Petroleum jelly layers	E/CFD	[97]
2015	Study of swelling of soft solid layers	Water and NaOH solution	Poly(vinyl acetate) (PVAc) and gelatin films	E/CFD	[98]
2016	Measurement of cake thickness in ultrafiltration	TiO_2 suspension in water	TiO_2 cake	E/CFD	[111]
2016	Measurement of biofilm thickness on cylindrical surfaces	Nutrient medium	*Pseudomonas fluorescens* biofilms	E/CFD	[99]
2016	Cake fouling studies in cross-flow filtrations	Water	Yeast deposits	E/CFD	[100]
2016	Swelling and hydration studies	Alkaline solutions	Egg yolk layers	E	[112]
2016	Thickness measurement of soft layers	Water, sucrose solutions, glycerol and paraffin oil	316 SS discs	E/CFD	[6]
2017	Investigation of cake fouling in cross-flow microfiltration	Kraft lignin suspension in water	Kraft lignin cakes on membranes	E	[101]
2017	Studies of cake thickness and strength for microfiltration	Kraft lignin suspension in water	Kraft lignin cakes on membranes	E	[113]
2017	Assessment of adhesion of *Bacillus* spores	Water	*Bacillus* films	E	[114]
2018	Study of cleaning for complex food soils	Water and NaOH solution	Layers of complex fat, protein and carbohydrate soil mixture	E	[115]
2018	Investigation of cake thickness and cohesive strength in microfiltration	Kraft lignin suspension in water	Kraft lignin cakes on membranes	E	[116]

2018	Measurement of thickness and strength of biofilms	Nutrient medium	*Escherichia coli* and *Burkholderia cepacia* biofilms	E	[117]
2018	Measurement of thickness and strength of biofilms in cross flow filtration system	Nutrient medium	*Pseudomonas aeruginosa* PAO1 biofilm	E	[118]
2018	Study of biofilm and spore removal	Water	*Rhodopseudomonas palustris* biofilms, *Bacillus cereus* and *B. megaterium* spore	E	[8]
2019	Study of fouling layers on membrane surfaces	Microcrystalline cellulose (MCC) suspension in water	MCC fouling layers	E	[119]
2019	Study of initial swelling of soft sold layers	Water and NaOH solution	Petroleum jelly, poly(vinyl acetate), gelatin and complex model soil layers	E/CFD	[120]
2019	Study of soil layers immersed in various liquids	Water, UHT milk, Washing-up liquid, 1 wt% and 3 wt% carboxy-methylcellulose solutions	Skimmed milk ice films	E/CFD	[121]

2.3.3 CFD Studies of FDG

Tuladhar *et al.* [28] reported that the forces induced by FDG flows on soft layers could cause deformation of the surface, which resulted in inaccuracy to thickness measurements. However, due to the deformation, the gauging flows could be employed to estimate the strength of sample layers. In order to understand the FDG flow patterns and estimate the stresses imposed on the layer surface, calculation methods are required.

The first numerical investigations for FDG were conducted by Chew *et al.* [102], using the commercial partial differential equation solver, *Fastflo^{TM}* to solve the governing continuity and Navier-Stokes equations. Different axisymmetric FDG nozzle shapes with Newtonian liquid flows were simulated to estimate wall shear stress distributions.

Colombo and Steynor [122] performed experiments in a geometry similar to FDG using a non-Newtonian fluid (carboxymethyl cellulose (CMC) solution) at various concentrations (less than 1%). They observed that the ratio profile of mass flow rate and clearance were similar to those for Newtonian fluids. The CMC solution could be simulated as a Newtonian fluid by characterising the C_d values and Metzner–Reed Reynolds number [123]. Chew *et al.* [102]

tested the applicability of this approach for FDG with power-law fluids. However, the shear stress distribution of FDG could not be calculated, because in the approach, a constant viscosity was used, which could not describe the local behaviour of CMC.

Chew *et al.* [92] subsequently simulated the flow field and stress distribution on a porous surface (membrane), where Darcy's law was used to quantify the local flux through the membrane. The predicted pressures agreed with measured pressures, demonstrating that the flow patterns depended on the Reynolds numbers of nozzle throat and filter paper, and h/d_t.

Gu *et al.* [89] presented CFD simulations for FDG in turbulent annular flows ($14000 < Re < 32000$) and on a curved surface using the commercial finite-element-based software COMSOL Multiphysics®. Good agreement between experimental and simulation results was obtained for quasi-static case, but for turbulent case, the simulations could not be attempted due to divergence at high Reynolds numbers. Gu *et al.* [105] subsequently simulated FDG in steady, laminar, duct flows. The numerical solutions showed good agreement in C_d with the experimental results, within 6 %, and proved the applicability of CFD simulations for predicting the flow fields of FDG. Peralta *et al.* [108] used CFD simulations to find the optimal nozzle external geometry of the FDG nozzle. The numerical results were compared with analytical solutions based on lubrication assumptions and very good agreement was obtained.

These simulations focused on Newtonian fluids; however, in the food and biotech sectors, many cases involve non-Newtonian fluids, such as ketchup [124] and honey. In order to estimate the FDG flow pattern, CFD simulations including a viscosity model are needed. The other issue is that the surface being gauged has, up to now, been assumed to be flat and rigid. The case of coupled flows, of FDG interacting with a deformable soil layer, remains to be studied. This would allow one to derive more information from gauging tests on such layers.

2.4 Summary

Cleaning is an important operation in the food and pharma sectors and optimisation of cleaning operations is important for improving the sustainability of these industries. This requires quantitative knowledge of cleaning mechanisms, soil properties and behaviour. Techniques for studying mechanisms and measuring the characteristics of fouling deposits have been

reviewed. Some challenges in these techniques have been identified, and this dissertation focuses on three employed in the P⁴G research group at Cambridge.

Millimanipulation

The current millimanipulation device proposed by Magens *et al.* [9] can only measure the removal force of soft solid layers, which limits its applicability. Other properties and removal behavior of soft solid layers are very important while exploring the cleaning mechanisms. Extending the capability of the device is required.

FDG

Two challenges for operating FDG devices been identified. One is that before measurements are made, a second method is needed to determine the location of the substrate, which affects the accuracy of thickness measurements. A second is that several minutes can pass after the sample is initially immersed before measurements can be made. Soft solid layers can change their properties significantly over this time period. Eliminating this initial period is desirable.

In order to deepen the understanding of cleaning processes and further find more sustainable operations, the above challenges need to be solved. This dissertation aims to improve the existing techniques and develop new devices. More quantitative information about soft solid layers is collected from the current millimanipulation device. It is tested by studying the removal behaviour of viscoplastic layers, including commercial petroleum jelly, pharmaceutical soft white paraffin and commercial toothpaste.

Two innovative FDGs are designed, constructed, and commissioned. One of which can feature the initial behaviour of samples while being immersed into liquid without delay. A series of demonstration tests are performed using this device for studying the swelling and removal behaviours, on soft layers of petroleum jelly, polyvinyl acetate, gelatin and a complex model soil. The other can determine the clearance and thickness simultaneously. The concept is tested for different substrates, including copper and mild and stainless steel as well as various gauging

liquids, including water, whole ultrahigh-temperature milk, commercial washing-up liquid and 1 and 3 wt % carboxymethylcellulose solutions (non-Newtonian).

In addition to the new devices, more information can be obtained from CFD modelling of the flow and the deformation of the soil. In the millimanipulation case, this is a free boundary problem with a soil of complex rheology as well as a moving wall. In the FDG case, with is a coupled two-phase problem between a Newtonian and a non-Newtonian fluid. A series of CFD models for both millimanipulation and FDG cases are constructed based on the real geometries and tested at different conditions. These are validated and compared with the experimental data.

The experience gained from developing these CFD approaches allows the author to consider other multiphase problems, and a short study of cleaning a viscoplastic soil by an impinging liquid jet is investigated and presented.

Chapter 3   Deformation of Viscoplastic Fluid in Millimanipulation

3.1   Introduction

As discussed in previous chapters, understanding the interaction between the soft solid layer and the substrate is required for designing an efficient cleaning system. A number of existing hydrodynamic methods have been used to quantify the removal behaviour of materials immersed in a liquid environment to mimic cleaning, such as the parallel disc flow chamber [53], impinging liquid jets [65], and fluid dynamic gauging [8].

Conventional methods have also been employed to measure deformation forces for layer materials at different length scales, such as atomic force microscopy (AFM)[44] at the nanoscale and indentation at the mm-scale. Indentation testing has been widely employed for measuring mechanical properties of materials. An indenter is pressed into the sample surface at a given speed, and the force, penetration depth and deformation are measured. A constitutive model is used to estimate the associated material properties. Huang *et al.* [125] used 'normal' indentation to assess the elastic modulus, yield stress, plastic flow consistency and plastic flow index for the model elastoviscoplastic material, plasticine®. Fig. 3.1 shows results for indentation on petroleum jelly and soft white paraffin. The profiles are noisy and do not present useful information for either materials. The mm-scale millimanipulation device presented by Magens *et al.* [9] is thus employed for studying the removal of such soft layers.
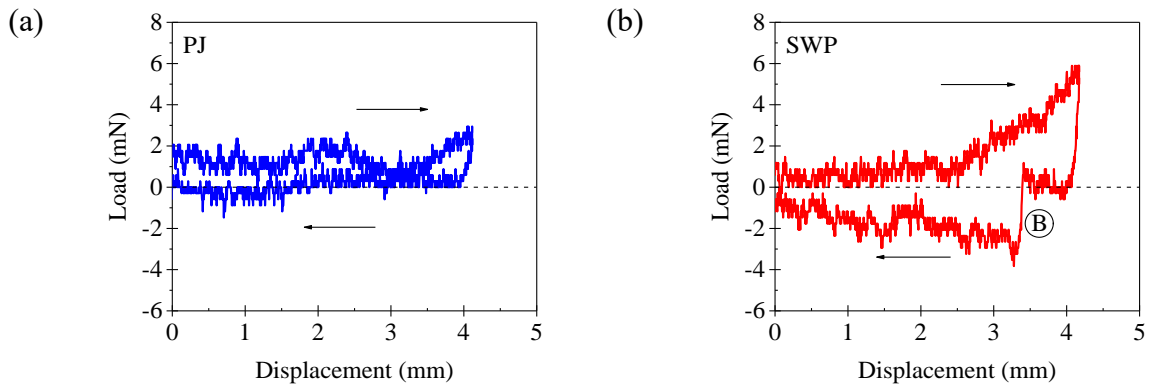
Fig. 3.1. Indentation results for (a) petroleum jelly and (b) soft white paraffin. 5 mm thick, 30 mm square samples were prepared on a 316 stainless steel substrate using a spreader. The tests were performed by the author using a texture analyser (TA.XT plus, Stable Micro Systems) equipped with a 14.23 mm diameter hemispherical probe at 20 °C. The probe speed and trigger force were 1 mm/s and 0.01 g, respectively. Black arrows denote the direction of the probe (→ downward; ← upward). The bump at B is caused by adhesion to the probe.

Fig. 3.2(a) shows the action of the millimanipulation device. A vertical blade moves horizontally through a sample layer with initial thickness, δ_0, and length, L, at a fixed velocity, V, and depth s, generating a heap ahead of the blade with height h_b and length b, leaving a layer of thickness δ behind the blade. The distance that the blade travels through the sample and the length upstream of the blade are labelled x and $L - x$, respectively. The force required to dislodge the layer has contributions from three regions (Fig. 3.2(b)). That in region I is associated with making the material deform; that in region II does work in pushing the dislodged material up the blade. The region III force overcomes the resistance experienced by the bottom of the blade, which can be mitigated by bevelling the edge [50].

36
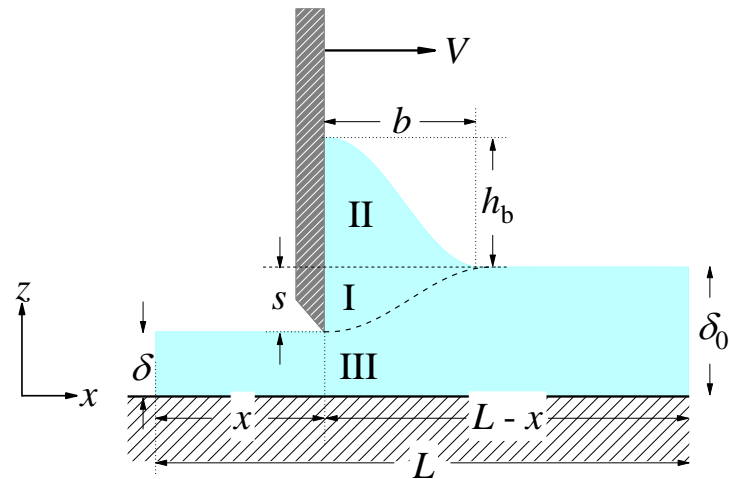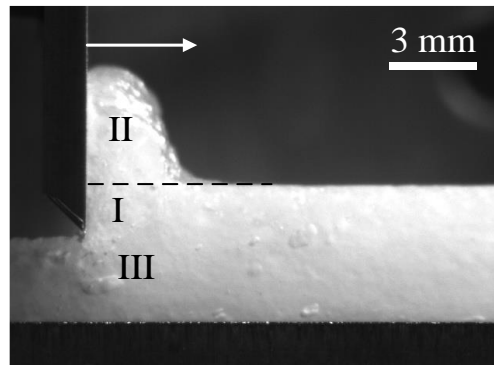
Fig. 3.2. (a) Schematic of millimanipulation action, adapted from Ali *et al.* [46], and (b) photograph of pharmaceutical soft white paraffin during millimanipulation testing ($\delta_0 = 5$ mm, $s = 2$ mm).

In this chapter, three viscoplastic materials, namely a pharmaceutical soft white paraffin, a commercial petroleum jelly and a personal care toothpaste, were used as test materials. Sample layers with different lengths and thicknesses were scraped by the millimanipulation device at different scrape depths and velocities. Visualisation was employed to capture salient dimensions during scraping, including berm length, berm height and sample length. Particle image tracking was used to capture the velocity distribution. The experimental data were compared with CFD simulation results obtained with the VOF approach and dynamic mesh algorithms. A series of sensitivity tests on the parameters of the viscosity models used in the simulations was conducted.

3.2   *Materials and Methods*

3.2.1 *Device*

The configuration of the millimanipulation device presented in Fig. 3.3 is similar to that reported by Magens *et al.* [9]. The sample layer is fixed on a two-axis, x-(horizontal) and z-(vertical) directions, moving platform, controlled by two linear slides (Standa 8MVT40-13-1-MEn1 and Standa 8MT50-100BS1-MEn1, respectively). The x-axis slide has a maximum speed of 20 mm/s with a resolution of 5 μm. A force transducer (ME-Meßsysteme GmbH KD40s ±2 N) is linked to a vertical blade, which hangs from an arm on a frictionless pivot, to measure the horizontal force when the blade contacts the layer. The measurement range of the transducer is ± 2 N. The transducer signal is amplified and collected as an analogue input by a multifunction I/O device (National Instruments, USB-6009, 8 AI (14-Bit, 48 kS/s)). The signal is converted to force using a calibration profile, which needs to be determined previously following the method presented by Liu [126]. The location and force data are collected and analysed using a control script coded by the author in Python 3.6.
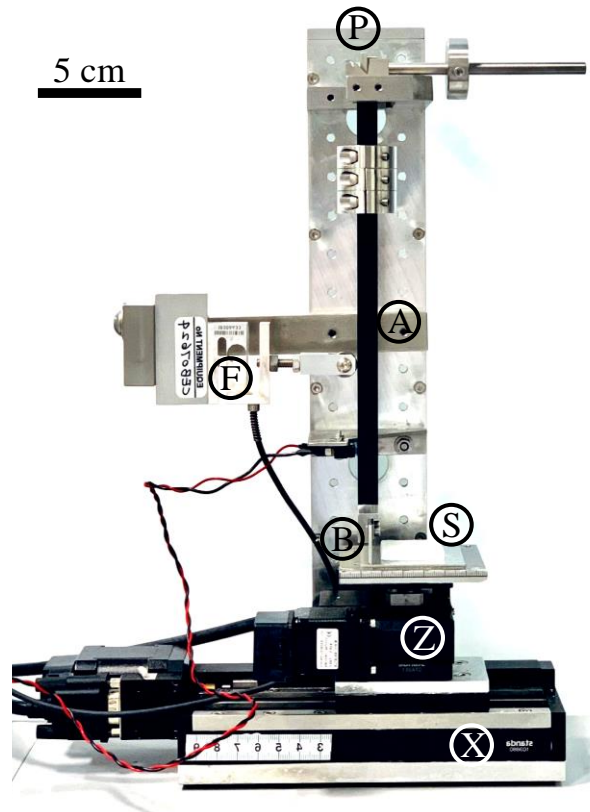
Fig. 3.3. Photograph of the millimanipulation apparatus. Components: A – arm; B – blade; F – force transducer; P – pivot; S – sample; X – horizontal positioner; Z – vertical positioner.

3.2.2 Sample preparation

A commercial petroleum jelly (Atom Scientific Ltd, GPS5220), a pharmaceutical soft white paraffin (GSK) and a commercial toothpaste (Cavity Protection Caries, Colgate) were selected as test materials. Layers of the petroleum jelly and soft white paraffin were coated on a 316 SS substrate (50×50 mm^2, thickness 2 mm) using a spreader tool [127], with variation in height of ± 0.07 mm and width of 30 mm [128]. The variation was measured using a confocal thickness sensor, which is described in section 4.3.4.1. Toothpaste layers were prepared by squeezing the toothpaste onto the same substrate, then shaping it using the spreader tool.

3.2.3 Visualisation

A high speed camera (Basler ace, acA640-750um) is mounted sideways on to the blade to capture the deformation of the sample layer as it is moved towards the blade. Fig. 3.2(b) is an example of an image captured by this camera. The videos were analysed using Python scripts.

For particle tracing tests, a commercial black spray (HYCOTE, Matt Black Spray Paint) was sprayed over a mask to create some black points on the side of the sample viewed by the camera. Care was taken to avoid points being too large, or too high, as this would cause poor resolution in the particle tracking algorithms. An open source python package, namely Trackpy v0.3.2, was employed for particle image velocimetry [129].

3.2.4 Rheology of test materials

Rheological tests on the materials were performed by PhD student Rubens Rosario Fernandes. Stress-controlled tests were performed at 20 °C on a Kinexus lab+ rotational rheometer (Malvern Instruments, UK) using roughened parallel plates and cone-plate with a diameter of 40 mm and a gap of 1 mm. Strain-controlled tests were also carried out using a ARES rheometer (TA Instruments, USA) with smooth parallel plates (diameter: 50 mm; gap: 1mm).

A number of methods are in regular use for determining the critical stress at which a viscoplastic fluid changes from predominantly solid-like to fluid-like behaviour. The term critical stress, τ_c, is used here, to be consistent with the rheological literature [130]: in mathematical treatments the term 'yield stress', alluding to a sharp bifurcation in behaviour, is commonly used. The critical shear stress was estimated from measurements made with increasing steady shear stress ramps [131]. The results obtained for petroleum jelly and soft white paraffin with ramps of 10 Pa/min are plotted in Fig. 3.4(a,ii) and (b,ii), respectively. The critical shear stress is marked by two features: an abrupt increase in shear strain and a sharp drop in apparent viscosity. The critical yield stresses for petroleum jelly and soft white paraffin were 280 ± 10 Pa and 460 ± 10 Pa, respectively. In Fig. 3.4(a,i) and (b,i), the shear stress-shear strain relationships for both materials below τ_c could be fitted by a line with gradient unity, indicating that the materials exhibit Hookean elastic behaviour below their yielding points (see plots-triangulation). Above τ_c, the materials deform more readily. Comparing the apparent

viscosity of SWP with that of PJ, the decrease at the critical stress for SWP is steeper, indicating that this material exhibits more strongly plastic behaviour. The difference of the normal stress differences, $N_1 - N_2$ for both materials have also been done, showing distinct behaviours around their critical shear stresses.
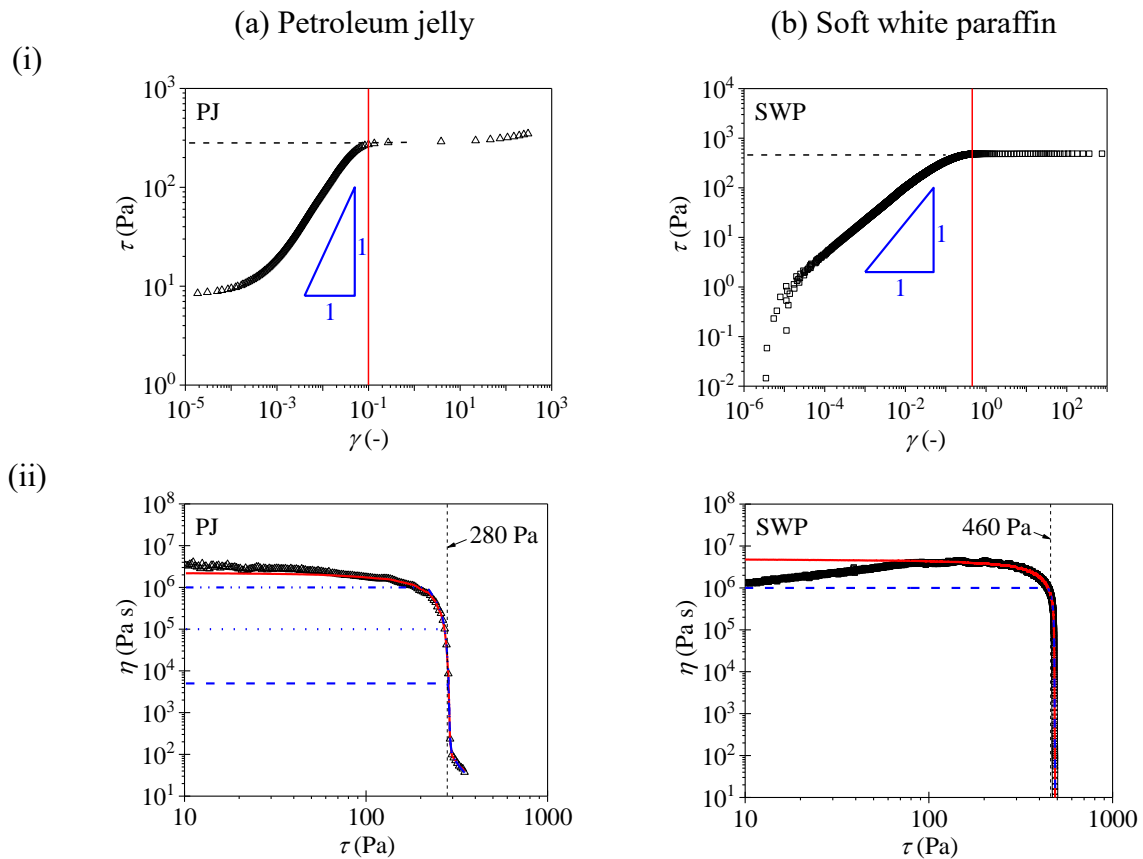
Fig. 3.4. Plots of (i) shear stress versus shear strain and (ii) apparent viscosity for (a) petroleum jelly and (b) soft white paraffin at 20 °C. Symbols – experimental data. Vertical line indicates critical shear stress. Loci in (ii): red line – regularised Bingham (Eq. (3.10)): blue dashed line – bi-viscosity model, with (a,ii) showing three values of μ_0, namely 5 kPa s, 100 kPa s and 1 MPa s considered in simulations. Triangles indicate Hookean elastic behaviour.

Fig. 3.5 shows the results obtained with toothpaste analysed using the same procedure. The rheological response is similar to PJ and SWP, and can be roughly classified into two trends, above and below the critical shear stress (around 126 Pa). However, the behaviour below the yield stress is significantly different with the apparent viscosity increasing strongly with shear stress. This results in dominance of elastic behaviour at low shear stress, which is similar to

that reported by Yang *et al.* [132] using an oscillatory time sweep measurement. By contrast, the apparent viscosity declines rapidly, when the applied shear stress exceeds 126 Pa. Shear-thinning behaviour was also observed by Ahuja *et al.* [133].
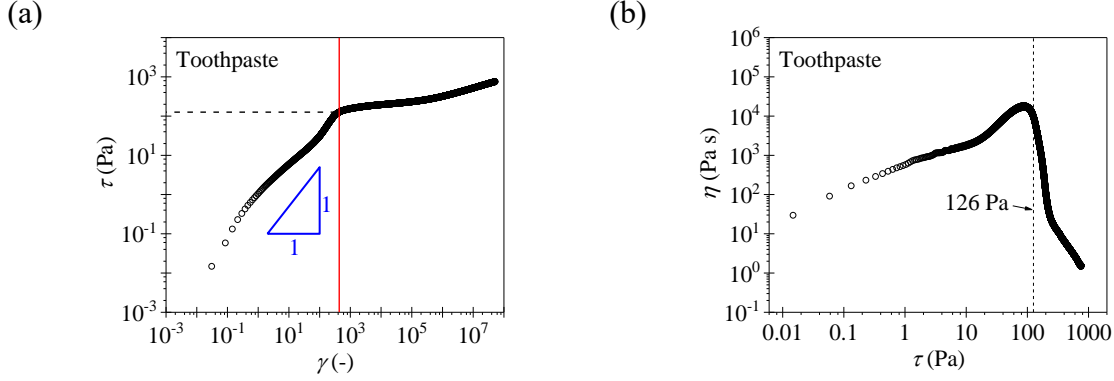
Fig. 3.5. Plots of (a) shear stress versus shear strain and (b) apparent viscosity for toothpaste at 20 °C. Symbols – experimental data. Triangle indicates Hookean elastic behaviour. Vertical dashed line (b) indicates critical shear stress.

3.2.5 Model Formulation

A simplified 2-dimensional, transient and symmetric millimanipulation model was created, since the ratio of the blade width to layer thickness is much greater than 10. The models were constructed in the open source software OpenFOAM version 4.0 on a SuperServer 1027R-WRF4+ server with 12 cores (Intel® Xeon® E5-2630V2 Processor 2.60GHz). The volume of fluid (VOF) method was employed for this study, in which all domains are solved by a momentum conservation equation using averaged density and viscosity:

$$\rho \left(\frac{\partial \mathbf{v}}{\partial t} + \mathbf{v} \cdot \nabla \mathbf{v} \right) = -\nabla p + \mu \nabla^2 \mathbf{v} + \rho \mathbf{g} \qquad (3.1)$$

Here ρ and μ are the average density and average viscosity, respectively. $\mathbf{v}$ is the velocity vector and p is the pressure. $\mathbf{g}$ is the gravity vector, but this term can be neglected for these viscoplastic materials due to their high yield stresses, τ_y. In the tests, the estimates of $\rho \mathbf{g} h_b / \tau_y$ for PJ and SWP are less than 0.14 and 0.089, respectively. The volume fraction of the sample phase in each grid cell is α, and the volume fraction of the air phase is $1 - \alpha$ ($0 \leq \alpha \leq 1$). The average density and viscosity in each cell are given by linear laws of mixtures, viz.

$$\rho = \alpha\rho_{\text{sample}} + (1 - \alpha)\rho_{\text{air}} \qquad (3.2)$$

$$\mu = \alpha\mu_{\text{sample}} + (1 - \alpha)\mu_{\text{air}} \qquad (3.3)$$

The mass continuity equation in terms of α, can be written as

$$\frac{\partial \alpha}{\partial t} + \nabla \cdot (\mathbf{v}\alpha) = 0 \qquad (3.4)$$

In this study, the rheology of the petroleum jelly and soft white paraffin were described by the bi-viscosity model and regularised Bingham model. Tests were also performed on toothpaste layers. Simulation of those tests was not performed due to this material (Cavity Protection Caries, Colgate) undergoing elastic deformation below its yield stress. The elasticity-dominated deformation cannot be describe by common viscosity models, such as Hershel-Bulkley. The standard OpenFOAM solver also did not support elastic fluids and extension to such materials was considered to be beyond the scope of this project.

CFD simulations for viscoelastic fluids increase the use of computation memory. One of the reasons why more memory is needed is the large number of variables to record. An additional term is required for calculating the polymeric extra stress tensor, τ_p. This term is used to describe the elastic behaviour. Eq. (3.1) can be re-written as

$$\rho\left(\frac{\partial \mathbf{v}}{\partial t} + \mathbf{v} \cdot \nabla\mathbf{v}\right) = -\nabla p + \mu\nabla^2\mathbf{v} + \rho\mathbf{g} + \nabla \cdot \boldsymbol{\tau}_p \qquad (3.5)$$

The polymeric stress tensor is then solved using an extra constitutive equation, and several methods have been proposed [134]. Taking the Oldroyd-B constitutive equation proposed by Oldroyd and Wilson [135] as an example, this gives:

$$\boldsymbol{\tau}_p + \lambda \overset{\nabla}{\boldsymbol{\tau}_p} = 2\eta_p\mathbf{D} \qquad (3.6)$$

Here η_p is the polymeric viscosity, λ is the relaxation time, and $\mathbf{D}$ is the rate of deformation tensor ($\mathbf{D} = \frac{1}{2}(\nabla\mathbf{v} + (\nabla\mathbf{v})^T)$). $\overset{\nabla}{\boldsymbol{\tau}_p}$ is the upper convected time derivative of τ_p, written as

$$\overset{\nabla}{\boldsymbol{\tau}_p} \equiv \frac{\partial \boldsymbol{\tau}_p}{\partial t} + \mathbf{v} \cdot \nabla \boldsymbol{\tau}_p - (\nabla \mathbf{v})^T \cdot \boldsymbol{\tau}_p - \boldsymbol{\tau}_p \cdot \nabla \mathbf{v} \tag{3.7}$$

Favero *et al.* [136] developed an OpenFOAM package including Oldroyd-B, Giesekus and FENR-P theories for simulating viscoelastic fluids. Habla *et al.* [137] used this OpenFOAM solver to simulate two common viscoelastic effects, namely the Weissenberg effect and die swell, and the results were compared with the literature. This package was also tested for the millimanipulation case here; however, it did not work and caused serious numerical issues. In addition, whilst an adhesive removal model for the cleaning of toothpaste has been reported by Yang *et al.* [132], a simulation including the cohesive failure of toothpaste has not yet been reported.

Specifying a constitutive model relating the stress and deformation generated by it is an important part of simulations.

(i) Bi-viscosity model (BVM):

This approach was proposed by O'Donovan and Tanner [138]. A creeping viscosity, μ_0, describes the fluid behaviour when the imposed shear stress is less than its yield stress, τ_y.

$$\mu = \begin{cases} \mu_0 & , \dot{\gamma} < \dfrac{\tau_y}{\mu_0} \\ \tau_y\big/_{\dot{\gamma}} + k_{HB}\dot{\gamma}^{n_{HB}-1}, & \dot{\gamma} \geq \dfrac{\tau_y}{\mu_0} \end{cases} \tag{3.8}$$

where $\dot{\gamma}$ is the shear rate. When the shear stress is larger than the yield stress, the viscosity is described by the Herschel-Bulkley model, in which k_{HB} and n_{HB} are the flow consistency and flow index, respectively. The standard OpenFOAM solver incorporates calculation routines to implement the bifurcation in behaviour, and the bi-viscosity model is determined by

$$\mu = min(\mu_0, \frac{\tau_y}{\dot{\gamma}} + k_{HB}\dot{\gamma}^{n_{HB}-1}) \tag{3.9}$$

(ii) Regularised Bingham model (RBM):

Regularisation is often used in numerical simulations to avoid the bifurcation in behaviour associated with yielding [139]. This Bingham-Papanastasiou model [57] was used here:

$$\mu = \mu_p + \frac{\tau_y}{\dot{\gamma}}\left[1 - e^{-m_{BP}\dot{\gamma}}\right] \tag{3.10}$$

where μ_p is the plastic viscosity and m_{BP} is the smoothing parameter, also called the regularisation parameter. The rheological parameters were obtained by fitting the experimental data to these expressions (see Fig. 3.4(ii)).

The fluid properties are summarised in Table 3.1.

Table 3.1. Fluid properties at 20 °C. Subscripts: PJ – petroleum jelly; SWP – soft white paraffin

Parameter		Value
μ_{air}		0.0148 mPa s
ρ_{air}		1 kg/m^3
μ_{PJ}	Bi-viscosity	Min(5000, 280/$\dot{\gamma}$ + 5.9) Pa s
		Min(10^5, 280/$\dot{\gamma}$ + 5.9) Pa s
		Min(10^6, 280/$\dot{\gamma}$ + 5.9) Pa s
	Regularised Bingham	12.4 + 249/$\dot{\gamma}$[1 – exp(–8869$\dot{\gamma}$)] Pa s
ρ_{PJ}		812 kg/m^3
$\sigma_{PJ\text{-}air}$[a]		0.07 N/m
μ_{SWP}	Bi-viscosity	Min(10^6, 460/$\dot{\gamma}$ + 21.5$\dot{\gamma}^{-0.9}$) Pa s
	Regularised Bingham	0.0881 + 452/$\dot{\gamma}$[1 – exp(–10934$\dot{\gamma}$)] Pa s
ρ_{SWP}		838.5 kg/m^3
$\sigma_{SWP\text{-}air}$		0.07 N/m

[a] σ is the surface tension [140].

These constitutive models are time independent, so the contribution of time dependent phenomena such as creep cannot be considered here.

The geometry of the simulation is presented in Fig. 3.6. AB is the blade and CD is the substrate. s is the scraped depth and L is the initial length of the sample layer. δ_0 and δ are the initial layer thickness and residual thickness, respectively. The blue area is specified as the sample layer. All walls (AB and CD) are set as rigid, no-slip and impermeable, because the VOF simulation cannot support other sample-substrate interactions. Other boundaries are considered as open to atmosphere ($p = 0$). Lengths AB and CD were specified as 10 mm and 50 mm, respectively. Other dimensions were set by the test conditions.

A thin and flat-shaped 3-dimensional geometry with a uniform-structured mesh (mesh size: 0.05 mm) was built in the mesh generator, blockMesh, since a 3-D mesh is necessary in OpenFOAM for calculation. The standard OpenFOAM solver, interDyMFoam, was used, as this is a VOF solver written for two immiscible fluids with optional mesh motion [141, 142]. The simulation results were validated according to the guidelines provided by NASA's NPARC alliance [143]. When the model was solved to $t = 10$ s, about 12 h was taken for computation.
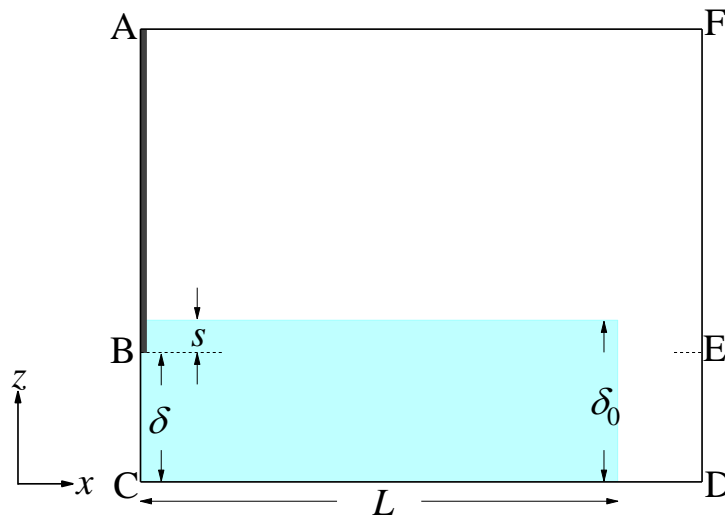
Fig. 3.6. Geometry for millimanipulation simulations.

3.2.6 Test case

Maillard *et al.* [49] reported an investigation for the deformation of Carbopol® 980 gels in a configuration, which was similar to the millimanipulation device, but at larger length scale. The Carbopol which exhibited Herschel-Bulkley behaviour was filled in a 140 cm × 12 cm channel, and a 12 cm wide blade was used. As with the millimanipulation device, the channel base was moved at speeds between 1 and 100 mm/s to bring the gel layer into contact with the vertical blade. The test ranges of initial thickness of Carbopol and scrape depth were 5-37 mm and 3-10 mm, respectively. A crude PIV measurement was carried out by observing the velocities of the bubbles inside the fluid. Maillard's PhD dissertation [144] included a short CFD study with a predetermined berm shape: she did not consider the free boundary problem.

The yield stress of Carbopol depends on its concentration [145]. The yield stresses of the Carbopol solutions studied [49] were 42, 49 and 98 Pa, which are noticeably lower than those of petroleum jelly and soft white paraffin. The $\rho \mathbf{g} h_b / \tau_y$ value here is more than 4, so the gravity term cannot be neglected in the simulation. The dynamic similarity can be gauged from the Bingham number, *Bn*, with a characteristic shear rate, *V/s*, giving

$$Bn = \frac{\tau_y}{k_{HB}} \left(\frac{s}{V}\right)^n \tag{3.11}$$

The values of *Bn* for the Maillard *et al.* cases taken for comparison (Table 3.2), were 1.7 and 3, but the values for PJ and SWP were 9.5-949 and 16-26, respectively. The lower *Bn* in the Maillard *et al.* cases indicate that viscous and yielding contributions both contribute strongly to the flow behaviour, while the larger *Bn* values in the PJ and SWP tests indicate that plasticity dominated these.

The dynamic mesh employed here cannot simulate the scenario of a confined space filled with Carbopol employed in the Maillard *et al.* work (*i.e.* all boundaries apart from the top surface are specified as walls), so the open boundary was used to approach it. All boundary conditions were the same as the models for PJ and SWP, but the dimensions differed. Lengths AB and CD (Fig. 3.6) were 150 mm and 800 mm, respectively. Other sizes were set by the test conditions. Table 3.2 lists the properties of Carbopol for the cases considered here.

Table 3.2. Parameters for Carbopol tests, taken from Maillard *et al.* [49]

Fluid	Parameter	Value
Air	μ_{air}	0.0148 mPa s
	ρ_{air}	1 kg/m^3
	$\sigma_{Carbopol\text{-}air}$	0.07 N/m
Carbopol	$\mu_{Carbopol}$	Min(10^4, $98/\dot{\gamma} + 58\dot{\gamma}^{-0.65}$) Pa s
		Min(3.33×10^4, $98/\dot{\gamma} + 58\dot{\gamma}^{-0.65}$) Pa s
		Min(10^5, $98/\dot{\gamma} + 58\dot{\gamma}^{-0.65}$) Pa s
	$\rho_{Carbopol}$	1000 kg/m^3
	Test conditions	$\delta_0 = 7$ mm, $s = 5$ mm, $V = 1, 5$ mm/s
		$\delta_0 = 20$ mm, $s = 5$ mm, $V = 1$ mm/s
		$\delta_0 = 25$ mm, $s = 5$ mm, $V = 5$ mm/s

3.3   Results and Discussion

3.3.1 Experiments

3.3.1.1   Effect of scrape depth

The force measured by the millimanipulation force transducer is presented as the normalised removal force, F_w, which is the force per unit width of the blade in contact with the layer (here, 30 mm). Fig. 3.7(a) shows the evolution of F_w with time (and displacement) for PJ with $\delta_0 = 5$ mm and various scrape depths. The removal force increases with scape depth, which is

expected since the volume of petroleum jelly being deformed increases (see average removal force, $\bar{F}_w$ in inset).

In Fig. 3.7(a): there is an initial rise in F_w over the fast few mm (distance varying between material) followed by a steady increase, at a less rapid rate, as more material is deformed and the berm builds up. For scrape depths of 1 and 2 mm, F_w remains approximately constant to the end of the test; however, at $s = 3$ mm, the force declines a small amount after $t = 3$ s. This is attributed to occurrence of slip, which is discussed in the next section.

The soft white paraffin profiles in Fig. 3.7(b) show a similar trend to those for petroleum jelly, whereby the removal force increases with scrape depth. However, the force increases gradually after the initial rapid increase. This is because compared to petroleum jelly, a larger fraction of the dislodged material climbed up along the blade during scraping, meaning that more material experienced deformation so that the force required is larger (see Fig. 3.8(a) and (b)). The volume of SWP involved is smaller than in the PJ case.

Toothpaste behaved noticeably differently from both petroleum jelly and soft white paraffin. Fig. 3.7(c) shows that a more gradual initial rise followed by a steady increase. This initially slow rise is due to the fact that elasticity dominates as the imposed stress is less than its yield stress (Fig. 3.5). The elastic behaviour is also evident from the shape of berm (see Fig. 3.8(c)), where the whole sample deforms while being scraped.

(a)
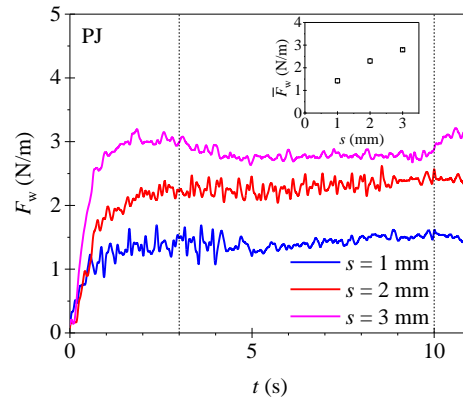
(b)
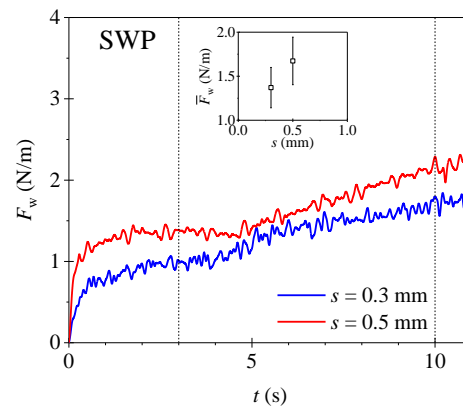
(c)
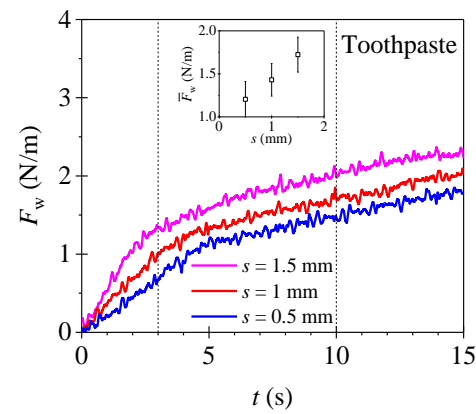
Fig. 3.7. Evolution of F_w for (a) petroleum jelly, (b) soft white paraffin and (c) toothpaste. Test conditions: $\delta_0 = 5$ mm for PJ and SWP, $\delta_0 = 2$ mm for toothpaste, $L = 30$ mm, $V = 1$ mm/s. Insets show average removal force, $\bar{F}_w$, for the period from $t = 3$ s to 10 s (between dashed lines).
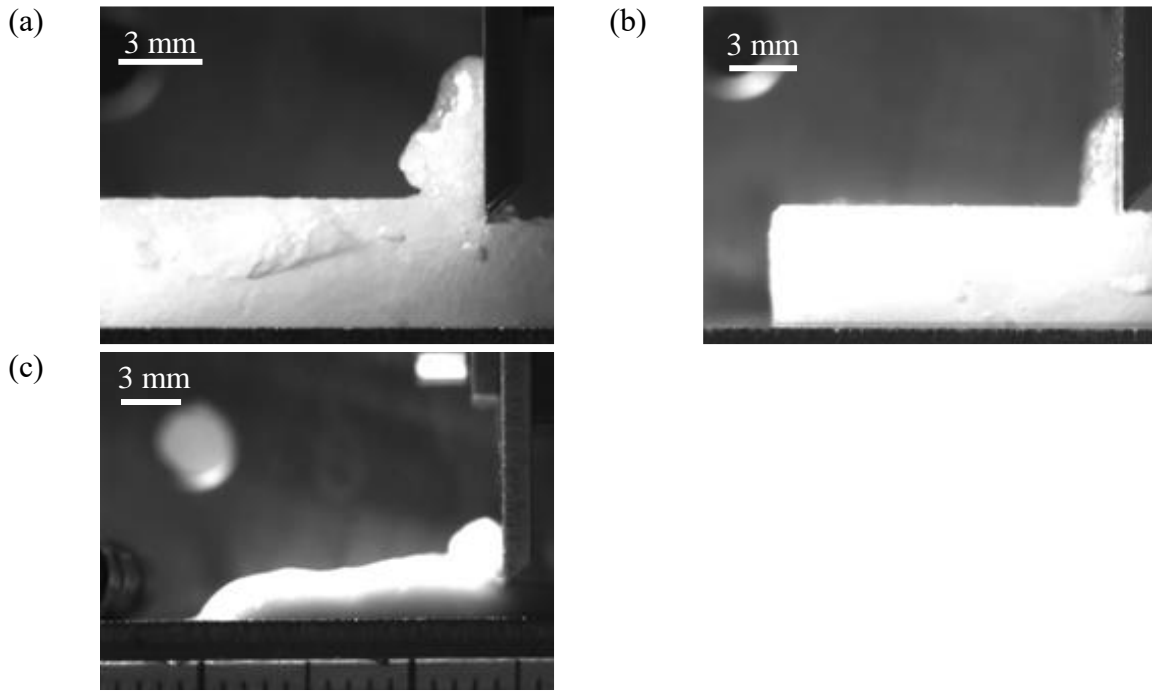
Fig. 3.8. Images for (a) petroleum jelly at $s = 1$ mm, (b) soft white paraffin at $s = 0.3$ mm and (c) toothpaste at $s = 0.5$ mm, at $t = 15$ s. Test conditions: $\delta_0 = 5$ mm for PJ and SWP, $\delta_0 = 2$ mm for toothpaste, $L = 30$ mm and $V = 1$ mm/s.

3.3.1.2   *Slip*

The phenomenon of wall slip has been observed with a number of soft solid and viscoplastic materials such as potato granules [146]. Slip is an example of adhesive failure, occurring when the force required to overcome the internal interactions of the sample (cohesive failure) is larger than that for the sample-substrate interaction (adhesive failure). Petroleum jelly and soft white paraffin also exhibited slip under some conditions. Chang *et al.* [147] studied a method to eliminate the wall slip effect occurring in a rheometer for Vaseline® (petroleum jelly). Slip for petroleum jelly and soft white paraffin was studied by comparing the results using a smooth cone with that using rough parallel plates in rheological tests. A lower force is needed at a given shear stress when slip is present (smooth cone). In Fig. 3.9, the stress difference between the smooth cone and rough plate for soft white paraffin is more than the difference for petroleum jelly, meaning that soft white paraffin exhibits more slip behaviour than petroleum jelly.
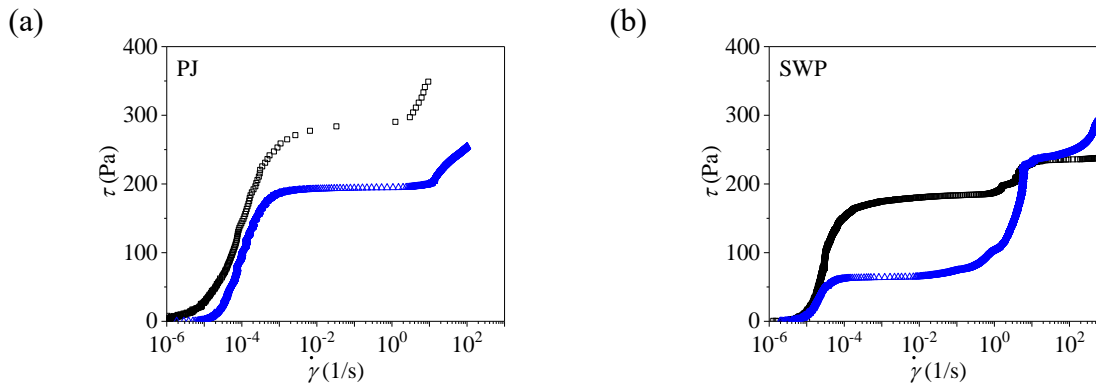
Fig. 3.9. Plots of shear stress versus shear rate using smooth cone and rough parallel plate for (a) petroleum jelly and (b) soft white paraffin. Colour: black – rough parallel plate; blue – smooth cone.

The scrape depth and sample length were selected based on the occurrence of slip. For a petroleum jelly sample with a length of 30 mm, the maximum scrape depth which would not result in slip was 2 mm. The occurrence of slip can be identified by the length of the sample ahead of the blade, $L - x$ (see Fig. 3.2). In general, without slip, the distance will decrease steadily during scraping. $L - x$ at $L = 20$ and 30 mm shown in Fig. 3.10(a,i) decrease over time, but in the shortest case ($L = 10$ mm) deviates from the expected trend at about 1.25 s, marked A, reaching an asymptotic value ($L - x = 7.22$ mm) after 9.5 s (marked B). This point indicates that the whole sample was being moved back and total adhesive failure had occurred (pure slip, see Fig. 3.11(a)). These behaviours are also manifested in the berm height. In Fig. 3.10(a,ii), the berm height for $L = 20$ and 30 mm increases steadily until the end of the test, but the growth rate of the 10 mm long sample decreases after point A and stops at B, which is consistent with the $L - x$ profile. This also indicates that the sample did not experience bulk deformation after B. These changes are reflected in the measured forces, in Fig. 3.10(a,iii). F_w at $L = 10$ mm deviates from others at A: by point B, the value is about 1.6 N/m and lower than those recorded for longer lengths. In contrast, the F_w profiles for $L = 20$ and 30 mm are identical because only cohesive failure is occurring (no slip, see Fig. 3.11(c)), meaning that the friction provided by both lengths is large enough to keep the sample in place.

The shear stress active at the wall can be estimated from $\tau_w = F_w/L$ and these values are plotted in Fig. 3.10(a,iv). The initial sample length, L, was used for calculation since the whole sample moved when slip occurred. The shear stress required to cause adhesive failure of petroleum jelly is about 160 Pa, which is less than the bulk yield stress (280 Pa) measured by the

rheometer. This is useful information for quantifying the adhesion strength, but cannot be employed for assessing deformation. Magens *et al*. [9] used the same device to measure the adhesion strength of baked cake batters on surfaces with different roughness and surface energy by fixing the cake sample within a meshed ring, which confined rupture to occur at the interface with the substrate.

A pair of tests for petroleum jelly with $s = 2$ mm to $L = 10$ and 20 mm are shown in Fig. 3.10(b). These results are similar to that with $s = 1$ mm, and slip only occurred with the 10 mm long sample. The point where slip happened (marked C) is close to that at $s = 1$ mm, but point D (occurrence of adhesive failure) is earlier than B. This is attributed to the larger scrape depth, giving rise to a larger force imposed on the sample. The predicted shear stress for causing complete slip (Fig. 3.10(b,iv)) is around 160 Pa, in agreement with the estimate from the smaller scrape depth, which confirms that the adhesion strength between PJ and 316 SS is about160 Pa and provides a method for measuring adhesive strength *in situ*.
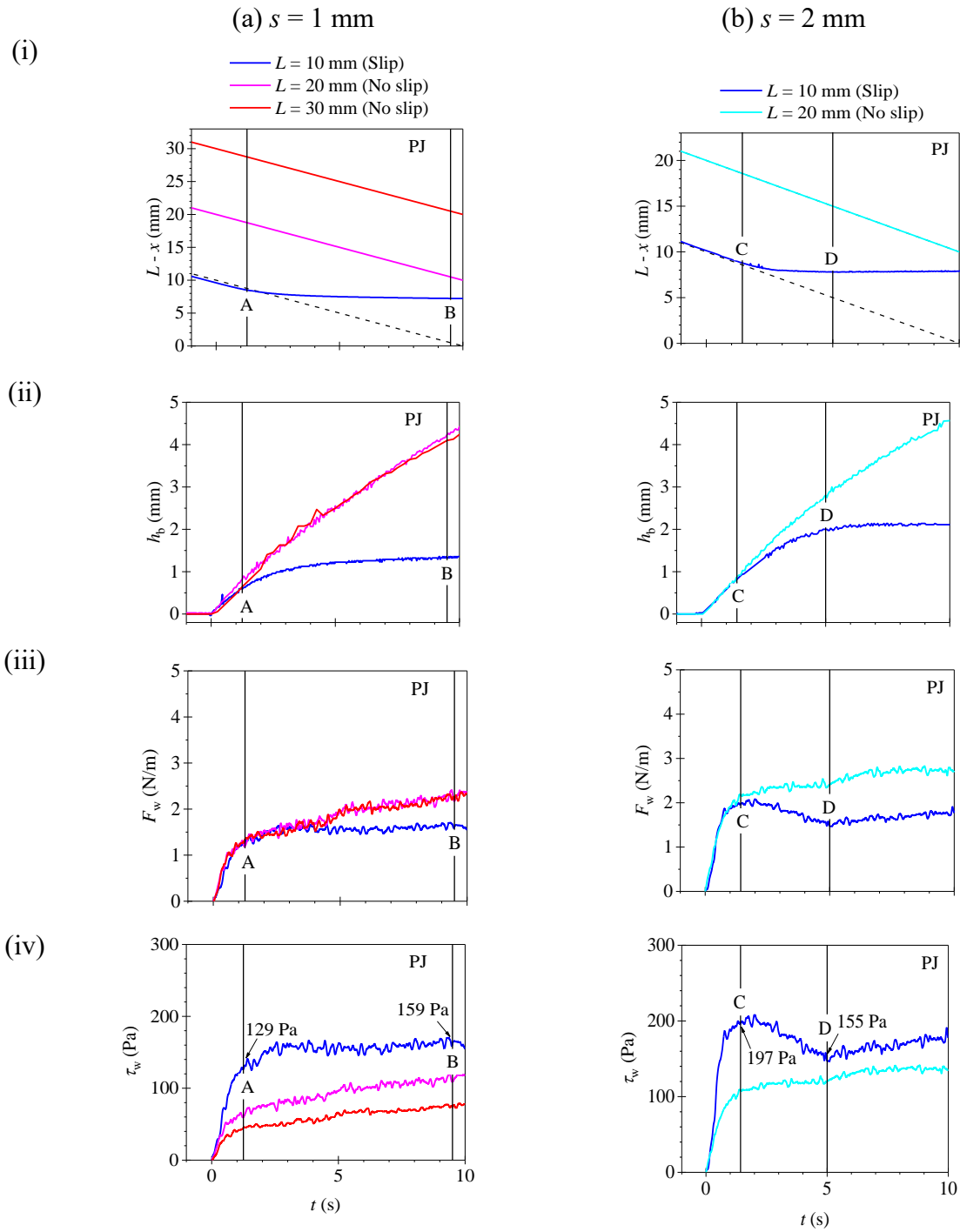
Fig. 3.10. Millimanipulation profiles showing occurrence of slip for petroleum jelly at $s =$ (a) 1 mm and (b) 2 mm: (i) length of layer behind blade, $L - x$; (ii) height of berm, h_b; (iii) removal force, F_w; and (iv) approximate wall shear stress, $\tau_w (= F_w/L)$, Black dashed line shows expected $L - x$ profile. Test conditions: $\delta_0 = 5$ mm, $V = 1$ mm/s, various sample lengths.
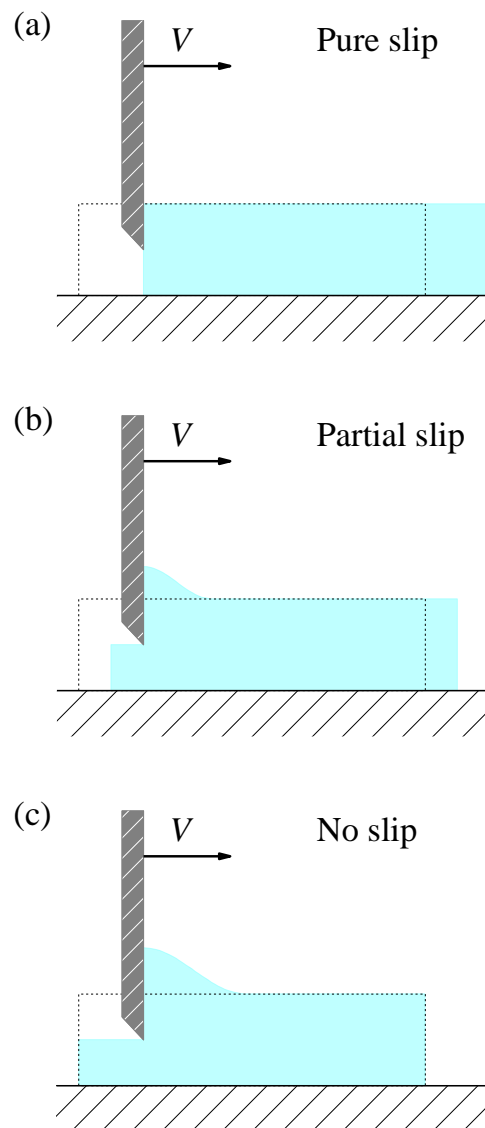
Fig. 3.11. Schematics of (a) pure slip, (b) partial slip and (c) no slip. Dashed line indicates the initial profile of the tested sample.

The results of testing slip for soft white paraffin at different scrape depths and sample lengths are shown in Fig. 3.12. The scrape depth required to cause slip is significantly smaller than that for petroleum jelly. In all cases, complete adhesive failure was not observed, indicating that a larger scrape depth is required. Labels A to E indicate the occurrence point of slip for different scrape depths. Fig. 3.12(b,i) shows that slip occurs later with sample length (points B, C, and D), indicating that longer samples provide more friction to prevent slip. The slip behaviour is similar to the observation in the petroleum jelly tests.

55

The F_w values in Fig. 3.12(iii) are similar before slip occurred, and do not show a significant relationship with the sample length. All the estimated average wall shear stress values in Fig. 3.12(iv) are less than the yield stress obtained from the rheometer. The force measured before reaching complete slip contained contributions from both cohesive and adhesive failure (partial slip, see Fig. 3.11(b)), so these values cannot be utilised to calculate the adhesion strength.
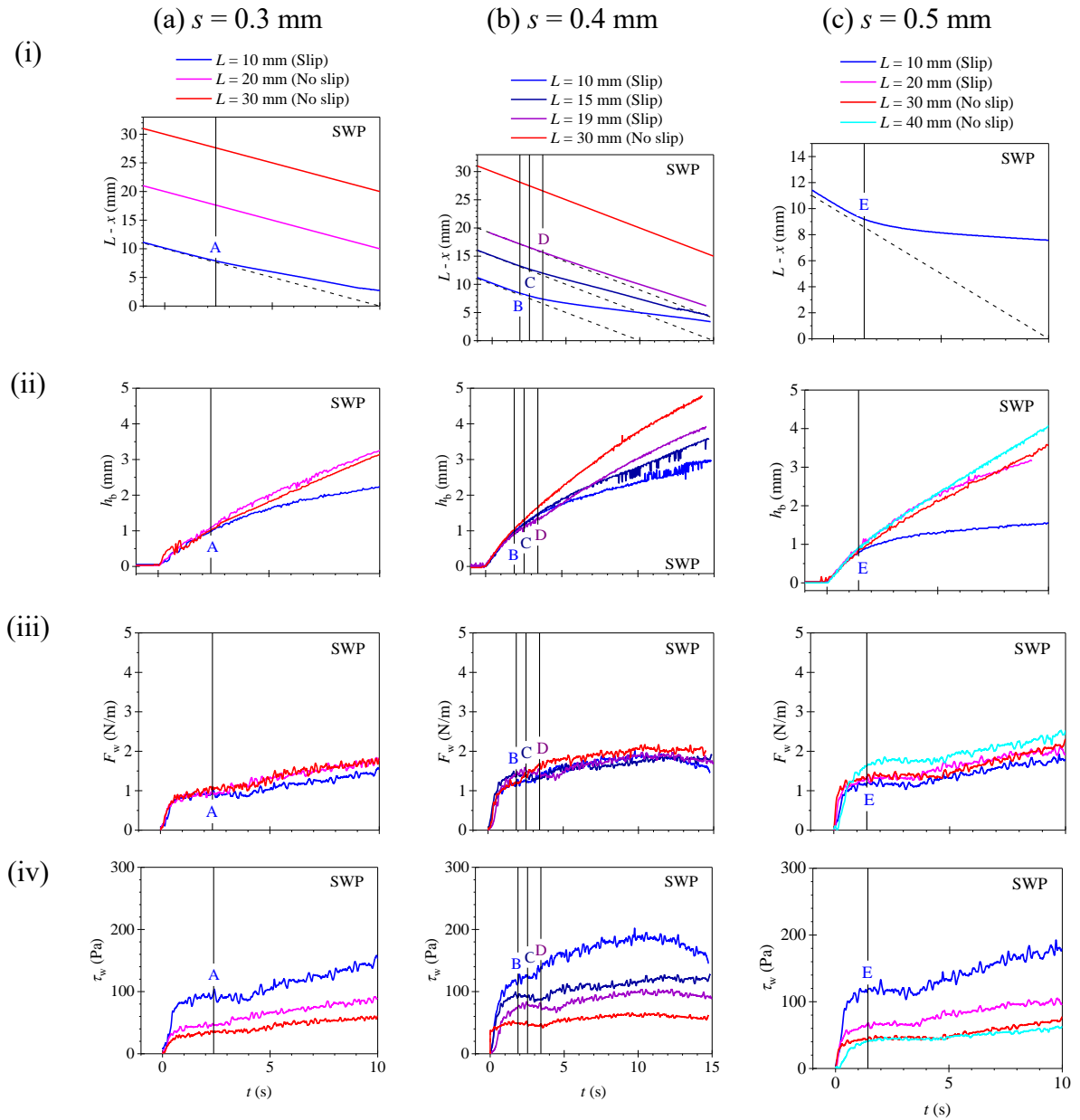
Fig. 3.12. Millimanipulation profiles showing occurrence of slip for soft white paraffin at s = (a) 0.3 mm, (b) 0.4 mm and (c) 0.5 mm: (i) length of layer behind blade, $L - x$; (ii) height of berm, h_b; (iii) removal force, F_w; and (iv) approximate wall shear stress, $\tau_w (= F_w/L)$, Black dashed line shows expected $L - x$ profile. Test conditions: $\delta_0 = 5$ mm, $V = 1$ mm/s, various sample lengths. Note: The width of camera frame is 20 mm, so the $L - x$ profile for $L = 20$ mm cannot be recorded.

3.3.1.3 Effect of scrape velocity

Fig. 3.13 shows the effect of scraping velocity for the three materials. Petroleum jelly, soft white paraffin and toothpaste exhibit similar trends, with F_w increasing with increasing scraping speed, indicating that the values contain a contribution from viscous forces. The increases of F_w for three materials are not linearly proportional to the speed, indicating that these materials are not a Newtonian fluid. The F_w-V behaviour of PJ and SWP will be discussed in detail in section 3.3.2.
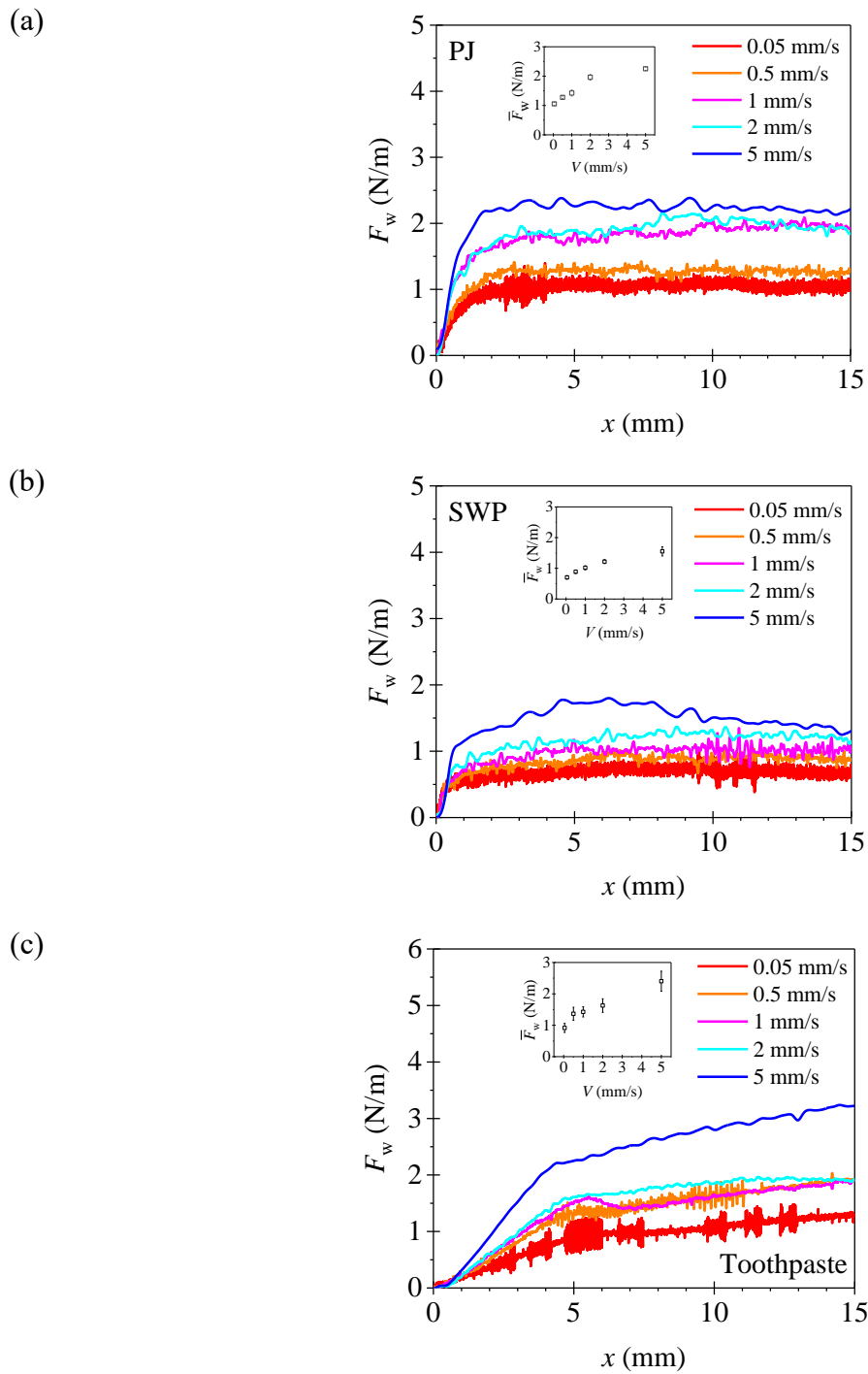
Fig. 3.13. Effect of scrape speed on F_w for (a) petroleum jelly, (b) soft white paraffin and (c) toothpaste. Test conditions: $L = 30$ mm; petroleum jelly, $\delta_0 = 5$ mm and $s = 1$ mm; soft white paraffin, $\delta_0 = 5$ mm and $s = 0.3$ mm; toothpaste, $\delta_0 = 2$ mm and $s = 1$ mm. Insets show average removal force, $\bar{\bar{F}}_w$, for the period from $t = 3$ s to 10 s.

3.3.1.4   *Particle image visualisation*

Fig. 3.14 compares images and relative velocity distributions calculated from particle image tracking for petroleum jelly at various scrape depths. The data are noisy. Each coloured point represents a (black) point identified on the layer wall by the software. Its velocity was then estimated and is presented as V^*, where V^* is the scaled velocity. At $s = 1$ and 2 mm, higher relative velocities only occurred above and ahead of the level of the blade ($V^* > 0.2$), while other regions were nearly static. This indicates that only this region underwent deformation. The relative velocity increases with berm height and close to the blade. This is because as the blade scraped, the petroleum jelly in the layer ahead of the blade experienced cohesive failure. After the berm was generated, the top of berm continued to be shunted upwards. This area therefore has the highest velocity compared to other regions. In Fig. 3.14(b,ii), there are only a few coloured points in the region of $V^* \sim 0.3$. This is attributed to folding of petroleum jelly while being scraped. This would make some points be hidden by the berm and result in the disappearance of identified points.

By contrast, at $s = 3$ mm (Fig. 3.14(b,iii)), a large region is deformed, and extends to the bottom edge of the blade. When the blade continued to move, the region of measurable deformation – the yield zone – reaches the substrate. The whole sample then moved, indicating that a mixture of adhesive failure and bulk deformation was occurring, as discussed above. This case is one of those where slip occurred (see Fig. 3.10).
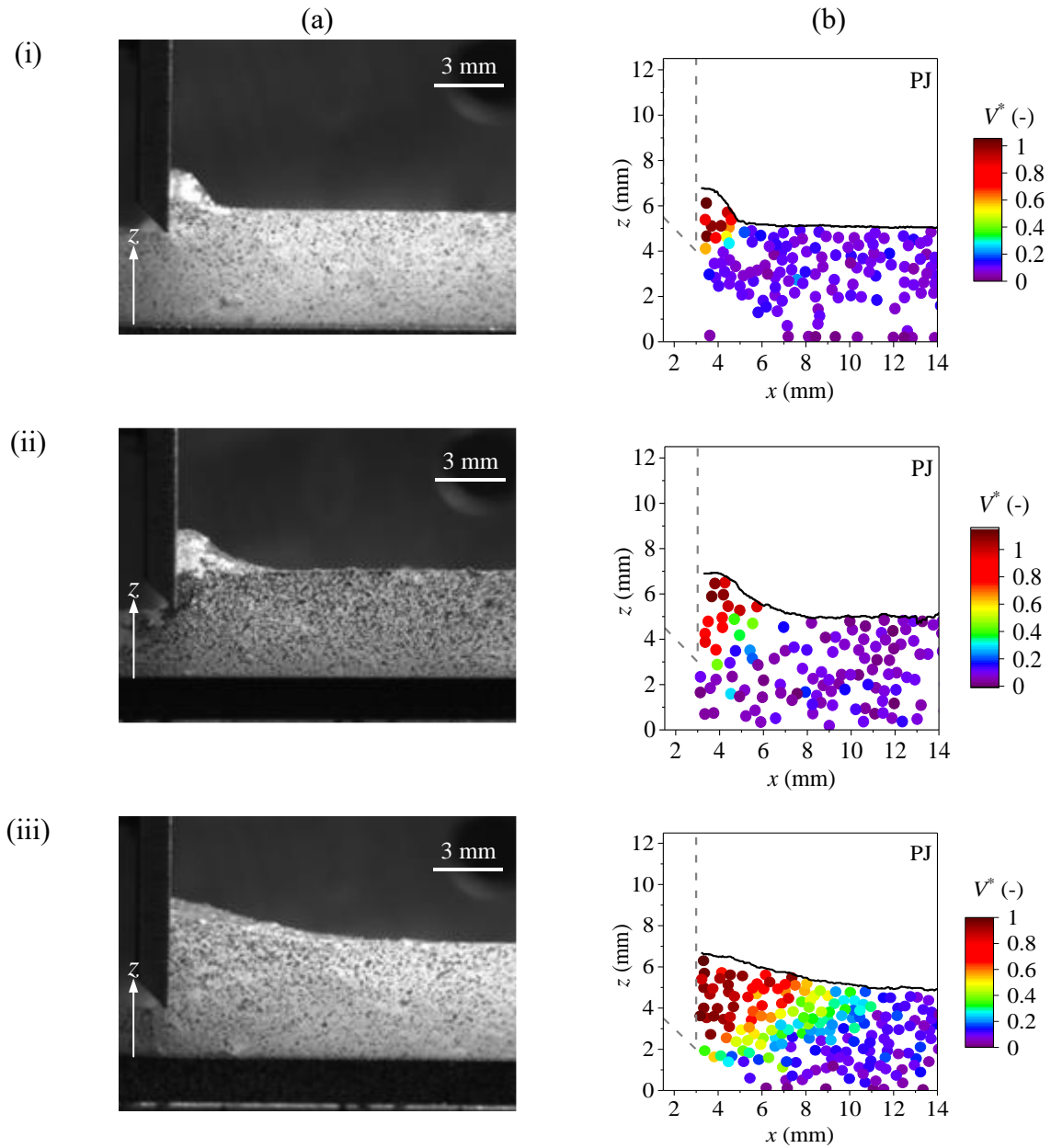
Fig. 3.14. Deformation of petroleum jelly: (a) image and (b) distribution of relative velocity, $V^* = \bar{v}/V$, where $\bar{v}$ is the mean local velocity measured from particle image tracking. Test conditions: $\delta_0 = 5$ mm, $L = 30$ mm, $V = 1$ mm/s, and $t = 3$ s, with (i) $s = 1$ mm; (ii) $s = 2$ mm; and (iii) $s = 3$ mm. Grey dashed line in (b) shows the blade position.

Fig. 3.15 presents images and relative velocity distributions for soft white paraffin at small scrape depths. The particle image tracking is again noisy. At $s = 0.3$ and 0.5 mm, deformation occurred above and behind the level of the blade, which is similar to petroleum jelly. The berms are steeper, which is consistent with the rheological tests (more plastic). However, at large scrape depth, the region where $V^* > 0.2$ is large, indicating that the whole sample was moving and slip had occurred. This is a case where slip was observed in the other performance measures (see Fig. 3.12).
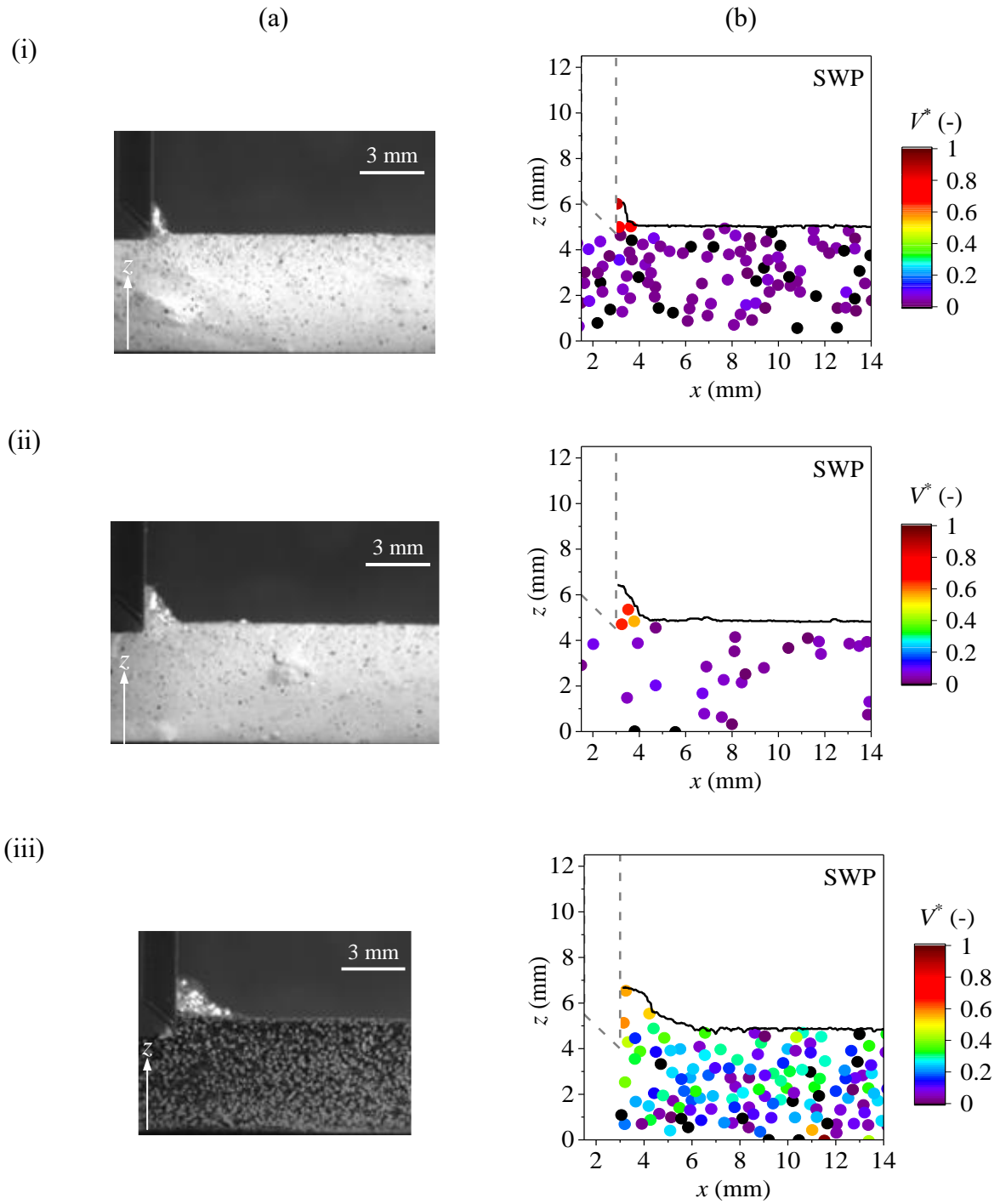
Fig. 3.15. Deformation of soft white paraffin: (a) image and (b) distribution of relative velocity, $V^* = \bar{v}/V$, where $\bar{v}$ is the mean local velocity measured from particle image tracking, for (i) $s = 0.3$ mm; (ii) $s = 0.5$ mm; and (iii) $s = 1$ mm. Test conditions: $\delta_0 = 5$ mm, $L = 30$ mm, $V = 1$ mm/s, and $t = 3$ s. Grey dashed line in (b) shows the blade position.

3.3.1.5 Relaxation

The rheological results in Fig. 3.4 indicate that petroleum jelly and soft white paraffin exhibit elastic behaviour when the imposed shear stress is lower than the critical stress. The BVM and RBM models employed for simulating PJ and SWP are not time-dependent, so time dependent phenomena such as elastic behaviour cannot be captured. Chou *et al.* [148] demonstrated that a series of sudden halts and restarts of steady paste extrusion could be used to estimate the viscous and plastic contributions to the force required to extrude ceramic pastes through cylindrical dies. This concept was applied here. A number of tests were performed with interrupted motion, moving the blade (5 s), holding it in place (60 s), then moving it again.

Fig. 3.16 shows results obtained from relaxation tests on PJ and SWP. Smaller scrape depths and long sample lengths were chosen to avoid slip. The profiles in Fig. 3.16 (i), show similar trends, namely a rapid increase in F_w to a plateau value, labelled F_C. After the blade stopped, F_w decreases abruptly from F_C to $F_{C'}$, and then declines gradually to a steady value, F_D, when the next scraping cycle starts ($F_{C'}$ to F_D). The value of $F_C - F_{C'}$ is greater than $F_C/2$ for both materials. The sharp decrease is attributed to the absence of the viscous contribution. This can be determined by a characteristic shear rate, V/s, exerted in region I (see Fig. 3.2). These characteristic shear rates for PJ and SWP are 1 and 3.33 s^{-1}, respectively. From the rheological results (Fig. 3.4(i)), the shear stress at these shear rates is larger than the yield stress, indicating that the viscous contributions are important.

This measure of the viscous contribution, ($F_C - F_{C'}$) provides an estimate of the apparent viscosity from the scaling relation, ($F_C - F_{C'}$)/$s \sim \mu(V/s)$. The values calculated for PJ and SWP are 940 and 570 Pa s, respectively: both are significantly lower than the values measured in the low shear rate region in Fig. 3.4. At these conditions, the samples did not yield, which is expected.

F_D is a residual force associated with yielding, and is about 0.5 N/m in both cases. The decay trends were fitted to a simple exponential decay relationship, giving

PJ $$F_{C'} - F_D = 0.35e^{\frac{-t}{15.6}} \qquad R^2 = 0.837 \qquad\qquad (3.12)$$

SWP $$F_{C'} - F_D = 0.30e^{\frac{-t}{25.9}} \qquad R^2 = 0.749 \qquad\qquad (3.13)$$

Here t is the time elapsed since the blade stopped moving.

The estimated characteristic times, about 16 s for PJ and 26 s for SWP, could be caused by creep or spreading of the sample after scraping stopped, shown in Fig. 3.17. The scraping system is not completely 2-D, since the material spreads not only upwards but also sideways.

A series of stress relaxation tests with different initial strains using the rheometer were performed by PhD student Rubens Rosario Fernandes. These tests were conducted with imposed a single strain, holding for a long time, and results are plotted in Fig. 3.16(iii). τ_{60} is the measured stress at $t = 60$ s. The profiles are similar to those obtained for millimanipulation, plummeting sharply followed by an exponential decay.

Whilst the relaxation data obtained from the millimanipulation device fitted the exponential decay well, the rheological data did not fit a simple exponential decay as well. Also, the characteristic times in the millimanipulation tests are consistently longer than those in the rheometer. The characteristic times obtained from the rheometer for PJ are from 12.3 s to 14 s, and the values for SWP are between 14.8 s and 16.7 s.

This finding about the decay times obtained with the millimanipulation do not map simply to the decay times in the rheometer, even though the profiles of $F_{C'}$ and τ were fitted directly (given as follows and Fig. 3.16(iv), respectively).

PJ $$F_{C'} = 0.50 + 0.35e^{\frac{-t}{14.6}} \qquad R^2 = 0.838 \qquad\qquad (3.14)$$

SWP $$F_{C'} = 0.49 + 0.29e^{\frac{-t}{13.0}} \qquad R^2 = 0.785 \qquad\qquad (3.15)$$

The consistent deviation of the characteristic times could be attributed to the geometry difference between the millimanipulation device and rheometer. The F_D value is associated with the yield stress, providing an opportunity to predict τ_y, which will be discussed in the following section.
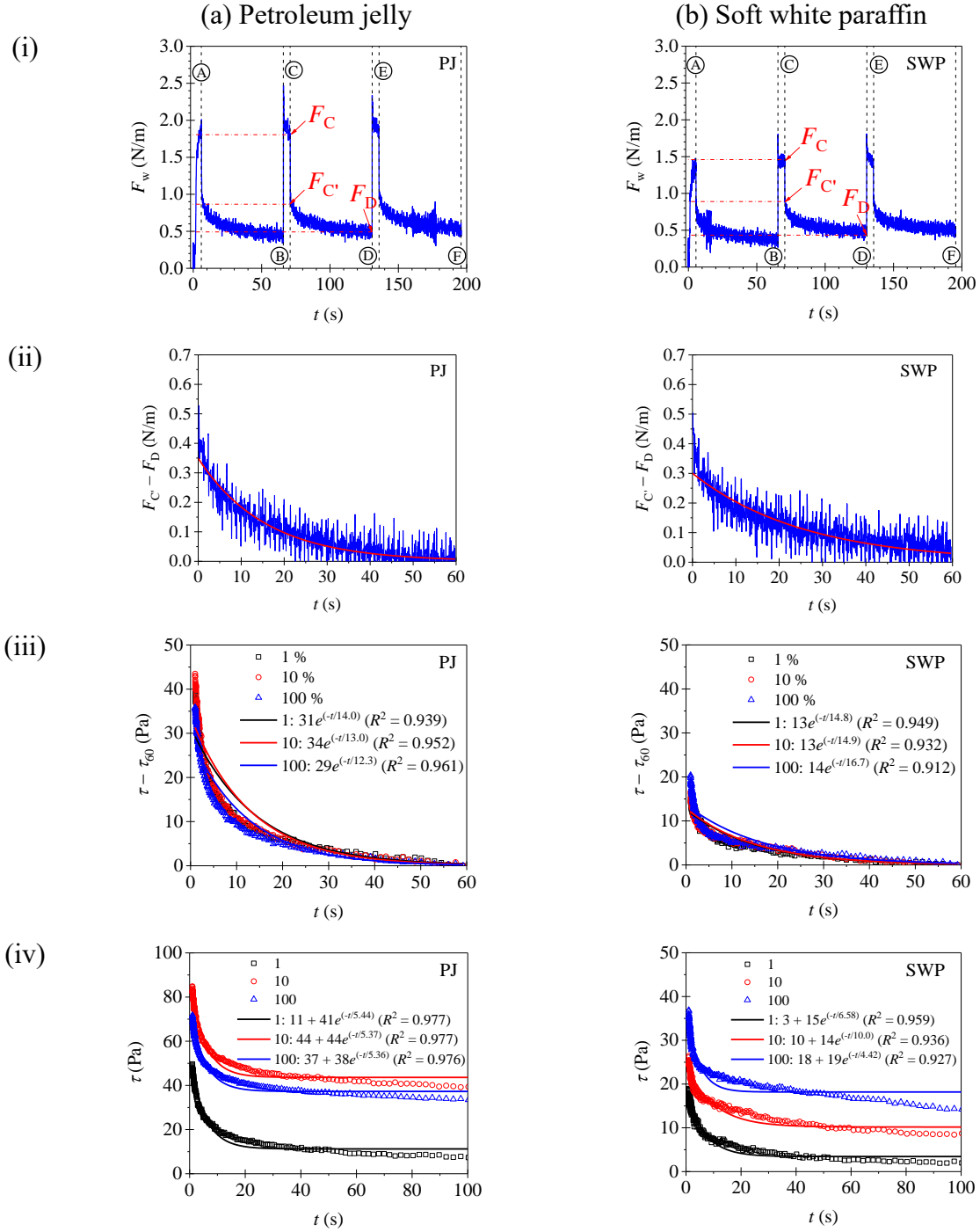
Fig. 3.16. Interrupted testing of (a) petroleum jelly, and (b) soft white paraffin: (i) F_w - Labels A, C, E indicate the end of motion, B, D, F the restart; (ii) $F_{C'} - F_D$, red line shows fit to exponential decay, Equations (3.12) and (3.13); (iii) $\tau - \tau_{60}$ and (iv) τ at different applied strains (in %). Test conditions: $\delta_0 = 5$ mm, $L = 30$ mm, $s = 1$ mm for PJ and $s = 0.3$ mm for SWP, $V = 1$ mm/s, scraping time = 5 s, relaxation time = 60 s.

Fig. 3.17. Images of petroleum jelly subject to interrupted scraping, taken at times labelled A, B and C in Fig. 3.16(a,i). Conditions: $\delta_0 = 5$ mm, $s = 1$ mm, $V = 1$ mm/s, scraping time = 5 s, and relaxation time = 60 s.

Interrupted testing of toothpaste is reported in Fig. 3.18. The trend is slightly different from PJ and SWP. As the blade contacts the toothpaste, the measured force increased rapidly, followed by a graduate increase, not reaching a plateau, as with steady deformation (Fig. 3.7(c)). The maximum value of F_w (F_C) in each cycle increases with time. Even though F_D also increases with time, the value of $F_C - F_D$ is not constant. Also, the restart points (B and D) are not sharp.

The relaxation trend is similar to the trends of PJ and SWP with $F_C - F_{C'} < F_C/2$. The decay over the relaxation period was also fitted to the equation of quasi-exponential decay.

Toothpaste $$F_{C'} - F_D = 0.48e^{\frac{-t}{8.22}} \qquad R^2 = 0.800 \qquad (3.16)$$

$$F_{E'} - F_F = 0.55e^{\frac{-t}{11.22}} \qquad R^2 = 0.840 \qquad (3.17)$$

However, the decay time changes from one cycle to the next, which is different from the constant decay times of PJ and SWP.

(a)

(b)
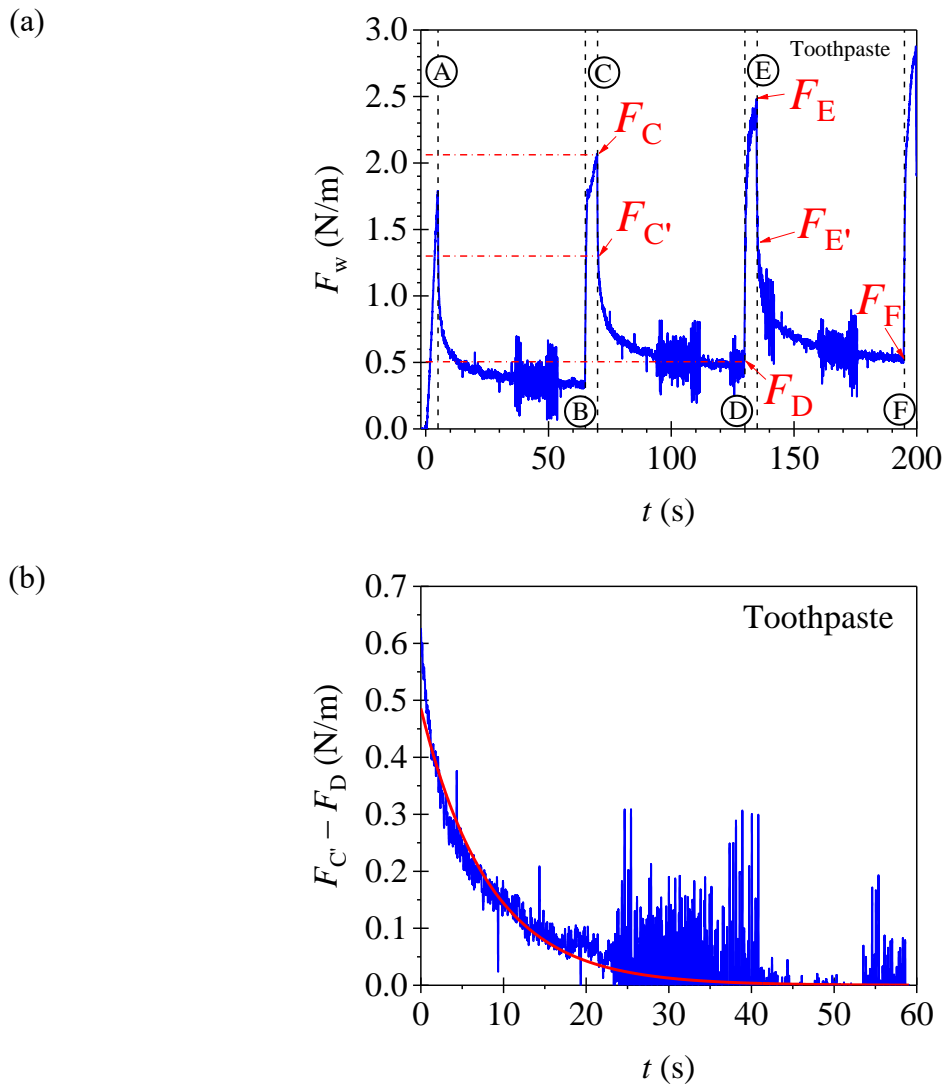
Fig. 3.18. Interrupted testing of toothpaste: (a) F_{w}: Labels A, C, E indicate cessation of motion, B, D, F the restart; (b) $F_{\mathrm{C'}} - F_{\mathrm{D}}$; red line shows fit to exponential decay, Equation (3.16). Test conditions: $\delta_0 = 2$ mm, $L = 30$ mm, $s = 1$ mm, $V = 1$ mm/s, scraping time = 5 s, relaxation time = 60 s.

3.3.1.6 *Estimation of yield stress*

The F_{D} values of PJ and SWP provide a possible route to estimate the material's yield stress. The vertical blade has similarities to a metal cutting blade, the theory of which [149, 150] is well developed. Using F_{D} as an indicator of the force due to plastic deformation gives a way of estimating the critical shear stress. Fig. 3.19 is a schematic of the metal cutting model. Assuming a linear yield plane OA, the force imposed on the material to cause yield is $F_{\mathrm{w}}\sec\phi$, so the yield stress, $\tau_{\mathrm{y}}^{\mathrm{el}}$, can be estimated from

$$\tau_y^{e1} = \frac{F_w \tan \phi}{s} \qquad (3.18)$$

Here ϕ is the cutting angle, and is calculated from the berm length, b (extracted from photographs), and the scrape depth, s.
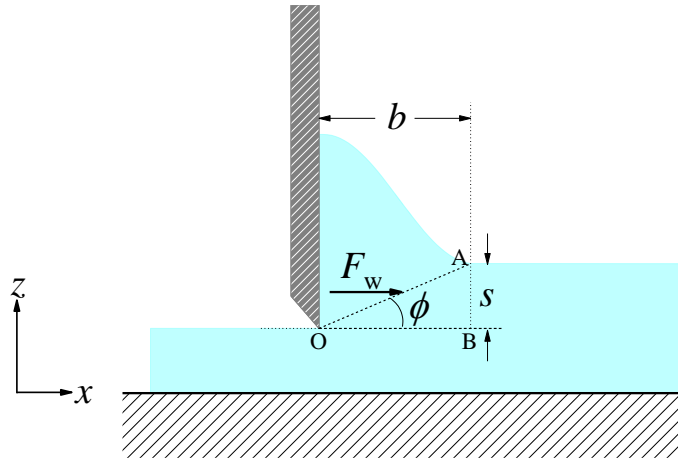
Fig. 3.19. Schematic of the cutting model.

The evolution of the berm lengths and estimated yield stresses for PJ and SWP are plotted in Fig. 3.20. The τ_y^{e1} value in each case fluctuates due to the fact that the materials were not homogeneous so the surface of the berms were not smooth. The average values of τ_y^{e1} for PJ and SWP are about 550 Pa and 790 Pa, respectively, and are larger than the τ_c values obtained from the rheometer. However, the F_w values are expected to be affected by the viscous contributions. The viscous contributions can be calculated by the relationship obtained from the interruption tests (see Fig. 3.16 (i)), $\tau_y^{e2} = \tau_y^{e1} \times (F_{C'}/ F_C)$ and $\tau_y^{e3} = \tau_y^{e1} \times (F_D/ F_C)$. Good agreement between τ_y^{e2} and the rheological value, τ_c, for both materials is evident in Fig. 3.20(a) and (b). Appling this estimation method for other cases (Fig. 3.20(c)), the τ_y^{e2} values also agree with τ_c. These results indicate that τ_y^{e2} can be employed to estimate the yield stress of a new material.

These results also indicate that the millimanipulation device allows to measure the cohesive and adhesive strengths of viscoplastic materials by the interrupted testing shown here and the method proposed by Magens *et al*. [49], respectively.
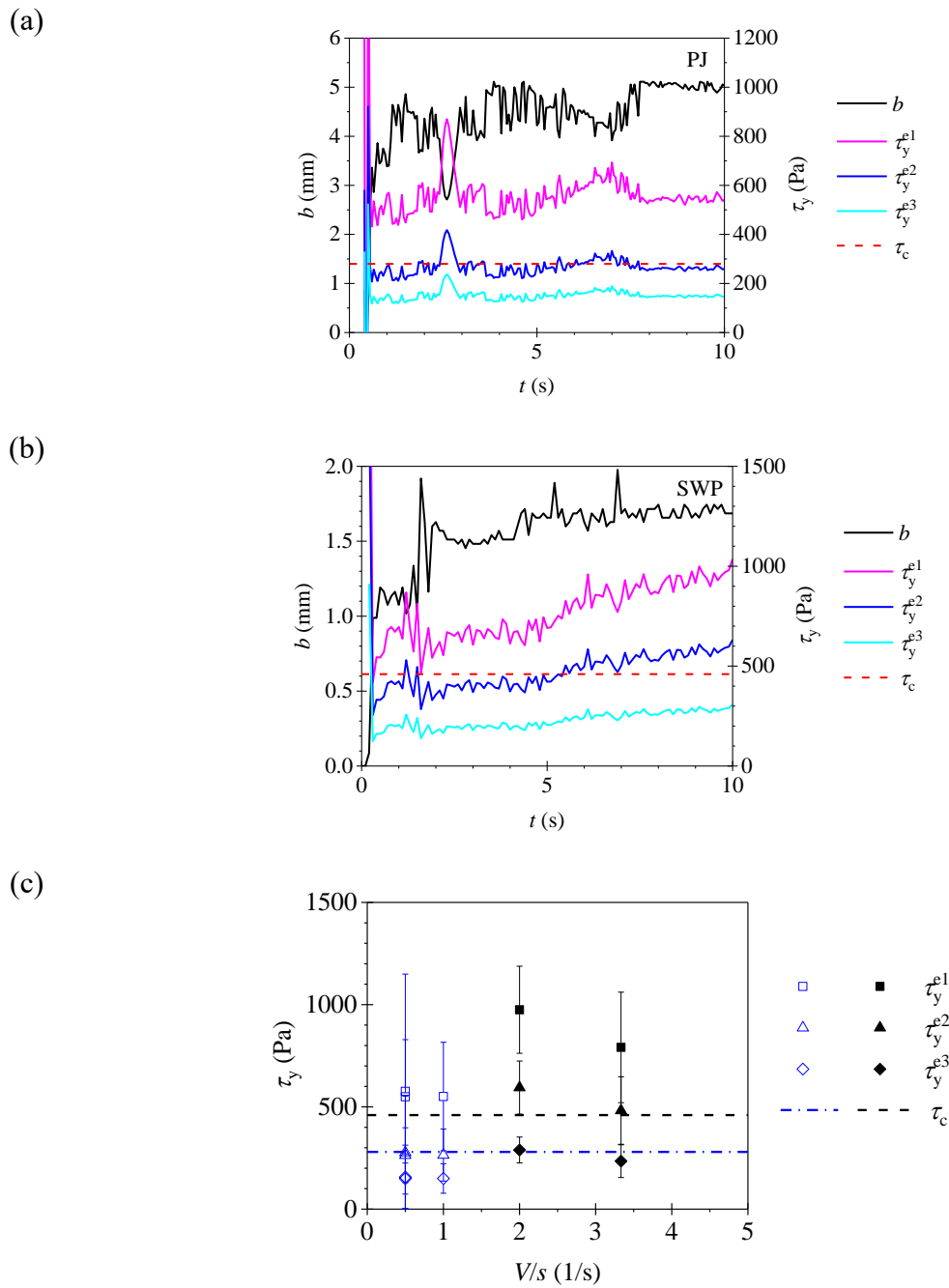
Fig. 3.20. Evolution of the berm length (black line) and estimate of yield stress from cutting theory (Equation (3.18), red line) for (a) petroleum jelly, $s = 2$ mm, $L = 20$ mm and (b) soft white paraffin, $s = 0.3$ mm, $L = 30$ mm. Test conditions: $\delta_0 = 5$ mm, $V = 1$ mm/s. Horizontal dashed lines indicate the yield stress obtained from rheometrical testing. (c) Effect of characteristic shear rate on estimated yield stress. Symbols: open – PJ; solid – SWP.

The berm length profiles and estimates of toothpaste for different scrape depths are presented in Fig. 3.21. With three different values of s, the yield stress obtained from the rheological test lies between the estimates of τ_y^{e2} and τ_y^{e3}, but the τ_y^{e2} values of PJ and SWP are similar to τ_c. This could be attributed to two reasons, namely the inconsistent deformation of toothpaste and selection of reference force (F_C, $F_{C'}$ and F_D).

The deformation of toothpaste is different from that of PJ and SWP, because toothpaste deforms when the applied shear stress is below τ_c. The phenomenon can be observed from the rheological data in Fig. 3.5(b). This also results in larger deformation region (see Fig. 3.22). The whole sample deforms at $t = 10$ s (Fig. 3.22(c)), which causes overestimation of visualisation. Moreover, the measured force increases with time and did not reach a steady value during tests. The reference values, F_C, $F_{C'}$ and F_D are not sufficient to describe the change of F_w, and more factors are required.

(a)

(b)

(c)
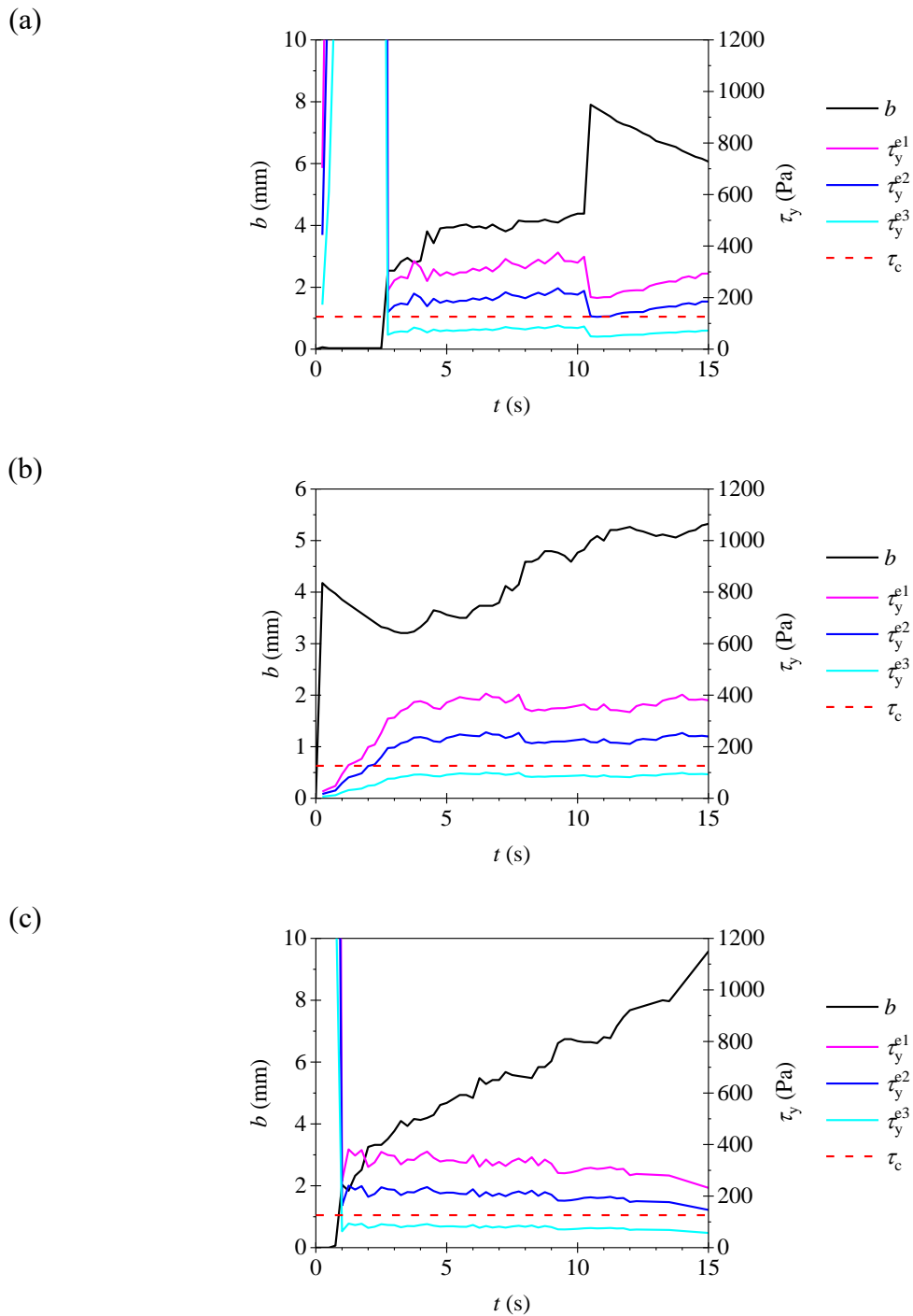
Fig. 3.21. Evolution of the berm length (black line) and estimate of yield stress from cutting theory (Equation (3.18), red line) for toothpaste at $s =$ (a) 0.5 mm, (b) 1 mm and (c) 1.5 mm. Test conditions: $\delta_0 = 2$ mm, $L = 30$ mm, and $V = 1$ mm/s. Horizontal dashed lines indicate the yield stress obtained from rheometrical testing.
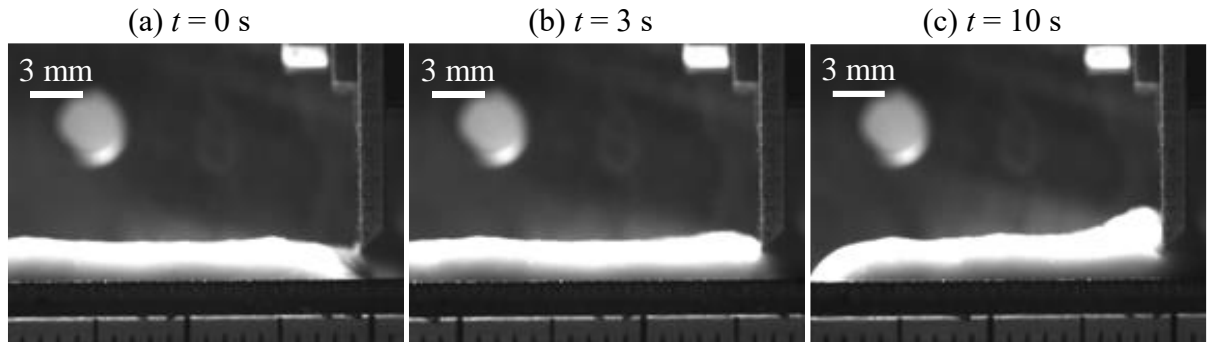
Fig. 3.22. Images for toothpaste as the blade scraped at t = (a) 0 s, (b) 3 s and (c) 10 s. Test conditions: $\delta_0 = 2$ mm, $s = 0.5$ mm, $L = 30$ mm and $V = 1$ mm/s.

3.3.2 CFD simulations

3.3.2.1   Test cases

Maillard *et al*. [49] did not present full data sets of removal forces, berm length and berm height at any one condition, so comparisons are made based on some of the cases which were presented as figures in their paper. Fig. 3.23 compares the predicted topographies of berms and images reported by Maillard *et al*. at different blade displacements. The predicted shapes are similar to the experimental ones, but slightly larger. One difficulty is that Maillard *et al.* did not provide a scale bar for their images and these images were not completely profile pictures.

A Carbopol model without gravity is solved (Fig. 3.23(a)). The predicted berm height is larger if **g** is not considered. There is relatively good agreement if gravity is included.

(a) $x = 150$ mm   (b) $x = 300$ mm
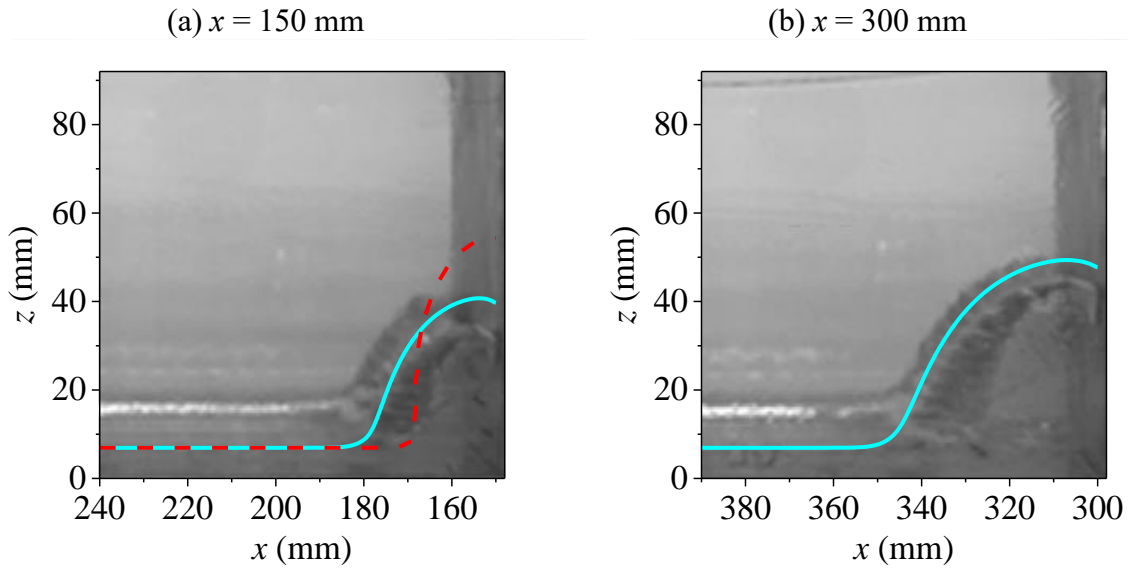
Fig. 3.23. Comparison of predicted topography using bi-viscosity model ($\mu_0 = 100$ kPa s) with the experiments reported by Maillard *et al.* [49] for Carbopol at $x =$ (a) 150 mm and (b) 300 mm. Maillard *et al.* did not provide a length scale in their images so the fitting is subject to some uncertainty. Test conditions: $\delta_0 = 7$ mm, $s = 5$ mm, and $V = 5$ mm/s. Cyan lines show simulation results. Red dashed line in (a) indicates calculation without gravity.

Fig. 3.24(a) shows the normal force acting on the blade (*i.e.* horizontal) and the tangential force (acting upwards) extracted from the simulations using the biviscosity model with different values of μ_0, as well as the experimental values reported by Millard *et al*. The evolution of predicted normal forces acting against the blade are consistent with the measured forces, but overestimate the experimental data by about 50%. One possible reason is the experimental configuration. Maillard *et al*. left a 1 mm gap between the sides of the 120 mm-wide blade and channel edges to mitigate wall friction, which allowed relaxation and flow at the boundary and could affect the measurement.

The tangential forces obtained from the simulations are similar to the measured forces for $x < 100$ mm. After that, the predicted values decrease gradually. This is attributed to the dynamic mesh algorithm in OpenFOAM. Too much change in a mesh will cause numerical issues, resulting in some inaccuracy and uncertainty. For example, when the model was solved to $x = 100$ mm, the region where mesh changed covered one quarter of the whole geometry. The simulation results do not show noticeable differences between $\mu_0 = 100$ kPa s and 10 kPa s, indicating that the creeping viscosity does not have significant impacts on the forces exerting

on the blade. The application of the Herschel-Bulkley model to represent the thixotropic fluid, Carbopol, is widely used [151-153], and the steady state data in the paper show good agreement.

Maillard *et al*. [49] proposed a relationship between the berm height and length, $h_b^2 = \kappa(b - b_0)$, where κ is a factor and b_0 is the fast initial increase of berm length. Fig. 3.24 (b) compares the squared berm height and berm length between the simulations and experimental results reported by Maillard *et al*. Acceptable agreement is evident, and the experimental values are in the region covered by the predicted results using $\mu_0 = 100$ kPa s and 10 kPa s, indicating that modelling using a creeping viscosity between $\mu_0 = 100$ kPa s and 10 kPa s could provide better agreement. In addition, the predicted results for $\mu_0 = 10$ kPa s at $\delta_0 = 7$ mm and 20 mm show a similar trend to the experiments, namely the berm height at $\delta_0 = 7$ mm higher than that at $\delta_0 = 20$ mm.

Maillard *et al*. reported that a noticeable difference of the aspect ratio (h/b) was observed between $\delta_0 < 7$ mm and ≥ 7 mm. This phenomenon could be explained by the simulations. At $\delta_0 = 20$ mm and $s = 5$ mm, there was a gap beneath the blade, which allowed the Carbopol to flow through and resulted in a lower berm height. By contrast, at $\delta_0 = 7$ mm, the gap was too small (2 mm), so Carbopol accumulated in front of the blade and formed a higher berm during tests.

These results demonstrate that this CFD model is acceptable to be employed for predicting the deformation of Carbopol while being scraped, and can be applied for other materials in millimanipulation tests.

(a)

(b)
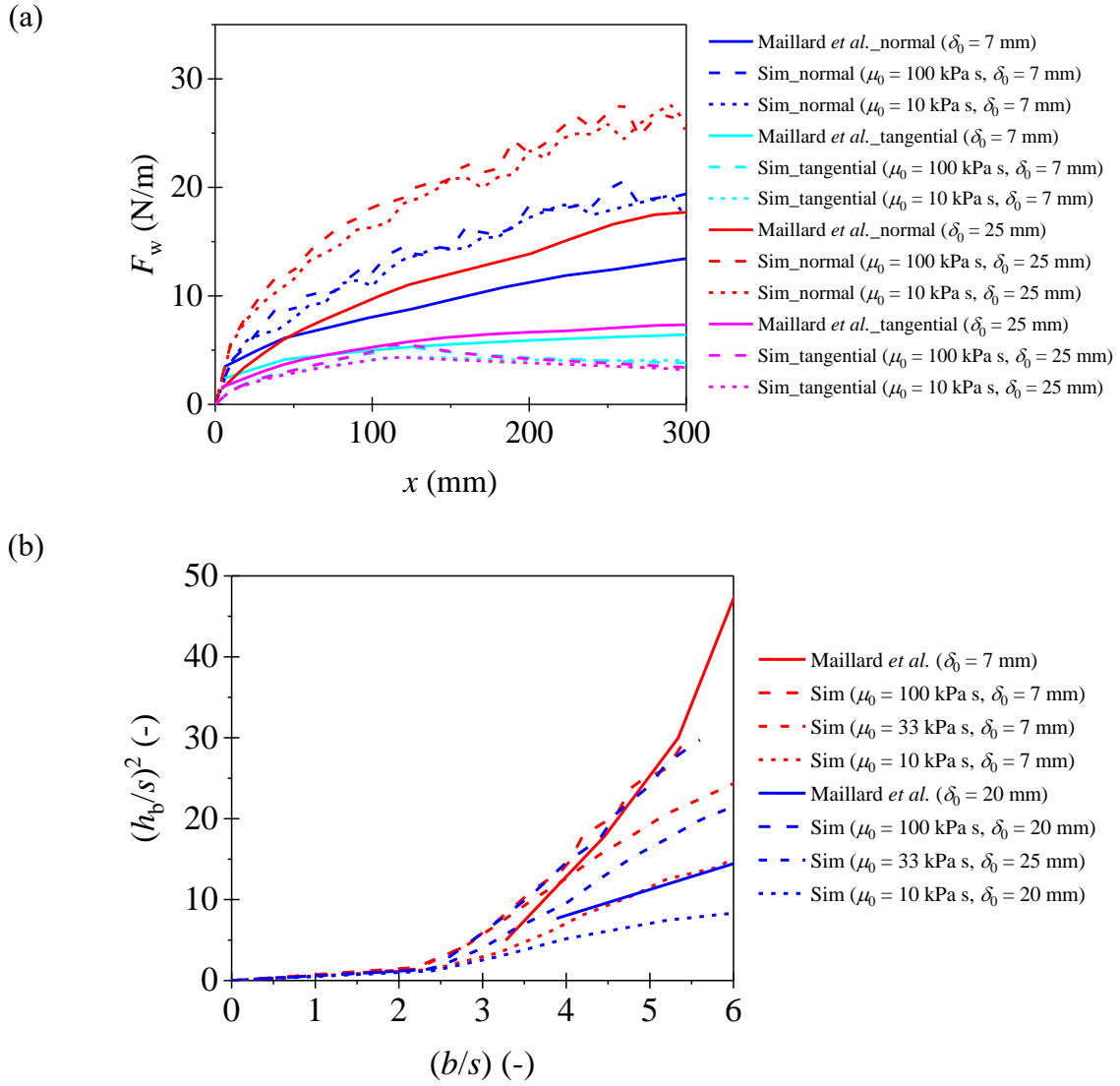
Fig. 3.24. Comparisons of simulations using bi-viscosity model and experiments reported by Maillard *et al.* [49] for Carbopol with $s = 5$ mm, $\tau_c = 98$ Pa, different δ_0: (a) removal forces, $V = 5$ mm/s; (b) squared berm height as a function of length of the heap formed behind the blade, b (see Fig. 3.2), $V = 1$ mm/s.

3.3.2.2   *Mesh sensitivity test*

Fig. 3.25 shows the results of a mesh sensitivity test using cubic elements and the regularised Bingham model for petroleum jelly at three different uniform mesh sizes. The berm shapes in Fig. 3.25(a) are similar and show good agreement with the image. Also, the predicted F_w values using the 50 μm and 20 μm elements are similar and agree with the experimental results, but F_w using the 100 μm mesh is lower than the measured value. These results indicate that both

77

50 μm and 20 μm mesh sizes are acceptable for the millimanipulation simulation. The 20 μm mesh is more computationally expensive, so the 50 μm mesh was chosen.
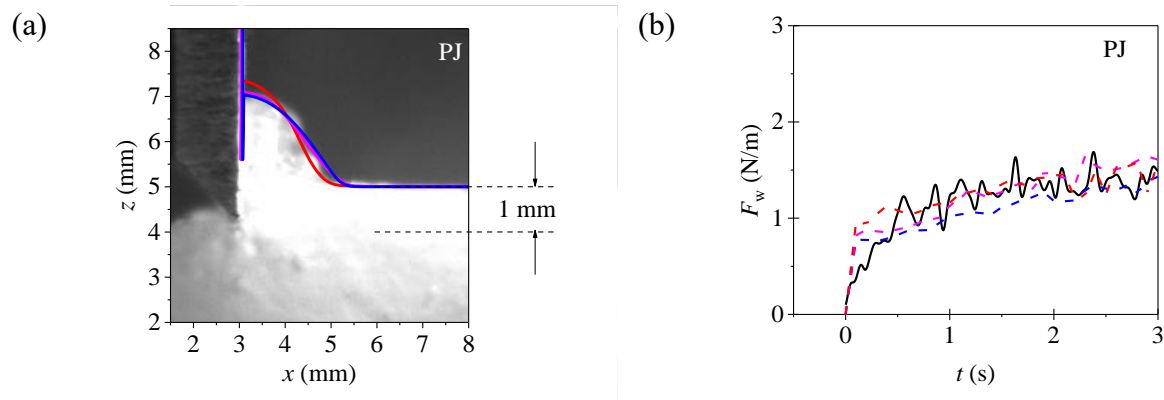
Fig. 3.25. Mesh sensitivity test using the regularised Bingham model for petroleum jelly at three different uniform mesh sizes (cubic elements): (a) predicted berm shapes with image and (b) predicted removal force. Test conditions: petroleum jelly, δ_0 = 5 mm, L = 30 mm, V = 1 mm/s, and t = 3 s. Colour indicates mesh size: blue – 100 μm; magenta – 50 μm; red – 20 μm.

3.3.2.3 Validation

Fig. 3.26(i) compares the predicted berm shapes for the bi-viscosity and regularised Bingham models with experimental images for petroleum jelly at the same time as that in Fig. 3.14 (t = 3s). These tests did not exhibit slip. With s = 1 mm, both models give similar shapes. It is difficult to prepare a petroleum jelly layer with a uniform and smooth surface, because the material is inhomogeneous. The agreement can be considered agreeable. For the larger scrape depth (Fig. 3.26(b,i)), the RBM gave better agreement. This is because the smoothing parameter in the RBM provides a better description around the yield stress (Fig. 3.4). Comparisons for other measures (forces and distributions) will be discussed later.

With the RBM giving better agreement, its predicted relative velocity distributions are plotted in Fig. 3.26(ii). Higher velocities occurred mainly close to the blade and above the level of the blade, which is similar to the experimental data in Fig. 3.14. This phenomenon was also reported by Millard *et al.* using Carbopol 980 [49]. The velocity distributions of the BVM did not differ noticeably from the results predicted with the RBM.

78
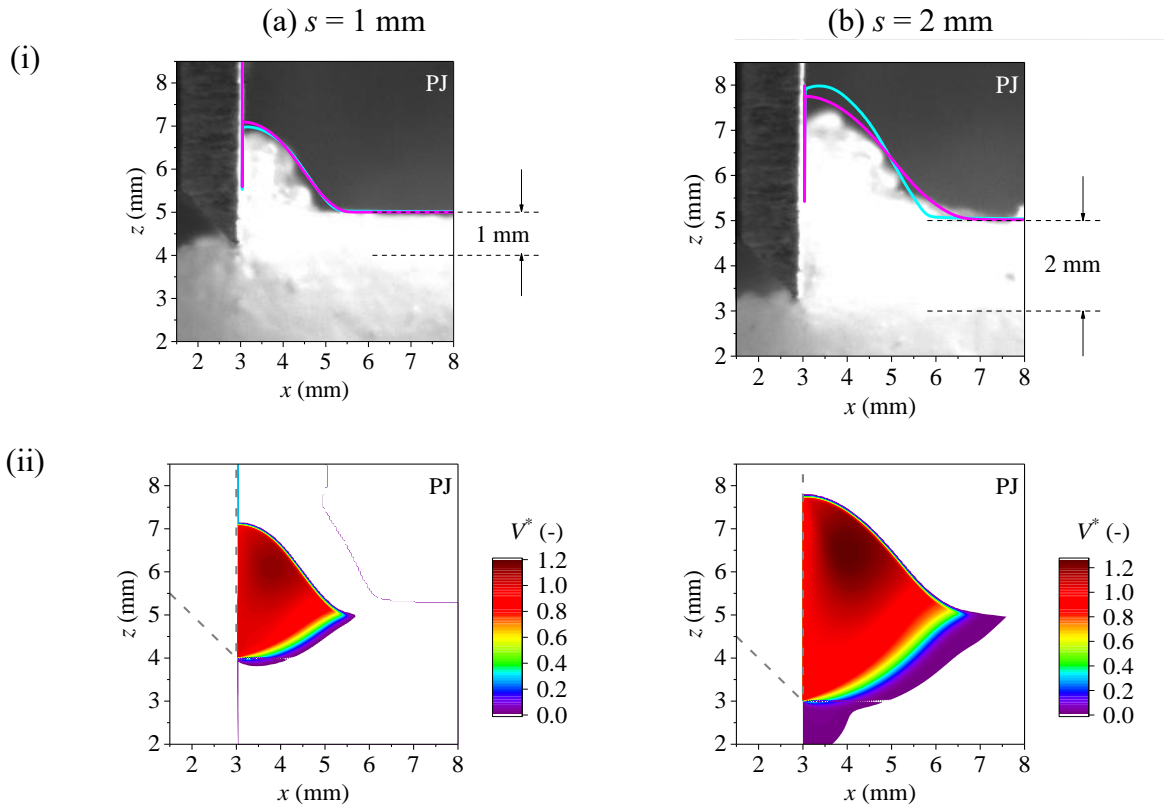
Fig. 3.26. Comparison of (i) berm shape predicted with regularised Bingham (cyan loci) and bi-viscosity (magenta) rheological models, and (ii) velocity distributions predicted with regularised Bingham model for petroleum jelly at $s =$ (a) 1 mm and (b) 2 mm. Test conditions: $\delta_0 = 5$ mm, $L = 30$ mm, $V = 1$ mm/s and $t = 3$ s.

Fig. 3.27(i) compares the berm shapes predicted for SWP with images at $t = 3$ s. The berm shapes obtained from both models are similar and slightly taller than that in the image. This is attributed to spreading outwards of the sample during the experiment. Unlike PJ, at larger s, the BVM shows better agreement than the RBM. This is because the bi-viscosity model describes the rapid transition at the critical shear stress well.

The relative velocity distributions in Fig. 3.27(ii) are also similar to the distributions observed in the experiments in the absence of slip (Fig. 3.15).
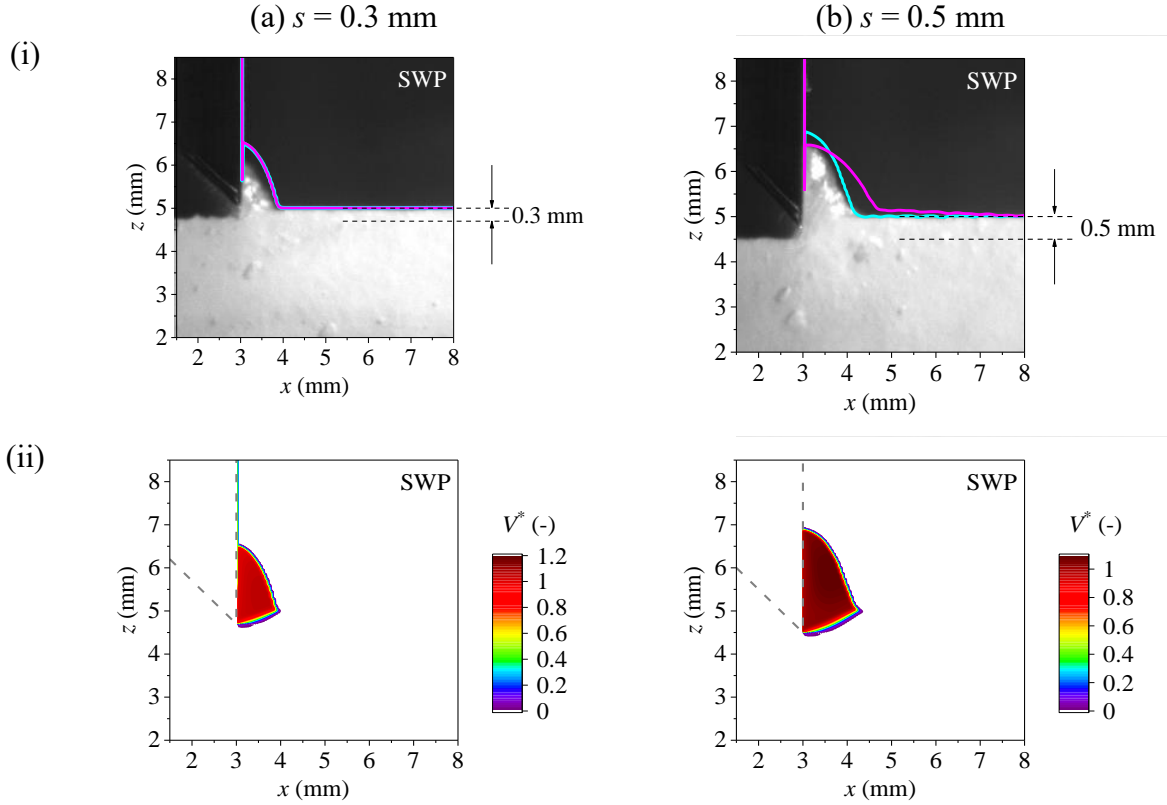
Fig. 3.27. Comparison of (i) berm shape predicted with regularised Bingham (cyan loci) and bi-viscosity (magenta) rheological models, and (ii) velocity distributions predicted with bi-viscosity model for soft white paraffin at $s =$ (a) 0.3 mm and (b) 0.5 mm. Test conditions: $\delta_0 = 5$ mm, $L = 30$ mm, $V = 1$ mm/s and $t = 3$ s.

The volume of the dislodged berm (patterned cyan area in Fig. 3.28(a)) can be calculated using the Maillard *et al.* relationship ($h^2 = \kappa(b - b_0)$) [49] with two assumptions, $b_0 = 0$ and a parabolic berm. In this study, the berm length and height were estimated by a visualisation programme, so b_0 could be very small and is assumed to be zero, which is different from the Maillard *et al.* experiment, in which b_0 was estimated visually. The relationship can be

$$Vts = \frac{2h_b^3}{3\kappa} \tag{3.19}$$

The volume is equal to the scraped volume, Vst, so $t \propto h_b{}^3$ or $b^{3/2}$. In Fig. 3.28(b) and (c), the profiles of PJ and SWP follow the relationship well at $t > 5$ s. The initial deformation does not meet the trend due to the main fact that the sample edge contacting the blade was not perfectly rectangular, increasing uncertainty of deformation.

(a)
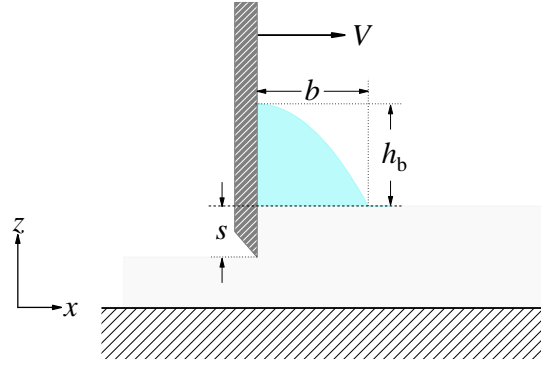
(b)
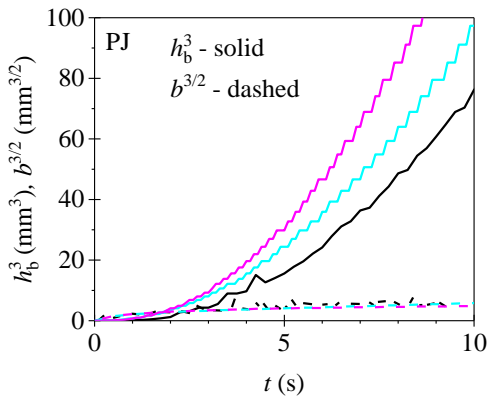
(c)
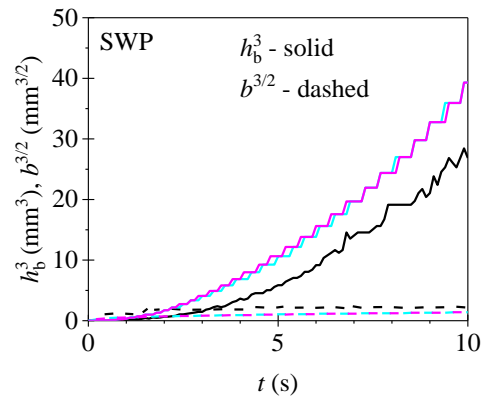
Fig. 3.28. (a) Schematic of berm volume estimated from $h_b^2 = \kappa(b - b_0)$. Comparisons of simulations using BVM and RBM and experiments: $t \propto h_b^3$ and $b^{3/2}$ for (b) petroleum jelly at $s = 1$mm and (c) soft white paraffin at $s = 0.3$ mm. Test conditions: $\delta_0 = 5$ mm, $L = 30$ mm, and $V = 1$ mm/s. Cyan area denotes estimated area. Colour: black – measured; cyan – bi-viscosity model; magenta – regularised Bingham model.

3.3.2.4   Quasi-steady state

The force profiles obtained with petroleum jelly at different values of *s* in Fig. 3.7(a) show an initially rapid increase, followed by an approach to an asymptote as the berm of dislodged material builds up. In order to compare the profiles with the model predictions, average values, $\bar{F}_w$, for experiments and simulations were calculated from $t = 3$ s to 10 s (see Fig. 3.7(a)) and are plotted in Fig. 3.29. The error bars represent the change of force over this period. The measured and calculated forces increase with *s*. The RBM overestimated $\bar{F}_w$ even though it fitted the rheological data and predicted the shape of berm well (shown above). By contrast, the biviscosity model gave good agreement with the experimental $\bar{F}_w$ values.

81

Comparing with the scrape depth for PJ, the depth used for SWP in the absence of slip is smaller, which limits the study of the scrape depth effect for SWP.
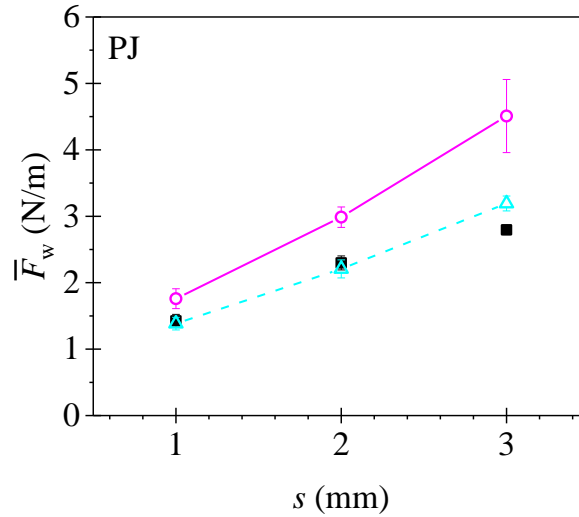
Fig. 3.29. Effect of scraping depth on removal force for petroleum jelly at $\delta_0 = 5$ mm, $V = 1$ mm/s and $L = 30$ mm. Symbols: black square – experimental data; cyan triangle – bi-viscosity model; magenta circle – Regularised Bingham model; model parameters in Table 3.1.

Fig. 3.13 shows that $\bar{F}_w$ for petroleum jelly and soft white paraffin increased with scraping speed. Compared the data with the simulation predictions using both viscosity models (Fig. 3.30), the $\bar{F}_w$ values are at the same order of magnitude. The predicted values using the RBM show good agreement at $V > 1$ mm/s, but at lower speed, $\bar{F}_w$ is overestimated.

The bi-viscosity model with a creeping viscosity of 5 kPa s gives good fits for PJ apart from $V = 0.05$ mm/s. Larger μ_0 values (100 kPas and 1 MPa s) were used to the apparent viscosity in Fig. 3.4(a,ii), which are more close to the apparent viscosity. However, the results do not give better agreement than that using $\mu_0 = 5$ kPa s, and the values at $V = 1$ mm/s are overpredicted. This indicates that $\mu_0 = 5$ kPa s is the upper limit for simulations. On the other hand, the bi-viscosity model cannot describe the transition of the material from solid to fluid well (see Fig. 3.4(a,ii)). Modelling using the BVM with a lower viscosity ($\mu_0 = 5$ kPa s) can be an alternative approach to simulate the transition.

Fig. 3.30(b) shows that neither viscosity model captures the effect of scraping speed for SWP. The order of magnitude is connect. Strongly plastic behaviour is evident in Fig. 3.4(b,i), where the stress is nearly constant as the stress is more than the yield stress. The simulations can capture the behavior and forces.

The interrupted testing discussed above has shown that both materials exhibit noticeable creep, which is important while being scraped at low speeds. Neither viscosity model captures the creeping motion below the yield point well [154], so the accuracy of the simulations at low velocity is not expected to be strong.

(a)
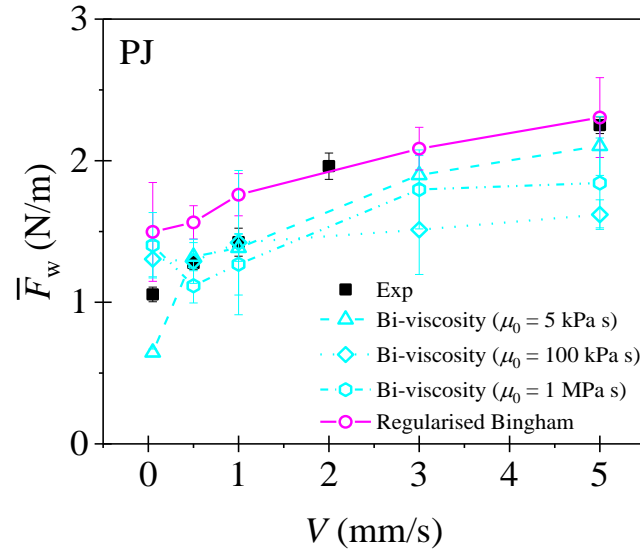
(b)
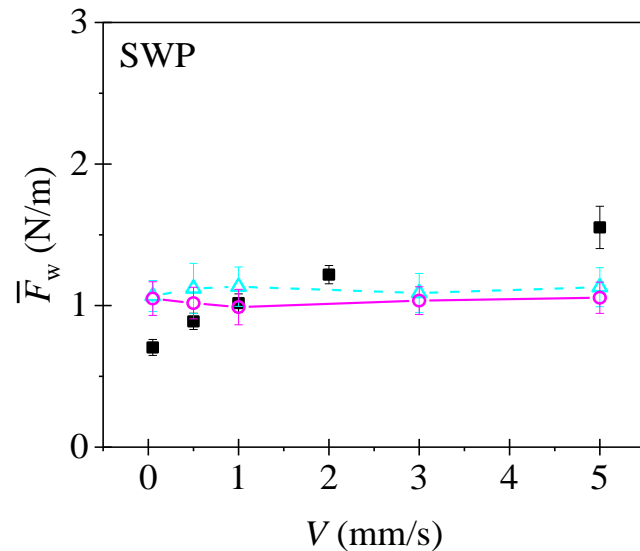
Fig. 3.30. Effect of scraping speed on removal force for (a) petroleum jelly, $s = 1$ mm and (b) soft white paraffin, $s = 0.3$ mm. Test conditions: $\delta_0 = 5$ mm and $L = 30$ mm. Symbols: black square – experimental data; cyan – simulation, bi-viscosity model, μ_0 values indicated; magenta circle – simulation, Regularised Bingham model.

3.3.2.5   *Simulated dynamics*

Fig. 3.31(i) and (ii) compare the predicted force, F_w, berm height, h, and berm length, b, profiles for the two viscosity models with the experimental data for petroleum jelly at different values of s. For the RBM, good agreement with the measured forces can be observed in both cases before $t = 3$ s, after which the model overestimated the values. By contrast, the bi-viscosity

model predicted F_w well over the test period. Both models show reasonable agreement for the berm length. The predicted berm heights from both models are slightly higher than the measured ones. This systematic error could be caused by the sideways movement of PJ when contacted by the blade (see Fig. 3.17). The simulation is 2-dimensional so it cannot capture this effect.

Fig. 3.31(a,i) shows that the RBM gave good agreement during the initial deformation. The longer term dynamics are considered less important in the cleaning applications. The noise in the F_w profiles mainly arises from the numerical peaks caused by the mesh motion. The values were estimated by integrating the pressure along the blade, so when the mesh moved, high pressure values occurred at the interface between static and moving mesh elements.

Maillard *et al*. [49] reported that the change of berm length and height with time in their Carbopol tests followed the relationship, $h_b^2 = \kappa (b - b_0)$. Fig. 3.31(iii) shows the data from Fig. 3.31(ii) plotted in this form. Both experimental and simulation results follow the trend roughly (with b_0 large). The trend could be attributed to the smaller influence by gravity (absence of slumping). Maillard *et al*. also used the ratio, $\left(\tau_y + k_{HB} \left(\frac{V}{s} \right)^n \right) / \rho g$, to classify material's deformation. The values for Carbopol® 980 reported by Maillard *et al.* were 0.007-0.021, indicating that compared to the influence of the shear rate, the effect of gravity is more important. The value for PJ is about 0.036, meaning that the effect of the shear rate is more significant than that of gravity.

One possible reason why the simulations cannot capture the long-term behaviour of the materials is that the contribution to the measured force from the dislodged material marked II in Fig. 3.2(b), was not captured well. Fig. 3.31(i) shows the rate of viscous dissipation in the material above the initial layer thickness (I/II interface), Q_D, calculated from by $F_w V$. $F_w V$ is the total rate of viscous dissipation by the blade. The viscous dissipations predicted from both viscosity models at $s = 1$ mm are similar and small. The contributions from viscous dissipation at larger scrape depth are higher, but still small.
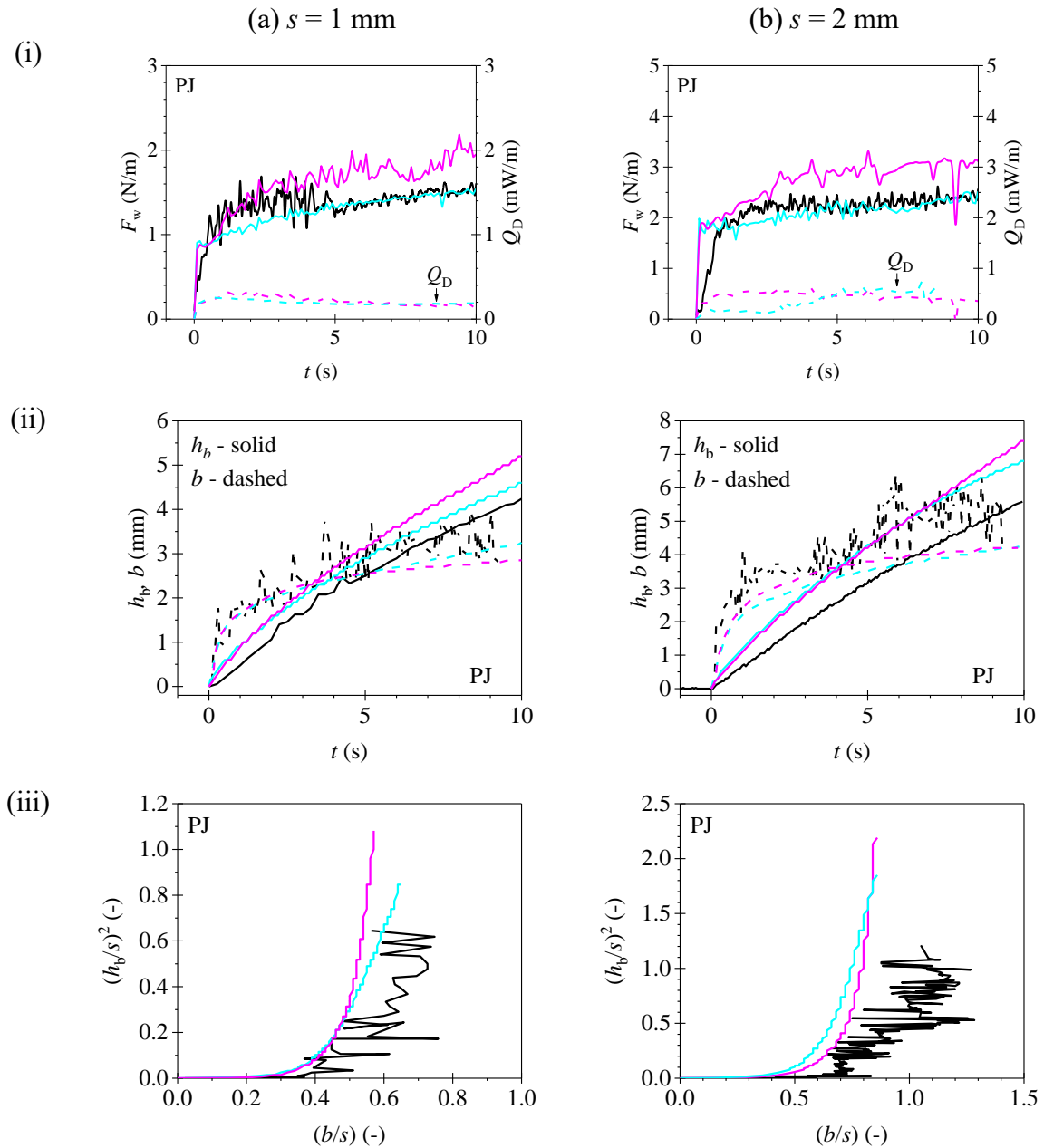
Fig. 3.31. (i) Comparisons of experimental and predicted removal forces as well as calculated viscous dissipation along *z*-axis, (ii) evolution of berm height, h_b, and length, b, and (iii) h_b^2 versus b, for petroleum jelly at *s* = (a) 1 mm and (b) 2 mm. Test conditions: δ_0 = 5 mm, *L* = 30 mm and *V* = 1 mm/s. Solid lines show F_w: black – measured; cyan –bi-viscosity model; magenta –regularised-Bingham model. Dashed lines – estimated contribution from viscous dissipation in the material moving up the blade.

Fig. 3.32 (i) shows that the bi-viscosity model gives better agreement with F_w for SWP in these two cases. The increase in F_w was not captured well. Although F_w for SWP is similar to the value for PJ at *s* = 1 mm, the rate of viscous dispassion is smaller. This is due to the smaller

deformation volume. Systematic errors are evident in the predictions of the berm height. In Fig. 3.32 (a,ii), both simulated berm lengths show nearly the same trend, but are lower than the measured height. The berm length should be related to the berm height via a mass balance. The difference could result from the visualisation process. The berm length was determined by measuring the horizontal distance between the blade and the first point of the change of surface slope, which is sensitive to the image resolution. For the larger scrape depth, both models give a better description of the berm length.

Fig. 3.32(iii) shows that the berm shapes of experimental and simulation data fit the quadratic relationship at $(h_b/s)^2 > 0.1$, and have similar trends. The ratio of shear to hydrostatic stress components for SWP is around 0.059 and higher than PJ, meaning that the shear contribution of SWP is stronger. On the other hand, the contributions from viscous dissipation in Fig. 3.32(i) are nearly negligible.

The consistent failure to overestimate the berm shape of PJ mainly due to the time-dependent sideways spreading, which has been observed by the interrupted tests (see Fig. 3.8). By contrast, folding behaviour of SWP during tests results in lower berm height than the predicted berm height. Both behaviours, including spreading and folding cannot be simulated by the model.
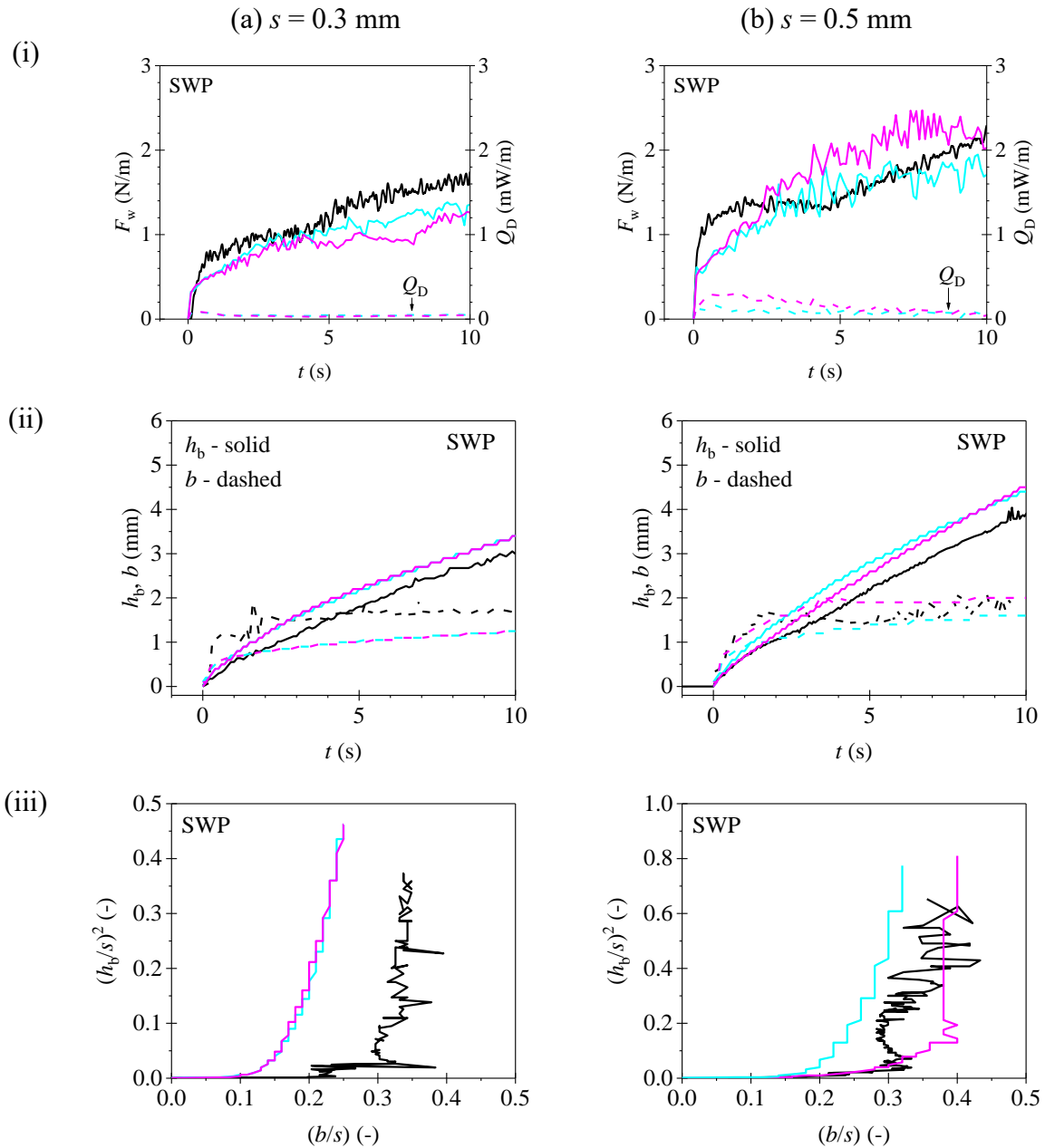
Fig. 3.32. (i) Comparisons of experimental and predicted removal forces as well as calculated viscous dissipation along z-axis, (ii) evolution of berm height, h_b, and length, b, and (iii) h_b^2 versus b, for soft white paraffin at s = (a) 0.3 mm and (b) 0.5 mm. Test conditions: δ_0 = 5 mm, L = 30 mm and V = 1 mm/s. Solid lines show F_w: black – measured; cyan –bi-viscosity model; magenta –regularised-Bingham model. Dashed lines – estimated contribution from viscous dissipation in the material moving up the blade.

3.3.2.6 *Model sensitivity*

Pervious sections compared the experimental data with the results predicted from two viscosity models, namely the regularised Bingham and the bi-viscosity model. The question to be answered is whether the millimanipulation device could be used to determine the rheology of the layer material from *in-situ* testing. The sensitivity of the model parameters needs to be established as this will indicate whether or not they could be estimated reliably from such tests.

Two cases using different model parameters are considered here.

Case I – Petroleum jelly using the regularised Bingham model

The rheological data in Fig. 3.4(a,ii) show that the RBM gave a better description of the apparent viscosity than the BVM. The effect of changing each parameter (τ_y: 249 Pa, m_{BP}: 8869, μ_p: 12.4 Pa s) in RBM by ± 20% is shown in Fig. 3.33. Changing the smoothing index and plastic viscosity by ± 20% gives negligible difference. By contrast, the effect of changing the yield stress is strong, especially on F_w, which is consistent with the high *Bn* value. These results indicate that it is possible to employ the millimanipulation device to estimate the yield stress. This applies to materials with large *Bn*, *i.e.* yield $\gg$ viscous contribution.
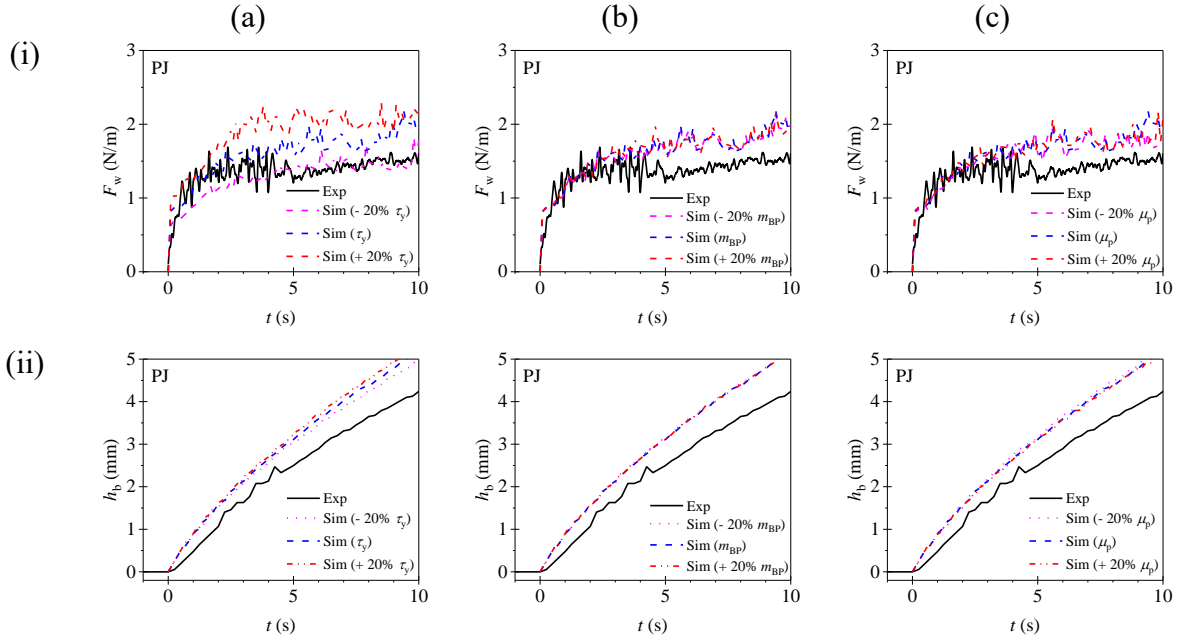
Fig. 3.33. Sensitivity study for regularised Bingham model. Effect on (i) removal force and (ii) berm height with changes in (a) yield stress τ_y, (b) smoothing index m_{BP}, and (c) plastic viscosity, μ_p. Test conditions: petroleum jelly, $\delta_0 = 5$ mm, $L = 30$ mm, $s = 1$ mm and $V = 1$ mm/s.

The profiles of F_w and h in Fig. 3.34 present the effect of changing the surface tension, $\sigma_{PJ\text{-air}}$ (0.07 N/m). Values of $0.1\sigma_{PJ\text{-air}}$ and $10\sigma_{PJ\text{-air}}$ are selected. While $10\sigma_{PJ\text{-air}}$ is not realistic, a high value is required to test the effect of the surface tension due to the high yield stress of PJ.

Decreasing $\sigma_{PJ\text{-air}}$ has less influence on F_w and h due to the fact that deformation is controlled by the yield stress. However, the results for $10\sigma_{PJ\text{-air}}$ shows smaller removal force and lower berm height. This is because under these conditions, the surface tension dominates during test. When the sample is scraped, the surface tension acts to decrease the surface area and reduces the height of the berm.

(a)

(b)
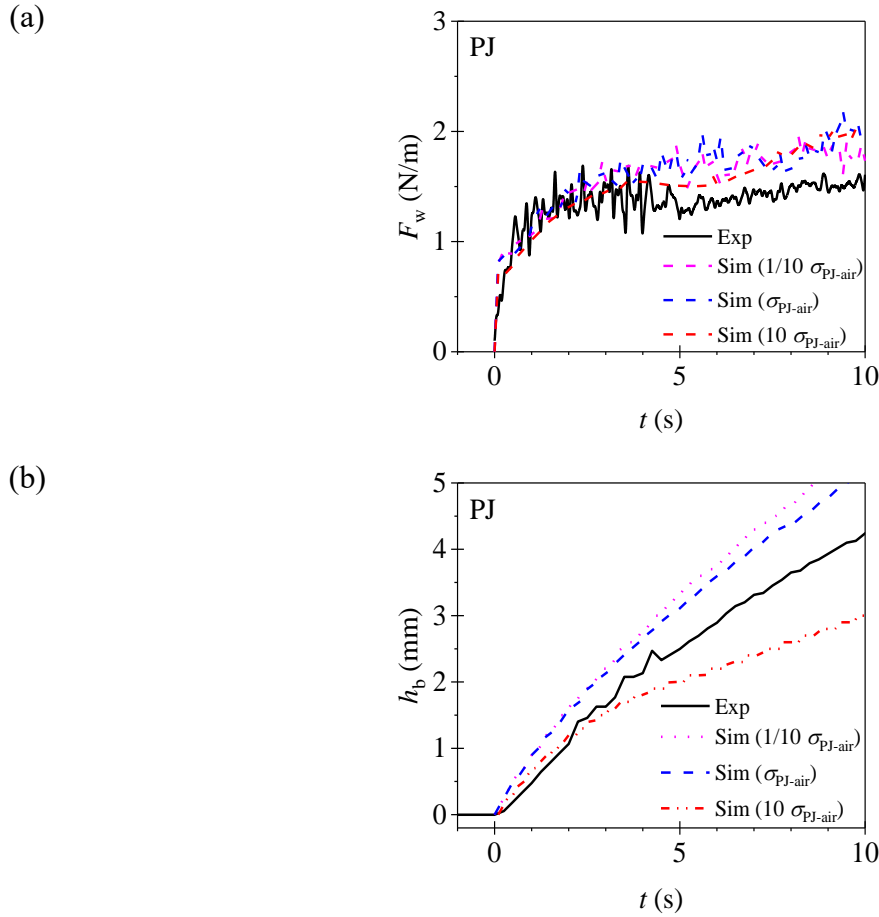
Fig. 3.34. Sensitivity study for surface tension. Effect on (a) removal force and (b) berm height. Test conditions: petroleum jelly, regularised Bingham model, $\delta_0 = 5$ mm, $L = 30$ mm, $s = 1$ mm and $V = 1$ mm/s.

Case II – Soft white paraffin using the bi-viscosity model

For the BVM, in order to observe the influence of changing a parameter (k_{HB} or n_{HB}), it is important to adjust another parameters to compensate for the effect. Taking changing n by $\pm$ 20% as an example, the viscosity above the yield stress can be rearranged to give the following results for the apparent viscosity.

$$\mu = \frac{\tau_y}{\dot{\gamma}}\left[1 + \frac{k_{HB}}{\tau_y}\dot{\gamma}^{n_{HB}-2}\right] \tag{3.20}$$

The characteristic shear rate, V/s, is used for $\dot{\gamma}$. k_{HB} is adjusted to maintain the value of $k_{HB}\dot{\gamma}^{n_{HB}-2}$ constant. The original model parameters for τ_y, k_{HB}, and n_{HB} are 460 Pa, 21.5 Pa s$^{0.1}$ and 0.1, respectively.

91

Fig. 3.35(a,i) shows that the yield stress has a significant impact on F_w, and F_w increases with τ_y. The behaviour is similar to the effect of changing scrape depth, in which a larger scrape depth cause more material to deform and the force required to dislodge material increases. In addition, by increasing the resistance for deforming the material, the berm height rises (Fig. 3.35(a,ii)), because it is more difficult to deform. The material is dislodged upwards directly when being scraped. This indicates that adjusting the value of yield stress to match the required force and berm height obtained from the experiments can be used to estimate material's yield stress.

By contrast, in Fig. 3.35(b) and (c), no noticeable influence is observed as n and μ_0 are changed. However, the berm height increases slightly with μ_0 (Fig. 3.35(c,ii)). A fluid with higher viscosity would exhibit more solid behaviour, which is similar to increasing τ_y. The profiles of berm height for $\mu_0 = 1$ MPa s and 10 MPa s are similar, which indicates that the upper limit of applied viscosity in this case is 1 MPa s.
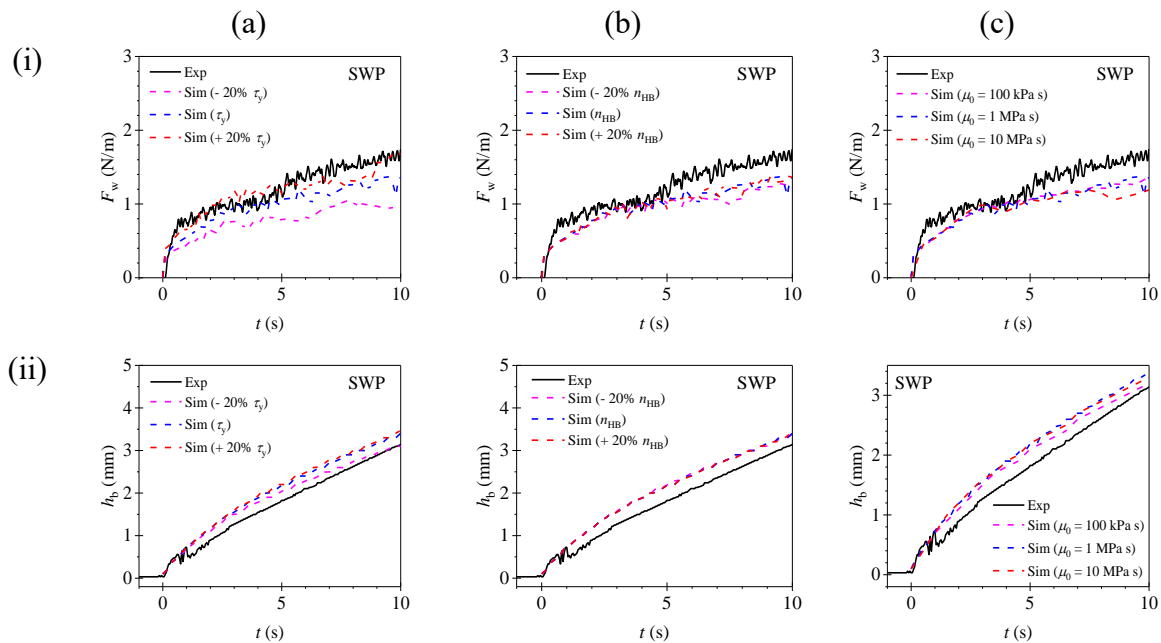
Fig. 3.35. Sensitivity study for bi-viscosity model. Effect on (i) removal force and (ii) berm height by changing in (a) yield stress τ_y, (b) flow index, n_{HB}, and (c) creeping viscosity, μ_0. Test conditions: soft white paraffin, $\delta_0 = 5$ mm, $L = 30$ mm, $s = 0.3$ mm and $V = 1$ mm/s.

3.4   Conclusions

In this chapter, the millimanipulation device reported by Magens *et al.* [9] was used to study the development of layers of petroleum jelly, soft white paraffin and toothpaste *in situ*. A computational fluid dynamics simulation with the RBM and the BVM was used to predict the deformation of PJ and SWP while being scraped.

A series of visualisation studies were performed to capture the shape and deformation of the layer during scraping. Wall slip was observed for PJ and SWP under some conditions. Combining visualisation with the force on the blade, the adhesive strength (slip) of soft layers could be estimated. Interrupted testing allowed the characteristic time for stress relaxation to be determined, and change in forces on interruption could be applied with a simple metal cutting theory to estimate the yield stress.

Rheological investigations of PJ and SWP indicated that both exhibited yield stress behaviour. The simulation results of PJ with the RBM gave better agreement with the experimental data, but SWP with the BVM showed good fits with the measured berm height and force. This is thought to be due to the description of the rheology in the yielding transition. The predicted velocity distributions were similar to those obtained from visualisation. The sensitivity tests for the rheological parameters in the simulations showed that the yield stress was the dominant factor for two viscosity models and the creeping viscosity in the bi-viscosity model was also important.

Based on these findings, the millimanipulation device could be employed to determine the basic rheological behaviour of soils, which are difficult to be loaded in a rheometer. Furthermore, after improving the resolution and accuracy of the visualisation, combining the method with the CFD simulation would be possible to estimate the rheological parameters.

In addition, the Maillard *et al.* [49] results could be simulated if a confined-space boundary condition could be simulated. More work on the model is needed, such as finding an alternative dynamic mesh algorithm.

Chapter 4   Fluid Dynamic Gauging Devices

4.1   Introduction

This chapter presents calibrations and fundamental studies for the ZFDG device created by Wang *et al.* [6] and two innovative FDG developments as well as the application to study swelling and shrinkage of soft solid layers. The first development is sideways ZFDG, namely SiDG, which was created using a horizontal FDG nozzle integrated with a vertical positioner as a conveyor to allow layers to be moved from air into the gauging liquid environment, and then measured immediately. This concept was proposed by PhD student Georgina Cuckston and Professor Ian Wilson. With the current ZFDG system, there is a delay lasting up to several minutes can elapse after the sample is initially immersed (to zero the nozzle) before reliable measurements can be made. Soft layers can change their properties significantly over this initial period and it would be advantageous to eliminate this delay.

The second development is integrated ZFDG, namely iFDG, in which an inductive proximity sensor (IPS) is installed with the FDG nozzle for replacing an extensive pre-calibration process. In the current ZFDG system, during calibration, h_o is set using feeler gauges, which can introduce inaccuracy in the measurement of layer thicknesses. It would be preferable to have a built-in location technique. The inductive sensor measures the distance between an inductive coil and a metallic target by generating a magnetic field using an oscillating voltage on the coil. An eddy current is induced in the target by the magnetic field, resisting the field and decreasing the amplitude of the voltage on the coil. As the coil approaches the metallic object, the induced eddy current increases and the oscillating voltage decreases more. The voltage change is thus employed to estimate the distance. This technique has been widely applied for non-contact measurement devices with benefits such as long life time and low maintenance [155].

Moreover, it will not be affected by non-metallic fouling and layer's liquid environment, and could be built into the FDG nozzle. Each of the FDG development, were designed, constructed

and commissioned. PhD student Georgina Cuckston provided complex model soil layers to test on the SiDG. A range of materials which undergo swelling were chosen, prepared, and measured using both FDG devices at different liquid environments.

Fig. 4.1 demonstrates the principle of FDG operation and geometry of a typical FDG nozzle head. The detailed FDG operation has been shown in section 2.3.2. The pressure drop, $P - P_0$, is a function of the nozzle throat diameter, d_t, nozzle rim width, w_r, nozzle rim thickness, w_e, inner diameter of the nozzle tube, d_i, converging angle of the nozzle, β, flow rate and h_o. Thus, the pressure drop can be used to estimate h_o, if other parameters are constant. The length of the nozzle tube is labelled as l. The key dimensions for all FDG devices employed in this chapter are shown in Table 4.1.
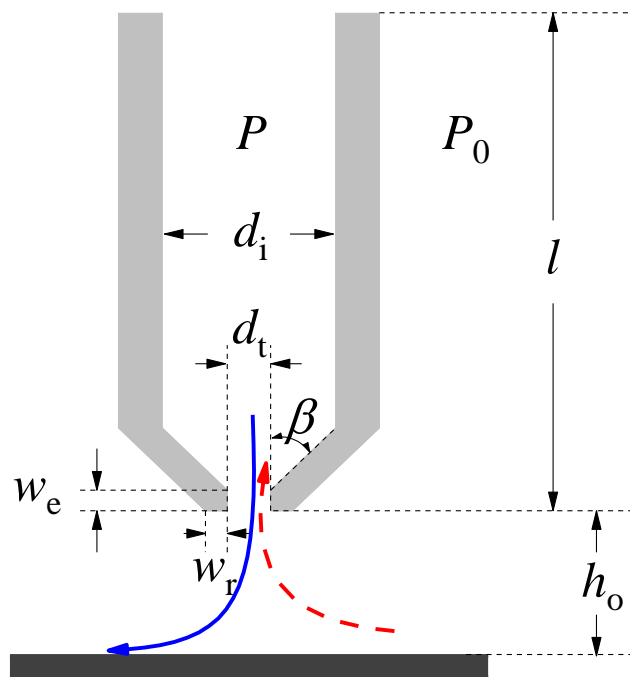
Fig. 4.1. Schematic of FDG nozzle geometry. Solid and dashed streamlines indicate ejection and suction modes, respectively.

Table 4.1. Comparison of design parameters of FDG test rigs

	Parameters	ZFDG	SiDG	iFDG
Gauging nozzle	d_t (mm)	1.0	1.0	0.95
	d_i (mm)	5.85	4	6
	d_o (mm)	10	6	20
	w_e (mm)	0.15	0.2	1
	w_r (mm)	1.0	0.5	5.02
	β (°)	45	45	45
	l (mm)	310	295	300
	Material	310 SS	316 SS	PEEK
Gauging surface	Material	316 SS	316 SS	316 SS
Gauging variables	Resolution	$\pm$ 10 μm	$\pm$ 10 μm	$\pm$ 10 μm
	Re_t regime	375~1312	375	0.0045~398
Gauging liquids		Deionised water	Deionised water, alkali solution	Deionised water, whole UHT milk, skimmed UHT milk, washing up liquid, 1% and 3% CMC solutions
Sample materials		Petroleum jelly	Petroleum jelly, gelatin, PVAc, complex model food soil (CMS)	Deionised water ice, whole UHT milk ice, skimmed UHT milk ice
Pressure transducer	Brand	SensorTechnics	SensorTechnics	OMEGA
	Operating limits	−8 ~ 9 kPa (E < 1%)[a]	−8 ~ 9 kPa (E < 1%)	0 ~ 35 kPa
Syringe pump	Brand	Harvard Apparatus (E < 1%)	Harvard Apparatus (E < 1%)	Harvard Apparatus (E < 1%)
Positioners	Brand	Zaber (*z*-axis) Standa (*x&y*-axis)	Zaber (*x&z*-axis)	Zaber (*z*-axis) Standa (*x&y*-axis)
	Resolution	2 μm (*z*-axis) 0.31 μm (*x&y*-axis)	2 μm (*x&z*-axis)	2 μm (*z*-axis) 0.31 μm (*x&y*-axis)

[a] E is error.

4.2 ZFDG

4.2.1 Materials and Methods

4.2.1.1   ZFDG Apparatus

Fig. 4.2 shows a schematic diagram and a photograph of the ZFDG apparatus. The ZFDG system was built by Wang *et al.*, and a detailed description of this system was reported by Wang *et al.* [6, 98]. A syringe pump (Harvard Apparatus PHD Ultra Series; Hamilton glass syringe, internal diameter 23 mm) infuses and withdraws liquid with accuracy better than 1%. A cylindrical Perspex tank of diameter 130 mm contains the gauging liquid, and the liquid depth is set at around 100 mm. The tank is fixed on a motorized XY scanning stage (8MTF-75LS05, STANDA) controlled by a two-axis stepper & DC motor controller (8SMC4-USB-B9-2, STANDA), which allows the nozzle to be moved to different locations in the tank. The nozzle is connected to a straight stainless steel tube of length 310 mm to develop laminar flow profile. The clearance from the nozzle to the layer surface is controlled by a positioner (Zaber Technologies, T-LSR075B).

For data collection, the pressure drop across the nozzle is measured by a pressure transducer (PT) (SensorTechnics HMAP001-BU7H5) connected to a tapping located approximately 40 mm above the nozzle exit, with a limit of between around −8 kPa and 9 kPa. The transducer generates a voltage, which is collected as an analogue input by a multifunction DAQ (National Instruments, USB-6210,16 AI (16-Bit, 250 kS/s)), and processed to give the pressure drop reading. The relationship between the real pressure, P_{true}, and voltage collected by the DAQ, V_{DAQ}, was calibrated by a digital pressure indicator (Druck DPI 600 (IS)), and an example of a calibration plot is shown in Fig. 4.3. The data were subjected to a linear fit, giving

$$P_{\text{true}} = -8700 + 3544 V_{\text{DAQ}} \ (R^2 = 0.9999) \tag{4.1}$$

The relationship is linear and is followed in both ejection (positive ΔP) and suction (negative ΔP) modes of operation.

The data collection and control for the original system was originally performed using a LabVIEW (National Instruments) application. As part of this work, the system has been migrated to a platform using the programming language Python 3.6. This made it simpler to

integrate with other equipment and software for data analysis and automatic control, as well as making it amenable for freeware.
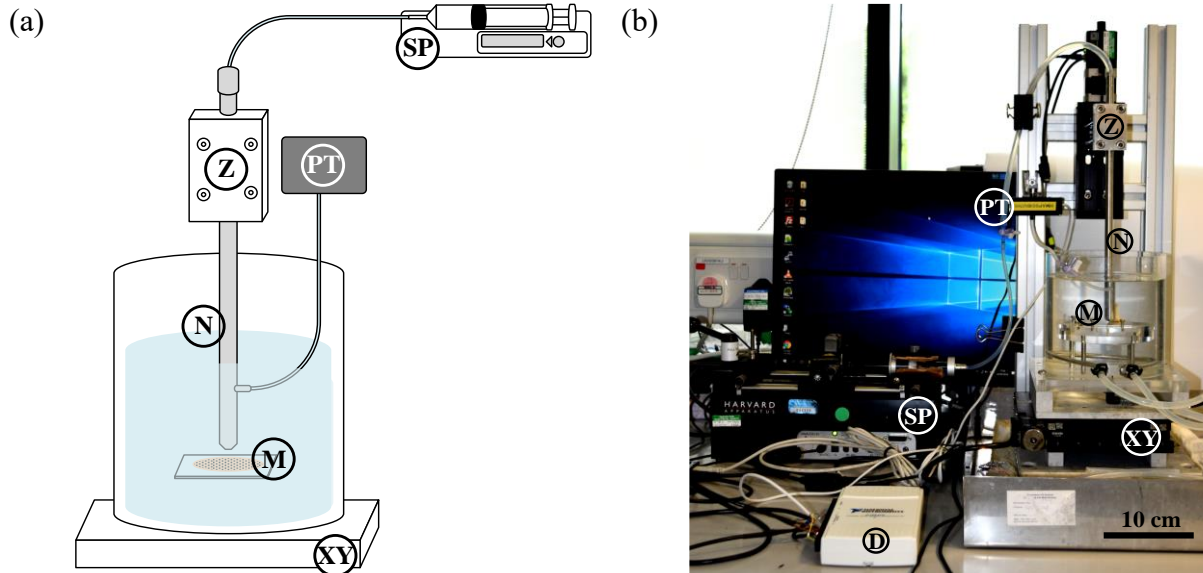
Fig. 4.2. (a) Schematic diagram and (b) photograph of ZFDG system. Components: D – DAQ; M – sample mount; N – nozzle; PT – pressure transducer; SP – syringe pump; XY – x- and y-axis positioner; Z – z-axis positioner.
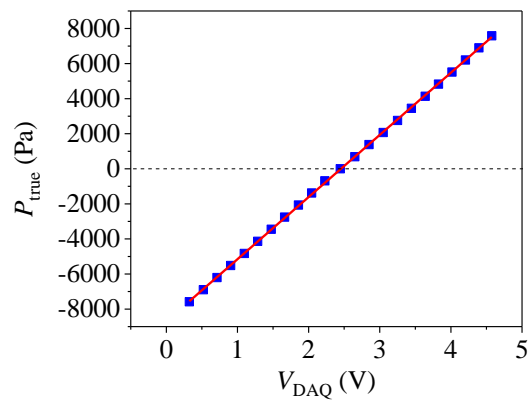
Fig. 4.3. Pressure transducer calibration plot. Symbols: blue square – measured pressure; red solid line – linear fitting.

4.2.2 Model Formulation

The geometry of the ZFDG apparatus has been reported by Wang *et al.* [6] and key nozzle dimensions are shown in Fig. 4.4. The nozzle internal diameter and throat diameter are 5.85 mm and 1 mm, respectively. The tank diameter is 130 mm, and the liquid depth is $60 + h_o$ mm.

A 2-dimensional, transient and axi-symmetric ZFDG model was created with water as the gauging liquid (isothermal, laminar regime with incompressible, Newtonian fluid). The CFD simulations are similar to the cases presented by Wang *et al.* [98], but the models are solved using the open source software OpenFOAM version 4.0 on a SuperServer 1027R-WRF4+ server with 12 cores (Intel® Xeon® E5-2630V2 Processor 2.60 GHz). The computational time required for the transient model to reach steady-state is about 3000 s.

4.2.2.1   Governing equations

The behavior of the liquid follows the Navier-Stokes (N-S) equation.

$$\rho \left(\frac{\partial \mathbf{v}}{\partial t} + \mathbf{v} \cdot \nabla \mathbf{v} \right) = -\nabla p + \mu \nabla^2 \mathbf{v} + \rho \mathbf{g} \tag{4.2}$$

Here, ρ is the liquid density, $\mathbf{v}$ is the velocity vector, p is the pressure, μ is the dynamic viscosity, and $\mathbf{g}$ is the gravity vector. Previous studies showed that gravity did not have a significant influence on the FDG flow field, so this term can be neglected [102].

The continuity equation applies, which for an incompressible fluid is

$$\nabla \cdot \mathbf{v} = 0 \tag{4.3}$$

The gauging fluid, water, is Newtonian with constant viscosity. The density and viscosity of water at 16.5 °C were 997.3 kg/s and 1.123 mPa s, respectively [98]. In OpenFOAM, the N-S equation is solved using the finite volume method [156] with a pressure-velocity coupling algorithm (pimpleFoam), consisting of a pressure-implicit split-operator scheme proposed by Issa [157] and a semi-implicit pressure linked scheme reported by Patankar and Spalding [158].

4.2.2.2 Boundary conditions

The boundaries of the simulation domain are labelled in Fig. 4.4 and boundary conditions are listed in Table 4.2. In Fig. 4.4, the fluid is injected and ejected *via* AK. Region EFGHIJK is the nozzle tube, which is solid. All walls are specified as no-slip and impermeable [98]. Plane BC represents surface being gauged. In order to reduce the calculation time, the simulation domain is shrunk and the boundary of the tank is replaced by open boundaries. **v** and p were set to be zero for all calculation domains as the initial condition.

A less well developed flow field often happens at a large clearance and in suction mode, as setting the inlet/outlet of the nozzle tube to be a parabolic velocity profile. Fig. 4.5(a) compares the effect of specifying a parabolic and a constant velocity profile at the outlet, for different nozzle lengths, l, at $h_o/d_t = 0.5$ in suction mode. The nozzle length cannot be shorter than 50 mm, since in suction mode, the recirculation region extends about 50 mm above the nozzle throat. The C_d values obtained with a parabolic velocity profile decrease with l. In contrast, the values obtained for the constant velocity outlet condition are similar (and close to the experimental value). This is because with a longer nozzle tube, a larger downstream area is required to develop the parabolic outlet velocity. When the downstream area is fixed, the flow pattern cannot become fully developed, resulting in a higher pressure drop (lower C_d). The less developed flow pattern can be observed by the predicted outlet velocity. In Fig. 4.5(b), the velocity distributions at $l = 100$ and 200 mm are fluctuated, but at $l = 60$ mm, the predicted velocity is the same as the boundary condition. A less well developed flow pattern calculated by OpenFOAM is different from that obtained from the commercial finite element software COMSOL Multiphysics®, which has been widely used for predicting the FDG flow pattern (section 2.3.3). In COMSOL, if the flow field cannot become fully developed, the predicted values on the boundary will be manipulated to match the boundary condition, but the values close to the boundary will fluctuate.
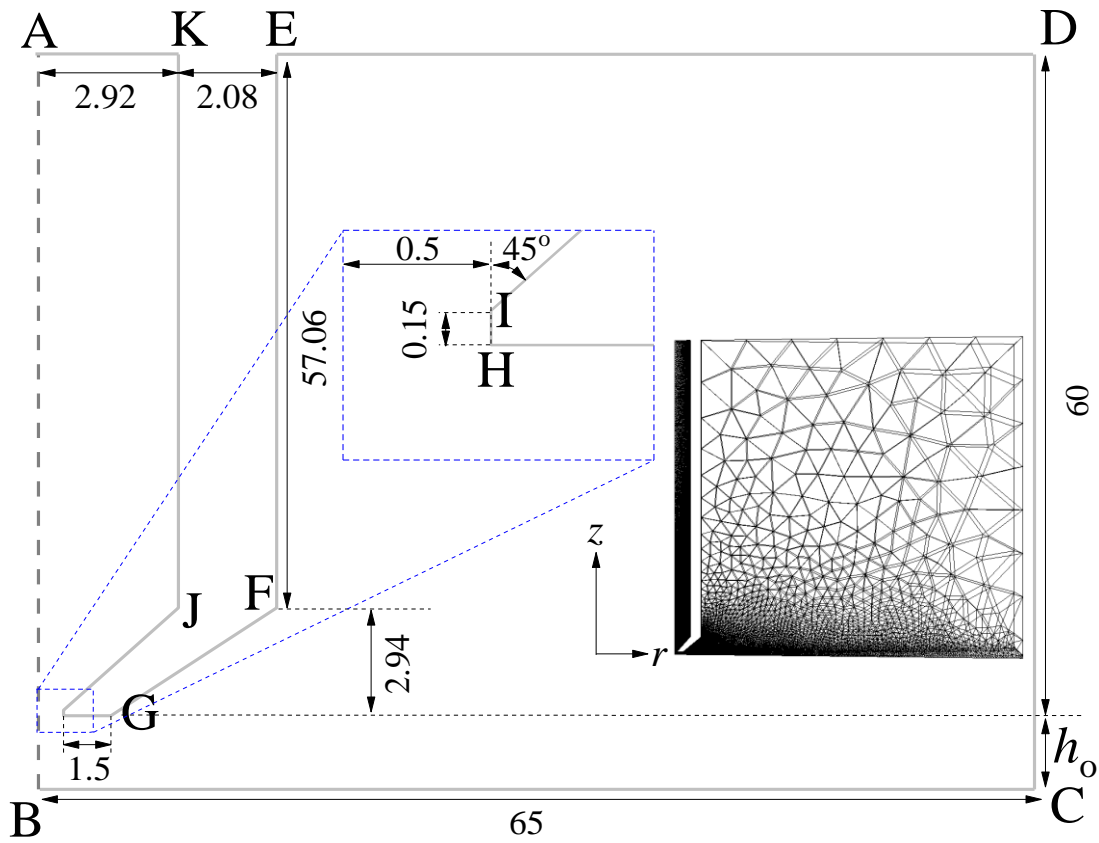
Fig. 4.4. Geometry and mesh distribution of ZFDG simulation. Inset shows mesh. All dimensions in mm.
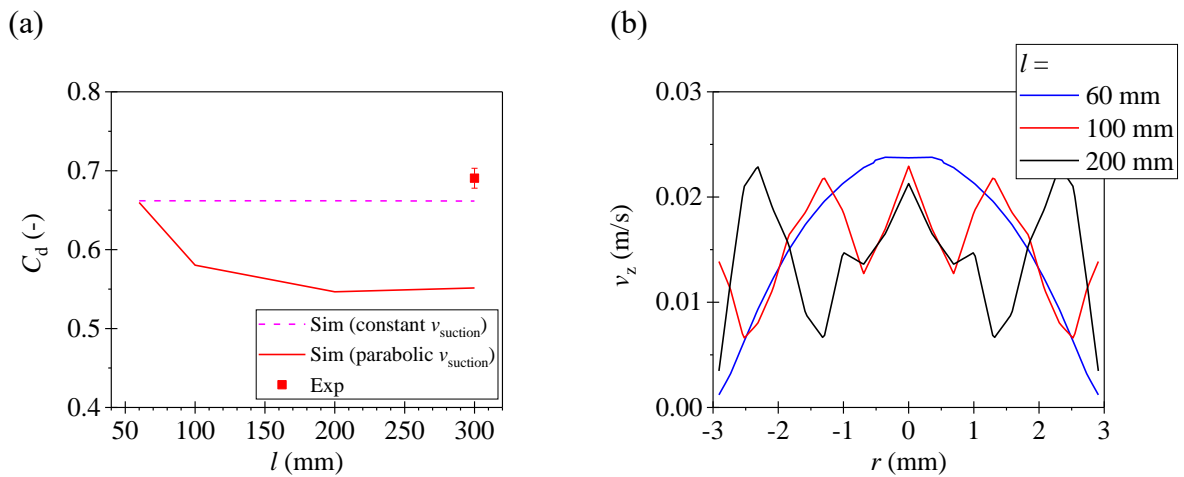
Fig. 4.5 (a) Effect of setting a parabolic velocity profile at the outlet on C_d. (b) Comparisons of velocity distributions at the outlet with a parabolic velocity outlet at different l. Test case conditions: $\dot{m} = 20$ ml/min and $h_o/d_t = 0.5$, suction mode.

Table 4.2 Boundary conditions in the CFD model (v_r and v_z are the radial and axial velocities, respectively.)

Boundary	Description	Boundary condition
AB	Axisymmetric	$\dfrac{\partial v_r}{\partial r} = 0$, $\dfrac{\partial v_z}{\partial r} = 0$ and $\dfrac{\partial p}{\partial r} = 0$
AK	Inlet/outlet	$v_{ejection} = \dfrac{8\dot{m}}{\rho \pi d_i^2}\left(1 - \dfrac{4r^2}{d_i^2}\right) or \dfrac{4\dot{m}}{\rho \pi d_i^2}$ [a] $\qquad$ $v_{suction} = \dfrac{-8\dot{m}}{\rho \pi d_i^2}\left(1 - \dfrac{4r^2}{d_i^2}\right) or \dfrac{4\dot{m}}{\rho \pi d_i^2}$
BC, CD, EF, FG, GH, HI, IJ, and JK	Wall	$v_r = 0$ and $v_z = 0$
DE	Open boundary	$p = 0$

[a] $v_{ejection}$ and $v_{suction}$ are the velocities for ejection mode and suction mode, respectively. Fully developed laminar flow or constant velocity profile is imposed at the inlet/outlet. $\dot{m}$ is the mass flow rate delivered by the syringe pump. r is radial distance and d_i is the internal diameter of the nozzle.

A comparison of discharge coefficient predicted from the models with a parabolic and a constant velocity inlet/outlet is plotted in Fig. 4.9(a). There is no significant difference between both boundary conditions for both modes. This indicates that both velocity profiles can be specified as the inlet/outlet boundary conditions; however, the predicted flow pattern is required to be checked while setting the oulet to be a parabolic profile. When using OpenFOAM to estimate the flow pattern of FDG, setting the inlet/outlet boundary condition to be a constant velocity profile is better for a preliminary study. In this study, the inlet/outlet of the gauging nozzle is set to have a parabolic velocity profile.

Non-uniform meshes were set up with triangular-shaped elements generated by a mesh generator, Gmsh (version 3.0.6), as shown in the inset on in Fig. 4.4. Although the model is axisymmetric 2-dimensional, a 3-dimensional mesh is required for OpenFOAM so a wedge shape mesh with an angle of 2.5° was created.

The mesh size around the nozzle rim gives rise to differences in the calculation of the pressure drop. A mesh resolution study (spatial convergence) was performed by monitoring the change in C_d while adjusting the mesh size around the nozzle for a given set of geometry and flow rate conditions. The results are shown in Fig. 4.6. C_d approaches an asymptote as the minimum mesh size is reduced, indicating that a mesh size of less than 5 μm around the nozzle is acceptable for this case. A minimum mesh size of 1.448 μm was chosen for the positions closest to the nozzle rim, while the mesh size expands to 2.871 mm on the tank wall far away from the nozzle. The simulations reported here employed 131776 mesh elements. The simulations followed the validation guidelines presented by NASA's NPARC alliance [143], and nearly 75000 iterations were solved for each conditions. The consistency of computation was tested by checking mass balance for the inlet and side boundaries, and the difference was less than 0.11 %. The temporal convergence is not applicable for this steady-state study.
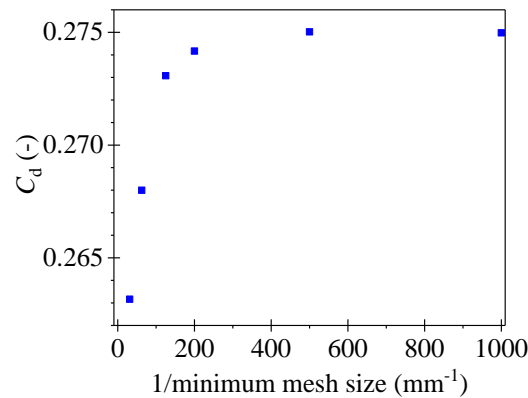
Fig. 4.6. Effect of the mesh size on C_d. Test case conditions: $\dot{m} = 20$ ml/min and $h_o/d_t = 0.1$, ejection mode.

4.2.3 Calibration

In FDG measurements, the pressure drop, ΔP, is expressed as a discharge coefficient C_d (Eq. (2.4)), which is a normalised energy loss across the nozzle [89]. Fig. 4.7 shows calibration plots of C_d against dimensionless clearance, h_o/d_t, for various flow rates. The hollow symbols represent cases where the pressure drop exceeded the measurement limit of the pressure transducer, from −8 kPa to 9 kPa. Fig. 4.7(a) shows that in ejection mode, C_d rises gradually

with increasing h_o/d_t, reaching around 0.7 at $h_o/d_t = 0.3$. After this, it drops slightly at $h_o/d_t = 0.35$ and then approaches a plateau. The gentle decline results from redistribution of eddies in the liquid beyond the outer edge of the rim, which will be discussed later. The eddy causes an increased pressure drop, so C_d decreases a small amount (the local velocities are low in this region). Similarly, C_d in suction mode rises smoothly with increasing h_o/d_t, but does not experience a gentle decline. This is because the structure of the flow field of suction mode does not change significantly as h_o/d_t increases.

In Fig. 4.7(b), (c) and (d), the difference in C_d value measured during ejection and suction modes diminishes with increasing flow rate. Moreover, as increasing flow rate, the difference becomes noticeable at lower values of h_o/d_t, which will be shown and to be due to the influence of vortices in ejection mode.

(a) $\dot{m}$ = 20 ml/min (Re_t = 375)   (b) 40 ml/min (Re_t = 750)

(c) 60 ml/min (Re_t = 1125)   (d) 70 ml/min (Re_t = 1312)
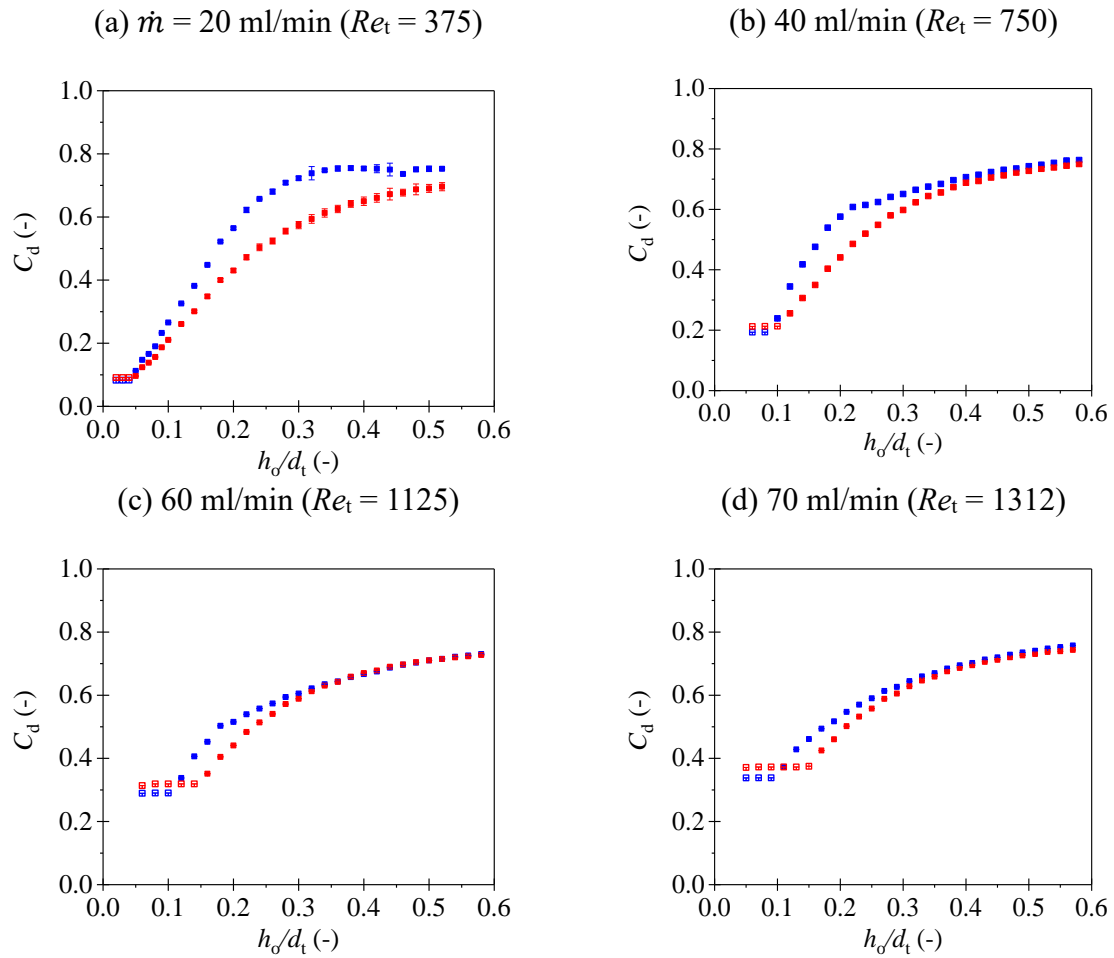
Fig. 4.7. Experimental calibration plots of C_d against dimensionless clearance for $\dot{m}$ = (a) 20 ml/min, (b) 40 ml/min, (c) 60 ml/min and (d) 70 ml/min. Solid symbols – experimental data; hollow symbols – experimental data out of measurement range; Colours: blue – ejection (E), red – suction (S).

4.2.3.1   *Experimental validation*

Chew *et al.* [102] reported that the flow patterns in FDG nozzles share similarities with radial laminar flow between parallel plates, whose solution has been presented by Middleman [159]. This analytical solution is used to assess the results from OpenFOAM CFD simulations. Fig. 4.8 shows distributions of velocity magnitude from the ZFDG simulations alongside the analytical solutions for $\dot{m}$ = 20 ml/min. At this mass flow rate, the Reynolds number at the throat of the nozzle is around 375, so the flow is in the laminar regime.

In Fig. 4.8(a), it is clear that at both (i) h_o/d_t = 0.05 and (ii) 0.20, the velocity magnitude is large near the inner rim of the nozzle, and then declines gradually with increasing radial distance.

The distribution becomes that of a fully developed laminar velocity profile at the outer rim of the nozzle. The maximum velocity for a given flow rate depends on the gap between the nozzle and the substrate. This is expected from conservation of mass (volume), where the volumetric flow rate, Q, is given by

$$Q = 2\pi r h v_r \qquad (4.4)$$

Fig. 4.8(b) show the radial velocity profiles at $r = 0.6$ mm, 1 mm and 1.4 mm at (i) $h_o/d_t = 0.05$ and (ii) 0.20. At $h_o/d_t = 0.05$, the CFD results are similar to the analytical solutions: the velocities decrease further along the gap. The predicted velocity profile at $r = 0.6$ mm and $h_o/d_t = 0.20$ is very different from the analytical solution. This is because there is a small eddy close to the inner rim, labelled A in Fig. 4.8(a) (ii). The eddy results in recirculation so that the velocity becomes negative at the upper wall. This phenomenon becomes significant with increasing clearance.
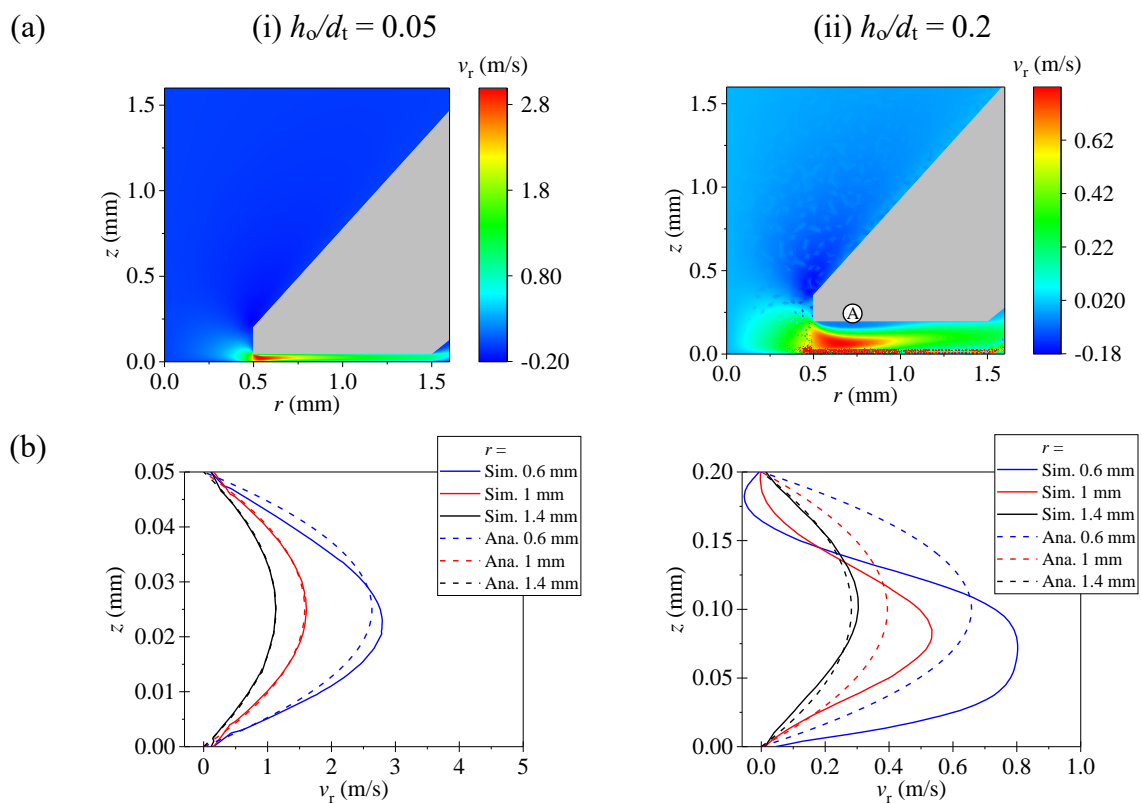
Fig. 4.8. (a) Distributions of radial velocity magnitude in ejection mode with $\dot{m} = 20$ ml/min at $h_o/d_t =$ (i) 0.05 and (ii) 0.2: (b) Comparison of velocity distributions in the gap under the rim at different radial locations.

Experimental data obtained for FDG calibration are plotted alongside ZFDG simulations in Fig. 4.9, for $\dot{m}$ = 20 ml/min and 40 ml/min in both ejection and suction modes. Fig. 4.9(a) shows good agreement between experimental and simulation results for both ejection and suction modes. The gentle decline in ejection mode mentioned above has been captured by the simulation. Fig. 4.10 shows the distributions of streamlines at h_o/d_t = 0.35 and 0.4. It is obvious that at h_o/d_t = 0.35, there are two eddies occurring outside the nozzle, one located near the nozzle edge and another one close to the substrate. By contrast, as h_o/d_t increases to 0.4, the original eddy on the edge of the nozzle disappears and another eddy become larger. This change of flow pattern is thought to cause the observed decrease in C_d values.

In Fig. 4.9(b), reasonable agreement between simulation and experimental results is obtained for h_o/d_t less than 0.2. The region of h_o/d_t below 0.15 is the one of interest for dynamic gauging, as C_d is linear in h_o/d_t. The gentle decline in C_d as a function of h_o/d_t happens at larger values of h_o/d_t in the simulation when compared to the experimental data; the deviation in suction mode is significant. These differences indicate that 2-D axi-symmetric model is not able to predict the FDG flow pattern accurately at higher flow rates and h_o/d_t. One reason is that when the flow rate increases, eddies in liquid may not be cylindrically symmetric.

(a) $\dot{m}$ = 20 ml/min (Re_t = 375) (b) 40 ml/min (Re_t = 750)
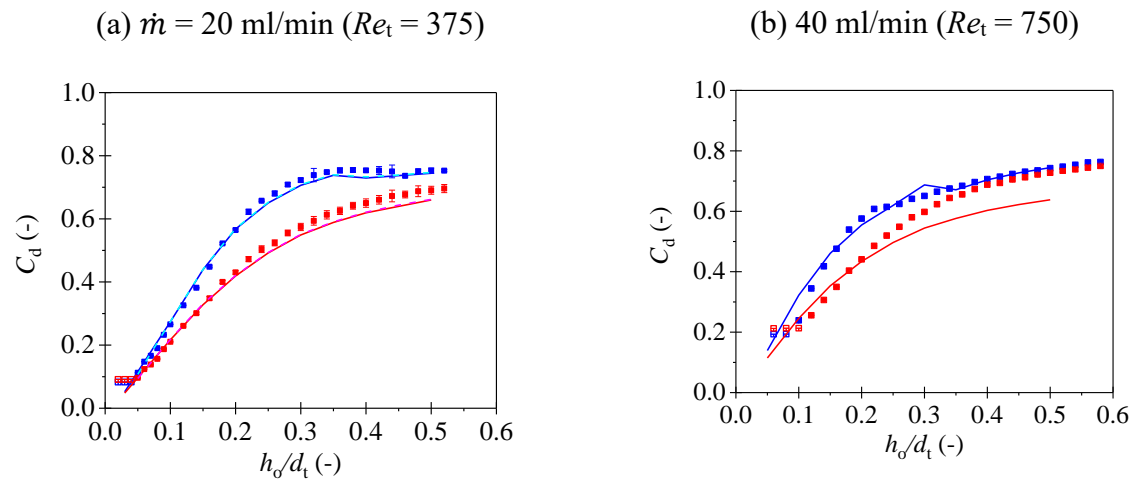
Fig. 4.9. Calibration plots of C_d against dimensionless clearance for $\dot{m}$ = (a) 20 ml/min and (b) 40 ml/min. Solid symbols – experimental data; hollow symbols – experimental data out of measurement range; lines – simulation results with a parabolic velocity inlet/outlet; dashed lines – simulation results with a constant velocity inlet/outlet. Colours: blue/cyan – ejection (E), red/magenta – suction (S).
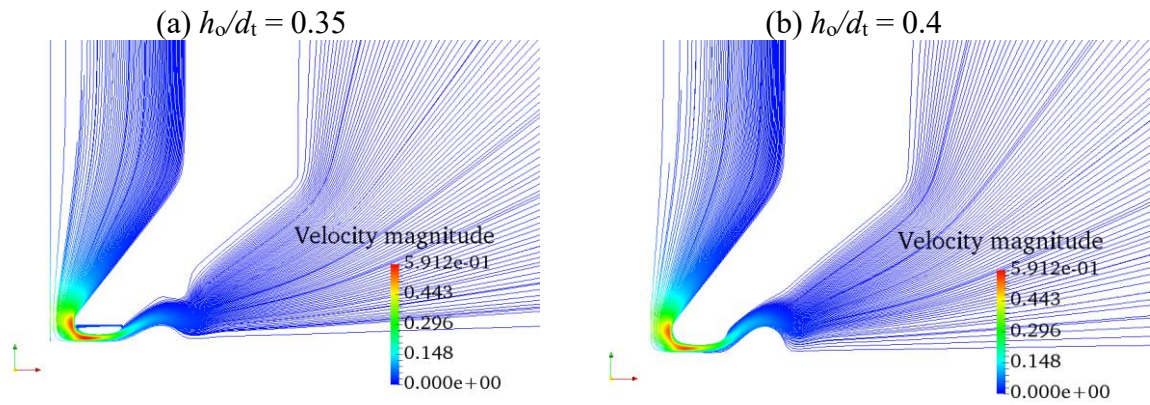
Fig. 4.10. Distributions of streamlines in ejection mode with $\dot{m}$ = 20 ml/min at h_o/d_t = (a) 0.35 and (b) 0.4.

Fig. 4.11 compares the distributions of the wall shear stress on the lower surface in both ejection and suction modes computed using both CFD and analytical approximation. The distributions in suction mode show good agreement with the analytical expression. The shear stress imposed on the substrate decreases as the velocity declines along the rim, or as the clearance increases. However, in ejection mode, there are noticeable peaks at the nozzle inner rim. These result from the velocities changing direction at the nozzle mouth, indicating that the flow changes are more significant in ejection mode than in suction mode. These results are consistent with the literature, for example, Yang *et al.* [97] suggested that suction to be better for studies the layer strength, because a lower flow rate of ejection mode should be used to prevent deformation caused by the shear stress peaks.
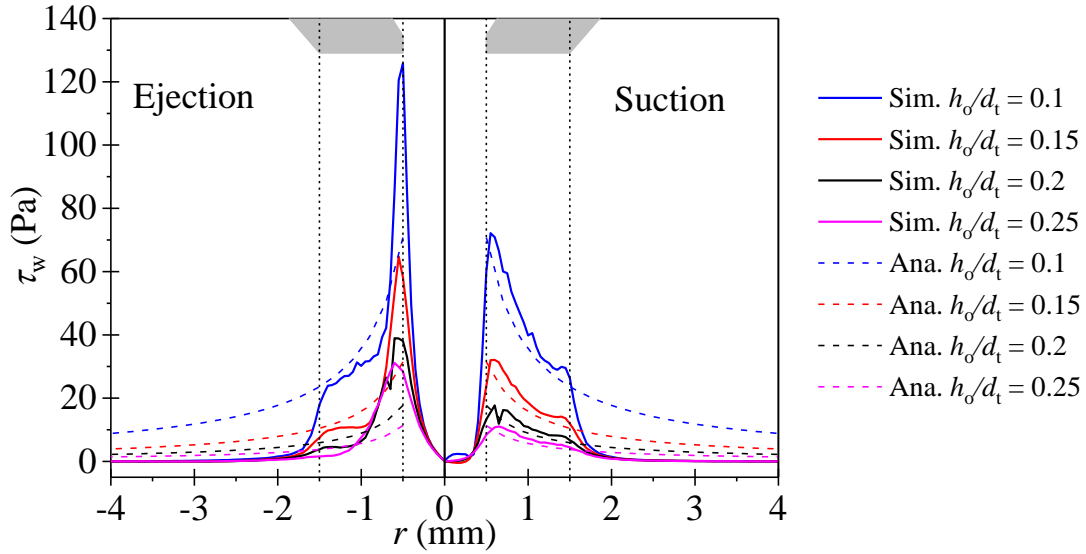
Fig. 4.11. Distribution of shear stress on base for $\dot{m} = 20$ ml/min. Solid lines – simulations: dashes – analytical solution. Blue: $h_o/d_t = 0.1$, red: $h_o/d_t = 0.15$, black: $h_o/d_t = 0.2$ and pink: $h_o/d_t = 0.25$.

The flow patterns and shear stresses generated by the FDG flow have been predicted by CFD simulations, and the results compared with analytical solutions and experimental indicators. They show good agreement, indicating that OpenFOAM is suitable for FDG flow field estimation.

4.3 SiDG

4.3.1 Construction

4.3.1.1   Device

A schematic diagram and a photograph for this SiDG device is presented in Fig. 4.12. As with the ZFDG apparatus, the syringe pump (Harvard Apparatus PHD Ultra Series; Hamilton glass syringe, internal diameter 23 mm) is employed to infuse and withdraw gauging liquid through a new 316 stainless steel tube, 295 mm long, to develop a laminar velocity profile, with a nozzle ($d_t = 1$, $d_i = 4$ mm, $\beta = 45°$ and $w_r = 0.5$ mm) connected to the end of the tube. The tube is

mounted horizontally and passed through a seal, whereby an O-ring is used with some petroleum jelly for lubrication and its location is at 110 mm from the base, in one wall of a Perspex cubic tank ($150 \times 150 \times 150$ mm^3) filled with gauging solution at a liquid level of around 130 mm. The tube is moved using a linear slide (Zaber Technologies T-LSR075B), with a repeatability of 2 μm and a backlash of less than 13 μm. The pressure drop, ΔP, across the nozzle is recorded by the same pressure transducer (SensorTechnics HMAP001-BU7H5, range −8 kPa to 9 kPa), which is connected to a tapping installed on the tube at approximately 50 mm away from the nozzle outlet. A K-type thermocouple is fixed on the wall close to the nozzle head to monitor the temperature of the gauging liquid, and the temperature can be controlled by a heating coil at the bottom of the tank. The thermocouple signal is transferred to an amplifier to enhance its amplitude.

Both transducer and thermocouple signals after amplifiers are then collected by the multifunction DAQ (National Instruments, USB-6210,16 AI (16-Bit, 250 kS/s)). The pressure drop is estimated from the signal based on the calibration test presented above. The sample substrate is mounted vertically on a suspended arm, which is fixed on a second positioner (Zaber T-LSR075B). This setup allows both the region and time of the sample submerged in the liquid environment to be controlled. All information, including measured pressure drop, positioner data, and temperature are collected using a program written in Python 3.6 script.

(a)

(b)
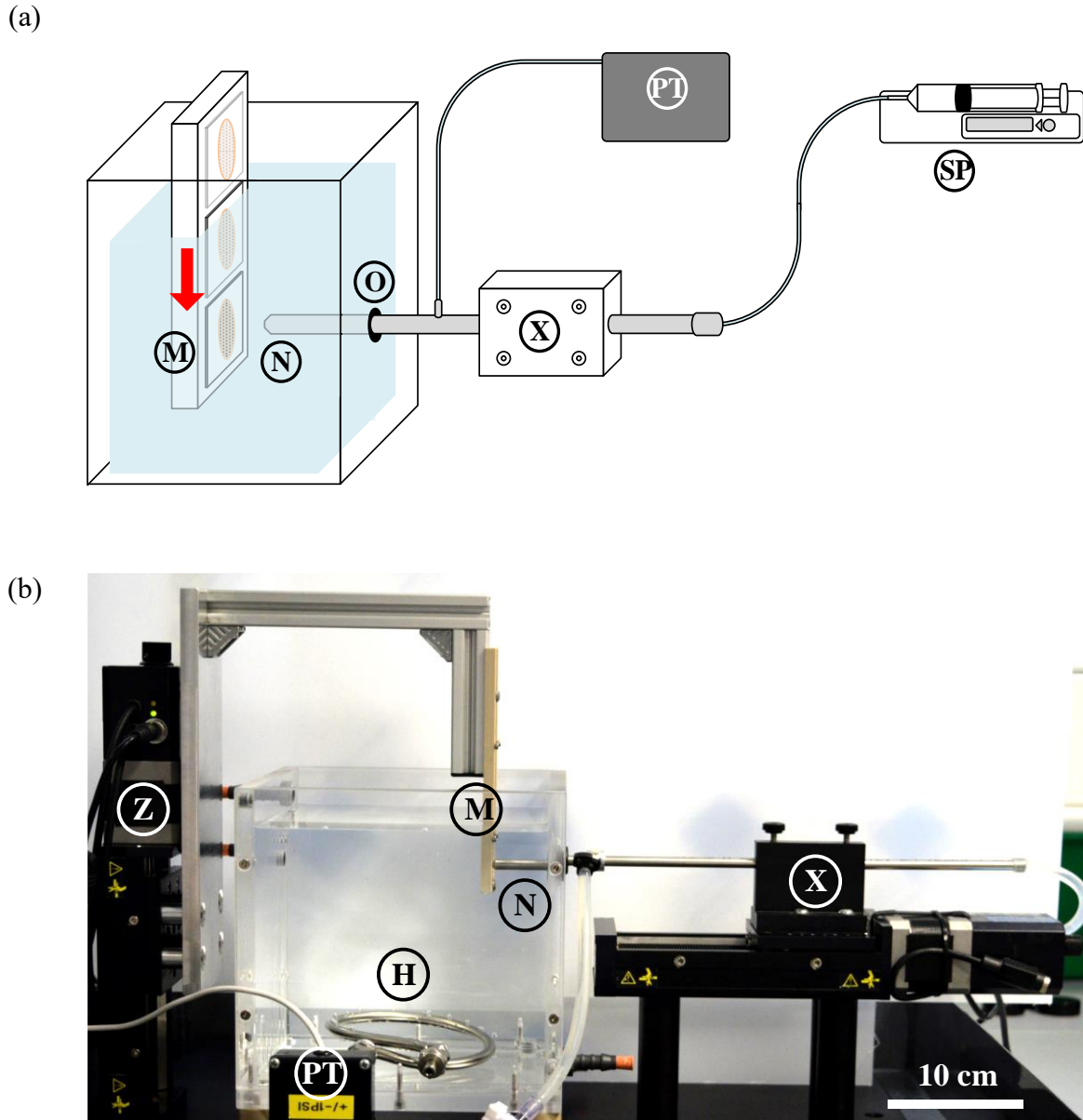
Fig. 4.12. (a) Schematic diagram and (b) photograph of SiDG apparatus. Components: H –
coil for heating/cooling liquid; M – sample mount; N – nozzle; O – o-ring seal; PT –
pressure transducer; SP – syringe pump; X – horizontal (nozzle) positioner; Z –
vertical (sample) positioner.

4.3.2 Model Formulation

The CFD model is similar to the ZFDG cases presented previously. The gauging fluid in this
study is water, and it density and viscosity are 997.3 kg m^{-3} and 1.123 mPa s (16.5 °C),
respectively [98]. The algorithms and convergence criteria follow the previous case, but the
geometries and boundary conditions are different due to the fact that the liquid-air interface

above the nozzle is a free surface and quite close to the nozzle. Thus, the liquid surface cannot be neglected and an asymmetric model is not available. However, Chew *et al.* [92] reported that the simulation results were not sensitive to various boundary conditions with both permeable and impermeable walls. Also, feasibility of FDG operated in a duct flow with large Reynolds numbers has been proven [28, 105].

In order to investigate in the effect of the free surface, a 3-dimensional transient model and a 2-dimensional transient asymmetric model were created. Both geometries are presented in Fig. 4.13, and the boundary conditions are summarised in Table 4.3. Fig. 4.13(a) shows a simplified 3D geometry. The nozzle is located at the centre of a box and normal to the substrate (ACGE). ABFE is the open surface and was set to be a wall [92]. BDHF is the tank wall (no-slip and impermeable), and other boundaries are open boundary ($p = 0$). The key nozzle dimensions are the same as that in Fig. 4.13(b). In the 2D case, shown in Fig. 4.13(b), C'D' was set up as open boundary and all other boundaries are walls.

Non-uniform triangular-shaped meshes were created using Gmsh. The calculation time for the 2D transient model to approach a steady-state condition was around 3000 s, but for the 3D case, it took more than one week.
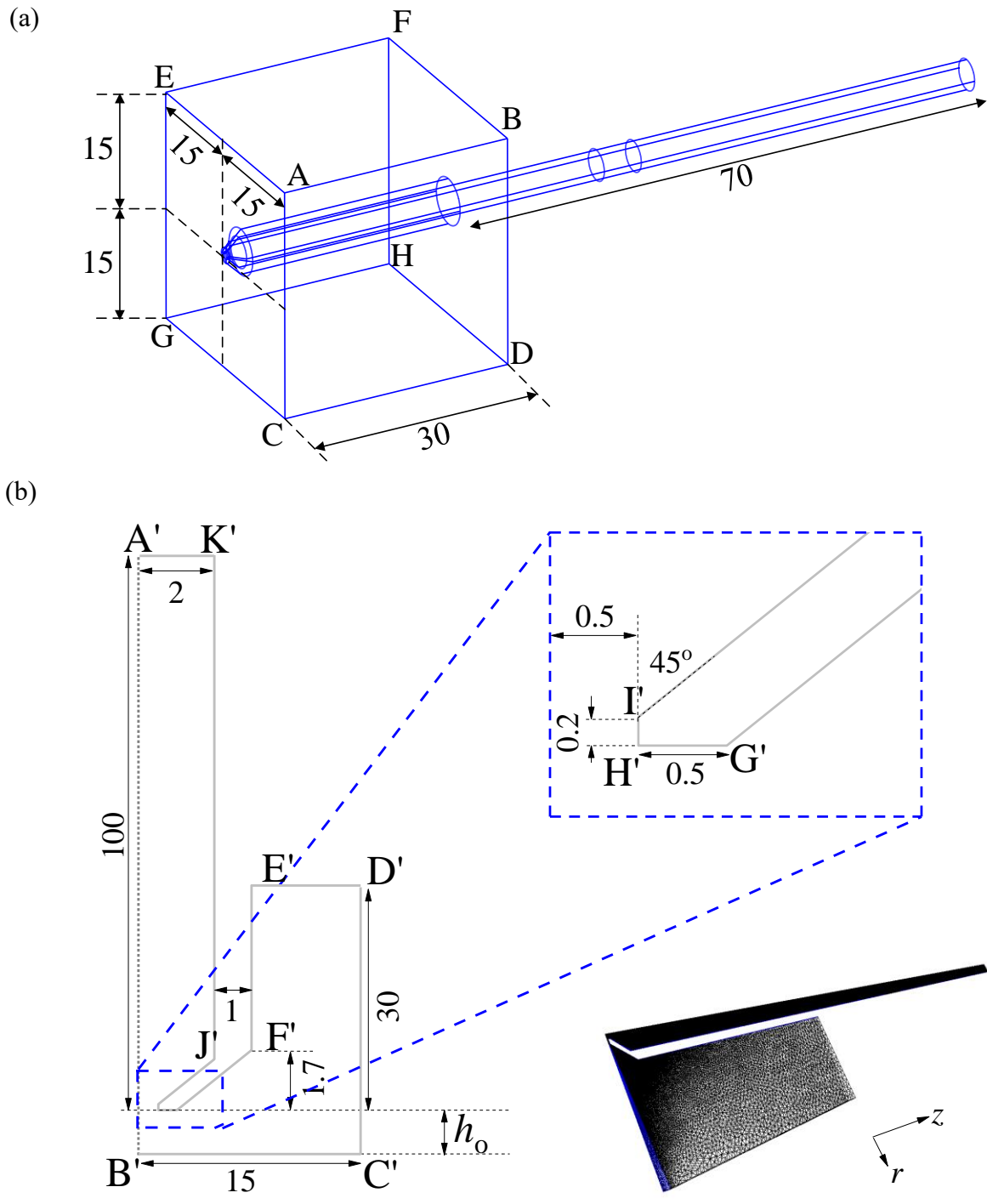
Fig. 4.13. Geometry of (a) 3D and (b) 2D axi-symmetric SiDG simulations. Inset shows mesh. All dimensions is mm. Boundaries defined in Table 4.3.

Table 4.3. Boundary conditions in the CFD models

3D Boundary (apart from nozzle, in Fig. 4.13(a))	2D Boundary (Fig. 4.13(b))	Description	Boundary condition
	A'B'	Axisymmetric	$\frac{\partial v_r}{\partial r} = 0, \frac{\partial v_z}{\partial r} = 0$ and $\frac{\partial p}{\partial r} = 0$ [a]
	A'K'	Inlet/outlet	$v_{ejection} = \frac{8\dot{m}}{\rho \pi d_i^2}\left(1 - \frac{4r^2}{d_i^2}\right)$ [b]
			$v_{suction} = \frac{-8\dot{m}}{\rho \pi d_i^2}\left(1 - \frac{4r^2}{d_i^2}\right)$
ACGE, BDHF and	B'C', D'E', E'F', F'G', G'H', H'I', I'J', and J'K'	Wall	$\mathbf{v} = 0$
ABDC, CDHG and EFHG	C'D'	Open boundary	$p = 0$
ABFE		Free surface	$\mathbf{v} = 0$ (Wall) or $p = 0$ (Open boundary)

[a] v_r and v_z are the radial and axial velocities in 2D, respectively.

[b] $v_{ejection}$ and $v_{suction}$ are the velocities for ejection mode and suction mode, respectively. Fully developed laminar flow is imposed at the inlet/outlet. $\dot{m}$ is the mass flow rate delivered by the syringe pump. r is radial distance and d_i is the internal diameter of the nozzle.

The numerical study followed the validation procedure proposed by NASA's NPARC alliance [143]. About 75000 iterations were computed for 2D and 3D simulations. The error in the mass balance between the inlet and open boundaries was about 0.26%, indicating that the simulation consistency is acceptable. The temporal convergence is not applicable for this case, because it is a steady-state simulation. Fig. 4.14 shows a mesh sensitivity study for spatial convergence using the discharge coefficient (pressure drop) as an indicator. The test was conducted by refining the mesh size in the domain beneath the nozzle rim, since ΔP is based on the flow

pattern beneath the nozzle rim. In Fig. 4.14, there is no significant change when the mesh element size is less than 10 μm. A minimum mesh size of 3.56 μm was set around the nozzle rim and expended to 1.33 mm near the side boundaries. About 190 000 mesh elements were used in the models.
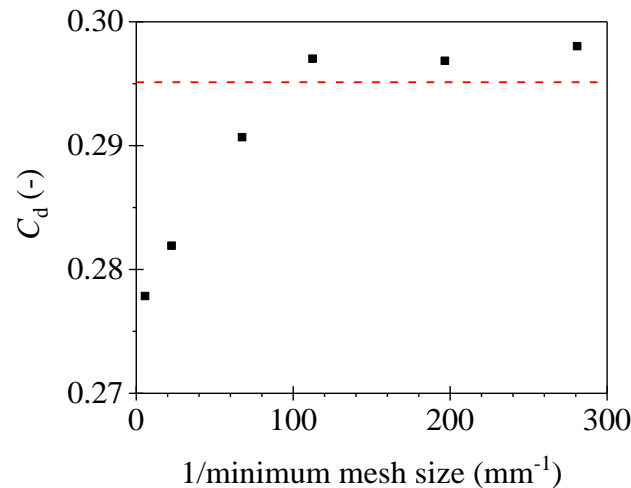
Fig. 4.14. Effect of mesh size on C_d, axisymmetric simulation. Test case conditions: water at 20 °C, $\dot{m}$ = 20 ml/min, h_o/d_t = 0.1, ejection mode. Horizontal dashed line indicates experimental value at this condition.

4.3.3 *Commissioning*

Fig. 4.15 shows a comparison of the local speed distributions estimated for the 3D and 2D asymmetric models. It is clear that the maximum velocities appear under the nozzle rim in both cases, which is similar to previous studies [97], and there is no obvious difference between both models. Comparing the estimated pressure drop of the 3D model with the 2D result at $\dot{m}$ = 20 ml/min, h_o/d_t = 0.1, the difference in suction mode was below 1%, and that in ejection mode was around 7%. Both errors are less than 10% and acceptable for engineering applications. These results indicate that the assumption of 2D asymmetric model is acceptable to be utilised for prediction of the SiDG flow pattern. There are significant differences between both modes. In ejection mode, shown in Fig. 4.15(a), a parabolic velocity profile exists beneath the nozzle rim and decays downstream. However, in suction mode, Fig. 4.15(b), a fast stream flows up the centre of the tube, and circulation occurs close to the wall.

Fig. 4.16(a) plots the discharge coefficient versus the dimensionless clearance for SiDG. It is obvious that at smaller h_o/d_t, C_d in both ejection and suction modes increases remarkably with increasing clearance, followed by approach to an asymptote of about 0.72. This trend is similar to that of ZFDG shown above and other FDG configurations. The deviation between both modes from $h_o/d_t \sim 0.1$ to 0.4 is attributed to the difference of flow fields, which are evident in the simulations and has been discussed in section 4.2.3. At $h_o/d_t < 0.05$, C_d in both modes approaches a low asymptotic value (around 0.08), which is different from that presented in Fig. 4.7. This is attributed to bending of the arm, on which the substrate is mounted. The arm bent and the clearance between the nozzle and substrate became larger, while being imposed by a force, so the measured C_d values are higher than the predicted ones. Compared the simulation results with the experimental data, good agreement can be observed, indicating that the simulations can be employed to predict the SiDG flow field.
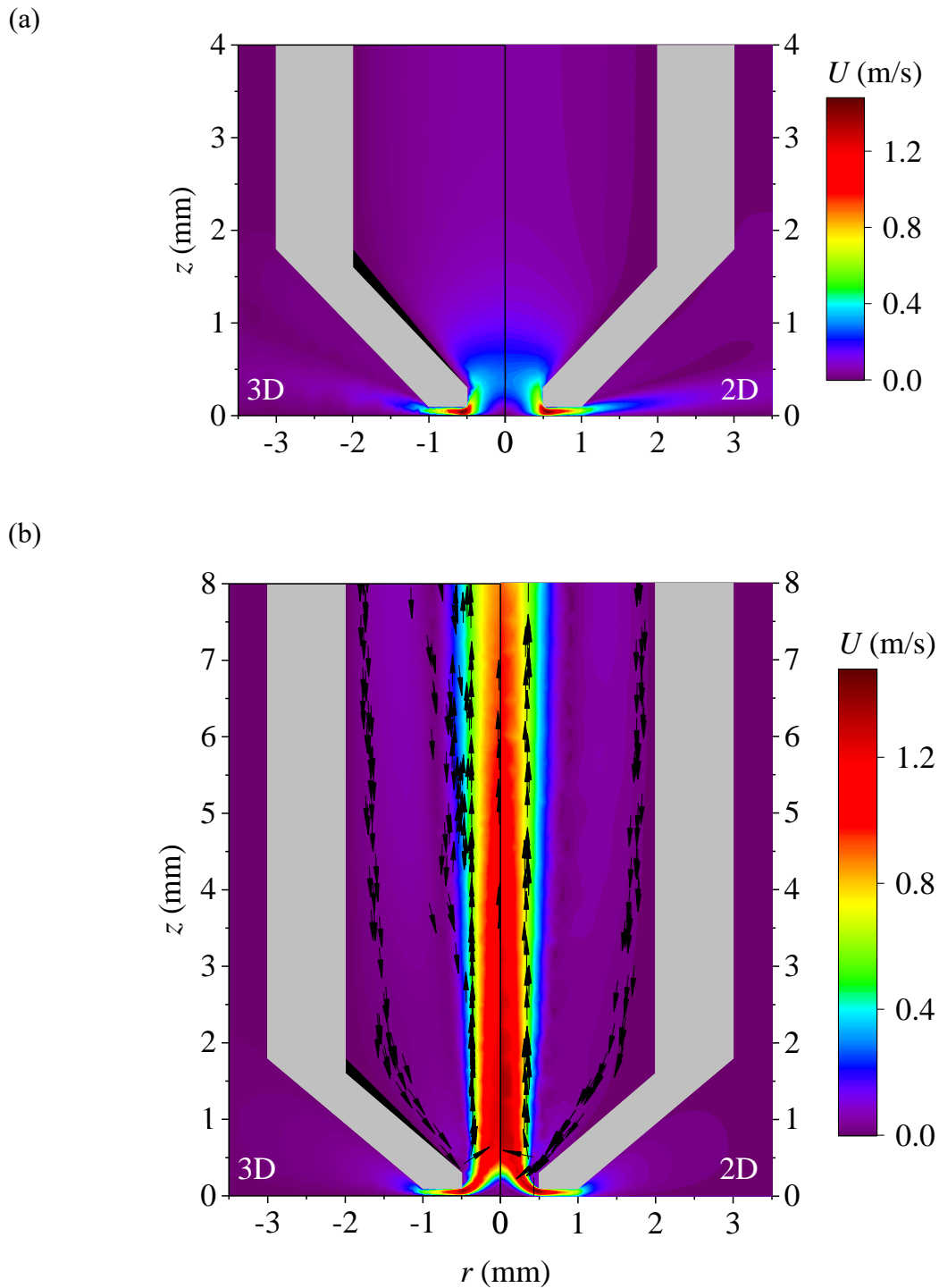
Fig. 4.15. Comparison of predicted speed (velocity magnitude) distributions in 3D (left) and 2D asymmetric (right) simulations for (a) ejection mode and (b) suction mode. Arrows in (b) indicate flow direction, and are not to scale. Conditions: $\dot{m} = 20$ ml/min, $h_o/d_t = 0.1$.

A further test was conducted by gauging different locations along the SS substrate to confirm that the sample mount was truly vertical. The results in Fig. 4.16(b) show that the discharge

coefficient decreases gradually with increasing z, indicating that the clearance between the nozzle head and substrate decreases as the gauging location approaches the top of the substrate. This corresponds to a slope of the substrate of 0.121°, which was used for selecting an initial gauging clearance to prevent the nozzle head touching the layer surface.
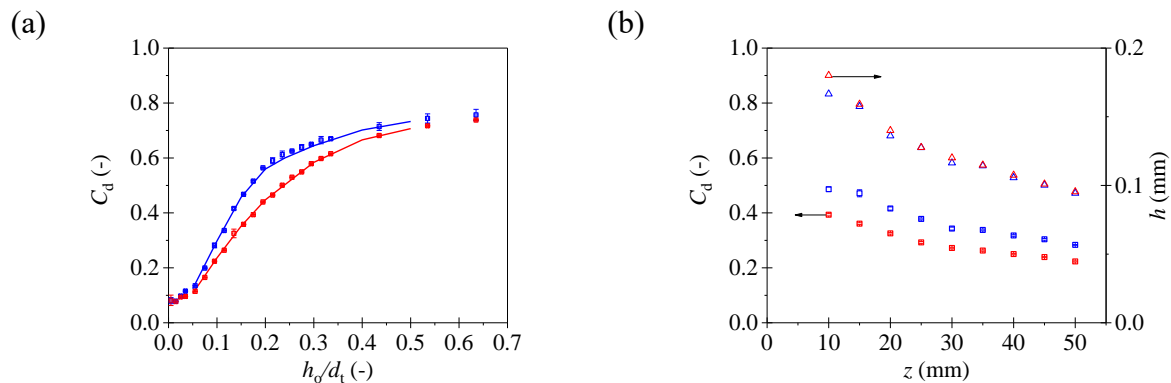
Fig. 4.16. Calibration plots of (a) C_d against dimensionless clearance and (b) positions on sample mount. Experimental conditions: water at 20 °C, $\dot{m}$ = 20 ml/min, Re = 375. Lines – simulation; Open square symbols – experimental C_d: blue – ejection; red – suction; Open triangle symbols – estimated h: blue – ejection; red – suction.

Fig. 4.17 shows distributions for predicted wall shear stress at h_o/d_t = 0.05, 0.1, 0.15 and 0.2 in ejection and suction modes. At $h_o/d_t \leq 0.1$, large shear stresses were induced by the gauging flow beneath the nozzle rim, and the values differ significantly between the two modes. In ejection mode, a sharp peak is generated at the inner edge of the rim, resulted from the redistribution of velocity. By contrast, the shear stress is relatively smooth and lower magnitude in suction mode at larger clearances, indicating that this mode is more suitable for soft solid layers with its low deformation stresses.

Fig. 4.17 also presents dimensionless shear stresses, τ^*_w, on the right axis. τ^*_w is calculated from $\tau_w / \frac{1}{2}\rho U^2$, whereby $\frac{1}{2}\rho U^2$ is the inertial head in the flow and U is the mean velocity at the nozzle throat. An useful information has been observed: the predicted shear stress value would be close to the initial head (τ^*_w = 1) at $h/d_t \sim 0.05$ in suction mode.
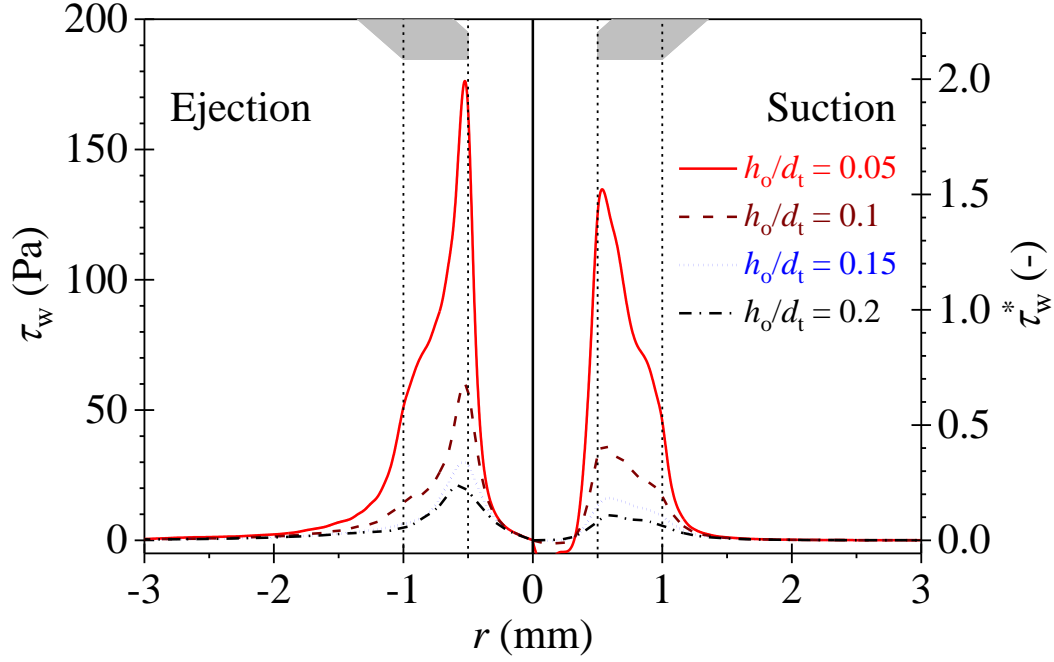
Fig. 4.17. Distribution of predicted shear stress on gauged surface calculated by OpenFOAM simulations for the cases in Fig. 4.16(a), for $h_o/d_t = 0.05$ (red); 0.10 (brown); 0.15 (blue); 0.20 (black). Conditions: $\dot{m} = 20$ ml/min, $Re_t = 375$. Vertical dashed lines and grey shaded pattern indicate the region of the nozzle footprint. Note: $r < 0$ – ejection mode; $r > 0$ – suction mode. Second y-axis shows scaled wall shear stress, $\tau_w^* = \tau_w/\frac{1}{2}\rho U^2$, where U is the mean velocity in the nozzle throat.

Another useful reference result is the average wall shear stress, $\bar{\tau}_w$, imposed on the substrate under the nozzle rim between $r = r_i$ and r_o. Zhou *et al.* [114] estimated the average wall shear stress induced by the FDG flow using an approximation, which has been mentioned above and is shown as follows [159].

$$\bar{\tau}_w = \frac{1}{r_o^2 - r_i^2} \int_{r_i}^{r_o} 2r\tau_w dr$$

$$= \frac{\mu Q}{4\pi(h/2)^2} \frac{2}{r_i + r_o}$$

(4.5)

and the dimensionless form:

$$\bar{\tau}_w^* = 4\pi \frac{\mu r_i}{\rho Q} \left(\frac{r_i}{h}\right)^2 \frac{r_i}{r_i + r_o}$$

(4.6)

Fig. 4.18 compares the analytical solutions and the simulation results for both ejection and suction modes. The wall shear stresses in ejection mode are noticeably higher than those in

120

suction mode at $h_o/d_t > 0.2$, and greater than the analytical results. For $h_o/d_t \leq 0.15$, the results obtained from Eqn. (4.6) are 70 % larger than the simulation results. This is attributed to the assumption that, the flow profile beneath the nozzle rim is parabolic (fully developed), which is not correct at small clearances. The analytical result can be used for order of magnitude estimate for this quantity under these flow conditions. If more precise values are required, a series of simulations covering the range of interest would be required.
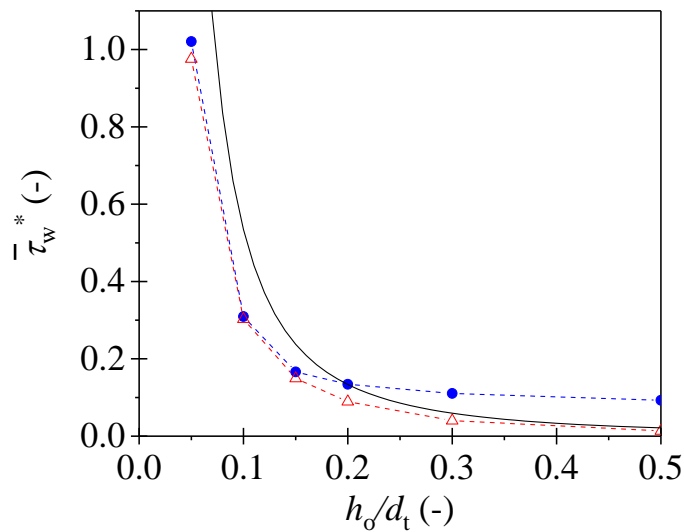
Fig. 4.18. Effect of clearance on dimensionless average wall shear stress under the nozzle rim, $\bar{\tau}_w^*$, for the cases in Fig. 4.17. Solid blue circles – ejection; open red triangles - suction. Locus shows the analytical result, Eqn. (4.6), assuming viscous flow between two parallel discs.

4.3.4 Applications

4.3.4.1 Materials and methods

In this study, all sample materials were coated on rectangular 316 SS substrates (25×100 mm^2, thickness 0.7 mm, $R_q = 2.391$ μm). These substrates were cleaned by three steps before sample were applied. Firstly, they were soaked in alkali solution (NaOH, pH = 12) for 24 h, which is a useful cleaning agent for protein. Next, the substrates were soaked in isopropyl alcohol and then acetone with sonication. If there was any residual sample remaining on the substrate, the

substrate was scrubbed with a plastic and steps 1 and 2 were repeated. Finally, they were dried in air.

A commercial petroleum jelly (Atom Scientific Ltd, GPS5220) was used to create model layers using a spreader tool on the substrates with a thickness of 0.7 ± 0.07 mm measured by a confocal LED thickness sensor (CTS: a Micro-Epsilon IFC2461 controller paired with an IFS2405 sensor). A detailed description of the spreader tool was given in Wang's dissertation [127].

In order to generate PVAc layers on the 316 SS substrates, a confined area (15×10 mm^2) on the substrate was surrounded by tapes firstly. A commercial glue (Evo-stik® Wood Adhesive Resin) was then squeezed on to the area, followed by scraping off extra glue using a rule. The surface tension of PVAc helped it to spread to give a uniform and flat layer after drying in air for more than 94 hrs [98]. The thickness of the dry film was about 0.3 mm measured by a digital micrometer (Mitutoyo absolute digital indicator, ID-C112MB). A PVAc layer with a thickness of 0.3 mm could be prepared by two layers of tapes (0.571 mm).

Layers of gelatin were prepared by dissolving 9 g gelatin (Dr. Oetker Platinum Grade Leaf Gelatine) in 100 ml deionised water at 85 °C for more than 30 min. A confined area (15×10 mm^2) was generated by tapes on the substrates, and then approximately 0.15 ml solution (three droplets) were then pipetted on this area, followed by drying in air for about 24 h. A uniform film was generated by the surface tension of the solution. The measured thickness of the dry layer was 0.8 ± 0.1 mm.

The complex model food soil (CMS) is made of 18% fat, 5.7% protein, 24% carbohydrate, 0.3% salt and 52% water. The detailed procedure for preparing the CMS soil has been described by Cuckston *et al*. [48]. The mixture soil was coated on the substrate in a confined area (15×10 mm^2), the same as that for previous layers, using the spreader with a fixed thickness of 0.4 mm. The wet thickness of the layer was averagely 0.4 ± 0.05 mm, after removing the tapes. The prepared layers were then dried in air for 24 h, and moved into a preheated oven to bake for 7 min at a fixed temperature 204 °C. The tray of samples was moved out for cooling to room temperature immediately after reaching 7 minutes. The initial dry thickness of the CMS layers were measured using the micrometer; however, the measurement was often overestimated due to the fact that the thickness recorded by the micrometer relies on the highest point of samples but there were lots of stubs on the CMS deposit.

The PVAc, gelatin and CMS layers could absorb solution up into the untested area due to their porous microstructures by capillary suction, resulting in prewetting in SiDG tests. Before tests, breaks between each test regions had to be created. A band of around 5 mm was generated by removing the layer using a scrap, shown in Fig. 4.20(e). For the 100 mm long substrates used in these tests, this resulted in four test regions.

The CTS measures a layer's thicknesses by detecting light reflected from a sample surface. The technique also enables thickness measurements for transparent materials by corrections of the material refractive index [160]. The region measured by the CTS is about 9 μm in diameter, compared to at least 2 mm in diameter, including the nozzle throat diameter and rim, for SiDG. With these benefits, the CTS sensor was thus employed to measure swelling of layers in wet conditions.

4.3.4.2   Results and discussion

Swelling of soft solid layers

In the repeatability and swelling studies for various soft solid layers, layers of petroleum jelly, gelatin, PVAc and the CMS were submerged in deionised water at 20 °C, followed by 50 gauging cycles. At initial 10 cycles, the syringe pump ejected, and then withdrawn with a duration of 2 s, which allowed the pressure drop to be measured over a short time. After this, both ejection and suction modes lasted 5 s and with an interspersion of 5 s between each cycle. The first measurement could be conducted 10 s after the sample contacted the solution. This delay was attributed to the slow response of the syringe pump. The shear stress induced by the gauging flow exerted on the sample surface becomes large with decreasing clearance. When the induced shear stress exceeds a material's yield stress, the layer will deform. In order to prevent deformation of layers and ensure measurement in the linear region of C_d vs. h_o/d_t, an upper limit of 500 Pa, and a lower limit of 140 Pa were set. The nozzle head would move 0.02 mm close to the surface, when the measured pressure was less than 140 Pa, and vice versa. The procedure is the same as the feedback mode discussed in Wang's dissertation [127].

Repeatability tests for SiDG were performed by gauging 3-4 sample points on a sample substrate using different materials, presented in Fig. 4.19. The CTS sensor was employed to

measure the initial dry thickness of petroleum jelly, since the stress imposed on the surface and induced by the micrometer is higher than the yield stress of petroleum jelly and will make the layer deform. In Fig. 4.19(a), very good repeatability for petroleum jelly is obtained with a deviation of less than 0.35 μm, which is higher than the resolution of SiDG. Similarly, it is noticeable in Fig. 4.19(b) that the repeated tests for gelatine demonstrate good intra sample repeatability with a deviation of less than 5 μm.

Fig. 4.19(c) shows good repeatability among four PVAc samples in suction mode with a deviation of about 2.4 μm, but after 800 s, there are two discontinuous points. This is attributed to the backlash of the *x*-axis positioner. When the measured pressure drop surpassed the maximum pressure limit, the nozzle would be triggered to move away from the layer surface. However, the O-ring installed on the tank wall for preventing flooding would resist the movement of the nozzle, which resulted in a smaller movement than the theoretical one.

Fig. 4.19(d) presents a repeatability study for CMS layers. The data for the three measurements fluctuate with time, but show good repeatability with a deviation of about 3.5 μm. The fluctuation is due to the rough surface of CMS. In the process of CMS preparation, layers broke after drying in air, causing a lot of cracks to be generated on the surfaces. These cracks changed the flow field of SiDG and then had influence on the measurement of SiDG. Overall, these results of repeatability testing indicate that this SiDG device can be employed for thickness measurements with confidence due to its good repeatability.
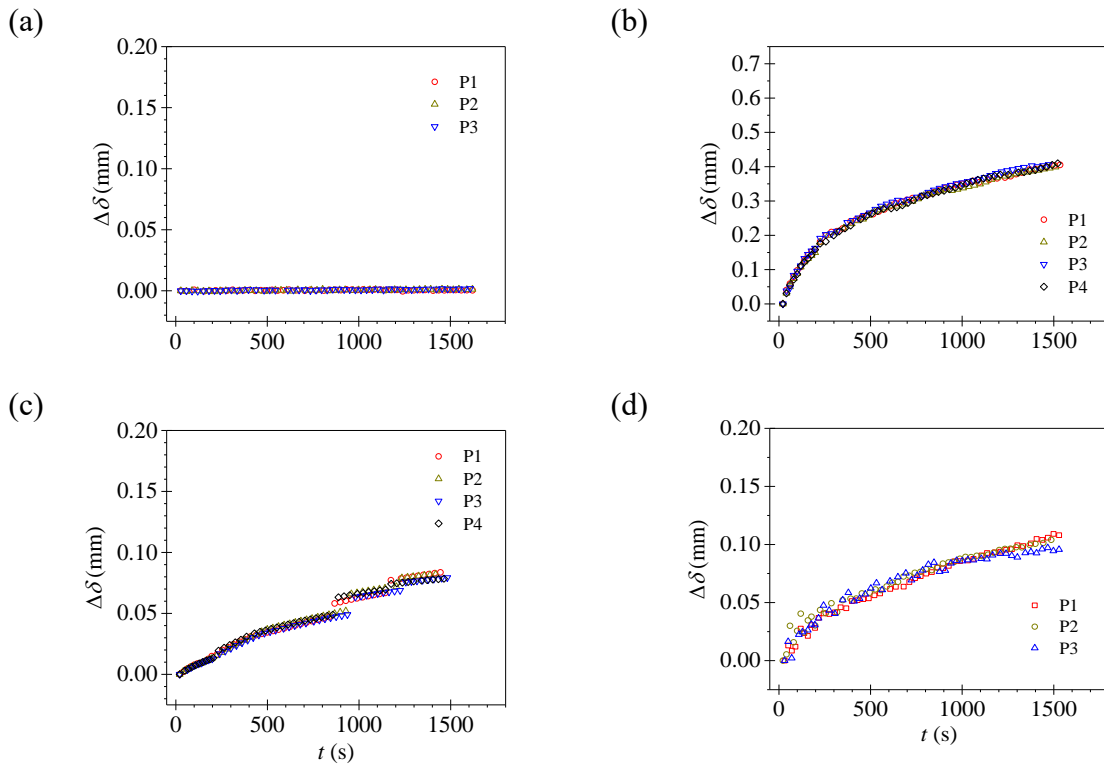
Fig. 4.19. Repeatability testing for (a) petroleum jelly film (δ_0: around 719 ± 70 μm), (b) gelatin films (δ_0: P1, 91 μm; P2, 91 μm; P3, 91 μm; P4, 85 μm), (c) PVAc glue layers (δ_0: P1, 341 μm; P2, 321 μm; P3, 314 μm; P4, 304 μm), and (d) CMS layers (δ_0: P1, 339 μm; P2, 343 μm; P3, 337 μm) immersed in deionized water (pH = 5.6, 20 °C) for $\dot{m} = 20$ ml/min, using suction mode.

Swelling profiles for 4 materials are shown in Fig. 4.20, using the change in thickness, $\Delta\delta$ (measured thickness, δ – initial dry thickness, δ_0). Fig. 4.20(a) presents that petroleum jelly film was gauged for 50 cycles, alternating between ejection and suction modes. No significant change was observed. This is because the shear stresses induced on the surface in both modes were less than the yield stress of the viscoplastic petroleum jelly (about 280 Pa, as discussed in section 3.2.4). For instance, the maximum shear stress obtained from simulations at a clearance of 0.05 in ejection mode is about 184 Pa. When the shear stress surpasses the yield stress, the material will undergo deformation.

The swelling profiles of gelatin for both ejection and suction modes in Fig. 4.20 are similar, with a small difference of about 20 μm. This is attributed to the elastic behaviour of gelatin. A larger estimated thickness from ejection mode than that of suction was also observed by Wang *et al.* using the ZFDG device [98]. Both profiles show a quick increase of thickness at the initial stage ($t < 300$ s) due to hydration of water, after which the swelling rate slows. These features

125

have been reported in previous FDG work [98, 109] and studies using a gravimetric tool [161, 162]. The volume fraction of the sample polymer due to swelling is defined as $\Delta\delta/\delta_0$, and the initial hydration caused around 2.4. Fig. 4.20(c) shows similar swelling behaviors with PVAc. This material swelled quickly over first 200 s, after which, it swelled gradually to the end of measurement.

However, in Fig. 4.20(d), the suction results for the CMS layers are larger than that from ejection mode, and both swelling profiles fluctuate. These are thought to result from the microstructure of the dry soil layers. Fig. 4.20(e) shows a photograph of a dry CMS layer, and it is noticeable that the sample was porous and with a lot of cracks on the surface (giving spongy characteristics). As the syringe pump ejected, the layer like a sponge was compressed and a smaller thickness would be observed. By contrast, it would be pulled up while being withdrawn, and a larger thickness was then estimated. The fluctuations were caused by non-smooth layer surfaces.
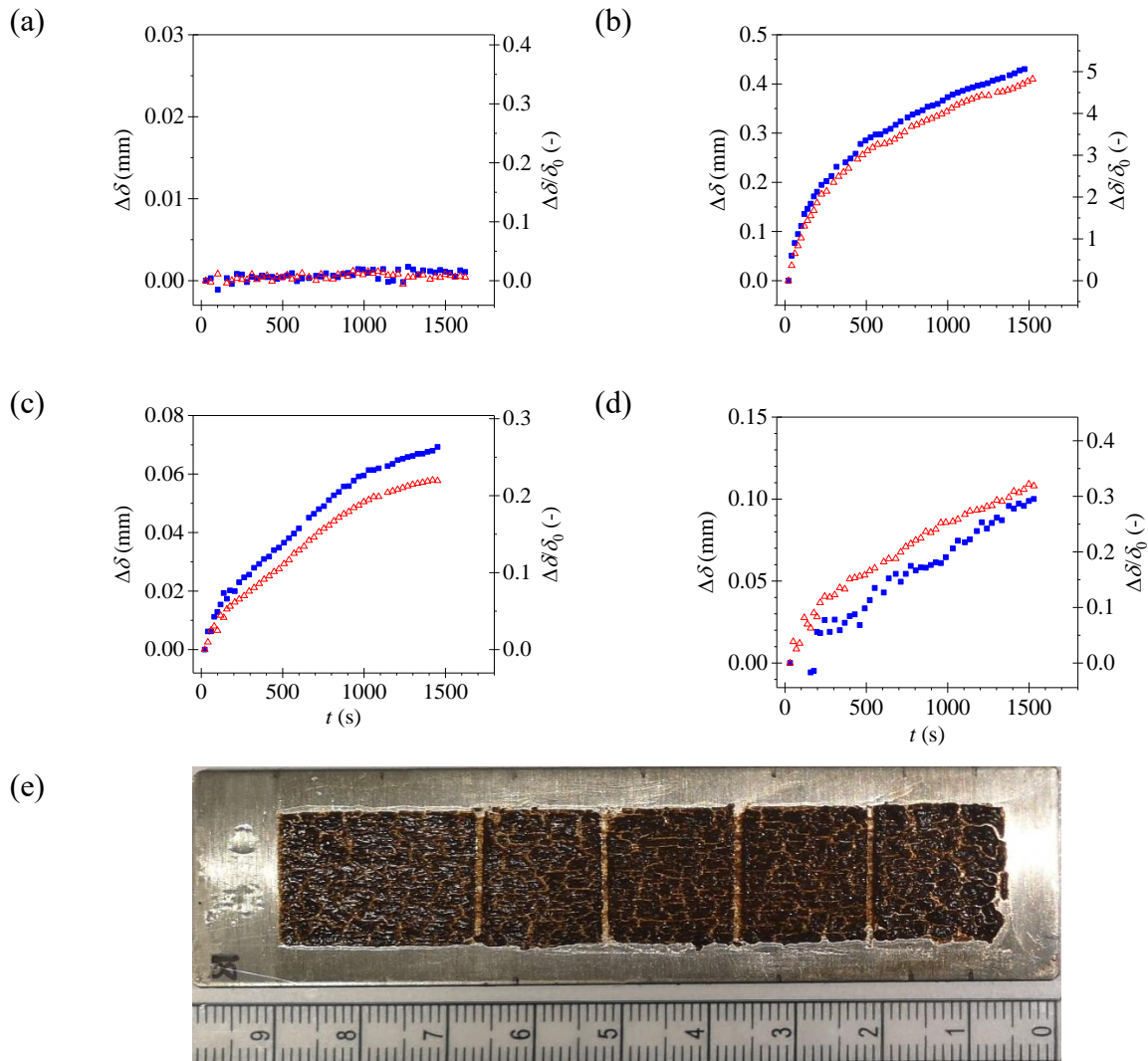
Fig. 4.20. Swelling profiles of (a) petroleum jelly (δ_0: 720 μm), (b) gelatin (δ_0: 85 μm), (c) PVAc (δ_0: 263 μm), (d) CMS (δ_0: 339 μm) immersed in deionized water (pH = 5.6, 20 °C) with $\dot{m}$ = 20 ml/min, and (e) photograph of dry CMS soil before immersion. Solid blue squares – ejection; open red triangles – suction.

Fig. 4.21 compares swelling profiles measured by CTS and SiDG. The swelling of the gelatin film measured by CTS was performed by CET IIB student, Cheyanne Xie [128], and the measurements for PVAc and CMS layers using CTS were conducted by PhD student Georgina Cuckston.

127
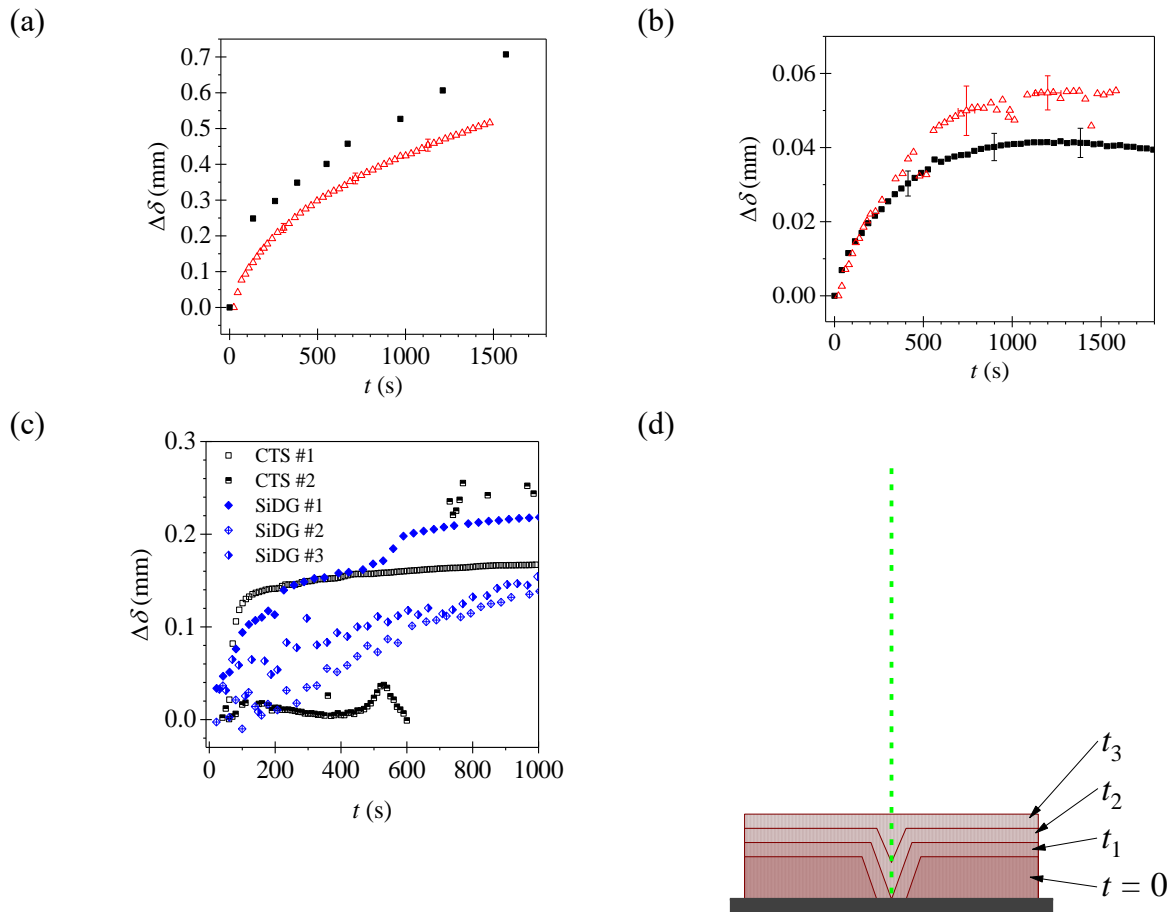
Fig. 4.21. Comparison of swelling behaviour measured by the CTS and SiDG devices ($\dot{m} =$ 20 ml/min, 2 repeats) (a) gelatin layers (δ_0 85 μm) submerged in pH 12 solution at 20 °C, suction mode; (b) PVAc layers (δ_0 around 196 μm) immersed in deionized water at 20 °C, suction mode; error bars show the range of repeated measurements. (c) CMS immersed in pH = 9 solution (δ_0 around 300 μm), ejection mode. Solid blue diamonds – SiDG, ejection; open red triangles – SiDG, suction; black squares – CTS (2 repeats). (d) Schematic of CTS beam located on a CMS crack during thickness measurement. Green dash line – CTS beam. Wine and grey shaded pattern indicate a crack and substrate ($t_3 > t_2 > t_1$).

In Fig. 4.21(a), both profiles show good agreement with a quick swelling at the initial hydration stage, followed by a nearly constant swelling rate to over 1500 s. However, a systematic difference between both measurements can be observed, which resulted from the measurement procedure for CTS. The peaks of water and gelatin could not be identified due to their similar reflection indexes. Thus, an alternative method was required, in which the gelatin layer was moved out from the liquid environment repeatedly for CTS measurements. Even though the sample layer was measured in air, there was still a residual water film on the sample surface,

causing the discrepancy. The test also demonstrates that SiDG is a valuable technique for thickness measurement of materials whose reflection indexes similar to solution.

The CTS measurement for PVAc is compared with the results measured by SiDG, in Fig. 4.21(b). Over the first 300 s, good agreement between two measurement techniques is obtained. After that, both approach asymptotic values with a small discrepancy of about 14 μm. This is attributed to the different initial layer thicknesses.

In Fig. 4.21(c), the swelling profiles for both CTS and SiDG show noticeable differences from that of PVAc and gelatin films. $\Delta\delta$ of CTS #1 test experiences a rapid increase due to hydration, and then approaches an asymptote of about 0.17 mm; however, the results of CTS #2 fluctuates before 600 s, followed by increasing markedly to above 0.2 mm. By contrast, the profiles of SiDG increase steadily, and at the end of tests, these reach similar values to that for CTS. This is caused by the presence of cracks in the of CMS layers. A schematic for this behaviour is presented in Fig. 4.21(d). t denotes the contact time of the CMS sample immersed in the gauging liquid, and $t_3 > t_2 > t_1$. It is possible to locate the CTS beam at a crack or at a flat surface (crack-free region) during measurements due to its small spot (9 μm). In Fig. 4.21(d), the beam is located at the centre of a crack, and the initial hydration stage cannot be observed. However, a rapid increase of thickness is measured when the crack merges after $t = t_3$. The expected swelling profile is similar to that of CTS #2. By contrast, the results of CTS #1 can be explained as being due to the CTS beam being located at a crack-free region. On the other hand, the SiDG measurements show an average value due to its layer diameter of about 2 mm. Compared to the size of cracks, the influence can be neglected, but the presence of cracks beneath the nozzle rim will decrease the pressure drop (overestimated C_d), resulting in an underestimated thickness. The effect of surface roughness on FDG measurements has been studied by Wang *et al.* [6].

A 3D simulation was reformed to investigate this phenomenon. A geometry with four triangular channels beneath the nozzle head simulating cracks, was created and is shown in Fig. 4.22(a).
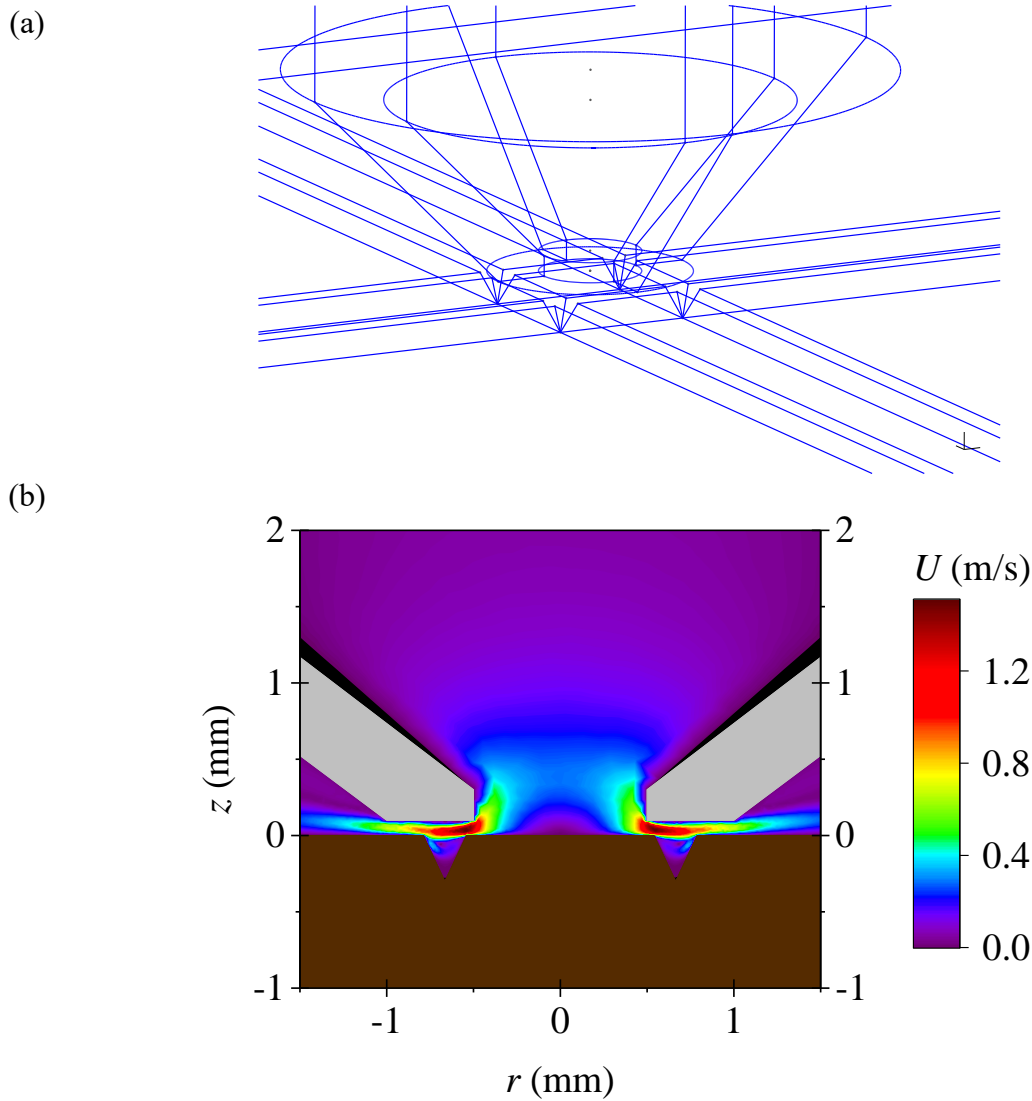
Fig. 4.22. Simulation of dynamic gauging on an idealized cracked surface, representing an unswollen CMS layer. (a) Geometry of 3D SiDG simulation with pairs of parallel V-notch (1.08 mm) cracks, and (b) estimated speed (velocity magnitude) distribution for ejection mode. Conditions: $\dot{m} = 20$ ml/min, $h_o/d_t = 0.1$.

The gauging conditions were $\dot{m} = 20$ ml/min, $h_o/d_t = 0.1$ for both modes, and the results showed 8% and 3% differences of C_d from measurements for suction and ejection, respectively. The predicted velocity distribution is plotted in Fig. 4.22(b), and it is evident that the velocity profile under the nozzle rim has been changed due to the cracks. These confirm the presence of cracks impacts the flow pattern.

Effect of pH

Acid or base conditions can make polymeric chains become charged, resulting in repulsion inside the matrixes. This is one of the mechanisms causing polymer swelling. A series of swelling tests for gelatin and PVAc layers at various pH were conducted using the ZFDG device by Wang *et al.* [98]; However, the early period swelling could not be investigated due to the ZFDG configuration. The SiDG allows the shortest time period of about 10 s to be monitored, and the results for gelatin and PVAc films swelling at different pH are shown in Fig. 4.23 and Fig. 4.24.

In Fig. 4.23, the swelling profiles for pH 5.6-11, show a similar trend, a rapid hydration increase at the beginning, followed by decreasing swelling rates with increasing time. By contrast, at pH 12, the falling rate behaviour is not significant at $t > 500$ s. This is because at high pH value, the amine groups in the gelatin are deprotonated, resulting in expansion of the matrix. A similar phenomenon was reported by Wang *et al.* [98] in a swelling test of gelatin film at pH 11.6. These swelling profiles were fitted by the Ritger and Peppas model [163]:

$$m = m_\infty k_D t^{n_D} \tag{4.7}$$

where m is the amount of solvent in the polymer taken up from the liquid environment after time t, m_∞ is the total amount of solvent taken up while reaching a swelling equilibrium, k_D is the kinetic constant, and n_D is the diffusion index. It is supposed that the amount of solvent is linearly proportion to the change of the layer thickness, $\Delta\delta$, and the equation can be written as

$$\Delta\delta = \delta - \delta_0 = (\delta_\infty - \delta_0)k_D(t - t_i)^{n_D} = k_m \Delta t_i{}^{n_D} \tag{4.8}$$

Here δ_∞ is the thickness at swelling equilibrium, t_i is the time when the polymer was submerged into solution, and k_m is a kinetic constant, equivalent to $k_D(\delta_\infty - \delta_0)$ [6]. As n_D is proves to be 0.5, the swelling behaviour is dominated by Fickian diffusion. Swelling data of pH 5.6, 11 and 12 are plotted against $(t - t_i)^{1/2}$ in Fig. 4.23(b). It is obvious that profiles of pH 11 and 12 show good linear relationships, but $\Delta\delta$ at pH 5.6 experiences a linear increase before 250 s, and then deviates from the initial trend, which indicates that there is a second swelling mechanism occurred at $t > 250$ s. This transition has been reported by Offner and Shott [164]. Also, the swelling study investigated by Wang *et al.* [98] showed a second swelling mechanism happened after 5000 s, and n_D increased with increasing pH. However, in this study, the initial

swelling is more interesting so that swelling tests for longer times were not conducted. The volume fraction of solvent in the polymer (voidage), ε, is defined as $1 - \delta_0/\delta$. In Fig. 4.23(a), the voidages for all cases increase rapidly to about 0.7 at the hydration stage, exceeding 0.8 at $t = 1500$ s, indicating that the relaxation of the gelatin matrix is very strong.
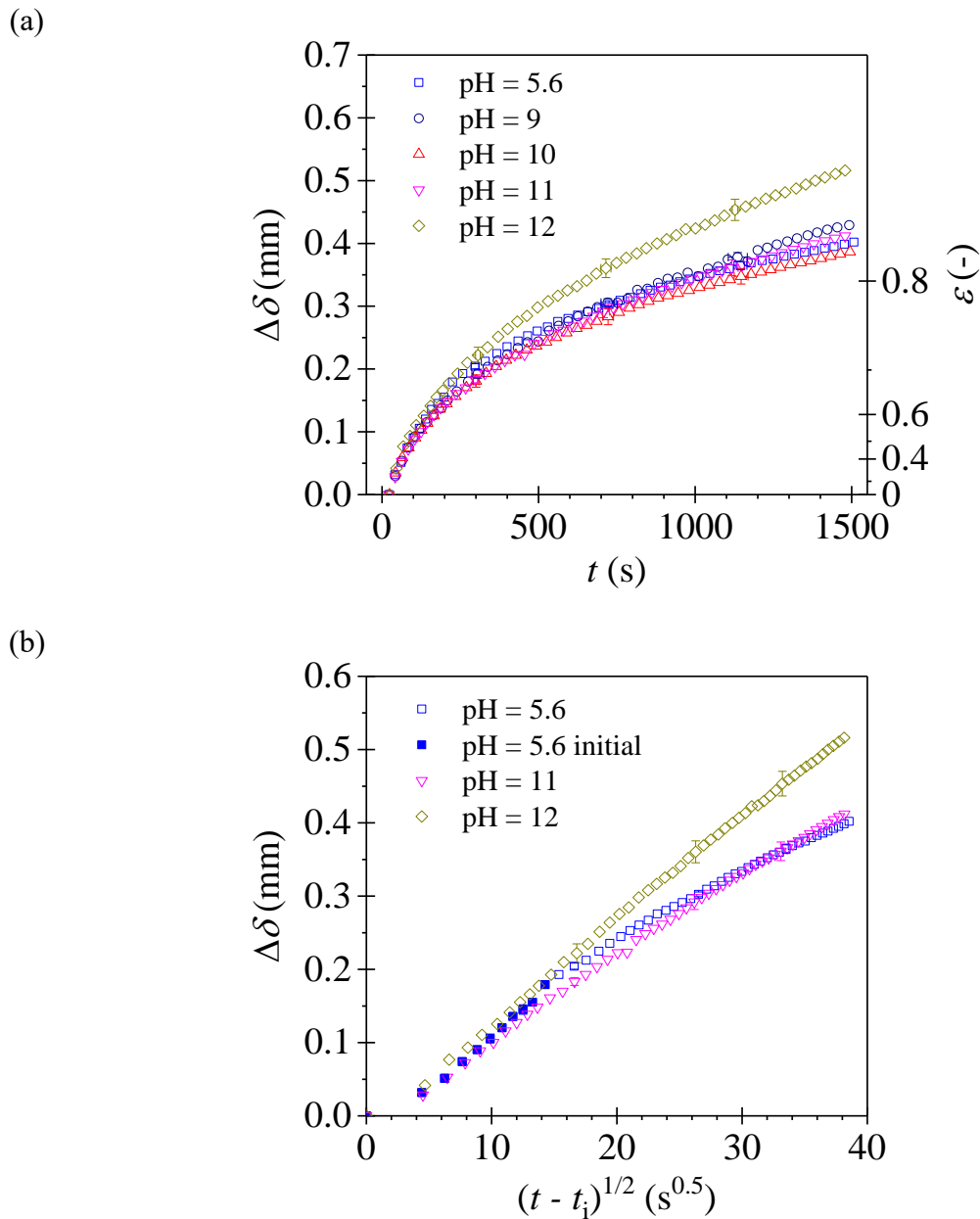
Fig. 4.23. (a) Comparison of effect of pH on swelling for gelatin layers. Conditions: $\dot{m} = 20$ ml/min, suction mode, water at 20 °C. (b) Some of the data sets fitted to Eqn. (4.8) with $n_D = \frac{1}{2}$.

In the PVAc films in Fig. 4.24(a), swelling at pH below 11 is not affected by pH noticeably and the swelling rates decreases steadily towards the end of measurements. This behavior is similar to that seen with gelatin layers and attributed to diffusion-dominated swelling. By contrast, the thickness at pH 11 increases rapidly at $t < 700$ s. Furthermore, profiles of pH 11.7 and 12 in Fig. 4.24(b) show a relatively strong influence by pH on swelling. These indicate that a different mechanism is active at higher pH. PVAc is one type of hydrogels, and in general,

swelling of hydrogels involves two mechanisms, being solvent diffusion inside the polymer matrix and relaxation of the polymer [165]. In a high pH environment, PVAc will experience hydrolysis and produce acetic acid and poly(vinyl alcohol) (PVA) [166]. The pK_a of PVA is 10.67 [167] so that base can cause PVA chains to be ionised and repel each other [168]. Thus, the mechanism at high pH can be expected to be "reaction-driven swelling".

All profiles at early times were fitted by Eq. (4.8) and the parameters obtained are summarized in Table 4.4. At pH < 11, n_D is at a region between 0.66 and 0.71, meaning that swelling was controlled by both diffusion and a second mechanism [169]. At pH ≥ 11, the diffusion indexes are around 1. This is attributed to a transition, from mixed diffusion-controlled swelling to reaction-driven swelling mentioned above. In both regions (pH < 11 and ≥ 11), the relaxation rate has a linear relationship with pH. Most of the literature on this topic is concerned with adhesive applications and focuses of the moisture content of the PVAc rather than its thickness. This study confirms that the water content of the PVAc material would increase with increasing pH due to hydrolysis-driven expansion, reported by Mathew *et al.* [170].

In terms of voidage, at pH < 11, the maximum ε is less than 0.25, but at pH ≥ 11, relaxation-controlled swelling occurred and the swelling behaviour became more complex. The voidage at pH 11 approaches about 0.28 at the end of initial linear increase, followed by falling swelling rate, and finally reaching approximately 0.38. At pH 11.7, the trend of voidage is similar to that of pH 11 at the beginning and the swelling rate decreased after 200 s. However, ε approaches a peak of about 0.37 at $t \sim 1230$ s. By contrast, at pH 12, the voidage reaches a peak value after swelling of mixed diffusion control, and then decreases due to shrinkage. After 800 s, the voidage maintains at about 0.32. These results demonstrate that the SiDG device enables swelling and shrinkage to be recorded at both early times and long times.

(a)

(b)
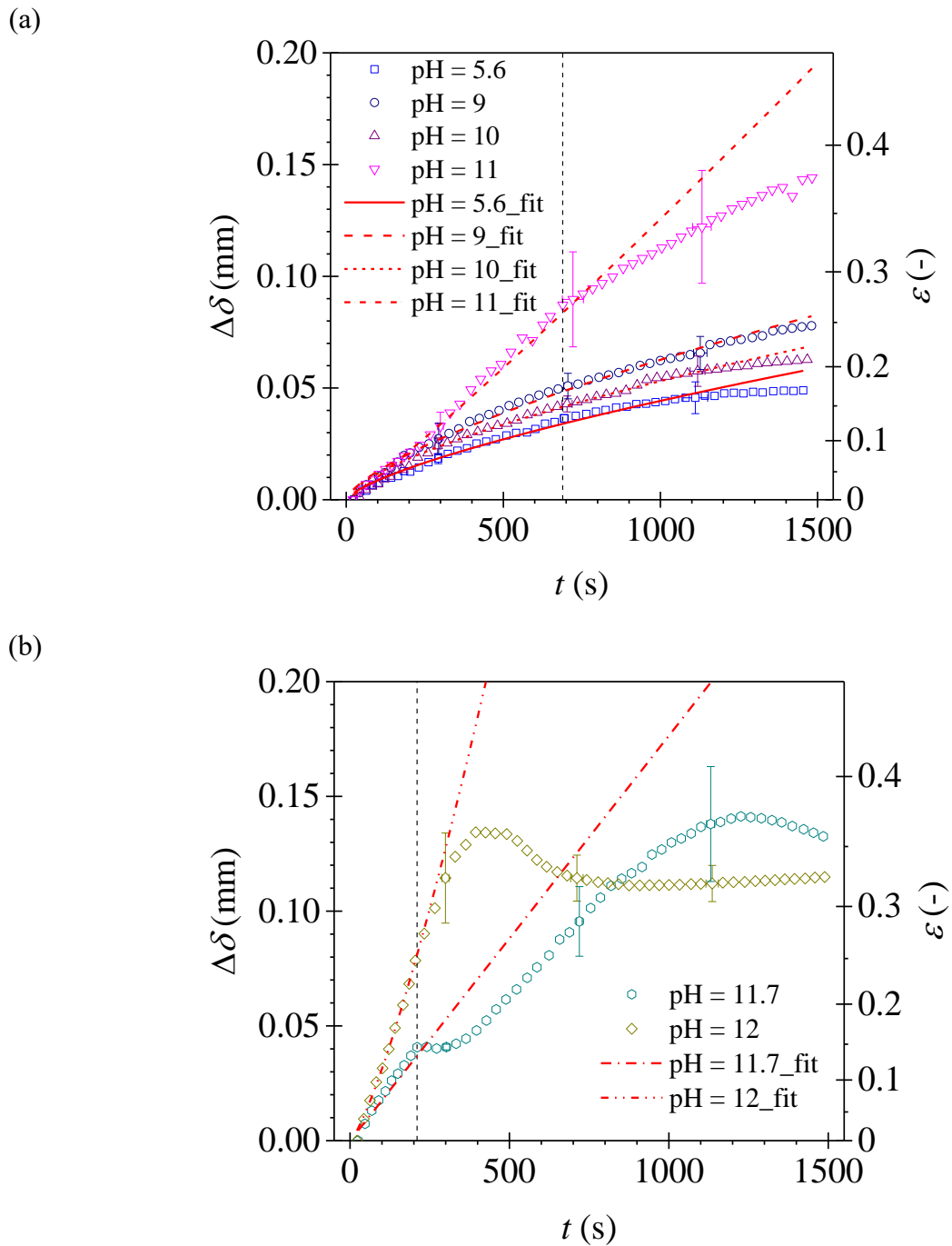
Fig. 4.24. Comparison of effect of pH on swelling (and void fraction) for PVAc films with swelling models (Eq. (4.8)) at (a) pH ≤ 11 and (b) pH > 11. Conditions: $\dot{m}$ = 20 ml/min, suction mode, water at 20 °C. Vertical dashed lines in (a) and (b) indicate the end of the linear fitting region for pH ≥ 11. The error bars describe the range of repeated tests.

135

Table 4.4. Swelling parameters obtained by fitting initial PVAc swelling data to Equation (4.8)

pH	k_m	n_D	R^2
	$\mu m/s^n$	-	
5.6	0.328	0.71	0.981
9	0.533	0.69	0.973
10	0.560	0.66	0.984
11	0.067*	1.09	0.995
11.7	0.174*	1.00	0.994
12	0.259*	1.06	0.981

* Since $n_D \sim 1$ in these cases, this is effectively the initial linear swelling rate.

4.4   iFDG

4.4.1 Construction

4.4.1.1   iFDG Concept

A non-contact technique, namely inductive proximity sensing (IPS), has been widely utilised for distance measurements with advantages such as long lifespan and low-maintenance [155]. This device is also feasible for operation in dirty and wet environments such as fouling, since influences on the measurement from non-metallic deposit components with low magnetic permeability can be neglected. The principle of IPS is to detect a coil approaching a metal target by measuring the change of the amplitude of an oscillating voltage. An oscillating voltage is supplied to a circuit with an inductive coil, and a magnetic field is generated around the coil. When the coil moves close to the target, an eddy current will flow in the metal object. The induction current will result in an increase of load on the circuit and decrease of the voltage

amplitude. Thus, the status of the metal target can be determined by measuring the change in the amplitude.

The configuration of the IPS used in this study contains three major parts, shown in Fig. 4.25(a): the sensor head, the processing circuit and the driving logic. The sensor head is composed of an inductive coil, a resonance capacitor and a cable connected to other parts. The coil was wound using an enamelled wire (solderable self-bonding enamelled copper wire, diameter 0.25 mm, Scientific Wire Company) with 61 turns, and then fixed beneath an original FDG nozzle head. The coil and nozzle head were then covered by epoxy (Marine Weld Waterproof Epoxy Adhesives, JB8272, JB Weld) for protection, then cut to the desired shape using a lathe. Fig. 4.25(b) shows the layout of the nozzle head. The inductance of the coil is 34.1 μH, measured by a RCL meter (PM6303, Philips). A capacitor labelled C_r (100 nF) is connected with the coil in parallel for adjusting the supplied frequency to reach a resonance frequency and receive a maximum oscillating voltage. A shielded cable with a length of 30 cm connects the sensor part to the processing circuit.

In the driving logic part, an input signal (AC sinusoidal waveform, 83.33 kHz, ±10 V) is supplied by a function generator (Feedback, FG601). However, the output current and voltage of the generator are not high enough to support the desired resolution for thickness measurements. Therefore, an amplifier with a voltage of 15 V for compensation, provided by a DC power supply (B&K Precision, Triple output DC power supply, model 1672) is employed to boost the amplitude. A commercial data acquisition device (National Instruments, USB-6210, 16 AI (16-Bit, 250 kS/s)) is used to collect the peak-to-peak voltage waveform (pk-pk) across the sensor part, and these data are processed by a programme in Python 3.6.

(a)

(b)
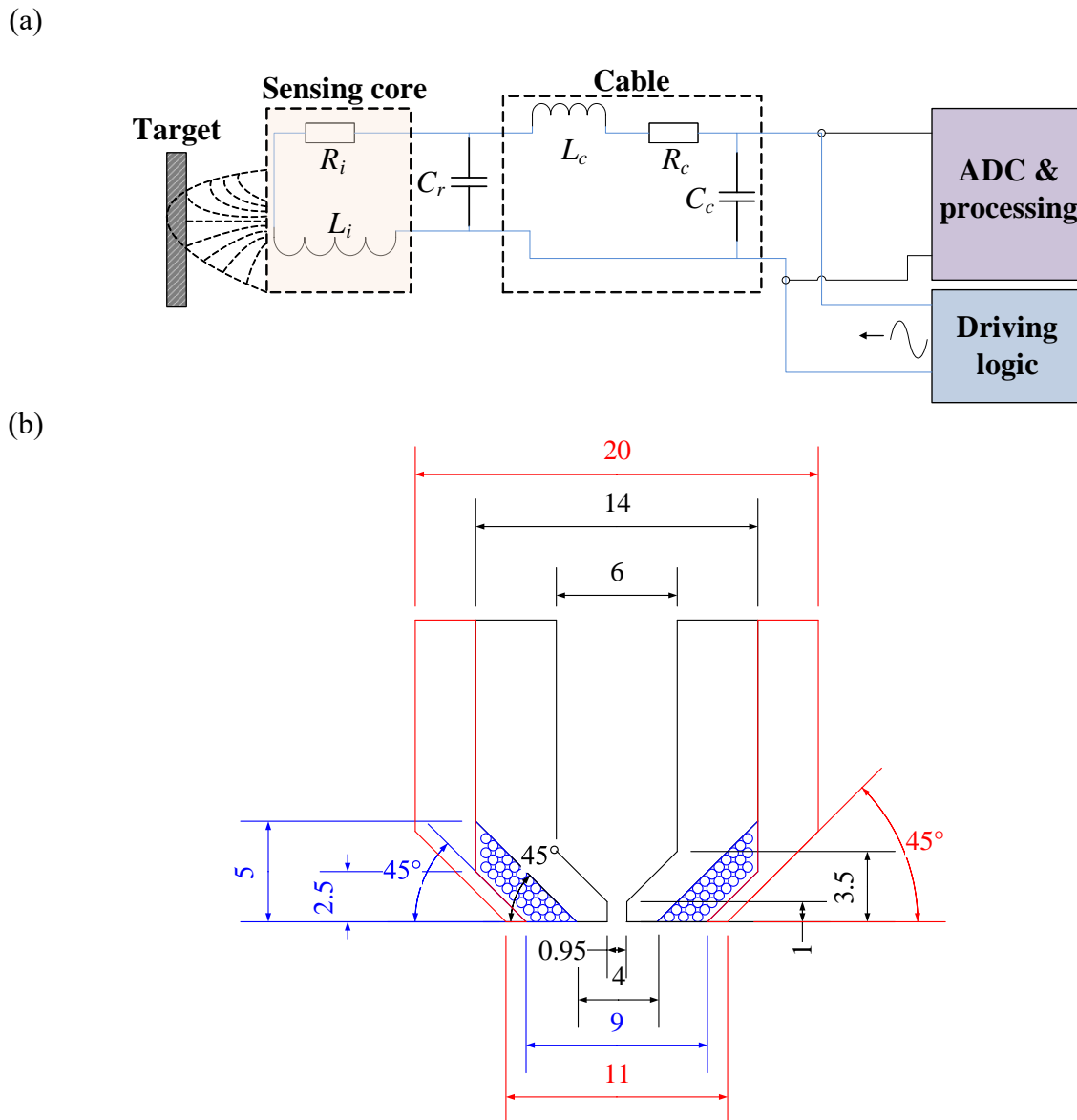
Fig. 4.25. (a) Schematic diagram of the inductive sensor system. (b) Geometry of the iFDG nozzle head. Symbols: Blue circles – inductive coils; Red – epoxy. All dimensions are mm.

4.4.1.2   FDG device

A schematic and a photograph for the iFDG device are presented in Fig. 4.26. This iFDG system was constructed based on the ZFDG system discussed in section 4.2.1. A Harvard syringe pump (Harvard Apparatus PHD Ultra Series; Hamilton glass syringe, internal diameter 23 mm) was utilised to eject and withdraw solution at a fixed flow rate. A rectangular Perspex tank (187×166 mm^2, and height: 100 mm) contained the gauging liquid, and the liquid level

was maintained at around 50 mm. In order to scan the sample surface, the tank was fixed above the motorised XY stage (STANDA, 8MTF-75LS05) driven by the controller (STANDA, 8SMC4-USB-B9-2), but with a space for the tubes supplying freezing liquid discussed later. The original FDG nozzle shown in Fig. 4.25(b) was made of polyethyletherketone (PEEK) with a length of 300 mm to develop a laminar velocity profile. This nozzle was mounted on a linear slide (Zaber Technologies, T-LSR075B) for controlling the clearance between the sample surface and nozzle head. A gauge pressure transducer (PT) (OMEGA, PXM409-350HGUSBH) was employed to monitor the pressure drop across the nozzle and located 50 mm above the nozzle throat with a measurement range of 0 ~ 35 kPa. These data were collected by the same program as the IPS.

Ice growth experiments were conducted using an integrated tank, whereby a CPU cooling block (EK-Velocity RGB - AMD Full Nickel, 58×58 mm^2) with a metal side for chilling and others are insulated, was embedded at the bottom of the tank and labelled as F in Fig. 4.26(b). The coolant was a water/ethylene glycol (1:1 by volume) mixture and circulated from a cooling bath (Thermo Scientific Haake DC30-K20 Digital Control bath, 115VAC 60Hz) through the block. The test solution was drawn from one side of the tank and then pumped back to the other by a peristaltic pump (Masterflex® L/S® Series Peristaltic Pumps) to enhance mixing. Three temperatures, namely that of the cooling bath, the bulk solution in the tank and the chilling side of the block, were monitored using K-type and two T-type thermocouples, respectively.
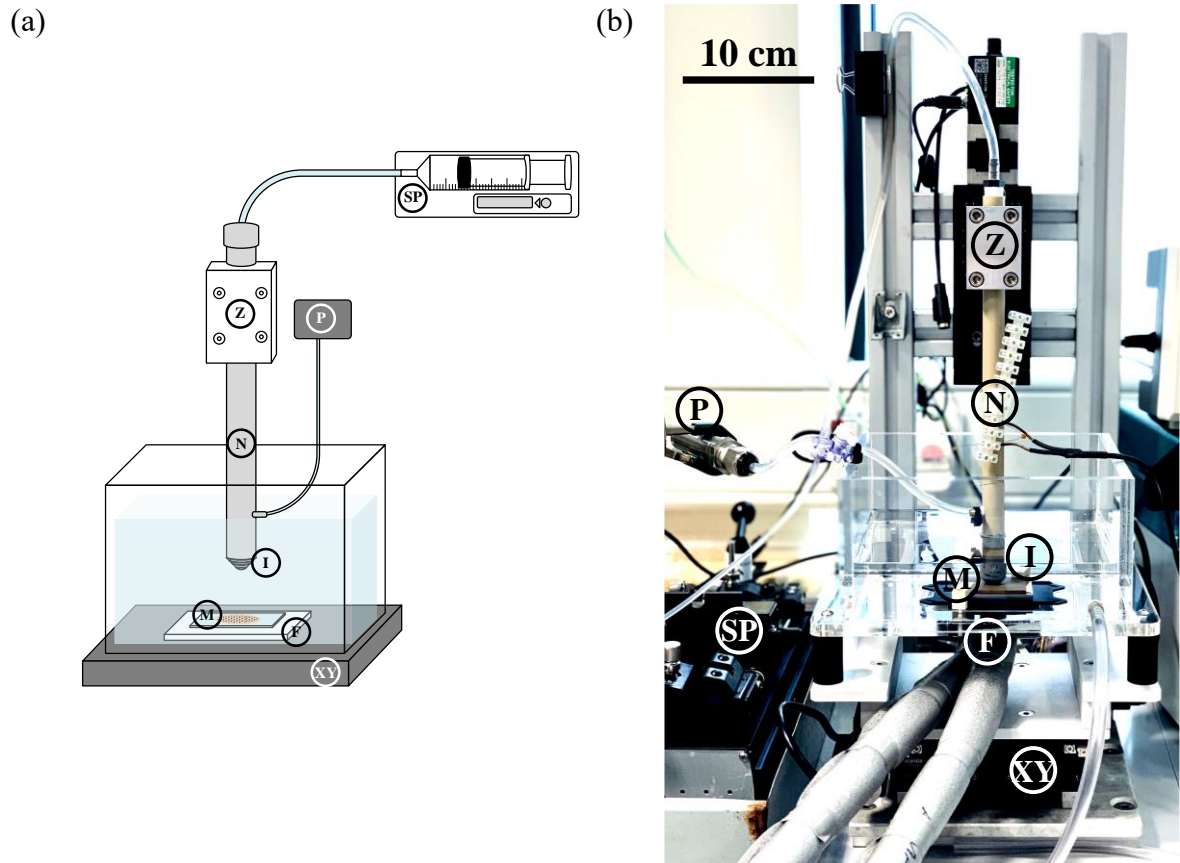
Fig. 4.26. (a) Schematic and (b) photograph of iFDG. Components: F – freezer; I – inductive coil; M – sample mount; N – nozzle; P – pressure transducer; SP – syringe pump; XY – *x*- and *y*-axis positioner; Z – *z*-axis positioner.

4.4.2 Model Formulation

The iFDG simulations used the same solvers and iterative converge criteria in OpenFOAM as the ZFDG models presented in section 4.2.2. A simplified 2D asymmetric model was employed to simulate the iFDG case due to the fact that the tank wall is far from the nozzle head and the flow out of the tube is unimportant [102]. The geometry and key dimensions are shown in Fig. 4.27. In Fig. 4.27, AB is the asymmetric axis and AK is the inlet, described as a fully developed laminar velocity profile. BC, DE, EF, FG, GH, HI, IJ, and JK are wall (no-slip). CD was set to be open ($p = 0$). The information about gauging solutions will be discussed in following section (summarised in Table 4.5).
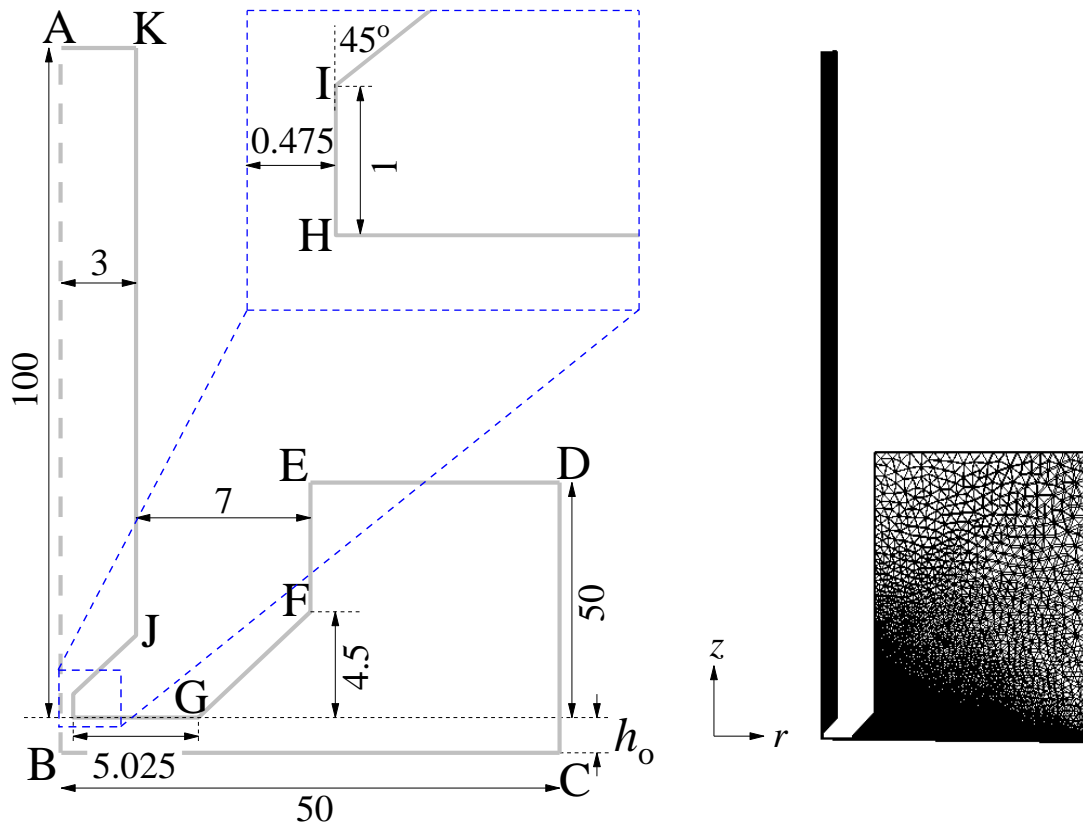
Fig. 4.27. 2D axi-symmetric iFDG simulations, and inset shows mesh. All dimensions is mm.

A series of converge tests were performed according to the validation guidelines reported by NASA's NPARC alliance [143]. Approximately 75000 iterations were computed to reach a steady value. The spatial convergence was checked by a mesh sensitivity study, shown in Fig. 4.28. In this study, different mesh sizes were tested, but following the same mesh growth rule, in which the minimum mesh element was generated around the nozzle rim and developed to the maximum mesh size at the side boundary. The pressure drop (then calculated to C_d) was chosen as reference, because Δp is sensitive to the meshes around the nozzle rim. In Fig. 4.28, it is noticeable that the model is not sensitive to the mesh size, and the C_d value approaches an asymptote (0.35), as the mesh volume is smaller than 1000 μm^3. This indicates that an element size of less than 1000 μm^3 is acceptable. Thus, the minimum mesh size was set to be about 2 μm^3 close to the nozzle rim, and expanded to the maximum size of around 2200 μm^3 at the outlet. Approximately 230000 mesh elements were employed in the simulation. The temporal convergence is not applicable here, which has been discussed above. The fundamental

consistency for the simulations was tested by calculating mass balance between the inlet and outlet, and the results show 0.22 % errors.
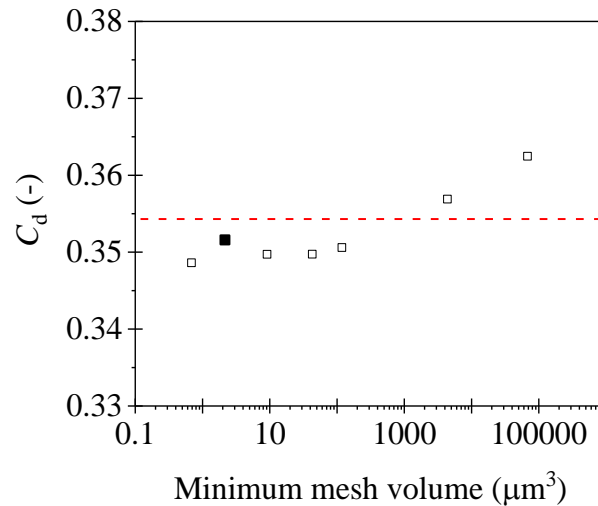
Fig. 4.28. Effect of mesh size on C_d. Conditions: UHT milk at 20 °C, $\dot{m}$ = 20 ml/min, Re_t = 165.8, for h_o/d_t = 0.2, ejection mode. Horizontal dashed line indicates experimental value at this condition. Solid black square is the mesh size used in the simulations.

4.4.3 Commissioning

4.4.3.1 Materials and methods

The iFDG concept was tested by three different metallic substrates: mild steel plate (50 × 50 mm^2, thickness 1.990 mm, relative permeability ~2000 [171]), 316 stainless steel plate (50 × 50 mm^2, thickness 1.852 mm, relative permeability ~1 [172]), and copper foil (50 × 50 mm^2, thickness 3.148 mm, relative permeability 1 [173], Goodfellow, 214-378-94, 99.9% copper). Furthermore, the mild steel substrate was covered by several layers of PVC tapes (PVC Electrical Insulation Tape, RoHS), thin glass slips (ACADEMY, glass cover slips) and microscope slides (Menzel Gläser) for testing the effects of different sample materials. The mild steel substrate was also tested in various liquid environments, including deionised water, milk, washing up liquid and carboxymethylcellulose (CMC) solutions.

The test liquids for testing the inductive proximity sensor and calibration of the iFDG device can be classified to four categories: Newtonian liquid with low viscosity – deionised water;

opaque Newtonian liquid with low viscosity – whole UHT milk (Sainsbury's Whole Long Life Milk); opaque Newtonian liquid with high viscosity – washing up liquid (Fairy Original, Procter and Gamble); non-Newtonian liquid – 1 wt% and 3 wt% carboxymethylcellulose (CMC) solutions. The CMC solutions were prepared by dissolving CMC powder (CMC sodium salt, BDH Laboratory Supplies) in deionised water, then agitating the solution at about 60 °C for more than 72 h.

The rheology of whole UHT milk, washing up liquid, 1 wt% and 3 wt% CMC solutions was measured by Dr. Simon Butler using a Malvern Kinexus lab+ rotational rheometer at 20 °C. These fluid properties are listed in Table 4.5 along with the Reynolds number at the nozzle throat, Re_t, utilised in the calibration experiments. The Reynolds numbers of power law fluids were calculated by [174]

$$Re_t = 2^{3-n}\left(\frac{n}{3n-1}\right)^n \frac{\bar{V}^{2-n} d_t^n \rho}{k} \tag{4.9}$$

Here n and k are the flow behaviour index and flow consistency index of the power law equation ($\mu = k(\dot{\gamma})^{n-1}$), respectively. $\bar{V}$ is the average velocity.

Table 4.5. Fluid properties of gauging liquids at 20 °C [98]. $\dot{\gamma}$ is the shear rate

Gauging solution	ρ (kg/m^3)	μ (Pa s)	Re_t (-)
Deionised water	997.3	1.12×10^{-3}	398
Whole UHT milk	1006.3	2.83×10^{-3}	166
Washing up liquid	1005.8	1.01	0.022
1 wt% CMC solution	984.2	Min(0.22, 0.476 $\dot{\gamma}^{-0.27}$)	1.4~3.4
3 wt% CMC solution	996.6	Min(37.62, 30.1 $\dot{\gamma}^{-0.57}$)	0.0045

The measured apparent viscosity for 1 wt% and 3 wt% CMC solutions are presented in Fig. 4.29(a) and (b). These show obviously shear-thinning behaviours at high shear rates. By

contrast, at the low shear rate region, a high viscosity plateau can be observed. These were fitted by the truncated Ostwald-de-Waele power law model used in OpenFOAM. The fitting results are shown in Table 4.5 and plotted on the figures.

As the concentration of CMC solutions is more than 2.5 wt%, the solution exhibits viscoelastic behaviour [175]. Thus, an oscillatory frequency sweep test was conducted for the 3 wt% CMC solution using an ARES rheometer (TA Instruments), by PhD student Janaki Umashanker. Fig. 4.29(c) shows good agreement between experiments and simulations using an 8 mode Maxwell model with $R^2 = 0.94341$. Its parameters are listed in Table 4.6. The data show that the suspension follows the Cox-Merz rule ($\eta(\dot{\gamma}) \sim \eta^*(\omega)$) reasonably well.
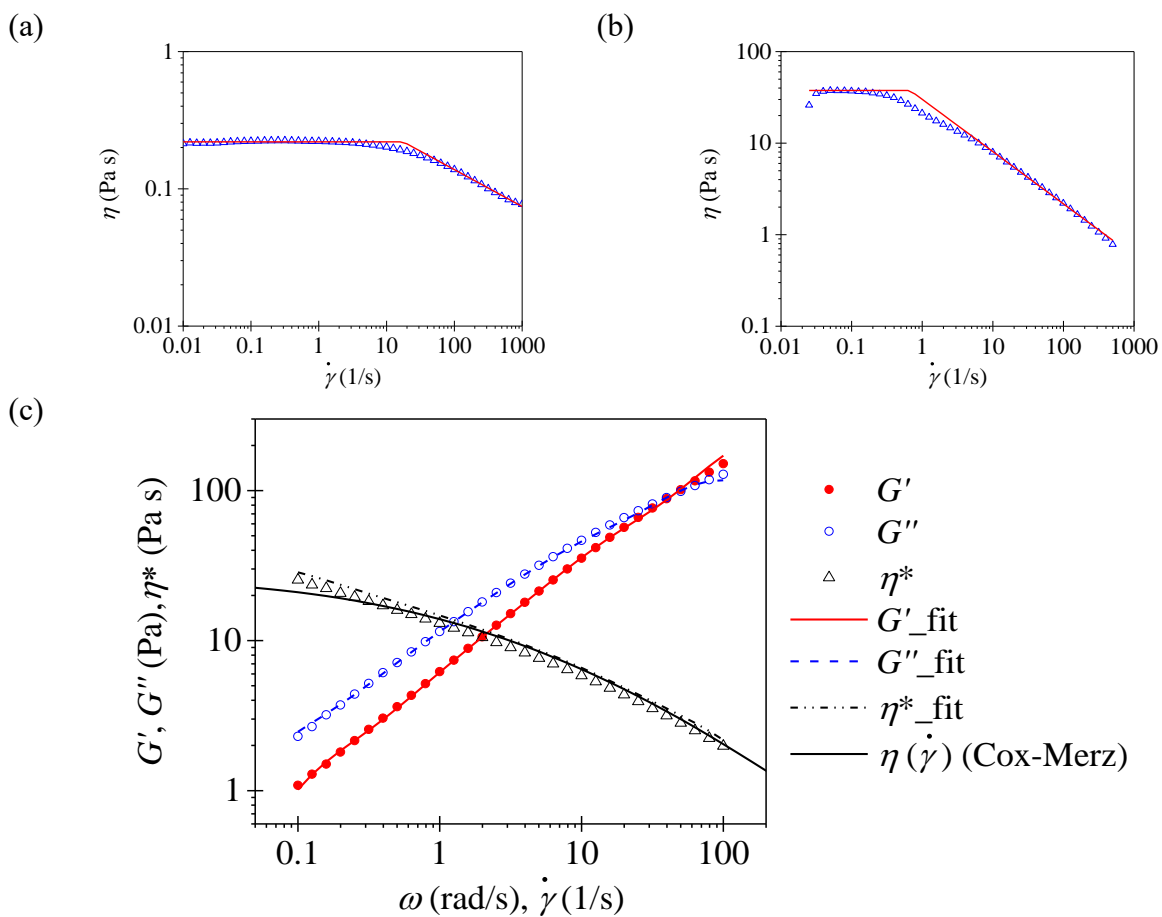
Fig. 4.29. Apparent viscosity of (a) 1 wt% and (b) 3 wt% CMC solutions at 20 °C and steady shear. Blue triangles – experimental data, red line – truncated power law model (parameters in Table 4.5). (c) Oscillatory shear sweep for 3 wt% CMC solution at 20 °C, shear stress amplitude: 13.6 Pa. Symbols – experimental data. Lines – fit to eight mode Maxwell model, shown in Table 4.6, and Cox-Merz rule.

Table 4.6. Parameters of eight mode Maxwell model

Mode	λ_i (s)	g_i (Pa)
1	10.0	1.82
2	3.73	0.157
3	1.39	3.45
4	0.518	5.98
5	0.193	12.6
6	0.0720	36.3
7	0.0268	0.0250
8	0.0100	223

4.4.3.2   Results and discussion

A calibration test for three different substrates was performed using deionised water as gauging solution, in which the nozzle head was located at 6 mm away from the substrates initially, and then moved close to them. The results are plotted in Fig. 4.30(a). For $h \leq 1$ mm, a linear relationship between the distance and measured peak to peak value for three substrates can be observed, which is applicable and viable to integrate with FDG measurements. The slopes at this region for these substrates are significantly different, which is attributed to different conductivities. When the magnetic field approaches a substrate with higher conductivity, a higher eddy current is induced on the substrate [176]. Thus, the slopes are in the order of mild steel (18.2 S/mm) < 316 SS (36 S/mm) < copper (62.7 S/mm), and these conductivities are listed in the inset of Fig. 4.30(a). As the inductive coil moves away from the metallic substrate, the region of magnetic field passing through the substrate become smaller and a lower eddy current is induced, causing the peak to peak voltage value to approach an asymptote of 12 V. The data of pk-pk value versus clearance were fitted by a linear model and shown in the caption of Fig. 4.30(a). These fittings indicate that at $h < 1$ mm, the change of peak to peak values can be employed as a position reference for the FDG device. However, in the IPS application, the

146

temperature of the coil causes effects on the pk-pk voltage, namely temperature drift. A temperature drift test was conducted, showing that the pk-pk voltage decreased with temperature and the deviation was about -1.5 μm/°C.

In order to study the effect of sample materials with low conductivity on the iFDG device, two and three microscope slips (thickness: 205 and 385 μm) and two and four layers of PVA tape (thickness: 119 and 238 μm) were fixed on the mild steel substrate with deionised water as gauging liquid and tested. The results are shown in Fig. 4.30(b). The trends with are the same as that without coating.

A further experiment was conducted with various glass slides placed on the mild steel substrate, plotted in Fig. 4.30(c). It is clear that these profiles are identical to the uncoated one. Both experiments demonstrate that non-metallic samples have no influence on the inductive measurement, and this technique is also feasible for studying samples on a non-metallic substrate by mounting the non-metallic substrate on a metallic holder.

Various liquids were tested with the inductive sensor and measurements were repeated 10 times for each liquid. These results in Fig. 4.30(d) show the same linear trends of peak to peak value with increasing clearance. Each measurement point can be identified from others, indicating that a resolution of $\pm$ 10 μm can be achieved. Moreover, it can be expected that using the copper and 316 SS substrates will give a better resolution due to their sharper slopes of pk-pk versus h. These results confirm that the iFDG concept is viable, and the main factor determining precision is the fluid flow relationship.
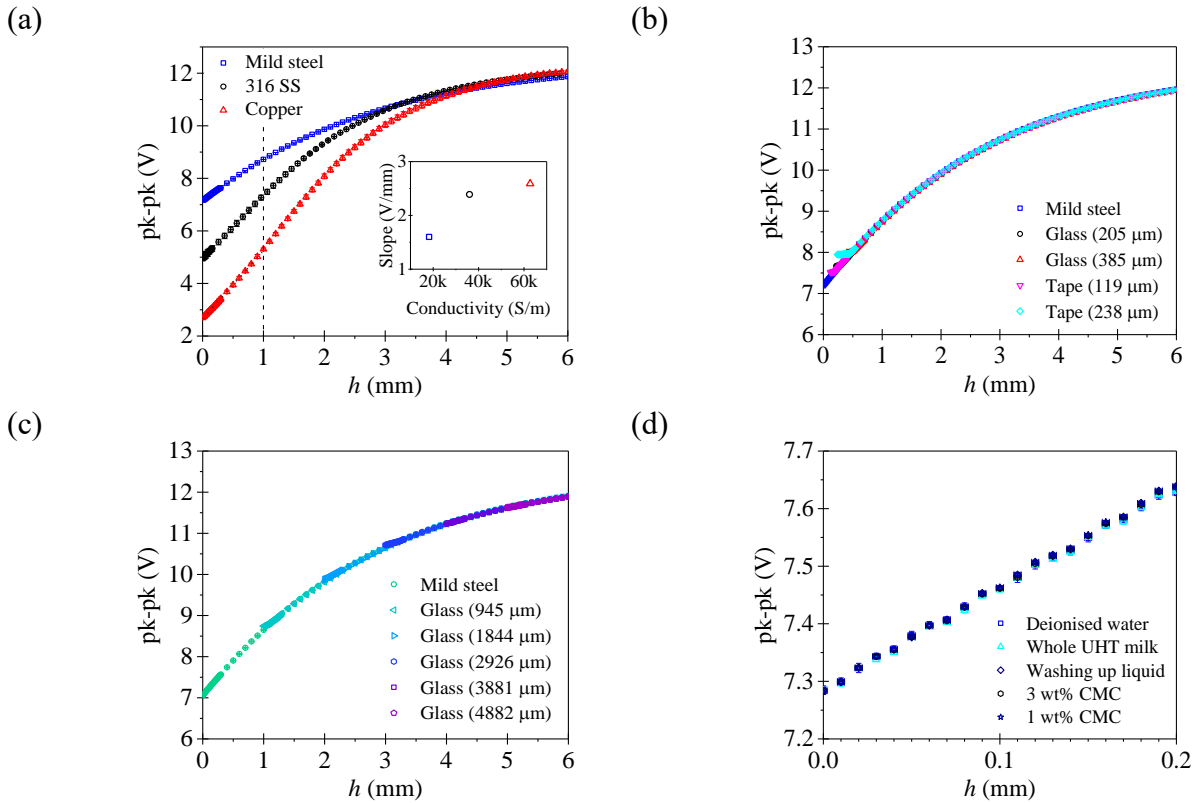
Fig. 4.30. Calibration plots of induction sensor head. (a) Gauging fluid, water; error bars show standard deviation over 10 repeats. Vertical dashed line shows limit of useful range for FDG measurements, $h/d_t = 0.25$ (long dashed line). Data in this region fitted to trend pk-pk = 7.17 + 1.6h (mild steel); 4.96 + 2.39h (316 SS); 2.66 + 2.59h (copper). Inset shows effect of conductivity on slope. (b) Mild steel substrate without and with tapes or glasses submerged in water. (c) Mild steel substrate with different layers of glass slides. (d) Different liquids with mild steel substrate, in the region of h/d_t used for locating the substrate for FDG tests.

Fig. 4.31 presents profiles of discharge coefficient versus dimensionless clearance for Newtonian fluids deionised water, whole UHT milk and washing up liquid at different flow rates. All profiles show a similar trend, with a linear increase of C_d with increasing h_o/d_t at low clearance, followed by approach to an asymptotic value at large h_o/d_t. This behaviour has been reported in previous FDG studies using different configurations. The plateau at large clearance is attributed to disappearance of pressure drop caused by the gap between the nozzle rim and the gauging surface.

In Fig. 4.31(a) and (b), it is evident that there is a difference of C_d value between ejection and suction modes at $h_o/d_t = 0.2{\sim}0.6$, which is attributed to difference of the flow patterns in both modes. This phenomenon has been observed from simulations, investigated by Chew *et al.*

[102] and Ali *et al*. [96]. Fig. 4.31(c) shows a slight difference between two modes. This is because at very low Reynolds number, viscous dissipation dominates, resulting in similar flow patterns and pressure drops. In Fig. 4.31(c), at $h_o/d_t < 0.145$, the profile levels off at low clearance, which is an artefact caused by the limit of the pressure transducer being reached.

The magnitude of the discharge coefficients at the asymptote in Fig. 4.31(a), (b) and (c) are in the order of the employed Reynolds number (deionised water (Re_t 398): 0.74 > UHT milk (Re_t 166): 0.65 > washing up liquid (Re_t 0.022): 0.0135). This behaviour was reported by Tuladhar *et al.* [7]. The values are small at low Re_t because C_d is defined in terms of inertial losses but at small Re_t viscouslosses dominate [79]. Fig. 4.31(a), (b) and (c) show good agreement between CFD predictions and experimental data, indicating that the simulations are valid. Also, Fig. 4.31(b) and (c) confirms that the iFDG device is feasible for use with opaque and viscous liquids, respectively.

(a)

(b)

(c)
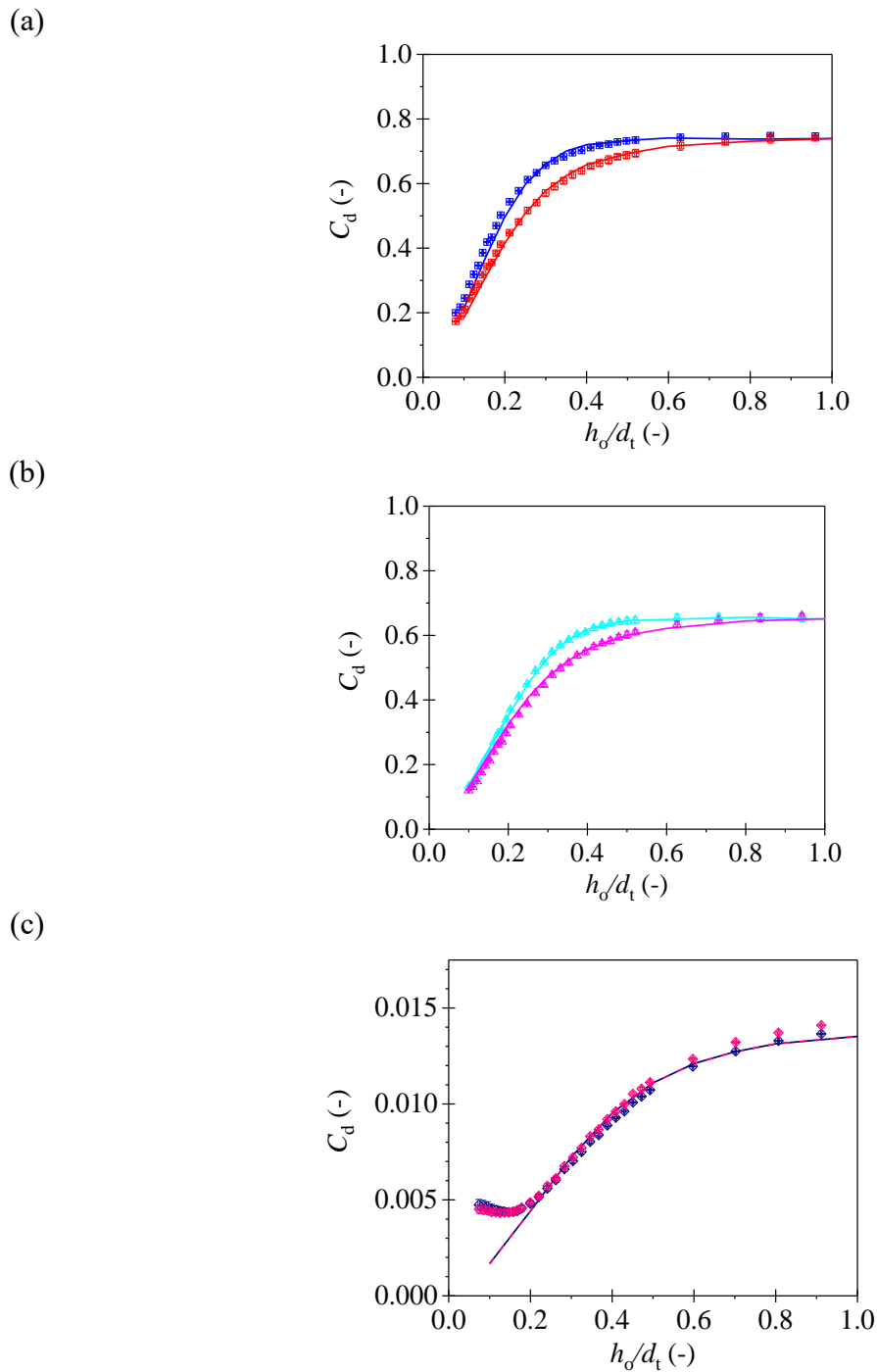
Fig. 4.31. C_d-dimensionless clearance profiles for Newtonian liquids at 20 °C. Lines – simulation; symbols – experimental data: (a) deionized water, $\dot{m}$ = 20 ml/min, Re_t = 398; blue – ejection, red – suction. (b) UHT milk, $\dot{m}$ = 20 ml/min, Re_t = 165.8; cyan – ejection; magenta – suction. (c) washing up liquid at 20 °C, $\dot{m}$ = 1 ml/min, Re_t = 0.022; navy– ejection; pink – suction.

Fig. 4.32 shows calibration plots of C_d against h_o/d_t for the 1wt% and 3 wt% CMC solutions. The operation regions (flow rate) were chosen based on the upper and lower limits of the

pressure transducer. The same trends as other liquids, namely a linear region at lower clearance followed by reaching an asymptote, is evident. By contrast, there are significant differences between ejection and suction modes at higher h_o/d_t, but the profile of the washing up liquid with higher Reynolds number does not exhibit this behaviour.

This could be attributed to the viscoelasticity of the CMC solutions, but the constitutive equations and models did not include viscoelastic behaviours, so that the behaviours cannot be predicted at both concentrations. However, the valuable finding is that the simulation results fits between the experimental suction and ejection data. Moreover, the interesting region in FDG measurements is the linear region (at $h_o/d_t < 0.3$), meaning that the iFDG technique is viable for applications of non-Newtonian liquids.

(a)
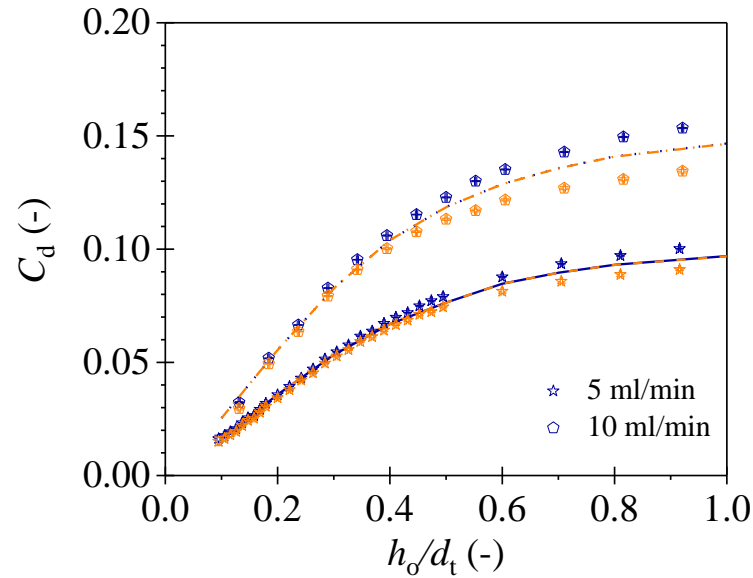
(b)
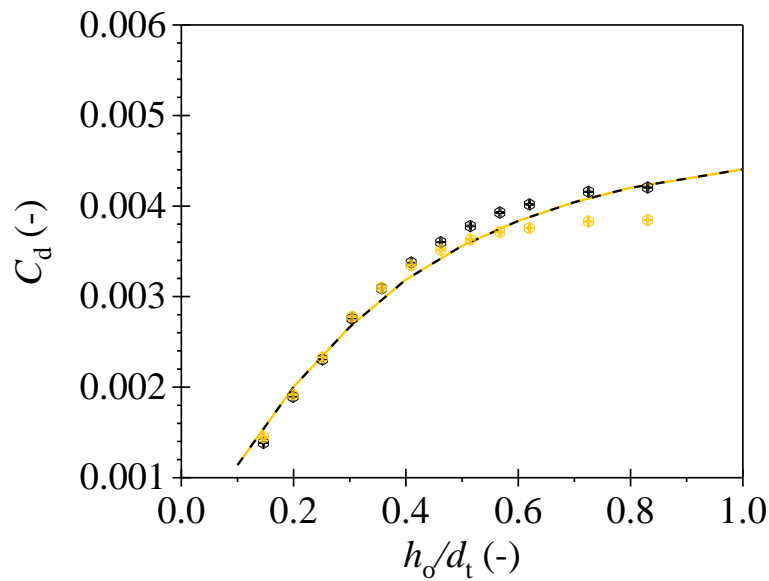
Fig. 4.32. C_d-dimensionless clearance profiles for CMC solutions at 20 °C. Lines – simulation; symbols – experimental data: (a) 1 wt% CMC solution at $\dot{m}$ = 5 and 10 ml/min, Re_t = 1.4 and 3.4, respectively; blue – ejection; orange – suction. (b) 3 wt% CMC solution, $\dot{m}$ = 0.5 ml/min, Re_t = 0.0045. Lines – simulation; Black– ejection; yellow – suction.

Based on the good agreement between the experimental data and simulation results above, the OpenFOAM models can be employed to predict the distribution of shear stress induced by the FDG flow on the gauging surface. The estimated distributions of shear stress over the main region of interest for washing up liquid and 1 wt% CMC solution are plotted in Fig. 4.33(a)

and (b), respectively. The results are compared with the inertial head at the nozzle throat, $\frac{1}{2}\rho U^2$, by calculating a scaled wall shear stress, $\tau_w^* = \tau_w / \frac{1}{2}\rho U^2$, plotted on the right y-axis. There is no noticeable difference between ejection and suction modes, since the flows are in the creeping flow regime at low Re_t. This is also evident from the fact that the τ_w^* values are much larger than the inertial heads.

Even though a significant difference between ejection and suction modes at small clearance has been reported in previous studies, which is not found in this investigation, some similar behaviours can be observed. A peak shear stress peak appears at the inner edge of the nozzle rim, followed by a smooth decay to the outer edge. Also, the wall shear stress decreases with increasing h_o/d_t. The other thing is that CMC is a shear thinning fluid - this does not introduce major difference in the shear stress distributions.
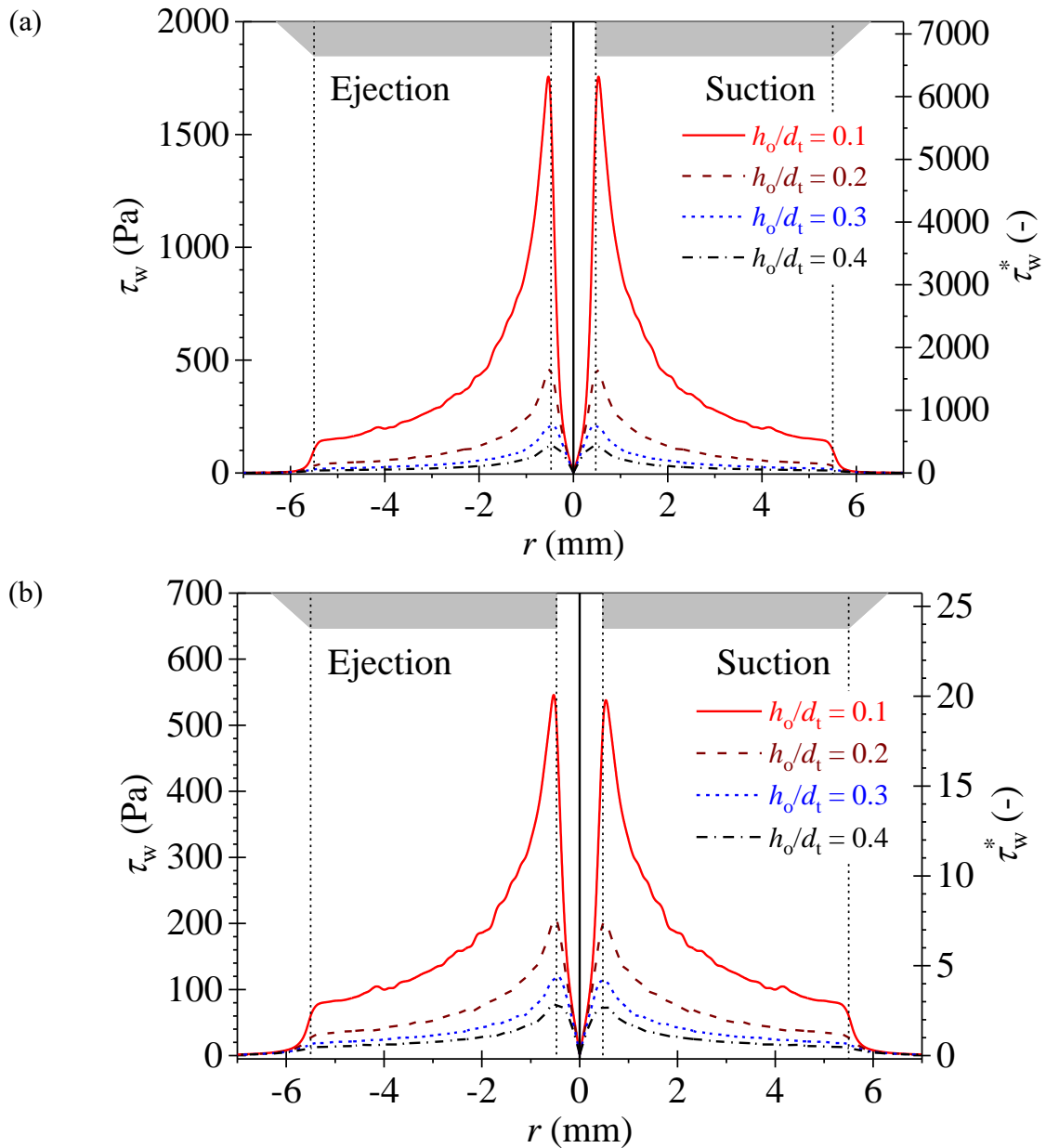
Fig. 4.33. Distribution of shear stress on gauged surface obtained from OpenFOAM simulations for (a) washing up liquid at 20 °C, $\dot{m} = 1$ ml/min, $Re_t = 0.022$, and (b) 1 % CMC at 20 °C, $\dot{m} = 10$ ml/min, $Re_t = 3.4$, for $h_o/d_t = 0.1$ (red); 0.2 (brown); 0.3 (blue); 0.4 (black). Vertical dashed lines and grey shaded pattern indicate the region of the nozzle footprint. Note: $r < 0$ shows results for ejection mode; $r > 0$ suction mode. Second y-axis presents scaled wall shear stress, $\tau_w^* = \tau_w / \frac{1}{2}\rho U^2$, where U is the mean velocity at the nozzle throat.

4.4.4 Measuring the Growth of a Soft Solid Layer

4.4.4.1   Calibration

There are two major steps for iFDG calibration. First of all, the inductive sensor was calibrated by setting a clearance using feeler gauges, and then the nozzle head was moved vertically using the positioner and the peak to peak voltage at each position was recorded to be a voltage-clearance reference. Next, the FDG part was calibrated by measuring the pressure drop at different locations to generate a C_d-h_o/d_t reference.

4.4.4.2   Materials and methods

An ice growth experiment was performed using skimmed UHT milk (Sainsbury's Skimmed Long Life Milk) as gauging liquid. The hardness of the ice produced from the skimmed milk was between that of whole milk (softer) and water (harder), which sewed to demonstrate iFDG's capacity. The temperature of the cooling bath was set to be $-10\,°C$ or $-15\,°C$.

During iFDG measurements, the substrate was submerged and mounted under the nozzle. The nozzle head was then moved towards to the surface at a certain clearance, and then the peak to peak voltage was recorded and analysed based on the pk-pk-h_o reference to calculate h_o. The gauging liquid was ejected and withdrawn for 5 s to generate a steady pressure drop, and the Δp was used to estimate h using the C_d-h_o/d_t reference. Finally, the ice layer thickness could be predicted from ($\delta = h_o - h$). When the measured pressure drop surpassed the upper limit of the sensitive region (1000 Pa), the nozzle moved away 0.3 mm from the surface. This procedure was set in the program for preventing the layer to undergo deformation or the nozzle head to be stuck in the ice. The induced shear stress exerted on the layer surface became large, and could cause deformation, as the FDG head was close to the surface. If the ice growth rate was fast, ice would grow to touch and then cover the nozzle head. By contrast, the nozzle moved 0.1 mm towards the substrate when the pressure drop was lower than 300 Pa.

4.4.4.3   Results and discussion

Tuladhar *et al.* [90] demonstrated a FDG application for measuring the rapid growth of an ice film on a cold surface in a duct flow. This experiment was an easy and simple way to confirm the feasibility of thickness and swelling measurements for soft solid layers using FDG. It is used here to show the benefits from the inductive senor without an extra pre-calibration.

In this study, the substrate was cooled by pumping coolant through the chilling block from the cooling bath but without heating in bulk, so the bulk temperature decreased gradually and finally reached an equilibrium temperature, which can be considered as a batch process. A sub-cooling condition is required for ice nucleation and ice crystallisation, so that before nucleation happened, the temperature on the substrate surface was lower than the freezing temperature of ice. Initially, deionised water was employed as gauging liquid to produce an ice layer; however, the growth rate was too fast to be measured and ice blocked the nozzle throat. As a result, skimmed UHT milk was chosen for the freezing experiments because of its lower ice growth rate. Its opaque characteristic can also be a challenge for the iFDG demonstration. Furthermore, whole milk was tested, but the ice grew very slowly in the case and the rate was slower than the removal rate of FDG. In this case, no noticeable thickness change could be observed.

An ice growth test was carried out by controlling the temperature of the cooling bath from 0 to −10 °C, and the result is shown in Fig. 4.34(a). The three temperatures decrease steadily until the surface temperature approaches −3.3 °C, at which point ice nucleation started and the temperature increases slightly (labelled N) due to recalescence. The ice growth rate is nearly constant, at about 0.01 mm/s: once the ice thickness reaches around 2.52 mm (labelled C) and starts to decrease. This is because the ice contacted part of the nozzle head, but did not block the nozzle throat. The gauging liquid still could be ejected and withdrawn through the throat, but the measured pressure drop was not for an asymmetric geometry and could not be trusted. The phenomenon was confirmed by draining the tank, and observing that ice had formed around the nozzle head.

Fig. 4.34(b) shows a thickness measurement after an ice layer had formed. It is evident that the ice growth rate decreases and the thickness approaches a plateau of about 6.2 mm over around 1800 s. The plateau means that the ice stopped to grow or a steady-state condition was reached (ice growth rate = removal rate by gauging flow). At $t \sim 1500$ s, a thickness jump is observed (labelled S), caused by non-uniform ice growth mentioned above.

(a)

(b)
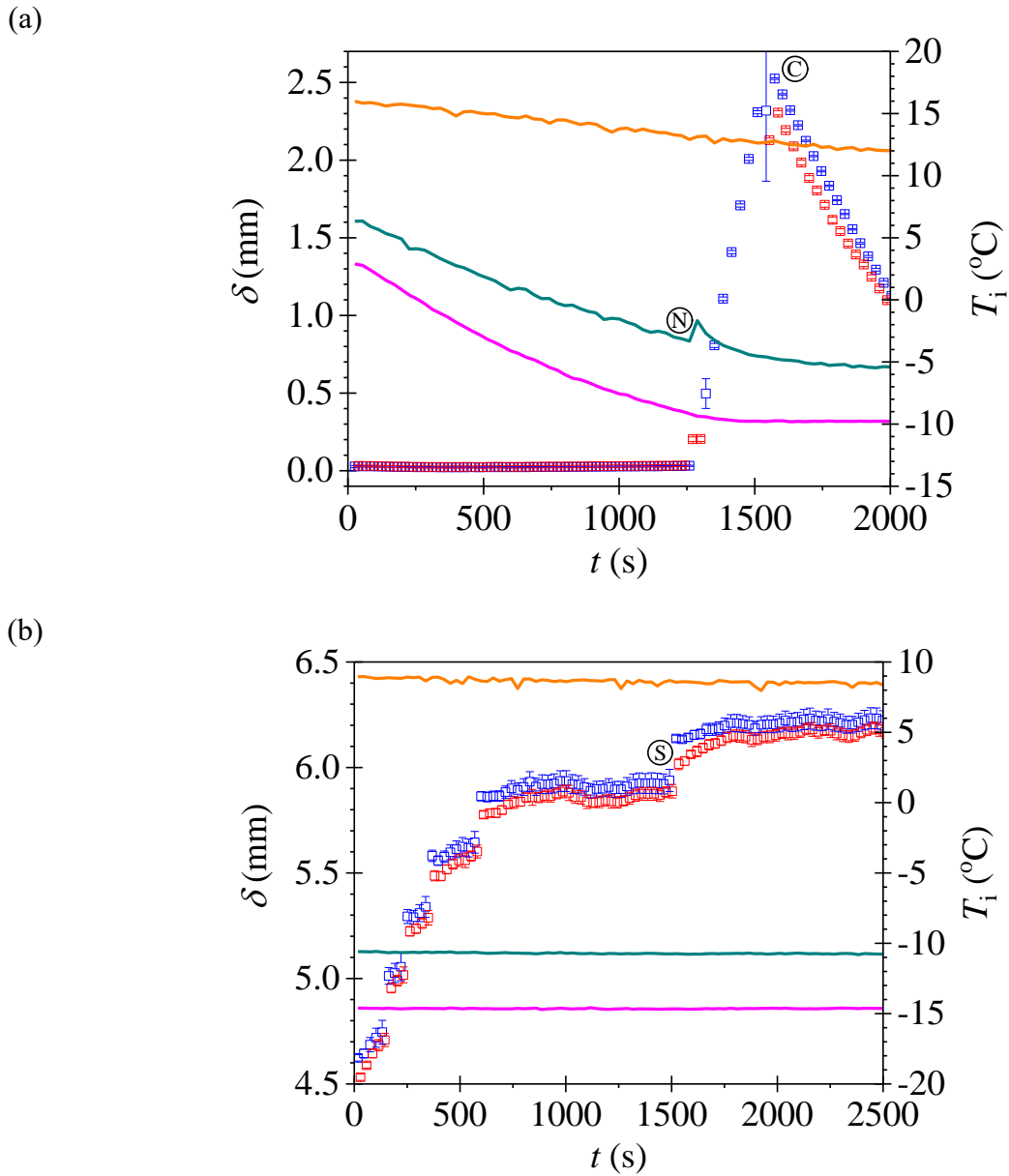
Fig. 4.34. Deposit thickness and temperature profiles for ice growth from UHT skimmed milk on a mild steel plate. (a) Onset of ice growth, coolant temperature −10 °C. Label N indicates nucleation event, C indicates contact with nozzle; (b) following initial ice formation, coolant temperature −15 °C. S indicates a sudden restart in ice growth. Symbols – FDG thickness measurement; lines – temperatures. Colors: blue – ejection; red – suction; orange – bulk; pink – cooling bath; dark cyan – substrate.

4.5 Conclusions

In this study, the existing ZFDG device was calibrated and the calibration plot shows similar behaviour to previous studies using different FDG configurations. A CFD model was created in OpenFOAM and compared with the experimental results. Good agreement has been observed, indicating that this simulation can be employed to describe the ZFDG flow patterns.

The ability of the SiDG device to monitor the early stage as well as long term behaviour of swelling for soft solid layers submerged in a liquid environment has been demonstrated. Swelling of gelatin, PVAc and CMS layers were measured at various pH, and these results show that all materials experienced an initial hydration over a short period. After the hydration stage, swelling of gelatin was controlled by Fickian diffusion. A similar tread can be observed on the swelling profile of PVAc at pH < 11; however, at pH ≥ 11, the relaxation control dominated due to the fact that hydrolysis and ionisation happened. On the other hand, cracks on a CMS sample surface had a significant impact on the measurements using SiDG. A 3-dimensional CFD model with cracks beneath the nozzle rim was solved and the results show 8% and 3% measurement errors for ejection and suction modes due to the presence of cracks, respectively.

The iFDG concept, which is to integrate an alternative method for locating the substrate, has been demonstrated. An inductive proximity sensor was incorporate with the FDG nozzle. A linear relationship between the measured peak to peak voltage and the clearance was obtained and employed to be a reference for the nozzle location. Mild steel, 316 SS and pure copper substrates were tested, and the results showed that the trend of the pk-pk voltage against the clearance changed with substrates' conductivities. By contrast, non-metallic layers including PVC tapes and glass slides did not have influence on the trend. The iFDG device was calibrated with deionised water, UHT milk (opaque), viscous washing up liquid and non-Newtonian CMC solutions, at different throat Reynolds numbers. CFD simulations were also conducted and showed good agreement with the experimental results. An ice growth test using the iFDG was performed, demonstrating the feasibility of iFDG measurements.

The iFDG concept was investigated after the SiDG concept. There is no fundamental reason preventing IPS being incorporated in the SiDG apparatus, further extending the device

reasonably. The iFDG concept brings with its scope for commercial exploitation, as the precision of the measurements is now independent of the accuracy of the linear drive.

Chapter 5   Multi-phase Modelling in Cleaning Applications

5.1   Introduction

The deformation of soft deposit layers has a significant impact on the thickness measurements using FDG [28]. Some soft solid materials are weak because they contain a lot of liquid. During FDG operations, shear and normal stresses are induced by the gauging liquid flow on the surface being gauged, which can result in layer deformation and cause difficulties in measurements. A study of the deformation of a soft solid layer caused by FDG flow is therefore required. In earlier chapters, the substrate has been set to be a rigid plane. Ultimately, the development of a simulation tool for modelling layer deformation would allow the soft layer's rheological properties to be evaluated. This requires a coupled model, where the flow of gauging liquid determines the shape of the layer and vice versa. This has not been considered previously. Viscoplastic layers are a good candidate material for studying coupled deformation, since (i) several fouling deposits exhibit viscoplastic behaviour during cleaning, namely deformation when the imposed shear stress is greater than its yield stress, and (ii) once the FDG flow stops the layer will remain in its deformed state, facilitating experimental investigation.

The interaction between viscoplastic layers and FDG flows are also related to flows in cleaning operations in the food and pharmaceutical sectors. For instance, in multiple-product factories, the process equipment needs to be cleaned frequently. Liquid jets - using water, solvents or other cleaning agents - are employed to remove layers of deposited material from equipment surfaces [63, 177]. The rate of removal of the deposit layer will depend on the film hydrodynamics and the layer deformation. The simulation tool created for coupled layers with FDG flow will be applied to the modelling of cleaning of a viscoplastic layer using an impinging water jet, which is an exploratory study for assessing the applicability of the model.

5.2 Coupled Deformation of Viscoplastic Layers and FDG Flow

5.2.1 Materials and Methods

The ZFDG device discussed in section 4.2 was employed for this study. The commercial petroleum jelly (Atom Scientific Ltd, GPS5220) was selected as the test soil material, which was the same batch as the petroleum jelly tested in section 3.2.4. It is hydrophobic and insoluble, and exhibits viscoplasticity at room temperature. This means that its properties are stable (do not change with time of contact with water, the gauging fluid). The material is used in the pharmaceutical sector as a component of ointments, where it poses cleaning problems. For these reasons, it is a suitable candidate for a model study.

The petroleum jelly was spread across square 316 SS substrates (50×50 mm^2, thickness about 1.97 mm) using a spreader tool to a depth of 2 ± 0.05 mm [128]. After preparation, samples were scanned by a confocal thickness sensor (CTS) (Micro-epsilon IFC2461 controller paired with an IFS2405 sensor) integrated with an automated x-y stage (8MTF-75LS05 and 8SMC4-USB-B9-2, STANDA), to measure the initial topography. The sample was then subject to a ZFDG gauging flow (water, 20 °C, flow rate: 20 ml/min) for a given clearance and flow rate (and direction) for a set time. A range of conditions were investigated. The samples were then exposed to air for at least one day after testing to allow the surface to dry, then scanned again using the CTS in order to determine any change in the layer topography.

5.2.2 Model Formulation

The ZFDG system described in section 4.2.2 was used in the simulation of deformation of soft layers. The geometry and dimensions are depicted in Fig. 5.1. The tank diameter and length were shortened to 10 mm and 12 mm, respectively, to reduce the calculation time, but the nozzle length remained at 60 mm to capture recirculation in the nozzle in suction mode.

In order to compare with experiments, a 2-dimensional, transient and cylindrically-symmetric ZFDG model was constructed with water as the gauging liquid. A petroleum jelly layer was created under the nozzle with a thickness 2 mm. The calculations were performed using OpenFOAM version 4.0.
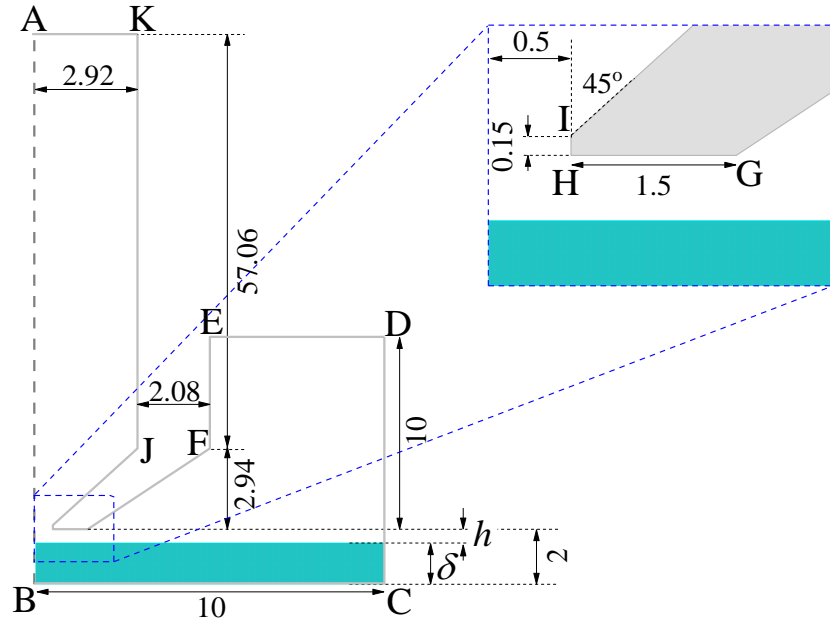
Fig. 5.1. Geometry of coupled deformation of petroleum jelly layer and FDG simulation. All dimensions in mm.

5.2.2.1 *Governing equations*

The OpenFOAM solver interFoam is chosen for this two-phase (water and petroleum jelly) system, employing the VOF method. In the VOF approach, the entire domain is described by a momentum conservation equation using average density and viscosity, and for each grid cell. The local volume fraction of petroleum jelly phase (PJ) is α and the volume fraction of water phase is $(1 - \alpha)$, with $0 \leq \alpha \leq 1$. The average density and viscosity in each cell are given by simple laws of mixtures.

$$\rho = \rho_{\text{PJ}}\alpha + \rho_{\text{water}}(1 - \alpha) \tag{5.1}$$

$$\mu = \mu_{\text{PJ}}\alpha + \mu_{\text{water}}(1 - \alpha) \tag{5.2}$$

The governing equations are the momentum equation;

$$\rho\left(\frac{\partial \mathbf{v}}{\partial t} + \mathbf{v} \cdot \nabla\mathbf{v}\right) = -\nabla p + \mu\nabla^2\mathbf{v} + \rho\mathbf{g} \tag{5.3}$$

and the mass continuity equation, written in terms of α.

163

$$\frac{\partial \alpha}{\partial t} + \nabla \cdot (\mathbf{v}\alpha) = 0 \tag{5.4}$$

The fluid properties are summarised in Table 5.1.

Table 5.1. Fluid properties (subscripts: water – water, PJ – petroleum jelly) at 20 °C [98]. Rheology data for petroleum jelly provided by PhD student Rubens Rosario Fernandes.

Parameter	Value
μ_{water}	1.123 mPa s
ρ_{water}	997.3 kg/s
$\sigma_{water\text{-}PJ}{}^{a}$	0.07 N/m
μ_{PJ}	$12.4 + 249/\dot{\gamma}[1 - \exp(-8869\dot{\gamma})]$ Pa s
ρ_{PJ}	812 kg/m^3

^{a} σ is the surface tension [140].

In Chapter 3, the Bingham-Papanastasiou model (Regularised Bingham model, RBM) was shown to describe the petroleum jelly's viscoplastic behaviour better than the bi-viscosity model. In this work, the RBM is used, with the rheological parameters (for the same batch) reported in section 3.2.4. The boundary conditions for this simulation are listed in Table 5.2.

There were some challenges in solving the model. A minimum mesh size of less than 30 μm was required for specifying the initial interface between water and petroleum jelly when the clearance was 0.03 mm. A 3-D model could not be constructed, since the computer could not support the number of these mesh elements required. Moreover, a 2-D axisymmetric geometry (wedge-shaped in OpenFOAM) with a dynamic mesh algorithm to refine the mesh could not be employed, because the complex FDG geometry required a non-uniform mesh, which was not accepted by the algorithm. The dynamic mesh algorithm will be introduced in next section.

In OpenFOAM, in order to simulate a 2-D axisymmetric condition, a 3D wedge-shaped mesh with an angle of 2.5°, which is a portion of the simulated cylinder, needs to be created.

A wedge-shaped geometry of 167600 structured mesh elements was generated initially with a minimum mesh size of 1 μm around and beneath the nozzle rim for capturing the deformation of petroleum jelly, using OpenFOAM's function 'blockMesh'. About 74000 mesh elements were used for petroleum jelly and the other elements were initially occupied by water. The model was calculated using the SuperServer 1027R-WRF4+ mentioned in section 4.2.2. The computational time required for solving 0.1 s was about 3 days.

Table 5.2 Boundary conditions in the CFD model (v_r and v_z are the radial and axial velocities, respectively)

Boundary	Description	Boundary condition of momentum	Boundary condition for species
AB	Axisymmetric	$\frac{\partial v_r}{\partial r} = 0, \frac{\partial v_z}{\partial r} = 0$ and $\frac{\partial p}{\partial r} = 0$	$\frac{\partial \alpha}{\partial r} = 0$
AK	Inlet/outlet	$v_{ejection} = \dfrac{8\dot{m}}{\rho \pi d_i^2}\left(1 - \dfrac{4r^2}{d_i^2}\right)$ [a] $v_{suction} = \dfrac{-8\dot{m}}{\rho \pi d_i^2}\left(1 - \dfrac{4r^2}{d_i^2}\right)$	$\alpha = 1$
BC, CD, EF, FG, GH, HI, IJ, and JK	Wall	$v_r = 0$ and $v_z = 0$	$\nabla \alpha = 0$
DE	Open boundary	$p = 0$	$\alpha = 1$

[a] $v_{ejection}$ and $v_{suction}$ are the velocities for ejection mode and suction mode, respectively. Fully developed laminar flow is imposed at the inlet/outlet. $\dot{m}$ is the mass flow rate delivered by the syringe pump. r is radial distance and d_i is the internal diameter of the nozzle tube.

5.2.3 Results and Discussion

Deformation tests were performed using the ZFDG apparatus in both ejection and suction modes at two clearances (h_o/d_t = 0.1 mm and 0.03 mm) with water at 20 ºC, $\dot{m}$ = 20 ml/min and durations of 1, 1.5, 2 and 3 s. The maximum shear stress at h_o/d_t = 0.03 obtained from simulations is around 800 Pa, higher than the petroleum jelly's yield stress, and the shear stress imposed on the layer under the nozzle rim is everywhere greater than the yield stress. For reference, the predicted maximum shear stress for h_o/d_t = 0.1 is lower than the yield stress.

The reproducibility of layer topography and pressure drop at h_o/d_t = 0.03 was low, and more than one hundred experiments were conducted for each mode. There were several factors which would affect the experimental reproducibility, such as the roughness and homogeneity of the petroleum jelly, resolution of the z-axis positioner, and the mounting platform not being completely level.

There were also some technical issues which limited the ZFDG tests. A stable and given pressure drop could not be created when the syringe pump was operated for less than 1 s due to tubing expansion, which is discussed below. Moreover, the response from the syringe pump was often delayed when a command was sent from the computer, resulting in shorter ejection/suction times than those set.

The pressure drop measured across the nozzle in suction mode at h_o/d_t = 0.1 with and without the petroleum jelly present are plotted in Fig. 5.2. In Fig. 5.2(a), the pressure drop initially decreases to a plateau value of around −1100 Pa, and stays at this value until the end of the flow, then rises to 0 Pa with some overshoot. When petroleum jelly is present (Fig. 5.2(b)), similar trends are seen, but in reaching the plateau and at the cessation of flow ($\Delta P \rightarrow 0$ Pa), the profiles are smooth with no overshoot. This is attributed to the petroleum jelly having finite elasticity (Fig. 3.4(a)) and therefore some relaxation at the cessation of flow.

(a)　　　　　　　　　　　　　　　　　(b)
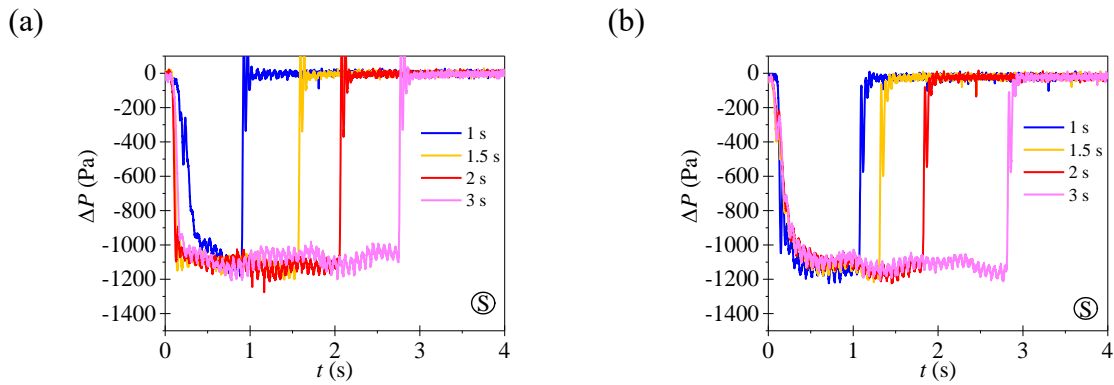
Fig. 5.2. Evolution of pressure drop across the nozzle (a) without and (b) with petroleum jelly. Suction mode, $\dot{m} = 20$ ml/min, $h_o/d_t = 0.1$.

For both cases, there is an initial period for the flow to be established (around 150 ms), which is attributed to compliance in the apparatus (tubing). The simulations did not replicate this.

Fig. 5.3 shows the pressure drop in ejection mode at $h_o/d_t = 0.1$ at the same flow rate with and without petroleum jelly. In Fig. 5.3(a), the profiles all rise rapidly to approximately 700 Pa, with some overshoots, followed by a steady value which persists until flow is stopped, when the pressure return to 0 Pa, again with some overshoot. When the layer is present (Fig. 5.3(b)), there is no overshoot, as with suction. However, when the flow is stopped and the pressure falls to 0 Pa, there is some overshoot in both cases. This is due to a hydraulic shock when the syringe pump is stopped.

Apart from the 'overshoot' and pressures reaching a plateau smoothly, there is no significant difference in the data for a clean plate and one coated in petroleum jelly. No measureable deformation appears to be occurring for $h_o/d_t = 0.1$ with $\dot{m} = 20$ ml/min.
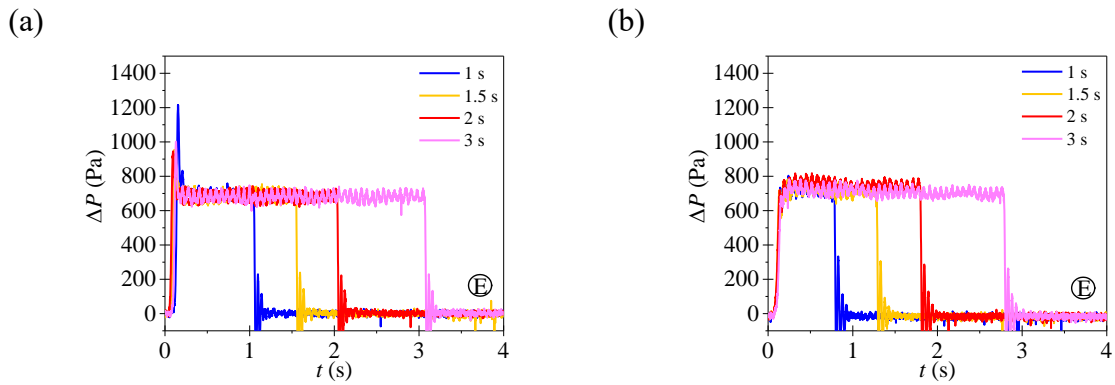
Fig. 5.3. Evolution of pressure drop across the nozzle (a) without and (b) with petroleum jelly. Ejection mode, $\dot{m} = 20$ ml/min, $h_o/d_t = 0.1$.

Fig. 5.4 shows the pressure profiles obtained in suction mode at $h_o/d_t = 0.03$ and the same flow rate: the stresses generated on the jelly layer are expected to be greater. The measurement limit of the pressure transducer is from approximately -8000 Pa to 9000 Pa. In the absence of petroleum jelly, the pressure decreases slowly and exceeds the measurement limit. After the cessation of flow, the pressure increases gradually to 0 Pa, which is different from the cases at larger clearances. A possible explanation for this observation is that the water pressure inside the nozzle caused the plastic tubing connecting the nozzle tube to the syringe to contract during suction. After the flow stopped, the plastic tubing returned to its original shape as water flowed into the tubing, extending the flow period for a few tenths of seconds.
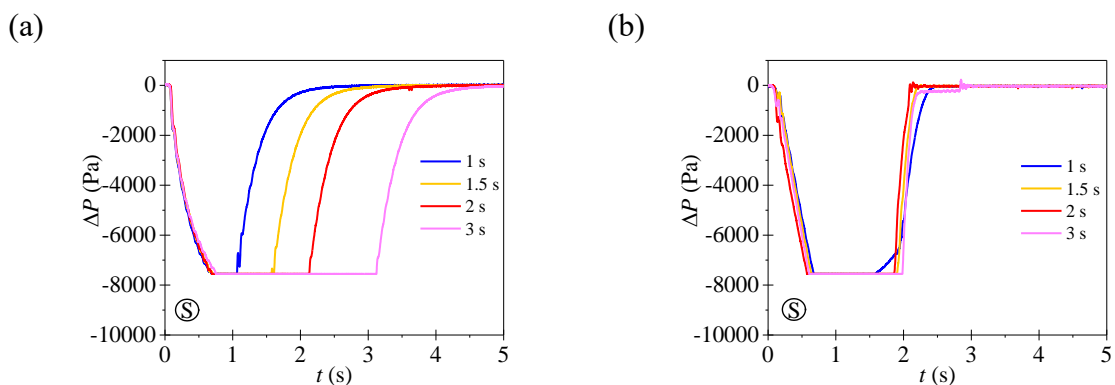
Fig. 5.4. Evolution of pressure drop across the nozzle (a) without and (b) with petroleum jelly. Suction mode, $\dot{m} = 20$ ml/min, $h_o/d_t = 0.03$.

The data in Fig. 5.4(b) differ considerably from Fig. 5.4(a). Whilst the way in which the measurement limit of -8 kPa is initially exceeded shows some similarity with Fig. 5.4(a), the

168

pressure recovery behaviour at all durations occurs at a similar time. Firstly, the data for 1 s appears anomalous since the pressure variation extends over 2 s. This is due to the nozzle 'sucking up' petroleum jelly, blocking it. The blockage remained after flow was stopped at $t =$ 1 s, but then slowly cleared away resulting in the rise in pressure seen at $t \sim 1.5$ s. Secondly, the data for $t = 1.5$ s shows similar behaviour to that for $t = 1$ s, due to the blocking effect. Thirdly, the data for $t = 2$ s shows significant difference to that for the clean plate. This is due to the formation of a 'cleaning crater', discussed further, which results in a sharp increase in h_o/d_t as material is removed that, in turn, lowers ΔP. The same behaviour occurs with the 3 s test: after 2 s the gauging flow has created a crater, which is why these data appear similar to those for 2 s despite a longer period of flow.

The effect of tubing shrinkage was investigated by using different length silicon rubber tubes at the same operating condition. The results are shown in Fig. 5.5(a). The pressure with a 37 cm tube increases more quickly than that with a 75 cm tube at the end of a test. This is because the volume of a 75 cm tube is larger, and needs longer time to recover to the original shape. Long tubes are not recommended for ZFDG operations: stiffened or metal tubing should be used to eliminate the tubing effect.
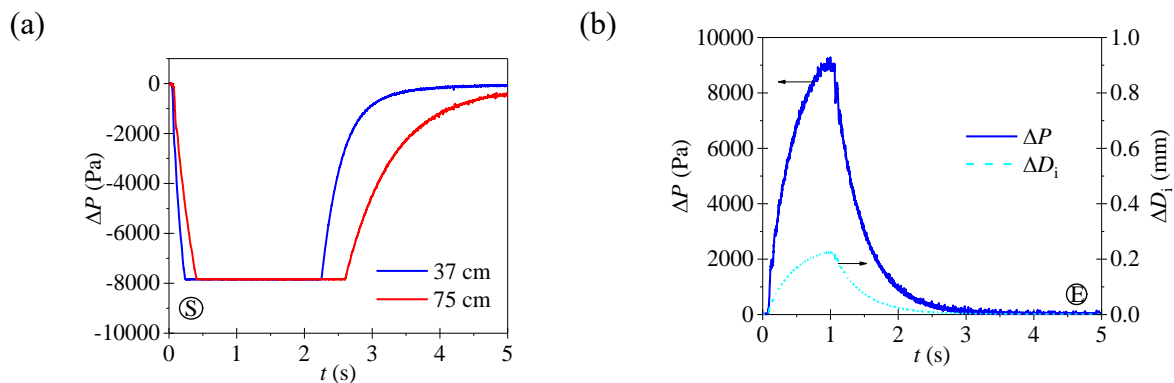
Fig. 5.5. (a) Evolution of pressure drop across the nozzle without petroleum jelly using 37 cm and 75 cm plastic tubes for a duration of 2 s in suction mode. (b) Ballooning effect using a 37 cm silicon rubber tube with 3/8 inch internal diameter, D_i for a duration of 1 s in ejection mode. $\dot{m} = 20$ ml/min, $h_o/d_t = 0.03$.

In addition to the effect from tubing shrinkage, the ballooning effect at the beginning of the test is important. Tubing ballooning often occurs in drilling and well completions, where the tubing expands radially and shortens due to the Poisson ratio effect when pressure is applied to

the inside of the tube [178]. Fig. 5.5(b) shows the evolution of pressure drop and estimated internal diameter change, ΔD_i, given by [179]

$$\Delta D_i = \frac{D_i^2 p}{4(D_o^2 - D_i^2)E} [(1 - v)D_i^2 + (1 + v)D_o^2] \tag{5.5}$$

where D_i and D_o are the internal and external diameters of silicon rubber tube, respectively. E is the modulus of elasticity and v is the Poisson's ratio.

The tube swelled while creating the pressure drop (filling the tube). At cessation of the syringe pump, the pressure and diameter recovered. Moreover, the operation took approximately 1 s to create the pressure drop, indicating that this ZFDG unit cannot reach steady operation within 1 s.

Fig. 5.6(a) shows that in ejection mode, the pressure drop without petroleum jelly decays steadily after the cessation of operation, and the length of the decay is independent of the test duration (see Fig. 5.6(c)). This behaviour results from release of pressure from the tubing mentioned above. By contrast, in the absence of petroleum jelly, the pressure increases over the first second and reaches a plateau of about 9000 Pa, which is the transducer limit. When flow stopped, it declined slowly to 0 Pa.

With petroleum jelly present, the pressure drop decreases immediately after reaching a peak of about 9000 Pa, and returns to a plateau value of around 220 Pa. This is because at this clearance, the shear stress induced by FDG flow exceeds the petroleum jelly's yield stress, and the jelly layer deforms rapidly to a new shape where the shear stress is at or lower than its yield stress. After deformation, the new topography still results in a pressure drop across the nozzle. The pressure drop is smaller because the clearance has increased from $h = 0.03$ mm to some value h_{new}, where $h_{new} \leq 1.05$ mm. Thereafter, the pressure remained at this new value until the cessation of flow. All deformation occurred within 1 s.

These $\Delta P(t)$ profiles all indicate that there is a machine-related timescale involved in starting the FDG flow (due to software activation and tubing compliance).
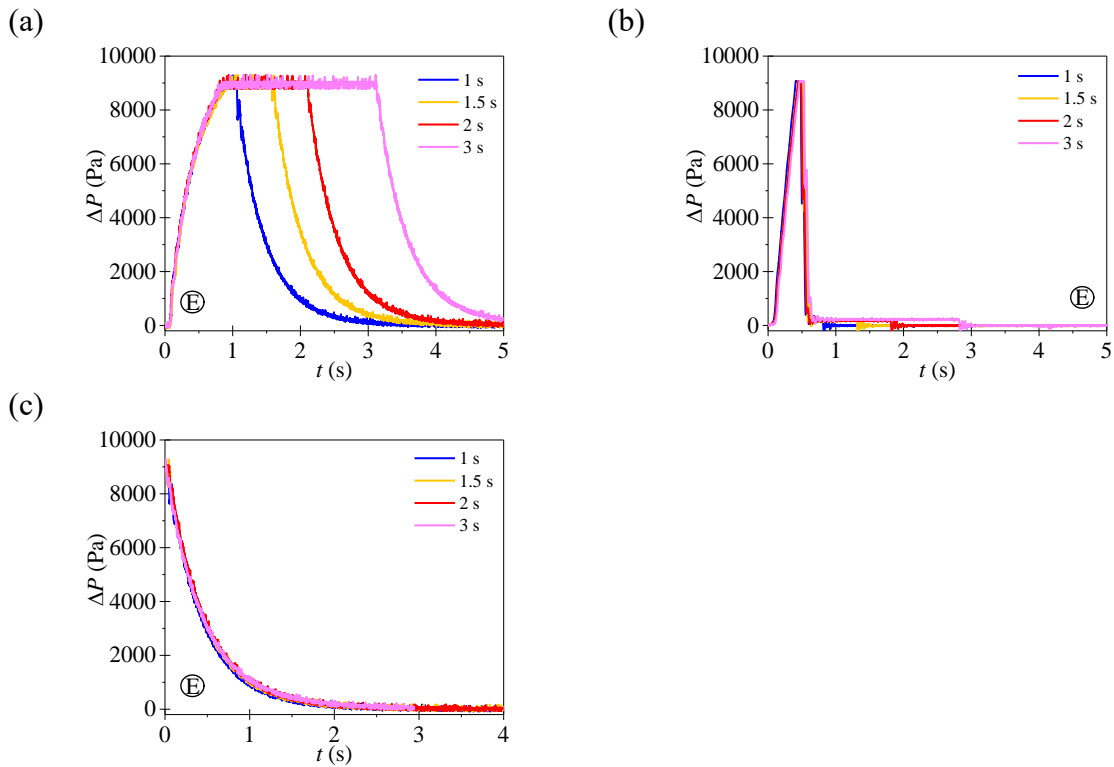
Fig. 5.6. Evolution of pressure drop across the nozzle (a) without and (b) with petroleum jelly; (c) the pressure decay against adjusted time, without petroleum jelly. Ejection mode, $\dot{m} = 20$ ml/min, $h_o/d_t = 0.03$.

5.2.3.1   CFD Simulations

The experimental results have shown that a test with a duration of less than 1 s could not be carried out reproducibly. At a small clearance ($h_o/d_t = 0.03$) in ejection mode, all deformation occurred within 1 s. Moreover, the crater shapes in ejection mode were at a steady-state condition, because the samples were taken out from the liquid environment and then scanned by the CTS after the event. These indicate that an alternative method is needed to study deformation occurring within the first 1 s.

Fig. 5.7 shows the topography of the layer measured by the CTS and those taken from simulations for suction mode FDG with $h_o/d_t = 0.1$ and $\dot{m} = 20$ ml/min at $t = 0.5$ s. Also plotted is the distribution of shear stress on the layer surface for the case with petroleum jelly. All the CTS topographies are nearly flat. The resolution of the CTS is 1 nm, and the measured roughness of the petroleum jelly is ± 0.05 mm. The variation is due to the natural variability in spreading the jelly (which is a dense suspension). The simulations show the same topography,

indicating that the petroleum jelly did not experience irreversible deformation during FDG treatment; there is good agreement between experiments and modelling. The maximum shear stress with these conditions is about 70 Pa, which is lower than the measured yield stress of the petroleum jelly (280 Pa) so plastic deformation is not expected.
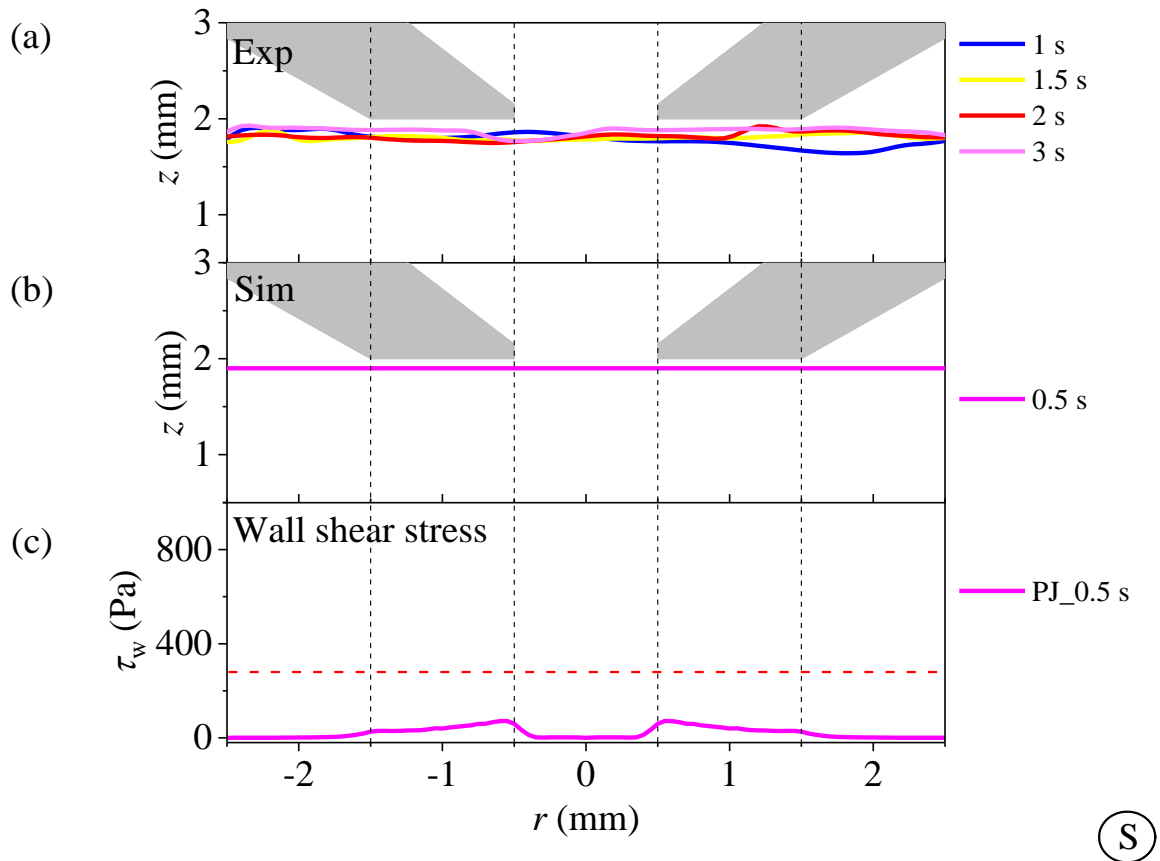
Fig. 5.7. Topography of the layer after gauging in suction mode, with $\dot{m} = 20$ ml/min at h_o/d_t = 0.1. (a) CTS measurements, (b) simulation results, (c) distribution of shear stress on soil surface. Vertical dashed lines and grey shape show nozzle region. Legend shows time of exposure. Red dashed line in (c) denotes yield stress.

Similarly, comparing ejection mode data with simulation predictions for the same values of h_o/d_t and $\dot{m}$, there is no observable deformation in either the experimental data or simulations, showing that the layer did not experience erosion during FDG.

Fig. 5.8 shows the results for a case where the maximum shear stress imposed by the gauging flow exceeded the jelly yield stress (Fig. 5.8(c) w/o PJ). The CTS measurements show small

peaks in the centre of the sample after 1 s and 1.5 s, indicating that the layer is being drawn into the nozzle. Petroleum jelly was found inside the nozzle tube after the experiments. Craters are evident after 2 s and 3 s. The clearance changed from the initial 0.03 mm to the maximum 1.05 mm. An obvious change between 1.5 and 2 s, from central hillocks to craters, suggests suction-induced breakage which was seen in the CFD simulations.

Fig. 5.8(b) shows that petroleum jelly was withdrawn into the nozzle continuously during FDG treatment, and withdrawal was then interrupted due to breakage. The breakage in the simulation could attributed to the non-uniform mesh size. The mesh size in the nozzle tube was larger than in the region beneath the nozzle rim to reduce the computational time. However, in the experiments, the breakage phenomenon could result from either the non-homogeneity of petroleum jelly or bubbles trapped inside the layer. Both conditions made the layer weak and be broken off easily. After interruption (breakage), the induced stress was not high enough to withdraw the material as well as to make the layer change again. The topographies thus remain at the condition of interruption. These larger craters result in a smaller pressure drop across the nozzle. These data show reasonable agreement between the CTS measurements and simulations. Time scales are considered below.

The predicted shear stresses at different times in Fig. 5.8(c) were smaller than the yield stress. In order to study the stress required to cause deformation, the von Mises stress (von Mises criterion) was employed, which is used to determine yielding of ductile materials [180]. The material will start yielding as the von Mises stress reaches its yield strength which is related to the shear yield stress by $\sqrt{3}\,\tau_y$. The stress is a scalar value and can be calculated from

$$\sigma_v = \sqrt{\frac{(\sigma_{11} - \sigma_{22})^2 + (\sigma_{22} - \sigma_{33})^2 + (\sigma_{33} - \sigma_{11})^2 + 6(\sigma_{12}^2 + \sigma_{23}^2 + \sigma_{31}^2)}{2}} \quad (5.6)$$

where σ_{ij} is a term in the Cauchy stress tensor, all of which are calculated by OpenFOAM.

The distributions of von Mises stress, σ_v, are plotted in Fig. 5.8(d), showing that at $t \leq 0.05$ s, the σ_v values at the centre are higher than $\sqrt{3}\,\tau_y$, indicating that the material was yielding and pulled up into the nozzle. The results also show that the upper normal force dominated while being withdrawn. By contrast, at $t \sim 0.05$ s and beyond, σ_v is below $\sqrt{3}\,\tau_y$, meaning that the layer stopped deforming.

173

Fig. 5.9 compares the evolutions of pressure drop between the experiments and simulation. The predicted timescale and pressure drop are shorter and higher than the experimental values, respectively. It is thought to be attributed to the difference between the experiment and the numerical simulation. From the numerical points of view, at the beginning of calculation, the variables are tested to match the governing equations from the initial condition. However, the inlet was specified to the desired value initially, which was different from other parts in the calculated domain. This caused numerical issues and high pressure. By contrast, although the syringe pump reached the set speed rapidly in the experiment, compared to the timescale of simulation, it is slower. The ballooning effect discussed above also delayed the operation about 1 s. Furthermore, the predicted pressure drop exceeded the measurement limit (-8 kPa), which increases difficulty of comparison between the experimental and simulation results. At $t > 0.1$ s, the predicted pressure drop plummeted to an asymptotic value (about 400 Pa). The value is higher than the experimental result at $t = 3$ s due to the difference of topography.
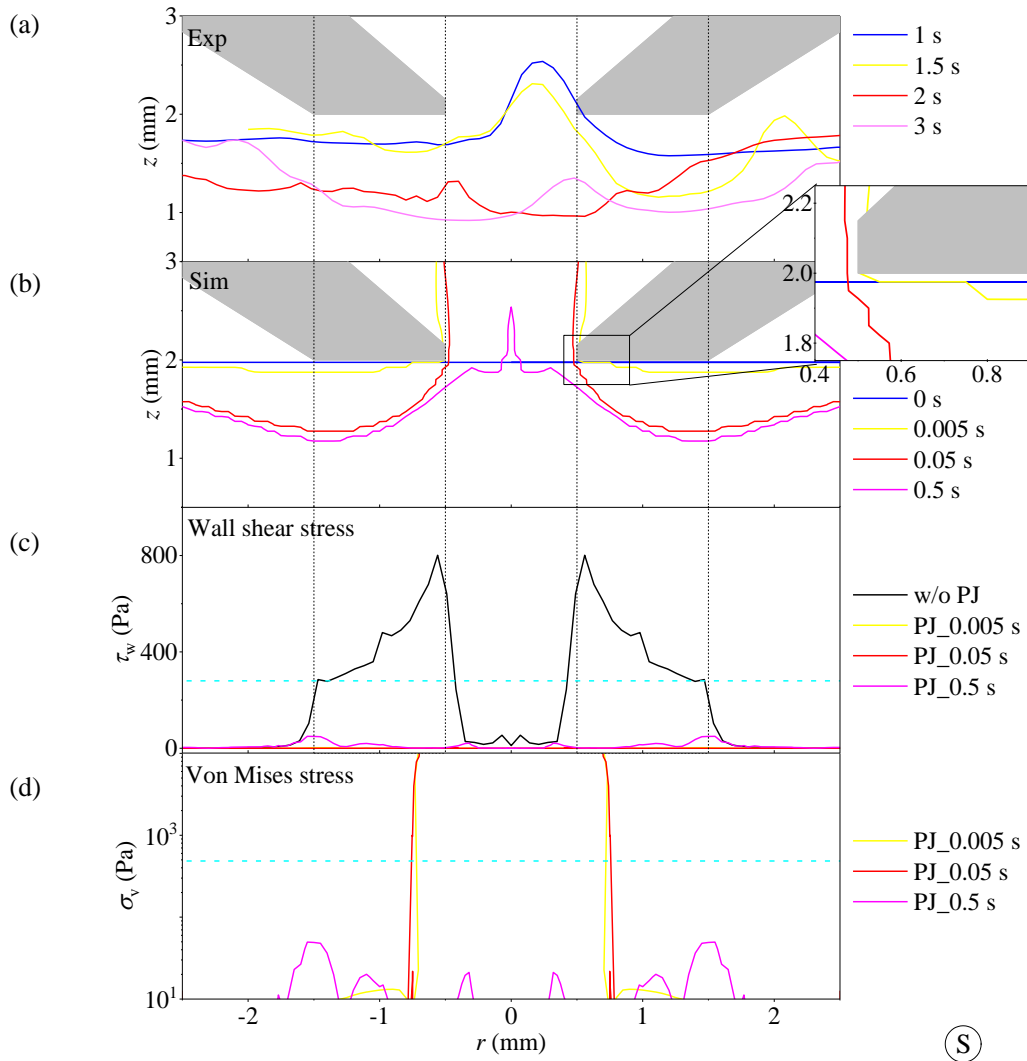
Fig. 5.8. Topography of the layer after gauging in suction mode, with $\dot{m} = 20$ ml/min at $h_o/d_t = 0.03$. (a) CTS measurements, (b) simulation results and distribution of (c) shear stress and (d) von Mises stress on soil surface. Vertical dashed lines and grey shape show nozzle region. Legend shows time of exposure. In (a) and (b), substrate is at $z = 0$ mm. The inset in (b) shows a zoomed-in picture for the gap between the nozzle head and layer. w/o PJ represents without petroleum jelly. Cyan dashed lines in (c) and (d) denote τ_y and $\sqrt{3}\tau_y$, respectively.
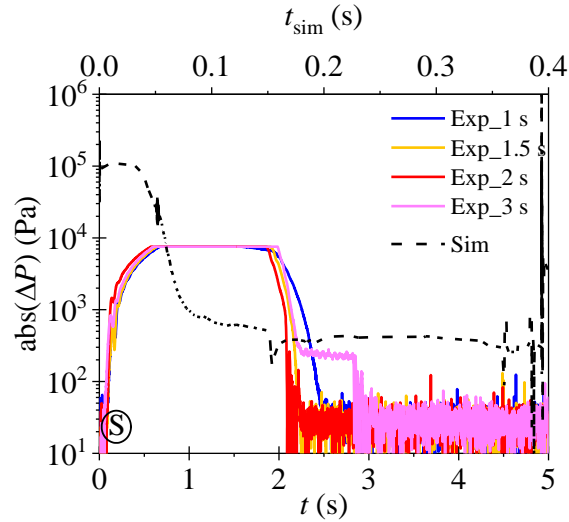
Fig. 5.9. Comparison of absolute pressure drop between experimental and simulation results. Suction mode with petroleum jelly, $\dot{m}$ = 20 ml/min, h_o/d_t = 0.03. t_{sim} denotes simulated time.

Experimental data and simulation results for the corresponding ejection mode case are shown in Fig. 5.10. The experimental profiles in Fig. 5.10 are all similar, indicating that deformation occurred within the first 1 s. The clearance increased from 0.03 mm to the maximum 1.53 mm, which is consistent with the observed reduction in pressure drop over this period.

Fig. 5.10(c) shows that all induced wall shear stresses were lower than the yield stress. The distributions of von Mises stress are plotted in Fig. 5.10(d). At $t = 0.005$ s, the σ_v values on the crater surface are higher than $\sqrt{3}\,\tau_y$, and the layer was deforming. By contrast, at $t \geq 0.05$ s, the σ_v values became lower than $\sqrt{3}\,\tau_y$ that at $t = 0.005$ s, and the predicted layer was static. In this case, the normal force imposed on the layer surface dominated. Fig. 5.10(d) shows that the largest stress initially occurred at the inner rim. The material in the centre was forced outward as a crater was formed. Once this gap had opened, the maximum pressure decreases until the material no longer deforms plastically. The average diameter and volume of the crater in the CTS measurements after all durations are about 3.12 mm and 7.78 mm^3, respectively. The diameter and volume of the predicted crater are smaller (at 3.04 mm and 2.56 mm^3, respectively), indicating that the simulation tended to underestimate the deformation. One reason for this could be the surface roughness of the petroleum jelly. The average roughness is about $\pm$ 0.05 mm, which is larger than the clearance (0.03 mm) and could result in the nozzle rim contacting the petroleum jelly. When the nozzle head contacted the layer, the pressure drop

176

increased during ejection and caused a deeper and larger crater to be generated. Another reason is that the rheological model does not capture the flow behaviour completely.

Comparing the predicted pressure drop to the experimental values (Fig. 5.11), it is similar to the trend in suction mode, namely shorter timescale and higher predicted initial pressure drop. This is mainly contributed to the ballooning effect discussed above. In addition, the predicted pressure drop after the crater formed is slightly higher than the experimental values, since the predicted gap between the layer surface and the nozzle rim (point A in Fig. 5.10(c)) is smaller than the CTS topographies, causing a higher pressure drop.
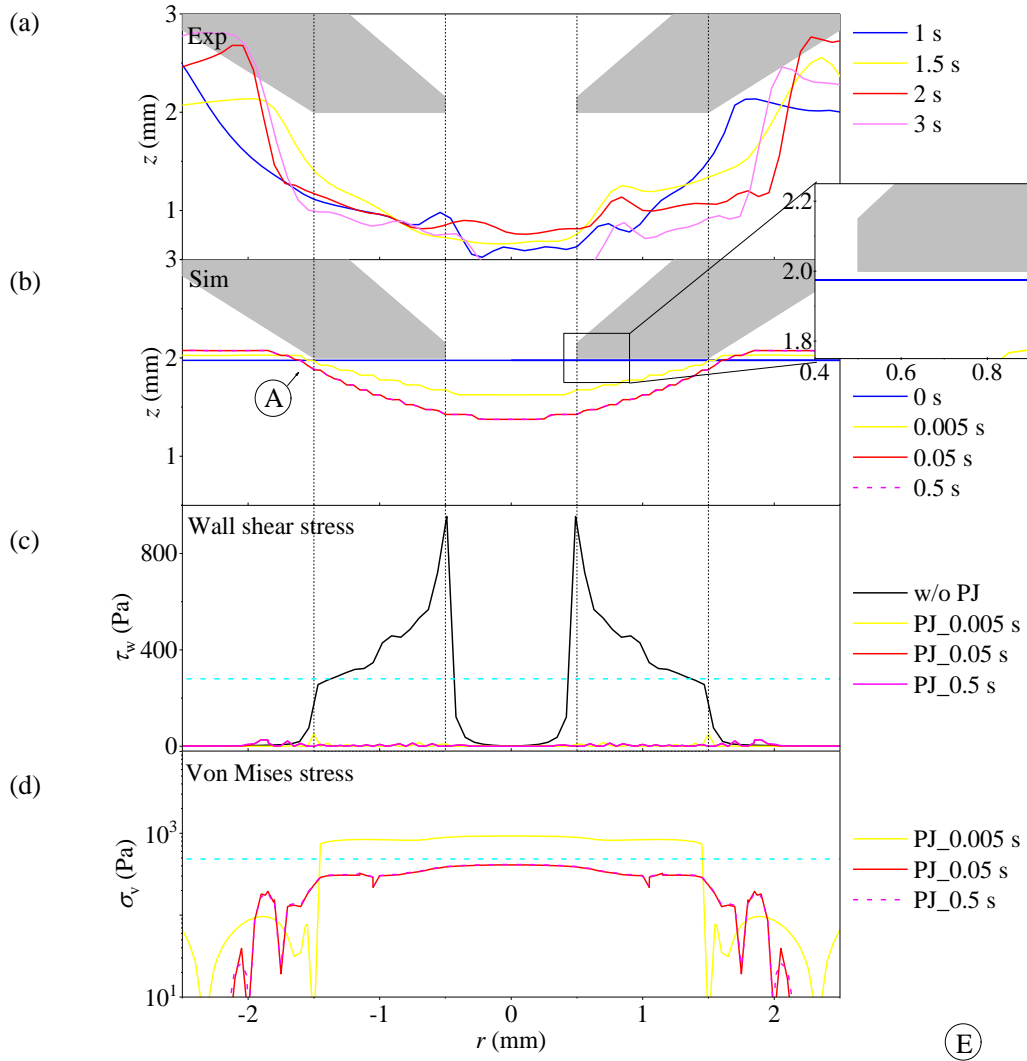
Fig. 5.10. Topography of the layer after gauging in ejection mode, with $\dot{m}$ = 20 ml/min at h_o/d_t = 0.03. (a) CTS measurements, (b) simulation results and distribution of (c) shear stress and (d) von Mises stress on soil surface. Vertical dashed lines and grey shape show nozzle region. Legend shows time of exposure. In (a) and (b), substrate is at z = 0 mm. The inset in (b) shows a zoomed-in picture for the gap between the nozzle head and layer. Cyan dashed lines in (c) and (d) denote τ_y and $\sqrt{3}\tau_y$, respectively.
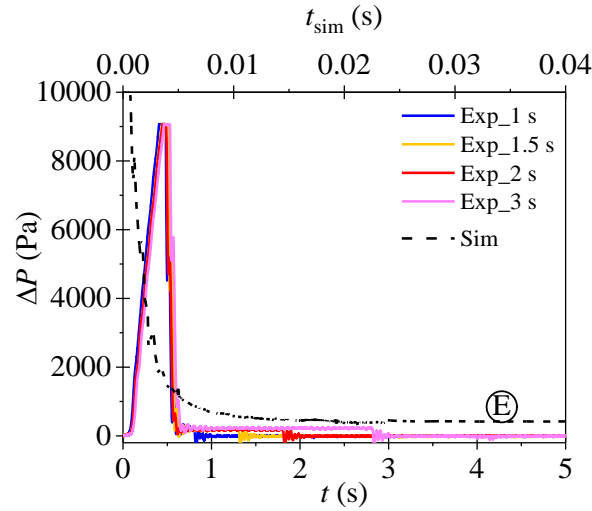
Fig. 5.11. Comparison of pressure drop between experimental and simulation results. Ejection mode with petroleum jelly, $\dot{m}$ = 20 ml/min, h_o/d_t = 0.03. t_{sim} denotes simulated time.

5.3 Conclusions

The volume-of-fluid method was employed with the FDG model to calculate the coupled deformation of viscoplastic layers and the gauging flow. The experimental measurements show that in ejection mode, deformation occurred within one second and did not change thereafter. However, in suction mode, petroleum jelly was withdrawn into the nozzle and then stopped after some finite time. As withdrawing was interrupted by breakage, the jelly surface became hill-shaped.

Acceptable agreement was obtained between the experimental and simulated deformation topographies in ejection mode. The distributions of predicted von Mises stress as a function of time indicated that in ejection mode, the FDG flow exerted a downward force at the centre of the layer, resulting in formation of a hole under the centre of the nozzle. The deviation from the CTS measurement could be attributed to the roughness of petroleum jelly and insufficient resolution of the z-axis positioner. In suction mode, the material was simulated to be withdrawn into the nozzle continuously, and the withdrawal was then broken off. However, in the simulations, the breakage was resulted from the non-uniform mesh size, but it was attributed to the inhomogeneity of layer and bubbles in layers.

179

The simulated timescale in both modes did not agree with the experimental timescale. These differences could be attributed to the simulation limits such as the ballooning effect and the numerical approach.

These findings may help understand the operation of ZFDG flows and characterise the removal behaviour of viscoplastic layers. Although the model could not capture the experimental dynamics well, some behaviours can be elucidated by the simulations.

5.4 Deformation of a Viscoplastic Soil Layer by an Impinging Jet

Reasonable agreement between experimental and simulation results for the shape of a petroleum jelly layer subject to dynamic gauging was obtained above, indicating that the CFD approach could be employed to predict the petroleum jelly behaviour while being cleaned. In this section, the simulation tool is extended to the modelling of removal of a petroleum jelly layer by an impinging water jet (see Fig. 5.12(c)). An impinging water jet was set normal to a horizontal Perspex plane with a petroleum jelly layer. This is a topic which has been investigated at some length in the P^{4}G research group, but has not been reported by others as a coupled CFD problem.

For studying the cleaning a soil layer using an impinging jet, people have either used a cleaning kinetic model based on (I) shear flow (where the water film drags the soil layer away from the point of impingement), such as the following equation reported by Yeckel and Middleman [60].

$$\frac{d\delta}{dt} = k_s \tau_w \tag{5.7}$$

where δ is the layer thickness, k_s is a kinetic constant, and τ_w is the wall shear stress, or (II) momentum flow rate (pushing the soil): Wilson *et al.* [64] presented a model for cleaning a viscoplastic layer from vertical and horizontal plates by water jets impinging normally on a flat substrate. The rate of growth the circular cleaned area (radius: *a*) was proportional to the momentum in the liquid film per unit length, *M*, giving

$$\frac{da}{dt} = k'M \tag{5.8}$$

180

where *k'* is a kinetic constant. The key part of this work was the assertion that some soft solids are removed by a peeling mechanism.

Glover *et al.* [65] subsequently used the Wilson *et al.* [64] model to calculate the momentum flow rate for estimating the rate of cleaning a layer of yield stress material. The model was modified to

$$\frac{da}{dt} = k'(M - M_Y) \tag{5.9}$$

where M_Y is the momentum flux required to cause yield.

Both cleaning kinetic models need calculation of hydrodynamic parameters, either the wall shear stress or the momentum flux. Bhagat and Wilson [66] subsequently presented a hydrodynamic model of flow in the liquid film including the development of boundary layers (see Fig. 5.12(a)). After the jet impinges normally on the surface, the velocity redistributes and a boundary layer forms. The film thickness, h_f, in the first zone, the boundary layer formation zone (BLFZ), was given by

$$\frac{h_f}{d_j} = 0.125 \left(\frac{d_j}{r}\right) + \frac{1.06}{\sqrt{Re_j}} \left(\frac{r}{d_j}\right)^{1/2} \tag{5.10}$$

Here d_j is the jet diameter, r is the radial position and Re_j is the Reynolds number of the jet based on the nozzle diameter. The momentum flux for BLFZ was

$$M = -1.3746\rho^{0.5}U_0^{1.5}\sqrt{\mu r} + \rho U_0^2 d_j \left[0.125 \left(\frac{d_j}{r}\right) + \frac{1.06}{\sqrt{Re_j}} \left(\frac{r}{d_j}\right)^{0.5}\right] \tag{5.11}$$

Here U_0 is the average velocity in the jet, μ is the dynamic viscosity of the liquid, and Q is the volumetric flow rate. The wall shear stress was given by

$$\tau_w = \mu \frac{U_0}{2.12\sqrt{\frac{\mu r}{\rho U_0}}} \tag{5.12}$$

The liquid then flows radially outwards as a fully developed laminar film. The film thickness in this laminar film zone (LZ) was given by:

$$\frac{h_f}{d_j} = \frac{3.792}{Re_j}\left(\frac{r}{d_j}\right)^2 + 0.1975\left(\frac{d_j}{r}\right) \tag{5.13}$$

with momentum flux

$$M = \frac{0.3516\rho U_0^2 d_j^3}{16r^2\left[\frac{3.792}{Re_j}\left(\frac{r}{d_j}\right)^2 + 0.1975\left(\frac{d_j}{r}\right)\right]} \tag{5.14}$$

and wall shear stress

$$\tau_w = \mu\frac{U_0}{4r\left[\frac{3.792}{Re_j}\left(\frac{r}{d_j}\right)^2 + 0.1975\left(\frac{d_j}{r}\right)\right]^2} \tag{5.15}$$

The flow undergoes a transition to a turbulent film at transition radius, r_t, given by

$$\frac{r_t}{d_j} = 0.2964\left(Re_j\right)^{1/3} \tag{5.16}$$

The film thickness in the turbulent region (TZ) is given by.

$$\frac{h_f}{d_j} = \frac{0.0209}{Re_j^{1/4}}\left(\frac{r}{d_j}\right)^{5/4} + \left(0.296 - 0.001356 Re_j^{1/2}\right)\left(\frac{d_j}{r}\right) \tag{5.17}$$

with

$$M = \frac{\rho\frac{64}{63}\left(\frac{Q}{2\pi}\right)U_0}{r\left[\frac{0.167}{Re_j^{0.25}}\left(\frac{r}{d_j}\right)^{9/4} + \left(2.37 - 0.0108 Re_j^{1/2}\right)\right]} \tag{5.18}$$

and

$$\tau_w = \frac{0.0478\rho}{Re_j^{1/4}}\left[\frac{U_0}{\frac{0.167}{Re_j^{0.25}}\left(\frac{r}{d_j}\right)^{9/4} + \left(2.37 - 0.0108 Re_j^{1/2}\right)}\right]^2\left(\frac{r}{d_j}\right)^{1/4} \tag{5.19}$$

Bhagat and Wilson compared the results from this model with published experimental data. Good agreement was obtained without the use of fitting parameters, indicating that the model was acceptable for predicting the average behaviour of the film generated by a coherent turbulent liquid jet impinging on a vertical surface. They did not consider wave formation.

The petroleum jelly used in this study is the same as that in section 5.2.1, and the methods of preparation and topography measurement (CTS) are also the same. The experimental data were taken from Fernandes *et al.* [68].
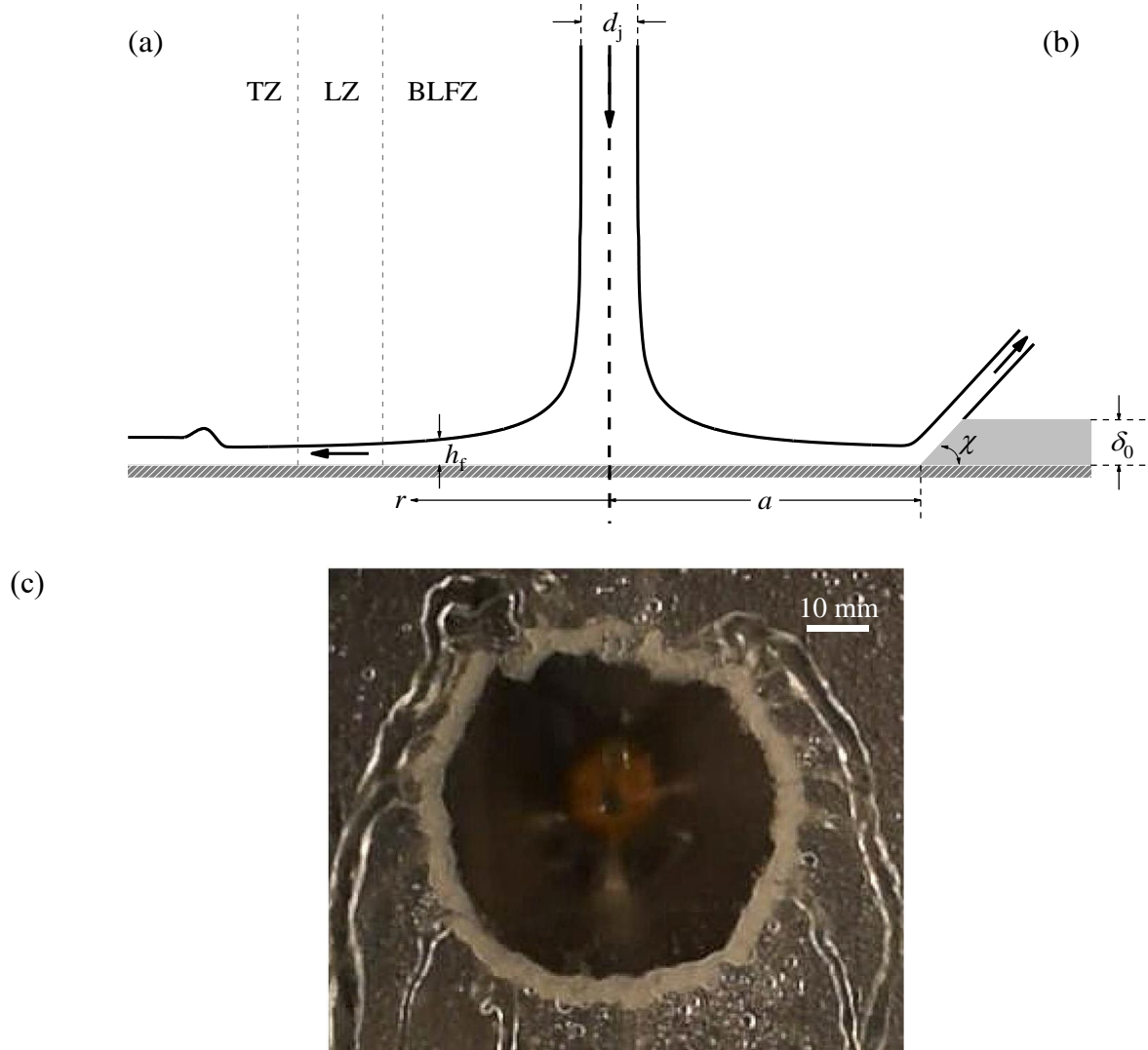
Fig. 5.12. Schematics of (a) flow pattern formed by a jet impinging normally on a wall, and (b) flow at a cleaned radius. (c) Photograph of a crater formed after impinging a petroleum jelly layer, adjusted from Fernandes *et al.* [68]. Grey area in (b) shows the soil layer. r is the radial position, d_j is the jet diameter, h_f is the water film thickness, a is the cleaned radius, χ is the slope angle and δ_0 is the initial soil layer thickness. BLFZ, LZ and TZ are the boundary layer formation zone, laminar film zone and turbulent zone, respectively.

5.4.1 Model formulation

In this work, the interactions between the jet flow and the petroleum jelly in the laminar flow zone (LZ on Fig. 5.12(a)) are studied and analyzed. The impinging jet system described above has been simplified for the simulation of deformation of a soft soil layer, which will be discussed later. In order to compare with experiments, a 3-dimensional, transient impinging jet

model with gravity was constructed with stagnant air at ambient temperature and pressure as one fluid and the other, moving, fluid the water jet (isothermal, laminar regime with incompressible, Newtonian fluid). The model will not simulate the formation of the hydraulic jump, since the hydraulic jump at this condition involves in turbulent flow.

A petroleum jelly layer of set uniform thickness lay above the rigid substrate. A 2-dimensional asymmetrical schematic of the geometry and dimensions is shown in Fig. 5.13. The radial position r will be presented by x below, since the model was created using the Cartesian coordinate system. Note that formation of the initial crater is not considered. The initial impact of the jet, where it clears out the jelly in the footprint area, was not modelled. At a flow rate of 2 L/min with a jet diameter of 2 mm at 20 °C, the jet Reynolds number is about 19000, and the transition from laminar to turbulent flow in the film calculated from Equation (5.16) was around 15.5 mm. This study focuses on the deformation in the BLFZ and LZ. The governing equations did not include the terms for turbulence, so that the diameter of the geometry was shortened to 30 mm to reduce the calculation time. Also, a dynamic mesh algorithm was employed to refine the mesh around the water interface, which will be discussed in detail later. During computation, modelling the formation of water splashes generated by interfacial instabilities would cause a dramatic increase in the refined mesh requirement, increasing the solution time. The domain above the soft layer was thus truncated for splash prevention, and the height of the geometry became 1 mm.

Fig. 5.13. Geometry of coupled deformation of petroleum jelly layer and impinging jet simulation at $t = 0$. All dimensions in mm. BC = 7.5 d_j. Colour: light cyan – water; grey – petroleum jelly. **g** denotes the direction of gravity.

5.4.1.1   Governing equations

The OpenFOAM solver multiphaseInterDyMFoam was employed for this three-phase (air, water and petroleum jelly) system, based on the volume of fluid (VOF) approach. In the algorithm, the entire domain is calculated by a momentum conservation equation using average density and viscosity. In each grid cell, the local volume fraction for each species (species i) is represented as α_i, with $0 \leq \alpha_\mathrm{i} \leq 1$. The sum of all fractions is 1.

$$\sum_i \alpha_i = 1 \tag{5.20}$$

The average density and viscosity in each cell are described by simple laws of mixtures.

$$\rho = \sum_i \rho_i \alpha_i \tag{5.21}$$

$$\mu = \sum_i \mu_i \alpha_i \tag{5.22}$$

The transport equation is

$$\frac{\partial \alpha_i}{\partial t} + \nabla \cdot (\mathbf{v}\alpha_i) = 0 \tag{5.23}$$

, and the velocity in each cell is solved by the momentum equation:

$$\rho\left(\frac{\partial \mathbf{v}}{\partial t} + \mathbf{v} \cdot \nabla \mathbf{v}\right) = -\nabla p + \mu \nabla^2 \mathbf{v} + \rho \mathbf{g} \tag{5.24}$$

The fluid properties are summarised in Table 5.3. The properties of water and air were taken from [98] and [181], respectively. The rheology of the petroleum jelly is described by Bingham-Papanastasiou model with parameters obtained by fitting experimental data, discussed in section 3.2.4.

Table 5.3. Fluid properties (subscripts: air – air, water – water, PJ – petroleum jelly) at 20 °C [98, 181]

Parameter	Value
μ_{air}	0.0148 mPa s
ρ_{air}	1.0 kg/m^3
$\sigma_{air\text{-}water}$ [a]	0.07 N/m
μ_{water}	1.123 mPa s
ρ_{water}	997.3 kg/s
$\sigma_{water\text{-}PJ}$	0.07 N/m
μ_{PJ}	$12.4 + 249/\dot{\gamma}[1 - \exp(-8869\dot{\gamma})]$ Pa s
ρ_{PJ}	812 kg/m^3
$\sigma_{PJ\text{-}air}$	0.07 N/m

[a] σ is the surface tension [140].

5.4.1.2   *Boundary conditions*

The boundary conditions for the boundaries labelled in Fig. 5.13 are listed in Table 4.2. In Fig. 5.13, water is ejected *via* AE in plug flow with velocity, v_{jet}. BC is the rigid substrate, and the petroleum jelly was assumed not slip at this boundary. In OpenFOAM, the interaction between the fluid and the wall is described by the wall adhesion model proposed by Brackbill *et al.* [182], where the surface normal of the fluid in the grid cell close to the wall is adjusted based on the given contact angle, θ_w. The surface normal, $\hat{n}$, in this dynamic boundary condition is given by

$$\hat{n} = \hat{n}_w cos\theta_w + \hat{t}_w sin\theta_w \tag{5.25}$$

Here $\hat{n}_w$ is the unit vector normal to the wall and $\hat{t}_w$ is the unit vector tangential to the wall. Contact angles for each two materials have been tested in this case, and the effect is negligible so it was not included in this model. In addition, the micro-scale interaction between the layer material and surface was not considered in the simulation. Cleaning of layers means there is no residual layer on the surface. CD and DE are air and specified as open ($p = 0$).

Table 5.4 Boundary conditions in the CFD model (v_z is the axial velocity)

Boundary	Description	Boundary condition of momentum	Boundary condition for Species
AE	Inlet	$v_z = v_{jet}$[a]	$\alpha_{air} = 0$, $\alpha_{PJ} = 0$, $\alpha_{water} = 1$
BC	Wall	$\mathbf{v} = 0$	$\nabla\alpha = 0$
CD, DE	Open boundary	$p = 0$	$\alpha_{air} = 1$, $\alpha_{PJ} = 0$, $\alpha_{water} = 0$

A 3-dimensional geometry was created initially with about 390,000 uniform 128 μm-structured mesh elements using the commercial CFD software, ANSYS version 18.0. The mesh file was exported from workbench to OpenFOAM for modelling using the 'fluent3DMeshToFoam' function. The dynamic mesh module 'multiphaseInterDyMFoam' was employed in OpenFOAM to decrease the total number of mesh elements used for calculation. In this algorithm, the maximum number of mesh points can be specified, and the mesh is refined and rearranged during calculation, based on the location of the interface between water and other species to increase the resolution of the interface. The minimum mesh size was set at 64 μm, and the convergence criteria were those employed for the millimanipulation model (Section 3.2.5). Calculations were performed on a cluster consisting of 20 Supermicro[®] servers with each server including twin 8-core Intel[®] Xeon processors clocked at 2.7 GHz. This cluster was constructed and maintained by Dr. Bart Hallmark. The computational time required for the simulation to reach $t = 0.5$ s is about 30 days.

5.4.2 Comparison with literature

Fernandes *et al.* [68] reported that the shape of the rims created by the water film depended on the ratio between the water film thickness and initial layer thickness, h_f/δ_0. When $h_f/\delta_0 \leq 0.4$ (with $\delta_0 = 0.86$ mm), the angle of inclination of the front layer to the substrate surface, χ (see Fig. 5.12(b)), was around 45°. By contrast, with a thinner layer ($h_f/\delta_0 > 0.4$ and $\delta_0 = 0.097$ mm), measured χ values lay in the range 10° to 30°. In order to understand the effect of layer thickness and compare with the results reported by Fernandes *et al.*, three cases for a water jet impinging on a vertical wall were considered as follows. Gravity was specified in the –y-axis direction.

i. $Q = 2$ L/min, 20 °C, with no a petroleum jelly layer

ii. $Q = 2$ L/min, 20 °C, with a petroleum jelly layer of initial thickness $\delta_0 = 1$ mm

iii. $Q = 1$ L/min, 20 °C, with a thin layer ($\delta_0 = 0.05$ mm)

The layer thicknesses were selected for comparison with experimental results for $\delta_0 = 0.86$ mm and $\delta_0 = 0.097$ mm. The initial mesh size in the simulations was 128 μm and the resolution of the mesh was not sufficient to describe the thinner layer. A finer initial mesh could not be created because the software could not support this. The computational time required for the case with a petroleum jelly layer of thickness 1 mm to reach 0.5 s real time is about 30 days. A shorter end time could be used for the clean substrate. For the case at $\delta_0 = 0.097$ mm ($\delta_0 = 0.05$ mm for modelling), the duration of the cleaning experiment reported by Fernandes *et al* was 497 s. The region coated with the layer in the model was thus specified at the same as the experiment to save the computation time.

The predicted water film thickness, momentum flux and wall shear stress for case (i) without petroleum jelly at the steady-state condition ($t = 0.1$ s) are compared to the Bhagat and Wilson model in Fig. 5.14. Reasonable agreement was obtained for h_f and M in the BLFZ and LZ, whereas the predicted τ_w value increased with r at $r < 4$ mm, followed by declining. This could be attribute to the velocity redistribution. These indicate that the simulation can be used to describe the water film with some confidence. The simulation result fluctuates owing to the dynamic mesh function. Peak values often occurred around the mesh-refined region. Fig. 5.14(a) also shows that the liquid film thickness is 0.1-0.2 mm *i.e.* smaller than the layer thickness in case (ii) and larger than the layer thickness in case (iii).

(a)

(b)

(c)
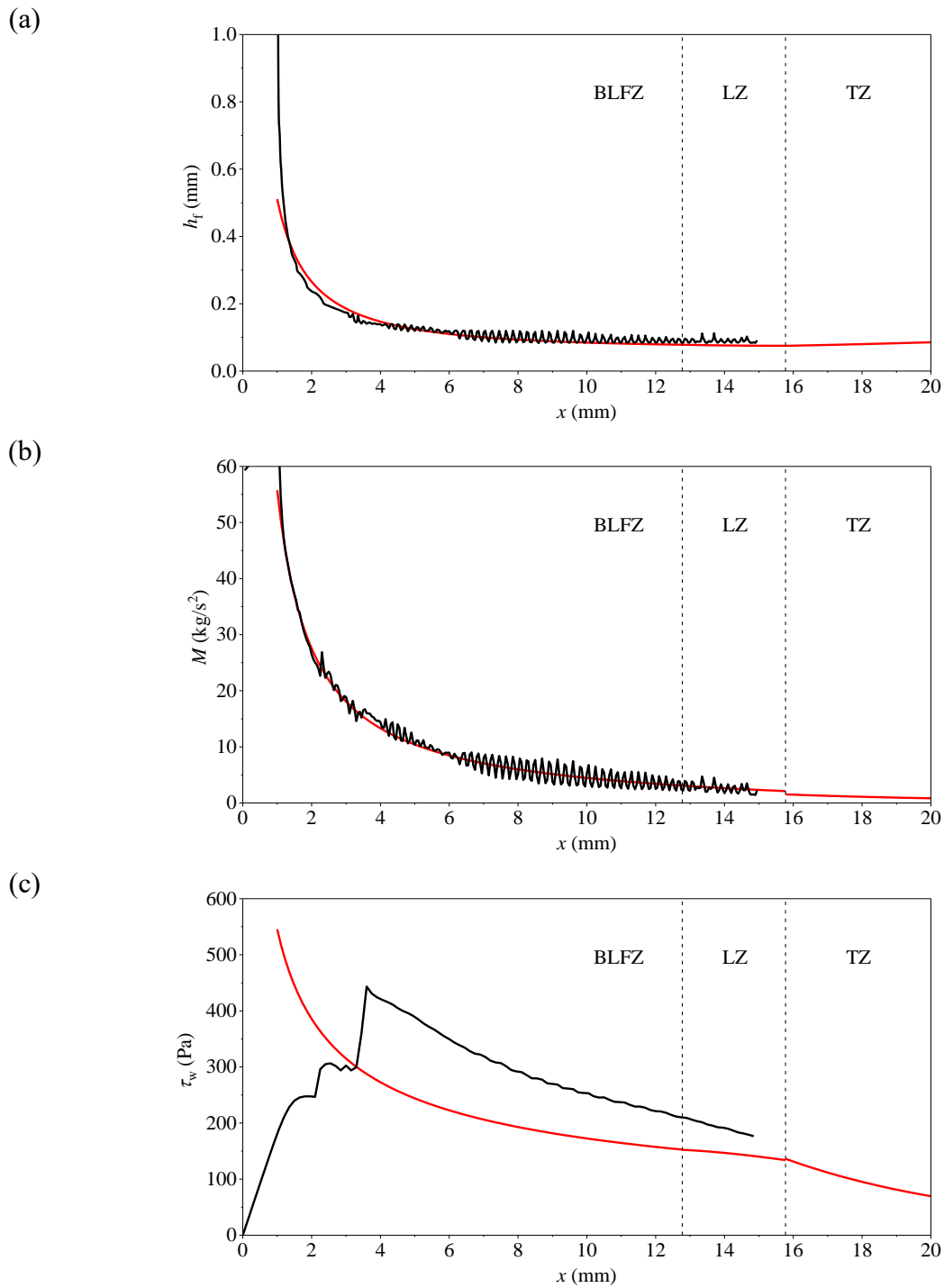
Fig. 5.14. Comparison of (a) liquid film thickness, (b) momentum flux and (c) wall shear stress predicted by the simulation with the Bhagat and Wilson [66] model. Test conditions: $Q = 2$ L/min, $d_j = 2$ mm. Colour: red – Bhagat and Wilson model (BLFZ, Eq. (5.10); LZ, Eq. (5.13); TZ, Eq. (5.17)); black – CFD.

The predicted velocity distributions of petroleum jelly with time for case (ii) at $\delta_0 = 1$ mm are presented in Fig. 5.15. The plots show the velocity distributions as well as the liquid/air and

191

liquid/soil interfaces. In Fig. 5.15(a), the water film flow (dashed line area) has dislodged the front layer out of the crater. The cleaning radius, a, is defined as the front edge of the petroleum jelly layer. There was no soil left on the substrate in the cleaned region. Fig. 5.15 (b) and (c) show a very unstable soil-liquid boundary which settled down to a curved wedge. The following figures show a similar trend. In addition, the results do not show the evolution of the shape of the berm of dislodged material because the domain was set to feature $z \leq 1$ mm.

Fig. 5.16(a) compares the evolution of the experimental and predicted cleaning radius for case (ii) with time, showing good agreement with the measured values. The radius increased rapidly at the beginning, reaching an asymptotic value of about 9.4 mm. The labels in Fig. 5.16(a) refer to the subfigures in Fig. 5.15.

The simple cleaning model proposed by Wilson et $al.$ [64] predicted that a grows proportionally to $t^{0.2}$, following

$$a^5 - a_0{}^5 = K^5(t - t_0) = K^5 \Delta t \tag{5.26}$$

where a_0, t_0 and Δt are the radius, time and total time when cleaning front is first seen in experiments, respectively. K is the cleaning rate parameter. Fig. 5.16(b) shows that the simulation data fit the simple model with $R^2 = 0.98795$. The predicted K value is 10.25 mm/s$^{0.2}$, slightly lower than the experimental value (11.67 mm/s$^{0.2}$). However, both experimental and simulation results show better fits with a non-zero intercept, indicating that the simple cleaning model is not suitable for this case.

The simulation results are plotted in the form of the Wilson et $al.$ model [64], $\frac{da}{dt}$ versus M in Fig. 5.16(c). The predicted values show a good fit to a linear relationship with $R^2 = 0.916$. Similarly, the experimental $\frac{da}{dt}$ value shows a linear relationship to the simulation M ($R^2 = 0.674$). The fitted M_Y values for the simulation and experimental data are 13.4 and 2.0 kg/s^2, respectively.
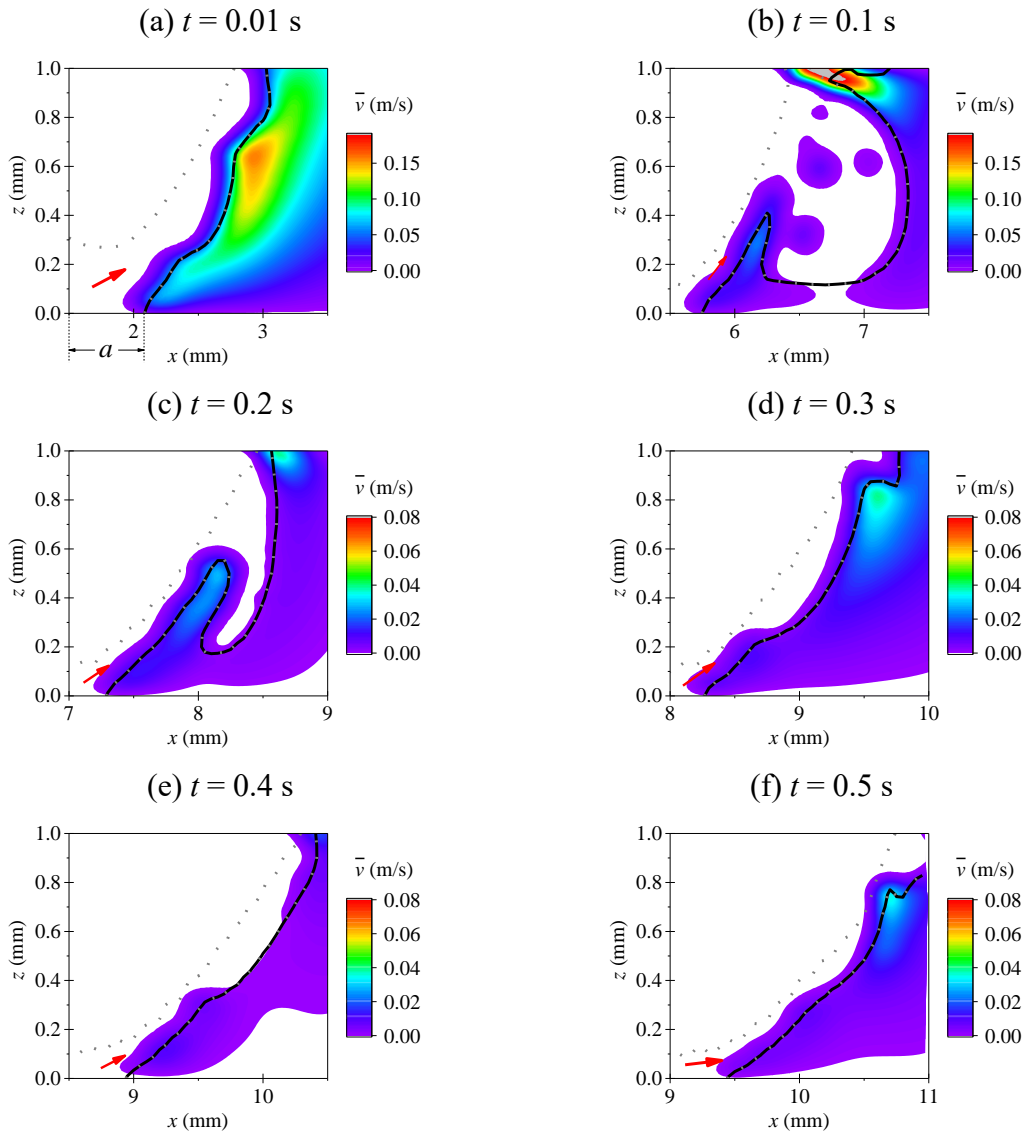
Fig. 5.15. Distributions of predicted average petroleum jelly velocity, $\bar{v}$, at t = (a) 0.01 s, (b) 0.1 s, (c) 0.2 s, (d) 0.3, (e) 0.4 s and (f) 0.5 s. Symbols: black solid line – petroleum jelly interface; grey dashed line – water interface. Red arrow denotes the direction of water flow.
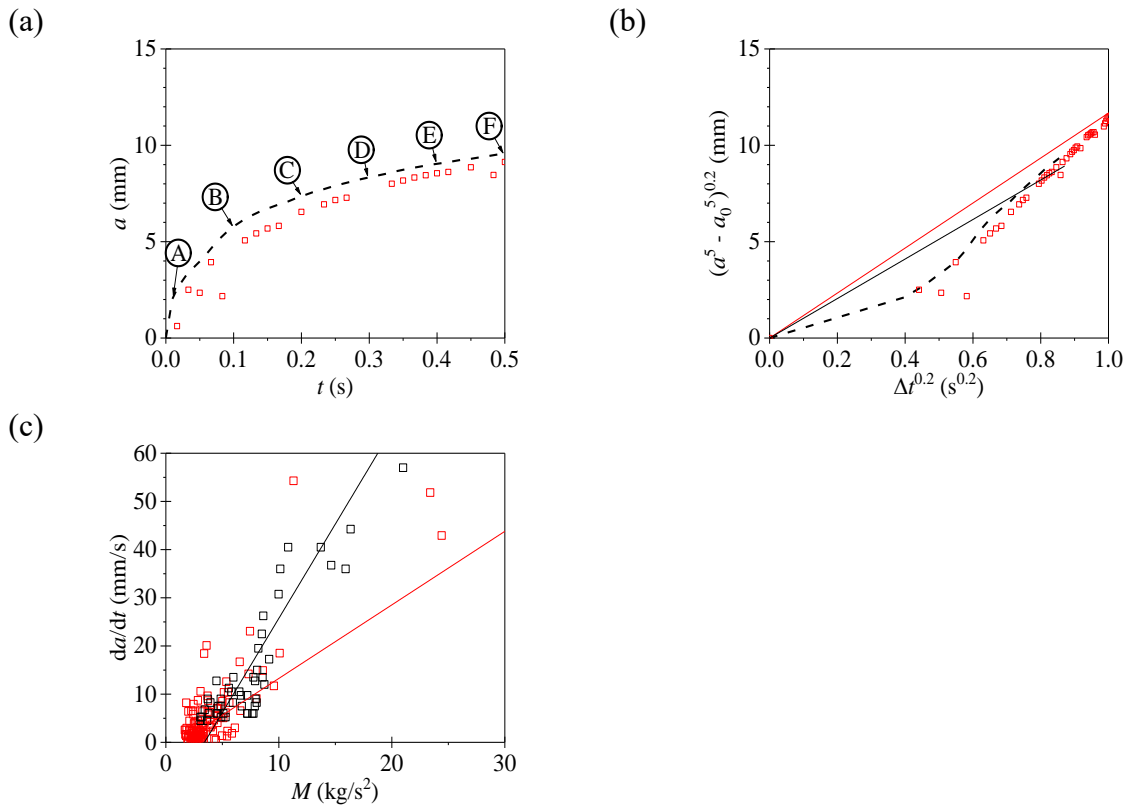
Fig. 5.16. Summary of case (ii) cleaning behavior. (a) Evolution of cleaned region radius, (b) $(a^5 - a_0^5)^{0.2}$ versus $\Delta t^{0.2}$, and (c) $\frac{da}{dt}$ versus M. Experiments were conducted by Fernandes *et al.* [68]. Test conditions: $Q = 2$ L/min, $d_j = 2$ mm, $\delta_0 = 0.86$ mm for experiment, $\delta_0 = 1$ mm for simulation. Colour: red – experiment; black – simulation. Labels (A), (B), (C), (D), (E) and (F) in (a) are related to Fig. 5.15(a), (b), (c), (d), (e) and (f), respectively. Solid loci in (b) show fit of data to Eq. (5.26). Solid lines denote fitting.

Fig. 5.17(a) and (b) compare the topographies of craters created by the impinging water jet reported by Fernandes *et al.* [68] at different operation times, t, alongside the simulation profiles. In this case ($h_f/\delta_0 \leq 0.4$), the simulation results show good agreement with the experimental data. The cleaning front is in the form of a wedge, as assumed by Glover *et al.* [65], with predicted and experimental angles both nearly 45°, indicating that the momentum flow rate causes internal yielding of the petroleum jelly layer [68].

(a)

(b)
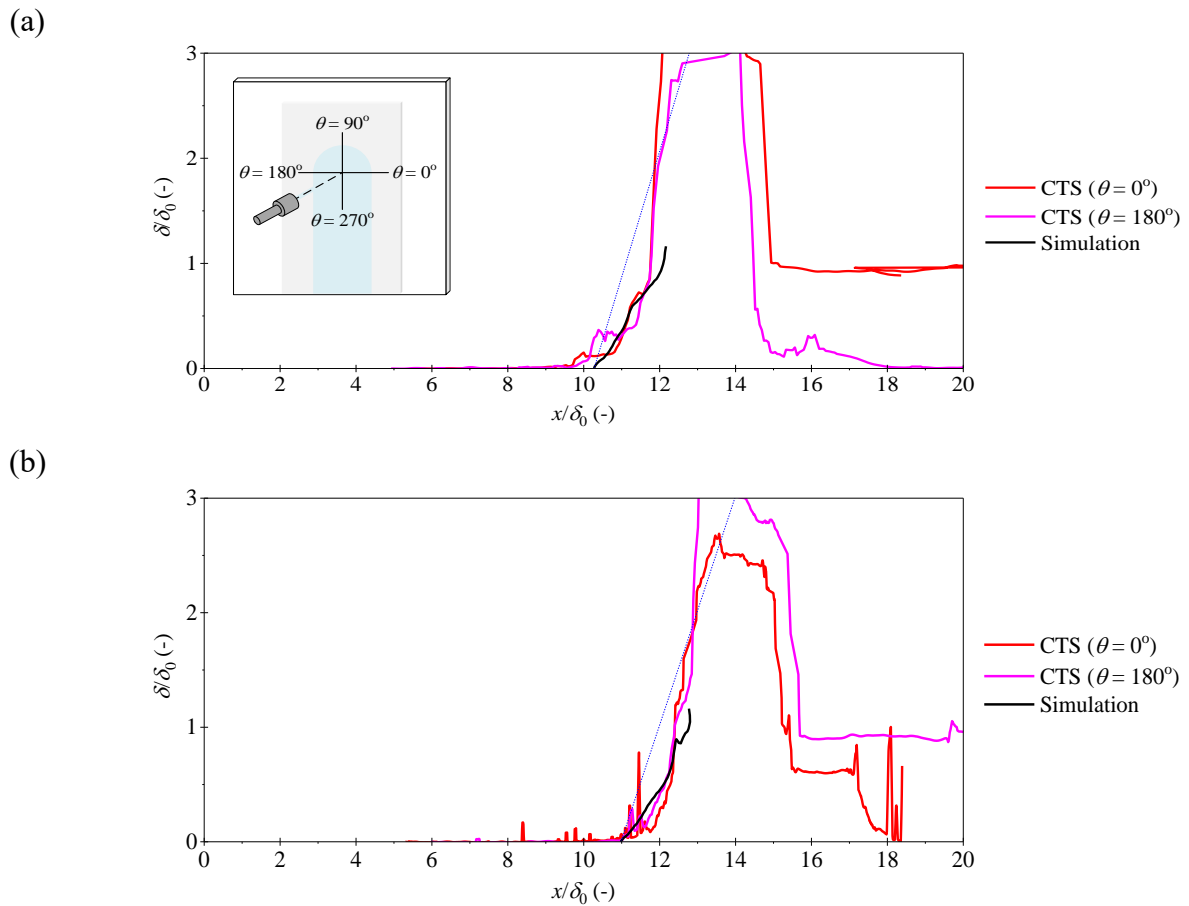
Fig. 5.17. Cross-sections through the soil layer obtained from (a) CTS measurements and simulations at $t = 0.38$ s and (b) CTS and simulations at $t = 0.5$ s. Test conditions: $Q = 2$ L/min, $d_j = 2$ mm, CTS with $\delta_0 = 0.86$ mm, and simulations with $\delta_0 = 1$ mm. The CTS results ae reproduced from Fernandes *et al.* [68]. $\theta = 0°$ and $\theta = 180°$ denote the topography measured along east and west directions, respectively (see inset in (a)). Inset in (a) shows coordinates used to describe the shape of the rim. Blue dashed line denotes 45°.

In Fig. 5.15, the maximum velocities were found near the interface between water and petroleum jelly. The VOF method requires both materials to have the same velocity on their interface. The velocities then decayed along the interface due to the kinetic energy consumed in making petroleum jelly deform. This phenomenon can be illustrated by the viscous dissipation occurring around the interface, which will be discussed below. The local velocities decrease with time, from around 0.2 m/s at $t = 0.01$ and 0.1 s to about 0.035 m/s at $t = 0.5$ s.

At $t = 0.2$ and 0.3 s, there was a cavity on the petroleum jelly layer, which resulted from the water splashes. This phenomenon was not observed in the experiments and is attributed to the

boundary around the layer (at $z = 1$ mm). Even though the boundary condition was specified as open boundary, it still caused some influences on the results during computation.

PhD student Rubens Rosario Fernandes and Professor Ian Wilson [183] reported that the rate of cleaning could be linked directly to the rate of viscous dissipation in the soil layer generated by the water film flow. The distributions of viscous dissipation rate, Φ, for the cases in Fig. 5.17 are plotted in Fig. 5.18. The maximum viscous dissipation rate is around 8×10^8 W/m^3 for both cases and occurred at the water-petroleum jelly interface. This agrees with the assumption reported by Fernandes and Wilson. In addition, the high values only occurred in the interface region because the VOF method couples the velocity at the interface.
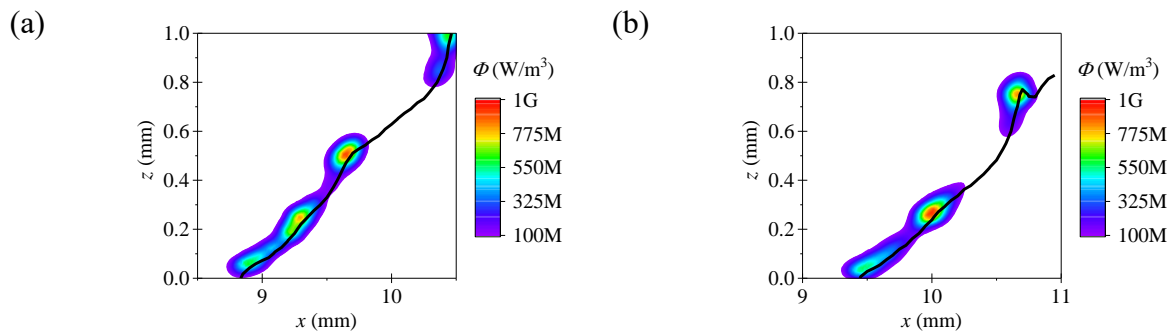
Fig. 5.18. Distributions of rate of viscous dissipation in the soil, Φ, for the cases (a) and (b) in Fig. 5.17(a) and (b), respectively. Symbols: black solid line – petroleum jelly interface; grey dashed line – water interface.

Fig. 5.19 shows distributions of von Mises stress, σ_v. It is obvious that as the higher σ_v values occurred at the water/soil interface. These results illustrate that the water film flow caused the deformation of the soil layer.
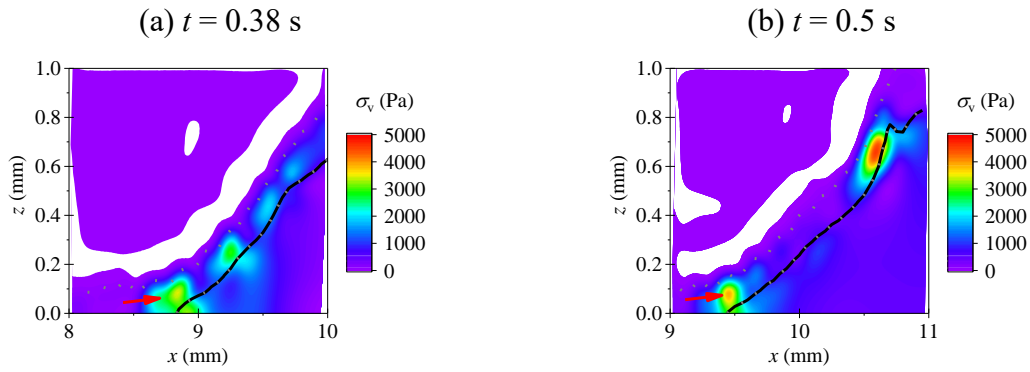
Fig. 5.19. Distributions of von Mises stress, σ_v, for cases (a) and (b) in Fig. 5.17(a) and (b), respectively. Symbols: black solid line – petroleum jelly interface; grey dashed line – water interface. Red arrow denotes the direction of water flow.

The topography of the front layer is focused in this study. In the case (iii) ($h_f/\delta_0 > 0.4$), a shorter time ($t = 0.1$ s) case predicted from the simulation was chosen in order to save the computation time. Fig. 5.20 shows reasonable agreement between the simulation results and CTS profiles. The slope angle predicted from the simulation is between 10° and 30°, which agrees with the CTS measurements. It is consistent with the behaviour observed by Fernandes *et al.* [68]: the h_f/δ_0 ratio had a significant impact on the shape of layers while being cleaned. Although the resolution of the initial mesh size was not sufficient to describe the real layer thickness, the effect of h_f/δ_0 could be captured by the simulations.
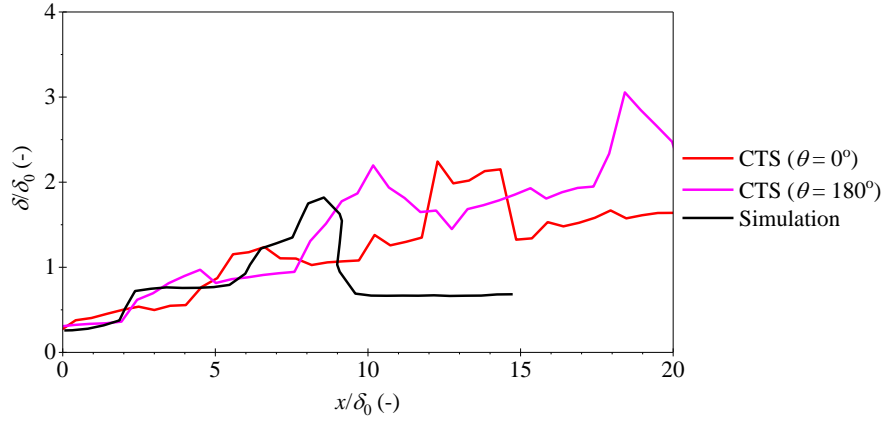
Fig. 5.20. Topography of the layer obtained from CTS ($t = 467$ s) and simulations ($t = 0.1$ s). Test conditions: $Q = 1$ L/min, $d_j = 2$ mm, CTS with $\delta_0 = 0.097$ mm and simulations with $\delta_0 = 0.05$ mm. The CTS results were adjusted from Fernandes *et al.* [68]. $\theta = 0°$ and $\theta = 180°$ denote the topography measured along east and west dictations, respectively. Blue dashed line denotes 45°.

5.4.3 Conclusions

The CFD simulation was extended to three-phases to simulate the cleaning of a petroleum jelly layer using an impinging water jet. The simulation hydrodynamics were compared with the analytical solutions, and reasonable agreement for the water film thickness and momentum flux was obtained, but the simulated wall shear stress did not agree with the theoretical values. This is owing to the redistribution of velocity. Comparing the predicted growth of cleaning radius with the experimental data, good agreement was observed. The predicted da/dt versus M showed a good linear fit ($R^2 = 0.91551$) with an intercept $M_Y = 13.4$ kg/s^2, indicating that the Wilson *et al.* model can be employed for predicting the cleaning rate with some confidence.

Comparing the simulation results with a petroleum jelly at $\delta_0 = 1$ mm with the experimental results, the predicted topographies of front layer agreed with the CTS measurements. Similarly, at small δ_0, reasonable agreement was obtained. The simulation results confirmed that the slope angle mainly depended on h_f/δ_0.

This work is a preliminary of impinging investigation. Further computation work is required, such as different h_f/δ_0 ratios and flow rates. Many of the parameters in the experiments for validating and comparing with the simulations cannot be measured directly. Fortunately, FDG

and millimanipulation allow some of the parameters to be estimated from small scale, low flow rate (see Fig. 5.21). Experiments on the FDG and millimanipulation devices are also needed.

Moreover, the model of cleaning a viscoplastic layer by an impinging water jet allows an industrial user to design a cleaning process for a layer in silico. Operating parameters, such as cleaning time, nozzle diameter and flow rate, can be estimated by the CFD simulation if information about the material's rheology is available. This can decrease the number of cleaning experiments required, which usually comsume a large amount of water, chemicals and energy, and generate equivalent volumes of waste. This approach is particularly valuable when the foulant layer contains hazardous species, *e.g.* nuclear fuel processing plant, chemical warfare agents, virus contaminated material, when even laboratory scale testing can generate hazards. Another application is with complex geometries: although analytical solutions of cleaning by impinging jets have been reported, these are usually for a simple geometry (*e.g.* a flat surface) and industrial equipment often features regions where the geometry is not simple. Numerical simulation is then required.
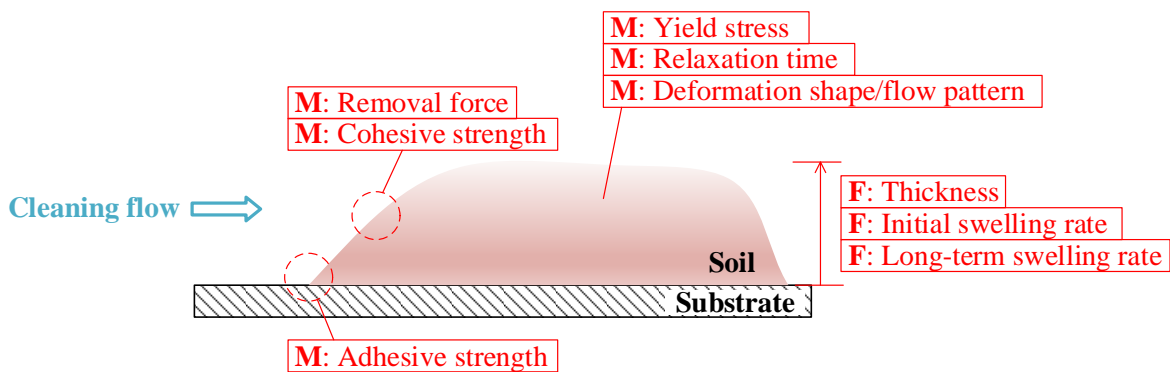
Fig. 5.21. Schematic of accessible fouling characteristics from the work. M and F denote the parameters which can be obtained from the measurement of millimanipulation and FDG, respectively.

5.5   *Other Application of Multi-phase CFD Modelling*

The results discussed above have demonstrated that the multi-phase CFD simulation can be employed to predict the interactions between two and three phases as well as their flow patterns in cleaning applications. The CFD code was also applied to a further two-liquid phase problem,

namely the motion of a silicon oil and saline (NaCl solution) in a sphere experiencing torsional oscillations. The liquids are immiscible, with the denser saline occupying the base of the sphere. The injection of silicon oil is often used to manage complicated retinal re-attachment surgery [184]; however, silicon oil is associated with emulsification during the saccadic rotation of the eyeball, resulting in serious complications such as cataracts and keratopathy [185, 186]. One of the hypotheses in this field is that droplets are generated by the shear stresses at the oil-saline interface induced by the saccadic motion of the eyeball [187]. An experimental study was investigated by PhD student Ru Wang using a 20 mm diameter glass sphere filled with a mixture solution of silicon oil and saline, rotated by a stepper motor. A CFD simulation of the experiment was constructed and is presented in Appendix B. Good agreement was obtained between experimental and CFD results at different conditions, indicating that the simulation can be used to predict the flow patterns and distribution of shear stress of silicone oil. The model could also be employed to estimate the likelihood of occurrence of oil droplets.

Chapter 6   Conclusions and Recommendations for Future Work

6.1   Millimanipulation

In this work, the millimanipulation device reported by Magens *et al.* [9] was employed to study the development of layers of petroleum jelly, soft white paraffin and toothpaste *in situ*. CFD simulations employing the regularized Bingham model (RBM) and the bi-viscosity model (BVM) (Section 3.2.5) were constructed to estimate the deformation and flow patterns of PJ and SWP while being scraped.

The range of information that can be obtained from millimanipulation testing was extended. In the visualisation studies, wall slip was observed for PJ and SWP under some conditions. Given this information and measurements of the force acting on the blade, the adhesive strength of these layers could be estimated. The characteristic time for stress relaxation could be determined by interrupted testing, and the material's bulk (cohesive) yield stress could be estimated from the interruption data and simple metal cutting theory.

The numerical results for PJ using the RBM showed better agreement with the experimental data, while for SWP the BVM gave better agreement with the measurements. This is mainly attributed to the description of the rheology in the yielding transition. The estimated velocity distributions were also similar to those calculated from the particle tracing method (visualisation). A sensitivity analysis for the rheological parameters in both viscosity models demonstrated that the yield stress dominated in each case. For the BVM, the creeping viscosity was also important.

Modelling of viscoelastic fluids

The standard OpenFOAM solver cannot support modelling of the visco-elastic behaviour of fluids. Elasticity plays an important role in the initial deformation of the viscoplastic fluids studied in this work. In order to understand the removal behaviour of such viscoplastic soils fully, development of an algorithm for the elastic behaviour is required.

Implementation of time-dependent viscosity model

In addition to the elasticity of soft solid materials, the results for the effect of scraping speed have shown that the simulations using both the RBM and BVM could not capture the creep behaviour at low scraping velocities. Further work in OpenFOAM, implementing a suitable time-dependent viscosity model, such as simple rate-controlled model [188], is required.

Modelling of slip

The current CFD model could not simulate wall slip due to the fact that slip is associated with the interaction between the soil material and substrate surface at the molecular scale. Molecular dynamics simulations [189] (or meso-scale) are one alternative approach to study the adhesive and cohesive failure in the millimanipulation tests.

Estimation of the rheological parameters using CFD simulation and visualisation

The sensitivity tests of the rheological parameters in the simulation have showed the feasibility of using the CFD simulation to estimate the material's rheological parameters. However, the resolution and accuracy of the current visualisation system were not good enough to support this. Improved hardware could be used to achieve this.

6.2   SiDG

In this dissertation, the SiDG device was conceived, designed, constructed and commissioned. Swelling of gelatin, PVAc and CMS layers were monitored at different pH and temperatures. The results showed that all materials underwent rapid initial hydration. After the hydration stage, the swelling profile of gelatin was controlled by Fickian diffusion. A similar trend was observed with PVAc at pH < 11, whilst at pH ≥ 11, relaxation (due to the hydrolysis and ionisation) controlled.

Cracks on the surface of the CMS layers caused uncertainty of the measurements using SiDG. A 3D CFD model with cracks beneath the nozzle rim was created, showing 8% and 3% measurement errors for ejection and suction modes due to the presence of cracks, respectively.

pH & temperature-controlled SiDG (batch reactor)

The experiments reported here were conducted at ambient temperature (20 °C). Changes in temperature are known to have significant effects on the swelling behavior of soft solid layers [109]. A SiDG integrated with temperature and pH controls would extend the capability of the device for studying the cleaning behavior of soil layers. In addition, cleaning generally involves chemical reactions as well as physical interactions. Installing a dosing system to adjust the pH or introduce reagents, to make the SiDG chamber become a batch reactor would be a logical next development [109].

6.3   iFDG

The iFDG device was conceived, designed, constructed, commissioned and demonstrated. Mild steel, 316 SS and pure copper substrates were tested, and the results showed that the slope of the pk-pk voltage against the clearance increased with substrate conductivity. Moreover, non-metallic layers (*e.g*. PVC tape and glass slides) did not affect this slope, indicating that the iFDG concept could be used to study layer growth and removal. Operation was demonstrated with a range of liquids: deionised water, UHT milk (opaque), and more viscous washing-up

liquid and non-Newtonian 1% and 3% CMC solutions. CFD simulations gave good agreement with the experimental data. An ice growth test using the iFDG device was conducted, demonstrating the viability of iFDG measurement.

Temperature drift-calibrated iFDG

Temperature drift can affect the inductive proximity sensor action significantly. In the current iFDG system, the thermocouple was mounted close to the nozzle, not on the coil, which resulted in some inaccuracy in coil temperature measurement. In addition, the magnetic field generated by the coil was affected by the thermocouple. To overcome these, the thermocouple needs to be installed close to the coil (embedded in the nozzle head) and a relay added to switch the thermocouple off while the proximity sensor works.

6.4   Coupled Deformation of a Viscoplastic Layer and ZFDG Flows

The experimental results showed that in ejection mode, deformation of the layer occurred within 1 s, and did not change thereafter. In suction mode, petroleum jelly was drawn into the nozzle and then stopped after some finite time. As withdrawing was interrupted by breakage due to inhomogeneity of petroleum jelly (Section 5.2), the layer surface became hill-shaped.

The VOF approach was employed in the CFD simulations to predict the change of topography of a petroleum jelly layer subject to ZFDG testing at different clearances. Acceptable agreement for the layer topographies between the CTS measurements and simulation results was obtained. The deviation of predicted topographies is attributed to the roughness and homogeneity of the layer, and the resolution of the nozzle positioner. The timescale of predicted pressure drop did not agree with the experiments mainly due to the ballooning effect, which could not be simulated.

Continuous FDG

The experiments of ZFDG showed that in suction mode, petroleum jelly was drawn into the nozzle. After the test, removing soil from the nozzle was required, indicating that suction mode was not suitable for measuring the thickness of such viscoplastic materials. However, the current syringe pump cannot support continuous infusion due to the fixed volume of syringe. A dual pump plumbing kit is therefore needed, which is a dual check valve for two syringes. Liquid is withdrawn from a reservoir, and infused out through another line.

Further study for FDG flows

The coupled deformation of the viscoplastic layer subject to ZFDG testing was difficult to study due to its fast deformation (taking less than 1 s). There are two other things that could be done: (i) capture the deformation using particle image velocimetry (PIV). PIV is an optical technique, in which fluid is seeded with tracer particles and then illuminated by a laser to track their flow trajectories. The PIV method could be employed with a transparent FDG nozzle tube for tracking the flow field around the nozzle head. (ii) image the layer from beneath the substrate, using an inverted or other confocal microscope.

6.5 Modelling of Cleaning a Viscoplastic Soil Layer Using an Impinging Water Jet

The multi-phase CFD model was also used to simulate a water jet impinging on a vertical plane coated with a petroleum jelly layer. Comparing the predicted shape of the crater to the experimental data, good agreement was obtained, indicating that the modelling could be employed to estimate the deformation of layers in cleaning processes. The results also confirmed that the ratio of the film to layer thickness, h_f/δ_0, had a significant influence on the shape of the cleaning front. Moreover, the rate of growth of the cleaned radius agreed with the measured values well and both showed good fits to the Wilson $et\ al.$ model [64].

There are a series of studies which could be done, including exploring the effect of h_f/δ_0, film physical properties, layer rheology etc. for comparison with the recent work by Fernandes and Wilson [183]. In addition, this work focused on the peeling mechanism, while the cleaning mechanisms, including diffusive dissolution, cohesive separation, viscous shifting and adhesive detachment, often do not occur alone. Further CFD simulations involving in mass transfer and reactions for different soft solid materials should be conducted.

6.6   *Achievements*

This dissertation has provided several new tools for studying the cleaning behaviour of soil layers on solid substrates and generated insights into the cleaning mechanisms involved with some soils.

The millimanipulation device reported by Magens *et al.* [9] has been developed to measure the adhesive and cohesive strengths of stiff soft solid layers as well as estimate their yield stresses *in situ*. The device could be employed to estimate the rheological behaviour of soft solid soils which cannot be loaded into a rheometer. A CFD model of millimanipulation has been constructed which describes the deformation of the layers while being scraped. This has been reported in Tsai *et al*. *J. Food Eng* (2020) 110086.

The ability of the SiDG device to measure the early stage and long term behaviour of swelling of soil layers immersed in a liquid environment has been demonstrated, reported in Tsai *et al. AlChE J*, 65 (2019) e16664.The iFDG concept, which integrates an inductive proximity sensor for locating the substrate into the gauging head, has been demonstrated for various substrates and gauging liquids. A CFD simulation of iFDG for high-viscosity and non-Newtonian fluids was also created, which enables one to quantify shear stress distribution generated by the gauging action (Tsai *et al.*, *Ind Eng Chem Res*, 58 (2019) 23124-23134).

A two-phase CFD model has been developed which captures the interaction between a viscoplastic soil layer and ZFDG flows. It has been extended to the case of a water jet impinging on a viscoplastic layer and captures several of the salient features.

These techniques provide quantitative information about cleaning mechanisms for soft solid layers and related fouling deposits which will allow currently empirical methods to be replaced, deterministic models constructed, and cleaning performance predicted.

References

[1] B. Carpentier, O. Cerf, Biofilms and their consequences, with particular reference to hygiene in the food industry, *J Appl Bacteriol*, 75 (1993) 499-511.

[2] L.C. Simoes, M. Simões, Biofilms in drinking water: problems and solutions, *RSC Adv*, 3 (2013) 2520-2533.

[3] W. Finnegan, J. Goggins, E. Clifford, X. Zhan, Global warming potential associated with dairy products in the Republic of Ireland, *J Clean Prod*, 163 (2017) 262-273.

[4] H. MÜLler-Steinhagen, M.R. Malayeri, A.P. Watkinson, Fouling of heat exchangers-new approaches to solve an old problem, *Heat Transfer Eng*, 26 (2005) 1-4.

[5] Dairy: World Markets and Trade, in, Department of Agriculture, United States 2019.

[6] S. Wang, F. Schlüter, N. Gottschalk, S. Scholl, D.I. Wilson, W. Augustin, Aseptic zero discharge fluid dynamic gauging for measuring the thickness of soft layers on surfaces, *Chem Ing Tech*, 88 (2016) 1530-1538.

[7] T.R. Tuladhar, W.R. Paterson, N. Macleod, D.I. Wilson, Development of a novel non-contact proximity gauge for thickness measurement of soft deposits and its application in fouling studies, *Can J Chem Eng*, 78 (2000) 935-947.

[8] S. Wang, K. Xu Zhou, G. Christie, D.I. Wilson, Development of zero discharge net flow fluid dynamic gauging for studying biofilm and spore removal, *Food Bioprod Proc*, 113 (2018) 60-67.

[9] O.M. Magens, Y. Liu, J.F.A. Hofmans, J.A. Nelissen, D. Ian Wilson, Adhesion and cleaning of foods with complex structure: Effect of oil content and fluoropolymer coating characteristics on the detachment of cake from baking surfaces, *J Food Eng*, 197 (2017) 48-59.

[10] E. Wallhäußer, M.A. Hussein, T. Becker, Detection methods of fouling in heat exchangers in the food industry, *Food Control*, 27 (2012) 1-10.

[11] M. Gryta, Calcium sulphate scaling in membrane distillation process, *Chemical Papers*, 63 (2009) 146-151.

[12] R.W. Bell, C.F. Sanders, Prevention of milestone formation in a high-temperature-short-time heater by preheating milk, skim milk and whey, *J Dairy Sci*, 27 (1944) 499-504.

[13] M. Schorr, B. Valdez, J. Ocampo, A. Eliezer, *Corrosion control in the desalination industry*, 2011.

[14] A.P. Watkinson, D.I. Wilson, Chemical reaction fouling: A review, *Exp Therm Fluid Sci*, 14 (1997) 361-374.

[15] A. Watkinson, Critical review of organic fluid fouling, 1988.

[16] M. Lalande, J.-P. Tissier, Fouling of heat transfer surfaces related to β-lactoglobulin denaturation during heat processing of milk, *Biotechnol Prog*, 1 (1985) 131-139.

[17] M. Simões, L.C. Simões, M.J. Vieira, A review of current and emergent biofilm control strategies, *LWT-Food Sci Technol*, 43 (2010) 573-583.

[18] B. Jessen, L. Lammert, Biofilm and disinfection in meat processing plants, *Int Biodeterior Biodegrad*, 51 (2003) 265-269.

[19] A. Matin, Z. Khan, S.M.J. Zaidi, M.C. Boyce, Biofouling in reverse osmosis membranes for seawater desalination: Phenomena and prevention, *Desalination*, 281 (2011) 1-16.

[20] N.P. Gule, N.M. Begum, B. Klumperman, Advances in biofouling mitigation: A review, *Crit Rev Environ Sci Technol*, 46 (2016) 535-555.

[21] M. Tiranuntakul, Evaluation of fouling in a pilot scale membrane bioreactor, James Cook University, 2011.

[22] D.I. Wilson, Challenges in cleaning: recent developments and future prospects, *Heat Transfer Eng*, 26 (2005) 51-59.

[23] G. Atkins, What to do about high coking rates, *Petro/Chem Eng*, 34 (1962) 20-25.

[24] H. Visser, T.J. Jeurnink, J. Schraml, P. Fryer, F. Delplace, Fouling and cleaning of heat transfer equipment,(ed.) Visser, H, *IDF Bulletin*, 328 (1997) 10-18.

[25] F. Brahim, W. Augustin, M. Bohnet, Numerical simulation of the fouling process, *Int J Therm Sci*, 42 (2003) 323-334.

[26] J. Quarini, Ice-pigging to reduce and remove fouling and to achieve clean-in-place, *Appl Therm Eng*, 22 (2002) 747-753.

[27] E. Curcio, X. Ji, G. Di Profio, A.O. Sulaiman, E. Fontananova, E. Drioli, Membrane distillation operated at high seawater concentration factors: Role of the membrane on CaCO3 scaling in presence of humic acid, *J Membr Sci*, 346 (2010) 263-269.

[28] T.R. Tuladhar, W.R. Paterson, D.I. Wilson, Investigation of alkaline cleaning-in-place of whey protein deposits using dynamic gauging, *Food Bioprod Proc*, 80 (2002) 199-214.

[29] D.I. Wilson, Fouling during food processing – progress in tackling this inconvenient truth, *Curr Opin Food Sci*, 23 (2018) 105-112.

[30] C. Huyskens, E. Brauns, E. Van Hoof, H. De Wever, A new method for the evaluation of the reversible and irreversible fouling propensity of MBR mixed liquor, *J Membr Sci*, 323 (2008) 185-192.

[31] K.R. Goode, K. Asteriadou, P.T. Robbins, P.J. Fryer, Fouling and cleaning studies in the food and beverage industry classified by cleaning type, *Compr Rev Food Sci F*, 12 (2013) 121-143.

[32] G.A. Blondin, S.J. Comiskey, J.M. Harkin, Recovery of fermentable sugars from process vegetable wastewaters, *Energy in Agriculture*, 2 (1983) 21-36.

[33] M. Joppa, H. Köhler, S. Kricke, J.P. Majschak, J. Fröhlich, F. Rüdiger, Simulation of jet cleaning: Diffusion model for swellable soils, *Food Bioprod Proc*, 113 (2019) 168-176.

[34] P.J. Fryer, K. Asteriadou, A prototype cleaning map: A classification of industrial cleaning processes, *Trends Food Sci Technol*, 20 (2009) 255-262.

[35] H. Köhler, V. Liebmann, M. Joppa, J. Fröhlich, J. Majschak, F. Rüdiger, On the concept of CFD-based prediction of cleaning for film-like soils in: Heat Exchanger Fouling and Cleaning, 2019.

[36] J. Escrig, E. Woolley, S. Rangappa, A. Simeone, N.J. Watson, Clean-in-place monitoring of different food fouling materials using ultrasonic measurements, *Food Control*, 104 (2019) 358-366.

[37] H. Xin, X.D. Chen, N. Özkan, Removal of a model protein foulant from metal surfaces,

AlChE J, 50 (2004) 1961-1973.

[38] C.R. Gillham, P.J. Fryer, A.P.M. Hasting, D.I. Wilson, Cleaning-in-Place of Whey Protein Fouling Deposits: Mechanisms Controlling Cleaning, *Food Bioprod Proc*, 77 (1999) 127-136.

[39] P. Saikhwan, J.Y.M. Chew, W.R. Paterson, D.I. Wilson, Swelling and Its Suppression in the Cleaning of Polymer Fouling Layers, *Ind Eng Chem Res*, 46 (2007) 4846-4855.

[40] J.G. Detry, P.G. Rouxhet, L. Boulangé-Petermann, C. Deroanne, M. Sindic, Cleanability assessment of model solid surfaces with a radial-flow cell, *Colloids Surf, A*, 302 (2007) 540-548.

[41] A.J. García, P. Ducheyne, D. Boettiger, Quantification of cell adhesion using a spinning disc device and application to surface-reactive materials, *Biomaterials*, 18 (1997) 1091-1098.

[42] Z. Zhang, M.A. Ferenczi, A.C. Lush, C.R. Thomas, A novel micromanipulation technique for measuring the bursting strength of single mammalian cells, *Appl Microbiol Biotechnol*, 36 (1991) 208-210.

[43] W. Liu, G.K. Christian, Z. Zhang, P.J. Fryer, Development and use of a micromanipulation technique for measuring the force required to disrupt and remove fouling deposits, *Food Bioprod Proc*, 80 (2002) 286-291.

[44] N. Akhtar, J. Bowen, K. Asteriadou, P.T. Robbins, Z. Zhang, P.J. Fryer, Matching the nano- to the meso-scale: Measuring deposit–surface interactions with atomic force microscopy and micromanipulation, *Food Bioprod Proc*, 88 (2010) 341-348.

[45] S. Ashokkumar, J. Adler-Nissen, Evaluating non-stick properties of different surface materials for contact frying, *J Food Eng*, 105 (2011) 537-544.

[46] A. Ali, D. de'Ath, D. Gibson, J. Parkin, Z. Alam, G. Ward, D.I. Wilson, Development of a 'millimanipulation' device to study the removal of soft solid fouling layers from solid substrates and its application to cooked lard deposits, *Food Bioprod Proc*, 93 (2015) 256-268.

[47] E. Fuchs, S. Kricke, E. Schöhl, J.-P. Majschak, Effect of industrial scale stand-off distance on water jet break-up, cleaning and forces imposed on soil layers, *Food Bioprod Proc*, (2018).

[48] G.L. Cuckston, Z. Alam, J. Goodwin, G. Ward, D.I. Wilson, Quantifying the effect of solution formulation on the removal of soft solid food deposits from stainless steel substrates, *J Food Eng*, 243 (2019) 22-32.

[49] M. Maillard, C. Mézière, P. Moucheront, C. Courrier, P. Coussot, Blade-coating of yield stress fluids, *J NonNewton Fluid Mech*, 237 (2016) 16-25.

[50] P. Wongsirichot, Deformation and removal forces in millimanipulation, in: Department of Chemical Engineering and Biotechnology, University of Cambridge, 2014.

[51] R. Mercadé-Prieto, B. Nguyen, R. Allen, D. York, J.A. Preece, T.E. Goodwin, Z. Zhang, Determination of the elastic properties of single microcapsules using micromanipulation and finite element modeling, *Chem Eng Sci*, 66 (2011) 2042-2049.

[52] M.C.M. van Loosdrecht, J. Lyklema, W. Norde, A.J.B. Zehnder, Bacterial adhesion: A physicochemical approach, *Microb Ecol*, 17 (1989) 1-15.

[53] D.P. Bakker, A. van der Plaats, G.J. Verkerke, H.J. Busscher, H.C. van der Mei, Comparison of velocity profiles for different flow chamber designs used in studies of microbial adhesion to surfaces, *Appl Environ Microbiol*, 69 (2003) 6280-6287.

[54] P.A. Cole, K. Asteriadou, P.T. Robbins, E.G. Owen, G.A. Montague, P.J. Fryer, Comparison of cleaning of toothpaste from surfaces and pilot scale pipework, *Food Bioprod Proc*, 88 (2010) 392-400.

[55] K. Alba, I.A. Frigaard, Dynamics of the removal of viscoplastic fluids from inclined pipes, *J NonNewton Fluid Mech*, 229 (2016) 43-58.

[56] D.A. de Sousa, E.J. Soares, R.S. de Queiroz, R.L. Thompson, Numerical investigation on gas-displacement of a shear-thinning liquid and a visco-plastic material in capillary tubes, *J NonNewton Fluid Mech*, 144 (2007) 149-159.

[57] T.C. Papanastasiou, Flows of materials with yield, *J Rheol*, 31 (1987) 385-404.

[58] R.L. Thompson, E.J. Soares, R.D.A. Bacchi, Further remarks on numerical investigation on gas displacement of a shear-thinning liquid and a visco-plastic material in capillary tubes, *J NonNewton Fluid Mech*, 165 (2010) 448-452.

[59] J.F. Freitas, E.J. Soares, R.L. Thompson, Viscoplastic–viscoplastic displacement in a plane channel with interfacial tension effects, *Chem Eng Sci*, 91 (2013) 54-64.

[60] A. Yeckel, S. Middleman, Removal of a viscous film from a rigid plane surface by an impinging liquid jet, *Chem Eng Commun*, 50 (1987) 165-175.

[61] T.T. Hsu, T.W. Walker, C.W. Frank, G.G. Fuller, Role of fluid elasticity on the dynamics of rinsing flow by an impinging jet, *Phys Fluids*, 23 (2011) 033101.

[62] T.W. Walker, T.T. Hsu, C.W. Frank, G.G. Fuller, Role of shear-thinning on the dynamics of rinsing flow by an impinging jet, *Phys Fluids*, 24 (2012) 093102.

[63] D.I. Wilson, B.L. Le, H.D.A. Dao, K.Y. Lai, K.R. Morison, J.F. Davidson, Surface flow and drainage films created by horizontal impinging liquid jets, *Chem Eng Sci*, 68 (2012) 449-460.

[64] D.I. Wilson, P. Atkinson, H. Köhler, M. Mauermann, H. Stoye, K. Suddaby, T. Wang, J.F. Davidson, J.P. Majschak, Cleaning of soft-solid soil layers on vertical and horizontal surfaces by stationary coherent impinging liquid jets, *Chem Eng Sci*, 109 (2014) 183-196.

[65] H.W. Glover, T. Brass, R.K. Bhagat, J.F. Davidson, L. Pratt, D.I. Wilson, Cleaning of complex soil layers on vertical walls by fixed and moving impinging liquid jets, *J Food Eng*, 178 (2016) 95-109.

[66] R.K. Bhagat, D.I. Wilson, Flow in the thin film created by a coherent turbulent water jet impinging on a vertical wall, *Chem Eng Sci*, 152 (2016) 606-623.

[67] R.K. Bhagat, A.M. Perera, D.I. Wilson, Cleaning vessel walls by moving water jets: Simple models and supporting experiments, *Food Bioprod Proc*, 102 (2017) 31-54.

[68] R.R. Fernandes, D. Oevermann, D.I. Wilson, Cleaning insoluble viscoplastic soil layers using static and moving coherent impinging water jets, *Chem Eng Sci*, 207 (2019) 752-768.

[69] H.H. Hu, Chapter 10 - Computational Fluid Dynamics, in: P.K. Kundu, I.M. Cohen, D.R. Dowling (Eds.) Fluid Mechanics (Fifth Edition), Academic Press, Boston, 2012, pp. 421-472.

[70] M. Joppa, H. Köhler, F. Rüdiger, J.-P. Majschak, J. Fröhlich, Experiments and simulations on the cleaning of a swellable soil in plane channel flow, *Heat Transfer Eng*, 38 (2017) 786-795.

[71] S. Burgess, X. Li, J. Holland, High spatial resolution energy dispersive X-ray spectrometry in the SEM and the detection of light elements including lithium, *Microscopy and Analysis*, 6 (2013) S8-S13.

[72] W. Li, G. Ling, F. Lei, N. Li, W. Peng, K. Li, H. Lu, F. Hang, Y. Zhang, Ceramic membrane fouling and cleaning during ultrafiltration of limed sugarcane juice, *Sep Purif Technol*, 190 (2018) 9-24.

[73] C. Hagsten, A. Altskär, S. Gustafsson, N. Lorén, L. Hamberg, F. Innings, M. Paulsson, T. Nylander, Composition and structure of high temperature dairy fouling, *Food Structure*, 7 (2016) 13-20.

[74] A.K. Chatterjee, 8 - X-Ray Diffraction, in: V.S. Ramachandran, J.J. Beaudoin (Eds.) Handbook of Analytical Techniques in Concrete Science and Technology, William Andrew Publishing, Norwich, NY, 2001, pp. 275-332.

[75] K.R. Goode, J. Bowen, N. Akhtar, P.T. Robbins, P.J. Fryer, The effect of temperature on adhesion forces between surfaces and model foods containing whey protein and sugar, *J Food Eng*, 118 (2013) 371-379.

[76] G. Binnig, C.F. Quate, C. Gerber, Atomic force microscope, *Phys Rev Lett*, 56 (1986) 930-933.

[77] P.-S. Joanna, T. Katarzyna, J. Marek, An analysis of milk fouling formed during heat treatment on a stainless steel surface with different degrees of roughness, *Czech J Food Sci*, 34 (2016) 271-279.

[78] M. Marvin, Microscopy apparatus, Google Patents, 1961.

[79] J.Y.M. Chew, W.R. Paterson, D.I. Wilson, Fluid dynamic gauging for measuring the strength of soft deposits, *J Food Eng*, 65 (2004) 175-187.

[80] S.A. Creber, T.R.R. Pintelon, D.A.W. Graf von der Schulenburg, J.S. Vrouwenvelder, M.C.M. van Loosdrecht, M.L. Johns, Magnetic resonance imaging and 3D simulation studies of biofilm accumulation and cleaning on reverse osmosis membranes, *Food Bioprod Proc*, 88 (2010) 401-408.

[81] J. Hennig, A. Nauerth, H. Friedburg, RARE imaging: A fast imaging method for clinical MR, *Magn Reson Med*, 3 (1986) 823-833.

[82] H. Yoshioka, P.M. Schlechtweg, K. Kose, Chapter 3 - Magnetic Resonance Imaging, in: B.N. Weissman (Ed.) Imaging of Arthritis and Metabolic Bone Disease, W.B. Saunders, Philadelphia, 2009, pp. 34-48.

[83] https://www.nanoscience.com/techniques/scanning-electron-microscopy/.

[84] M.A. Úbeda, W.B. Hussein, M.A. Hussein, J. Hinrichs, T.M. Becker, Acoustic sensing and signal processing techniques for monitoring milk fouling cleaning operations, *Eng Life Sci*, 16 (2016) 67-77.

[85] https://www.olympus-ims.com/.

[86] C. Larimer, J.D. Suter, G. Bonheyo, R.S. Addleman, In situ non-destructive measurement of biofilm thickness and topology in an interferometric optical microscope, *J Biophotonics*, 9 (2016) 656-666.

[87] https://www.keyence.com/ss/products/microscope/roughness/equipment/interferometers.jsp.

[88] N. Macleod, M.D. Cox, R.B. Todd, A profilometric technique for determining local mass-transfer rates: Application to the estimation of local heat-transfer coefficients in a nuclear reactor, *Chem Eng Sci*, 17 (1962) 923-935.

[89] T. Gu, Y.M.J. Chew, W.R. Paterson, D.I. Wilson, Experimental and CFD studies of fluid dynamic gauging in annular flows, *AlChE J*, 55 (2009) 1937-1947.

[90] T.R. Tuladhar, W.R. Paterson, D.I. Wilson, Dynamic gauging in duct flows, *Can J Chem*

Eng, 81 (2003) 279-284.

[91] J.Y.M. Chew, S.J. Tonneijk, W.R. Paterson, D.I. Wilson, Solvent-based cleaning of emulsion polymerization reactors, *Chem Eng J*, 117 (2006) 61-69.

[92] Y.M.J. Chew, W.R. Paterson, D.I. Wilson, Fluid dynamic gauging: A new tool to study deposition on porous surfaces, *J Membr Sci*, 296 (2007) 29-41.

[93] P.W. Gordon, A.D.M. Brooker, Y.M.J. Chew, D.I. Wilson, D.W. York, A scanning fluid dynamic gauging technique for probing surface layers, *Meas Sci Technol*, 21 (2010) 085103.

[94] S.A. Jones, Y.M.J. Chew, M.R. Bird, D.I. Wilson, The application of fluid dynamic gauging in the investigation of synthetic membrane fouling phenomena, *Food Bioprod Proc*, 88 (2010) 409-418.

[95] W.J.T. Lewis, Y.M.J. Chew, M.R. Bird, The application of fluid dynamic gauging in characterising cake deposition during the cross-flow microfiltration of a yeast suspension, *J Membr Sci*, 405-406 (2012) 113-122.

[96] A. Ali, G.J. Chapman, Y.M.J. Chew, T. Gu, W.R. Paterson, D.I. Wilson, A fluid dynamic gauging device for measuring fouling deposit thickness in opaque liquids at elevated temperature and pressure, *Exp Therm Fluid Sci*, 48 (2013) 19-28.

[97] Q. Yang, A. Ali, L. Shi, D.I. Wilson, Zero discharge fluid dynamic gauging for studying the thickness of soft solid layers, *J Food Eng*, 127 (2014) 24-33.

[98] S. Wang, D.I. Wilson, Zero-discharge fluid-dynamic gauging for studying the swelling of soft solid layers, *Ind Eng Chem Res*, 54 (2015) 7859-7870.

[99] M. Lemos, S. Wang, A. Ali, M. Simões, D.I. Wilson, A fluid dynamic gauging device for measuring biofilm thickness on cylindrical surfaces, *Biochem Eng J*, 106 (2016) 48-60.

[100] W.J.T. Lewis, A. Agg, A. Clarke, T. Mattsson, Y.M.J. Chew, M.R. Bird, Development of an automated, advanced fluid dynamic gauge for cake fouling studies in cross-flow filtrations, *Sens Actuators, A*, 238 (2016) 282-296.

[101] W.J.T. Lewis, T. Mattsson, Y.M.J. Chew, M.R. Bird, Investigation of cake fouling and pore blocking phenomena using fluid dynamic gauging and critical flux models, *J Membr Sci*, 533 (2017) 38-47.

[102] J.Y.M. Chew, S.S.S. Cardoso, W.R. Paterson, D.I. Wilson, CFD studies of dynamic gauging, *Chem Eng Sci*, 59 (2004) 3381-3398.

[103] P. Saikhwan, T. Geddert, W. Augustin, S. Scholl, W.R. Paterson, D.I. Wilson, Effect of surface treatment on cleaning of a model food soil, *Surf Coat Technol*, 201 (2006) 943-951.

[104] R.J. Hooper, W.R. Paterson, D.I. Wilson, Comparison of whey protein model foulants for studying cleaning of milk fouling deposits, *Food Bioprod Proc*, 84 (2006) 329-337.

[105] T. Gu, Y.M.J. Chew, W.R. Paterson, D.I. Wilson, Experimental and CFD studies of fluid dynamic gauging in duct flows, *Chem Eng Sci*, 64 (2009) 219-227.

[106] T. Gu, F. Albert, W. Augustin, Y.M.J. Chew, M. Mayer, W.R. Paterson, S. Scholl, I. Sheikh, K. Wang, D.I. Wilson, Application of fluid dynamic gauging to annular test apparatuses for studying fouling and cleaning, *Exp Therm Fluid Sci*, 35 (2011) 509-520.

[107] V.Y. Lister, C. Lucas, P.W. Gordon, Y.M.J. Chew, D.I. Wilson, Pressure mode fluid dynamic gauging for studying cake build-up in cross-flow microfiltration, *J Membr Sci*, 366 (2011) 304-313.

[108] J.M. Peralta, Y.M.J. Chew, D.I. Wilson, An analytical method for selecting the optimal

nozzle external geometry for fluid dynamic gauging, *Chem Eng Sci*, 66 (2011) 3579-3591.

[109] P.W. Gordon, A.D.M. Brooker, Y.M.J. Chew, N. Letzelter, D.W. York, D.I. Wilson, Elucidating enzyme-based cleaning of protein soils (gelatine and egg yolk) using a scanning fluid dynamic gauge, *Chem Eng Res Des*, 90 (2012) 162-171.

[110] P.W. Gordon, M. Schöler, H. Föste, M. Helbig, W. Augustin, Y.M.J. Chew, S. Scholl, J.-P. Majschak, D.I. Wilson, A comparison of local phosphorescence detection and fluid dynamic gauging methods for studying the removal of cohesive fouling layers: Effect of layer roughness, *Food Bioprod Proc*, 92 (2014) 46-53.

[111] X. Du, F. Qu, H. Liang, K. Li, H. Chang, G. Li, Cake properties in ultrafiltration of TiO2 fine particles combined with HA: in situ measurement of cake thickness by fluid dynamic gauging and CFD calculation of imposed shear stress for cake controlling, *Environ Sci Pollut R*, 23 (2016) 8806-8818.

[112] R. Pérez-Mohedano, N. Letzelter, S. Bakalis, Swelling and hydration studies on egg yolk samples via scanning fluid dynamic gauge and gravimetric tests, *J Food Eng*, 169 (2016) 101-113.

[113] T. Mattsson, W.J.T. Lewis, Y.M.J. Chew, M.R. Bird, The use of fluid dynamic gauging in investigating the thickness and cohesive strength of cake fouling layers formed during cross-flow microfiltration, *Sep Purif Technol*, (2017).

[114] K. Xu Zhou, N. Li, G. Christie, D.I. Wilson, Assessing the impact of germination and sporulation conditions on the adhesion of bacillus spores to glass and stainless steel by fluid dynamic gauging, *J Food Sci*, 82 (2017) 2614-2625.

[115] G. Cuckston, Z. Alam, J. Goodwin, M. Groombridge, E. Watson, D.I. Wilson, Development of novel experimental techniques to elucidate the cleaning of complex food soils, in: Chemeca 2018, Queenstown, New Zealand, 2018.

[116] T. Mattsson, W.J.T. Lewis, Y.M.J. Chew, M.R. Bird, The use of fluid dynamic gauging in investigating the thickness and cohesive strength of cake fouling layers formed during cross-flow microfiltration, *Sep Purif Technol*, 198 (2018) 25-30.

[117] O.P.W. Peck, Y.M.J. Chew, M.R. Bird, On-line quantification of thickness and strength of single and mixed species biofilm grown under controlled laminar flow conditions, *Food Bioprod Proc*, 113 (2018) 49-59.

[118] S.R. Suwarno, W. Huang, Y.M.J. Chew, S.H.H. Tan, A.E. Trisno, Y. Zhou, On-line biofilm strength detection in cross-flow membrane filtration systems, *Biofouling*, 34 (2018) 123-131.

[119] M. Zhou, T. Mattsson, Effect of crossflow regime on the deposit and cohesive strength of membrane surface fouling layers, *Food Bioprod Proc*, 115 (2019) 185-193.

[120] J.-H. Tsai, G.L. Cuckston, B. Hallmark, D.I. Wilson, Fluid-dynamic gauging for studying the initial swelling of soft solid layers, *AlChE J*, 0 (2019) e16664.

[121] J.-H. Tsai, B. Hallmark, D.I. Wilson, Integrated Fluid Dynamic Gauge for Measuring the Thickness of Soft Solid Layers Immersed in Opaque, Viscous, and/or Non-Newtonian Liquids in Situ, *Ind Eng Chem Res*, (2019).

[122] A.Q. Colombo, E.J. Steynor, Developing dynamic gauging., in: Department of Chemical Engineering, University of Cambridge, UK., 2002.

[123] R.P. Chhabra, J.F. Richardson, *Non-Newtonian flow in the process industries: fundamentals and engineering applications*, Butterworth-Heinemann, 1999.

[124] A. Koocheki, A. Ghandi, S.M.A. Razavi, S.A. Mortazavi, T. Vasiljevic, The rheological properties of ketchup as a function of different hydrocolloids and temperature, *Int J Food*

Sci Tech, 44 (2009) 596-602.

[125] Z. Huang, M. Lucas, M.J. Adams, A numerical and experimental study of the indentation mechanics of plasticine, *The Journal of Strain Analysis for Engineering Design*, 37 (2002) 141-150.

[126] Y. Liu, Adhesion and Removal of Fouling Layers from Anti-fouling Coatings, in: Department of Chemical Engineering and Biotechnology, University of Cambridge, 2015.

[127] S. Wang, The development of automated zero-discharge fluid dynamic gauging for studying soft solid surface layers, in: Department of Chemical Engineering and Biotechnology, University of Cambridge, 2017.

[128] C. Xie, Real Time Non-Invasive Swelling Measurements of Ionic Hydrogels, in: Department of Chemical Engineering and Biotechnology, University of Cambridge, 2018.

[129] D. Allan, Caswell, T., Keim, N., & van der Wel, C. , Trackpy, in, 2016. github.com/soft-matter/trackpy.

[130] C.W. Macosko, *Rheology: Principles, Measurements, and Applications*, Wiley, 1994.

[131] C. Chang, D.V. Boger, Q.D. Nguyen, The yielding of waxy crude oils, *Ind Eng Chem Res*, 37 (1998) 1551-1559.

[132] J. Yang, R.K. Bhagat, R.R. Fernandes, M. Nordkvist, K.V. Gernaey, U. Krühne, D.I. Wilson, Cleaning of toothpaste from vessel walls by impinging liquid jets and their falling films: Quantitative modelling of soaking effects, *Chem Eng Sci*, 208 (2019) 115148.

[133] A. Ahuja, G. Luisi, A. Potanin, Rheological measurements for prediction of pumping and squeezing pressures of toothpaste, *J NonNewton Fluid Mech*, 258 (2018) 1-9.

[134] A.N. Beris, M. Avgousti, A. Souvaliotis, Spectral calculations of viscoelastic flows: evaluation of the Giesekus constitutive equation in model flow problems, *J NonNewton Fluid Mech*, 44 (1992) 197-228.

[135] J.G. Oldroyd, A.H. Wilson, On the formulation of rheological equations of state, *Proc R Soc London, Ser A*, 200 (1950) 523-541.

[136] J.L. Favero, A.R. Secchi, N.S.M. Cardozo, H. Jasak, Viscoelastic Flow Simulation: Development of a Methodology of Analysis Using the Software OpenFOAM and Differential Constitutive Equations, in: R.M. de Brito Alves, C.A.O. do Nascimento, E.C. Biscaia (Eds.) Computer Aided Chemical Engineering, Elsevier, 2009, pp. 915-920.

[137] F. Habla, H. Marschall, O. Hinrichsen, L. Dietsche, H. Jasak, J.L. Favero, Numerical simulation of viscoelastic two-phase flows using openFOAM®, *Chem Eng Sci*, 66 (2011) 5487-5496.

[138] E.J. O'Donovan, R.I. Tanner, Numerical study of the Bingham squeeze film problem, *J NonNewton Fluid Mech*, 15 (1984) 75-83.

[139] I.A. Frigaard, C. Nouar, On the usage of viscosity regularisation methods for visco-plastic fluid flow computation, *J NonNewton Fluid Mech*, 127 (2005) 1-26.

[140] M. Heuberger, L. Gottardo, M. Dressler, R. Hufenus, Biphasic fluid oscillator with coaxial injection and upstream mass and momentum transfer, *Microfluid Nanofluid*, 19 (2015) 653-663.

[141] Z. Shen, D. Wan, P.M. Carrica, Dynamic overset grids in OpenFOAM with application to KCS self-propulsion and maneuvering, *Ocean Eng*, 108 (2015) 287-306.

[142] P. Schmitt, B. Elsaesser, On the use of OpenFOAM to model oscillating wave surge converters, *Ocean Eng*, 108 (2015) 98-104.

[143] J.W. Slater, Validation Assessment, NPARC Alliance CFD Verification and Validation

Web Site, 2008. https://www.grc.nasa.gov/www/wind/valid/tutorial/valassess.html.

[144] M. Maillard, Étalements de fluides à seuil, in: École Doctorale Sciences, Ingénierie et Environnement, Université Paris-Est, 2015.

[145] J. Boujlel, M. Maillard, A. Lindner, G. Ovarlez, X. Chateau, P. Coussot, Boundary layer in pastes—Displacement of a long object through a yield stress fluid, *J Rheol*, 56 (2012) 1083-1108.

[146] G.M. Corfield, M.J. Adams, B.J. Briscoe, P.J. Fryer, C.J. Lawrence, A critical examination of capillary rheometry for foods (exhibiting wall slip), *Food Bioprod Proc*, 77 (1999) 3-10.

[147] G.S. Chang, J.S. Koo, K.W. Song, Wall slip of vaseline in steady shear rheometry, *Korea-Aust Rheol J*, 15 (2003) 55-61.

[148] S. Chou, K. Sydow, P.J. Martin, J. Bridgwater, D.I. Wilson, Stress relaxation in the extrusion of pastes, *J Eur Ceram Soc*, 23 (2003) 637-646.

[149] J.P. Davim, *Machining: fundamentals and recent advances*, Springer Science & Business Media, 2008.

[150] A.M. Kovrizhnykh, Determining the shear angle, forces, and sizes of shearing elements during metal cutting, *J Appl Mech Tech Phys*, 50 (2009) 147-154.

[151] M. Dinkgreve, M. Fazilati, M.M. Denn, D. Bonn, Carbopol: From a simple to a thixotropic yield stress fluid, *J Rheol*, 62 (2018) 773-780.

[152] P. R. Varges, C. M. Costa, B. S. Fonseca, M. F. Naccache, P.R. De Souza Mendes, Rheological characterization of Carbopol® dispersions in water and in water/glycerol solutions, *Fluids*, 4 (2019) 3.

[153] P.R.d.S. Mendes, R.L. Thompson, A.A. Alicke, R.T. Leite, The quasilinear large-amplitude viscoelastic regime and its significance in the rheological characterization of soft matter, *J Rheol*, 58 (2014) 537-561.

[154] P. Lidon, L. Villa, S. Manneville, Power-law creep and residual stresses in a Carbopol gel, *Rheologica Acta*, 56 (2017) 307-323.

[155] S. Fericean, R. Droxler, New noncontacting inductive analog proximity and inductive linear displacement sensors for industrial automation, *IEEE Sens J*, 7 (2007) 1538-1545.

[156] J.E. Pilliod, E.G. Puckett, Second-order accurate volume-of-fluid algorithms for tracking material interfaces, *J Comput Phys*, 199 (2004) 465-502.

[157] R.I. Issa, Solution of the implicitly discretised fluid flow equations by operator-splitting, *J Comput Phys*, 62 (1986) 40-65.

[158] S.V. Patankar, D.B. Spalding, Paper 5 - A calculation procedure for heat, mass and momentum transfer in three-dimentional parabolic flows in: S.V. Patankar, A. Pollard, A.K. Singhal, S.P. Vanka (Eds.) Numerical Prediction of Flow, Heat Transfer, Turbulence and Combustion, Pergamon, 1983, pp. 54-73.

[159] S. Middleman, *An Introduction to Fluid Dynamics*, John Wiley & Sons, Inc., New York, 1998.

[160] https://www.micro-epsilon.co.uk/displacement-position-sensors/confocal-sensor/.

[161] H. Schott, Swelling kinetics of polymers, *J Macromol Sci Phys*, 31 (1992) 1-9.

[162] H. Schott, Kinetics of swelling of polymers and their gels, *J Pharm Sci*, 81 (1992) 467-470.

[163] P.L. Ritger, N.A. Peppas, A simple equation for description of solute release II. Fickian and anomalous release from swellable devices, *J Controlled Release*, 5 (1987) 37-42.

[164] C.M. Ofner, H. Schott, Swelling studies of gelatin I: Gelatin without additives, *J Pharm Sci*, 75 (1986) 790-796.

[165] F. Ganji, S. Vasheghani-Farahani, E. Vasheghani-Farahani, Theoretical description of hydrogel swelling: A review, *Iran Polym J*, 19 (2010) 375-398.

[166] S. Geng, F.U. Shah, P. Liu, O.N. Antzutkin, K. Oksman, Plasticizing and crosslinking effects of borate additives on the structure and properties of poly(vinyl acetate), *RSC Adv*, 7 (2017) 7483-7491.

[167] W.M. Hosny, P.A. Khalaf-Alaa, Potentiometric study and biological activity of some metal ion complexes of polyvinyl alcohol (PVA), *Int. J. Electrochem. Sci*, 8 (2013) 1520-1533.

[168] L. Brannon-Peppas, N.A. Peppas, Equilibrium swelling behavior of pH-sensitive hydrogels, *Chem Eng Sci*, 46 (1991) 715-722.

[169] R.S. Mahendran, Characterisation of cross-linking and moisture ingress detection in an epoxy/amine resin using fibre-optic sensors, in, University of Birmingham, 2010.

[170] A.P. Mathew, G. Gong, N. Bjorngrim, D. Wixe, K. Oksman, Moisture absorption behavior and its impact on the mechanical properties of cellulose whiskers-based polyvinylacetate nanocomposites, *Polym Eng Sci*, 51 (2011) 2136-2142.

[171] J.D. Kraus, Electromagnetics, International Edition, *New York: McGraw-Hill, Inc*, (1992).

[172] E.A. Saraiva, M.F. Souza, H.T. Filho, W.A. Junior, C.A. Benetti, C.A. Dartora, The FDTD Simulating the Attenuation of a Plan Electromagnetic Wave Crossing of a Radome in the Weather Radar, in: 2006 International Radar Symposium, 2006, pp. 1-6.

[173] Z. Yan, W. Jin, T. Li, Effect of rotating magnetic field (RMF) on segregation of solute elements in CuNi10Fe1Mn alloy hollow billet, *J Mater Eng Perform*, 21 (2012) 1970-1977.

[174] A.B. Metzner, J.C. Reed, Flow of non-newtonian fluids—correlation of the laminar, transition, and turbulent-flow regions, *AlChE J*, 1 (1955) 434-440.

[175] A. Benchabane, K. Bekkour, Rheological properties of carboxymethyl cellulose (CMC) solutions, *Colloid Polym Sci*, 286 (2008) 1173.

[176] D. Jiao, L. Ni, X. Zhu, J. Zhe, Z. Zhao, Y. Lyu, Z. Liu, Measuring gaps using planar inductive sensors based on calculating mutual inductance, *Sens Actuators, A*, 295 (2019) 59-69.

[177] B.B.B. Jensen, Tank cleaning technology: Innovative application to improve clean-in-place (CIP), *Yearbook 2011/2012*, (2011) 26-30.

[178] Chapter 4 - Drilling and Well Completions, in: W.C. Lyons, G.J. Plisga, M.D. Lorenz (Eds.) Standard Handbook of Petroleum and Natural Gas Engineering (Third Edition), Gulf Professional Publishing, Boston, 2016, pp. 4-1-4-584.

[179] W.F. Riley, *Mechanics of Materials*, John Wiley & Sons, Incorporated, 2006.

[180] R. von Mises, Mechanik der festen Körper im plastisch-deformablen Zustand, *Nachrichten von der Gesellschaft der Wissenschaften zu Göttingen, Mathematisch-Physikalische Klasse*, 1913 (1913) 582-592.

[181] H.G. Weller, G. Tabor, H. Jasak, C. Fureby, A tensorial approach to computational continuum mechanics using object-oriented techniques, *Comput Phys*, 12 (1998) 620-631.

[182] J.U. Brackbill, D.B. Kothe, C. Zemach, A continuum method for modeling surface

tension, *J Comput Phys*, 100 (1992) 335-354.

[183] R.R. Fernandes, D.I. Wilson, Modelling the cleaning of viscoplastic layers by impinging coherent turbulent water jets, *J NonNewton Fluid Mech*, 282 (2020) 104314.

[184] E. de Juan, B. McCuen, J. Tiedeman, Intraocular tamponade and surface tension, *Surv Ophthalmol*, 30 (1985) 47-51.

[185] C. Chan, E. Okun, The question of ocular tolerance to intravitreal liquid silicone: A long-term analysis, *Ophthalmology*, 93 (1986) 651-660.

[186] J. Haut, M. Ullern, M. Chermet, G. Van Effenterre, Complications of intraocular injections of silicone combined with vitrectomy, *Ophthalmologica*, 180 (1980) 29-35.

[187] Y. Toklu, H.B. Cakmak, S.B. Ergun, M.A. Yorgun, S. Simsek, Time course of silicone oil emulsification, *RETINA*, 32 (2012) 2039-2044.

[188] R.G. Larson, Y. Wei, A review of thixotropy and its rheological modeling, *J Rheol*, 63 (2019) 477-501.

[189] A. Jabbarzadeh, J.D. Atkinson, R.I. Tanner, Effect of the wall roughness on slip and rheological properties of hexadecane in molecular dynamics simulation of Couette shear flow between two sinusoidal walls, *Phys Rev E*, 61 (2000) 690-699.

[190] H. Köhler, H. Stoye, M. Mauermann, T. Weyrauch, J.-P. Majschak, How to assess cleaning? Evaluating the cleaning performance of moving impinging jets, *Food Bioprod Proc*, 93 (2015) 327-332.

[191] https://www.e-education.psu.edu/eme807/node/6.

[192] F.X. Milani, D. Nutter, G. Thoma, Invited review: Environmental impacts of dairy processing and products: A review, *J Dairy Sci*, 94 (2011) 4243-4254.

[193] J. Dvarionienė, J. Kruopienė, J. Stankevičienė, Application of cleaner technologies in milk processing industry to improve the environmental efficiency, *Clean Technol Envir*, 14 (2012) 1037-1045.

[194] S. Zouaghi, J. Frémiot, C. André, M.A. Grunlan, C. Gruescu, G. Delaplace, S. Duquesne, M. Jimenez, Investigating the effect of an antifouling surface modification on the environmental impact of a pasteurization process: An LCA study, *Acs Sustain Chem Eng*, 7 (2019) 9133-9142.

[195] M.H. Eide, J.P. Homleid, B. Mattsson, Life cycle assessment (LCA) of cleaning-in-place processes in dairies, *LWT-Food Sci Technol*, 36 (2003) 303-314.

[196] G. Gésan-Guiziou, A.P. Sobańtka, S. Omont, D. Froelich, M. Rabiller-Baudry, F. Thueux, D. Beudon, L. Tregret, C. Buson, D. Auffret, Life cycle assessment of a milk protein fractionation process: Contribution of the production and the cleaning stages at unit process level, *Sep Purif Technol*, 224 (2019) 591-610.

[197] M. Høgaas Eide, T. Ohlsson, A comparison of two different approaches to inventory analysis of dairies, *Int J Life Cycle Assess*, 3 (1998) 209-215.

[198] https://www.statista.com/statistics/263972/egg-production-worldwide-since-1990/.

[199] http://www.gewater.com/zero-liquid-discharge-zld.html.

[200] D. Bergquist, W. Stadelman, O. Cotterill, Egg science and technology, Food Product Press New York, NY, 1995, pp. 335-376 p.

[201] T.A.G. Langrish, W.C. Chan, K. Kota, Comparison of maltodextrin and skim milk wall deposition rates in a pilot-scale spray dryer, *Powder Technol*, 179 (2007) 84-89.

[202] M. Krokida, M. Taxiarchou, A. Politis, A. Peppas, K. Kyriakopoulou, Life cycle assessment (LCA) on European skimmed milk powder processing production plant, *Sci*

Bull Ser F Biotechnol, 20 (2016) 280-285.

[203] M. Yan, N.M. Holden, Life cycle assessment of multi-product dairy processing using Irish butter and milk powders as an example, *J Clean Prod*, 198 (2018) 215-230.

[204] L. Li, H.T. Lv, R.P. Deng, Z.K. Liao, X.E. Wu, X.D. Chen, Experimental investigation of egg ovalbumin scaling on heated stainless steel surface and scale-removal compared with that of whey protein, *Colloids Surf, B*, 107 (2013) 198-204.

[205] G. Wernet, C. Bauer, B. Steubing, J. Reinhard, E. Moreno-Ruiz, B. Weidema, The ecoinvent database version 3 (part I): overview and methodology, *Int J Life Cycle Assess*, 21 (2016) 1218-1230.

[206] N. Pelletier, M. Ibarburu, H. Xin, A carbon footprint analysis of egg production and processing supply chains in the Midwestern United States, *J Clean Prod*, 54 (2013) 108-114.

[207] J.A.W. Gut, J.M. Pinto, A.L. Gabas, J. Telis-Romero, Continuous pasteurization of egg yolk: thermophysical properties and process simulation *J Food Process Eng*, 28 (2005) 181-203.

[208] M. Helbig, S. Zahn, K. Böttcher, H. Rohm, J.P. Majschak, Laboratory methods to predict the cleaning behaviour of egg yolk layers in a flow channel, *Food Bioprod Proc*, 113 (2019) 108-117.

[209] F.A. Nasr, H.S. Doma, S.A. El-Shafai, E.A. Taleb, Management of industrial wastewater (case study) *J Appl Sci Res*, 8 (2012) 3004-3011.

[210] J. Yang, K. Kjellberg, B.B.B. Jensen, M. Nordkvist, K.V. Gernaey, U. Krühne, Investigation of the cleaning of egg yolk deposits from tank surfaces using continuous and pulsed flows, *Food Bioprod Proc*, 113 (2019) 154-167.

[211] https://www.rivm.nl/en/life-cycle-assessment-lca/recipe.

[212] R.W. Holloway, L. Miller-Robbie, M. Patel, J.R. Stokes, J. Munakata-Marr, J. Dadakis, T.Y. Cath, Life-cycle assessment of two potable water reuse technologies: MF/RO/UV–AOP treatment and hybrid osmotic membrane bioreactors, *J Membr Sci*, 507 (2016) 165-178.

[213] K. Tarnacki, M. Meneses, T. Melin, J. van Medevoort, A. Jansen, Environmental assessment of desalination processes: Reverse osmosis and Memstill®, *Desalination*, 296 (2012) 69-80.

[214] A. Berggren, LCA of egg phospholipids, 2013.

[215] S. Kim, B. Dale, Life cycle inventory information of the United States electricity system, *Int J Life Cycle Assess*, 10 (2005) 294-304.

[216] K. Kjellberg, Rotary jet head 'burst'cleaning technology delivers significant savings in cleaning costs, *EHEDG Yearbook 2015/2016*, (2016) 96-98.

[217] A.Y. Tamime, *Cleaning-in-place: dairy, food and beverage operations*, John Wiley & Sons, 2009.

[218] H. Xin, X.D. Chen, N. ÖZkan, Whey protein-based gel as a model material for studying initial cleaning mechanisms of milk fouling, *J Food Sci*, 67 (2002) 2702-2711.

[219] M.R. Bird, P.J. Fryer, Analytical model for the cleaning of food process plant, in: Institution of Chemical Engineers Symposium Series, 1992, pp. 325-330.

[220] R. Mercadé-Prieto, X.D. Chen, Caustic-induced gelation of whey deposits in the alkali cleaning of membranes, *J Membr Sci*, 254 (2005) 157-167.

[221] K.R. Morison, R.J. Thorpe, Spinning disc cleaning of skimmed milk and whey protein

deposits, *Food Bioprod Proc*, 80 (2002) 319-325.

[222] T. Pogiatzis, E.M. Ishiyama, W.R. Paterson, V.S. Vassiliadis, D.I. Wilson, Identifying optimal cleaning cycles for heat exchangers subject to fouling and ageing, *Applied Energy*, 89 (2012) 60-66.

[223] C. Arpagaus, F. Bless, M. Uhlmann, J. Schiffmann, S.S. Bertsch, High temperature heat pumps: Market overview, state of the art, research status, refrigerants, and application potentials, *Energy*, 152 (2018) 985-1010.

[224] J. Peng, L. Lu, H. Yang, Review on life cycle assessment of energy payback and greenhouse gas emission of solar photovoltaic systems, *Renew Sust Energ Rev*, 19 (2013) 255-274.

[225] Y.K. Chan, C.O. Ng, P.C. Knox, M.J. Garvey, R.L. Williams, D. Wong, Emulsification of silicone oil and eye movements, *Invest Ophth Vis Sci*, 52 (2011) 9721-9727.

[226] J. Valone, M. McCarthy, Emulsified anterior chamber silicone oil and glaucoma, *Ophthalmology*, 101 (1994) 1908-1912.

[227] R. Repetto, J.H. Siggers, A. Stocchino, Steady streaming within a periodically rotating sphere, *J Fluid Mech*, 608 (2008) 71-80.

[228] O. Abouali, A. Modareszadeh, A. Ghaffariyeh, J. Tu, Numerical simulation of the fluid dynamics in vitreous cavity due to saccadic eye movement, *Med Eng Phys*, 34 (2012) 681-692.

[229] H.H. Boushehrian, O. Abouali, K. Jafarpur, A. Ghaffarieh, G. Ahmadi, Relationship between saccadic eye movements and formation of the Krukenberg's spindle—a CFD study, *IMA J Math Appl Med Biol*, 34 (2016) 293-312.

[230] R. Repetto, A. Stocchino, C. Cafferata, Experimental investigation of vitreous humour motion within a human eye model, *Phys Med Biol*, 50 (2005) 4729-4743.

Appendix A Life Cycle Assessment (LCA) of Cleaning-in-Place Operations in the Production of Powdered Egg Yolk

A.1   Introduction

Generally, the food and biotech sectors consume large amounts of fresh water and energy for cleaning. Large volumes of wastewater will be produced and need to be treated, which is also a serious problem in other manufacturing sectors. In order to improve the sustainability of the food, the demands on water and power resources need to be reduced.

The impact of cleaning on the sustainability of a food processing operation is presented here as essential context for the scientific investigation of this PhD. The work was performed by the author during a 2 month placement with Professor Jen-Yi Huang at the Department of Food Sciences at Purdue University in autumn 2019. This original work has been submitted for publication in the Journal of Cleaner Production.

Estimation of the efficiency for cleaning mainly employs two methods, namely production-based metrics and life cycle assessment (LCA). Köhler *et al.* [190] reported the use of production-based metrics for cleaning of Xanthan gum soil layers using impinging water jets. The cleaning efficiency was assessed based on cleaning performance indicators calculated from time, fluid consumption, energy and cost. The effect of different operating parameters (*e.g.* nozzle diameter and pressure) on the performance indicators was evaluated. LCA is an accounting and management method for assessing the environmental impacts of a product, in which all resource uses and releases to the environment are considered (see Fig. A.1).
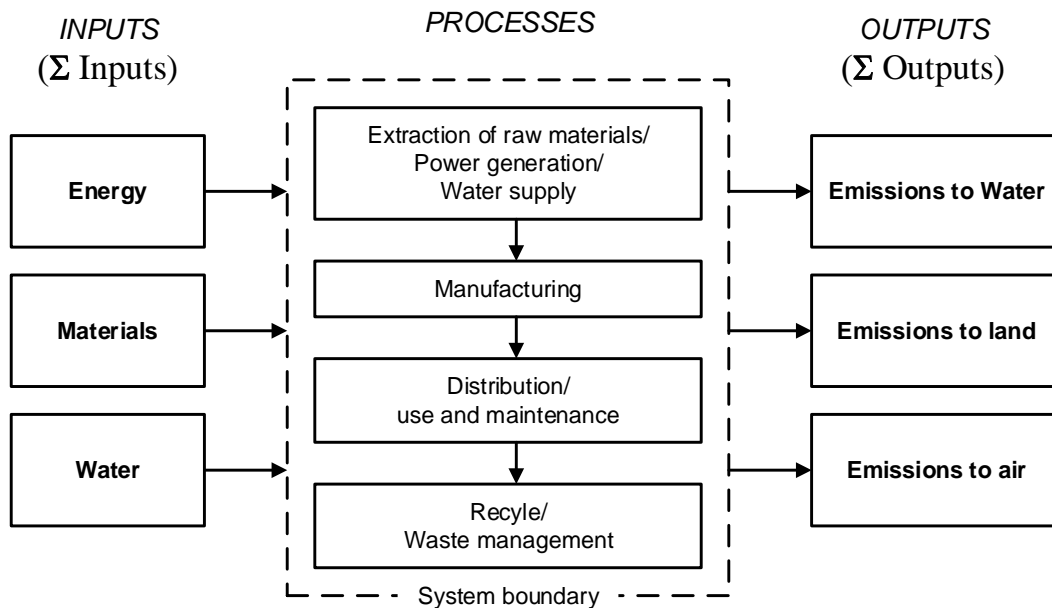
Fig. A.1. Schematic of how LCA works, adjusted from [191].

The dairy industry has attracted wide attention in the sustainability literature due to its large production volumes (approximately 2.3 million tonnes milk produced per day in 2018 [85]), and a series of LCA studies have been reported [3, 192-197]. About 2 litres of water is used for processing 1 litre milk [196]. In a dairy, milk collected from the farm typically undergoes three major processing steps, namely pasteurisation, homogenisation and separation. In order to avoid the growth of microorganisms, CIP processes are widely used for cleaning process equipment. Around one-third of the environmental impacts of a dairy has been linked to cleaning process steps [196]. Compared to other operation, the CIP operation after the pasteurisation process contributed the largest amount of wastewater [194]. Also, milk residuals in equipment and the chemical agents used for cleaning often cause serious eutrophication. More environmentally-friendly CIP methods such as the use of enzyme-based cleaners has, however, proved to be more expensive [195].

In this section, a simple LCA for a CIP process in an egg yolk powder factory is employed to demonstrate the impact of cleaning on the environmental footprint and economics. Egg yolk powder was selected as the demand for this dried product has increased significantly owing to benefits in transportation, storage life and control of bacteria growth. Around 80 Mte eggs were produced worldwide in 2017 and this has more than doubled since 1990 [198]. Global egg production has been forecasted to exceed 100 Mte. The growth in demand for egg powder is

partly due to its functional properties [199] and storage advantages [200]. Egg yolk powder is more popular than dried whole egg and egg white [85]. However, the spray dryers used can encounter severe deposition on the equipment surface [201]. LCA studies for manufacturing (and cleaning) milk powder [3, 202, 203] indicated that both the drying and pasteurisation processes were the major contributors to the environmental impacts [194, 202]. A life cycle analysis for the production of egg yolk powder has not been reported.

The production lines for egg yolk and milk powders are similar and involve proteinaceous fouling deposits; however, the cleaning operations are different [112, 204]. This section aims to demonstrate the impacts of different production and cleaning scenarios on the environment. The relationship between the environmental impact and process productivity is also investigated.

A.2   Methods

A.2.1 Goal and scope

The LCA task is to analyse the environmental impacts of an egg yolk powder plant located in Indiana, USA, and to compare a conventional continuous-flow CIP process with an alternative CIP method using pulsed flows for cleaning the spray dryer. The environmental impacts of different cleaning operations are compared and the optimal method is identified.

In LCA, the functional unit (FU) needs to be defined. FU is a quantified performance for the studied system and provides a reference to link both the inputs and outputs. In this case, the FU is 1 kg dried egg yolk product manufactured in a plant in Indiana, USA.

A.2.2 Life cycle inventory (LCI)

A common production line for dried egg yolk product consists of the four major stages shown in Fig. A.2: breaking of fresh eggs, refrigeration (storage), pasteurization, and powdering [85]. The inputs and outputs for each sub-process are summarised in Table A.1. Most of the

inventory data in the model are taken from the ecoinvent database v3.0 reported by Wernet *et al.* [205].

The present work aims to evaluate the impacts of the CIP processes, so only the major production stages and cleaning operations are considered. Breaking, storage and pasteurisation (BSP), CIP for cleaning the pasteurisation heat exchangers (CIP1), drying and CIP for cleaning the spray dryer (CIP2) are selected and studied. A gate-to-gate analysis is performed – only several steps in the entire production life cycle is considered and valued. This means that the steps before breaking, including farming, harvesting and transportation, and packaging after processing, are excluded. Fresh eggs transported from the farm are selected as the initial input [206].

The process flow is depicted in Fig. A.2. All resources and emissions for the BSP stage, including leakage of coolants, are taken from the literature [206]. A plate heat exchanger with a 7.6 m long holding tube is employed for pasteurisation [207]. After the pasteurisation operation has run for 8 h, the system is shut down and cleaned using CIP process 1 (CIP1).

The pasteurised egg yolk is conveyed to a spray dryer for drying, and the energy consumption and conversion ratio from egg yolk to powder are modelled based on a real industrial case [85]. The operation time of the spray dryer (cycle time) depends on the fouling thickness (criteria to clean: 0.273 kg fouling per m^2) on the dryer surface. For instance, the longest continuous production time for a spray dryer with a 5 m diameter, D, is about 10.3 h. After production, the unit is cleaned using CIP process 2 (CIP2).

The CIP1 operation includes 3 steps, namely (i) pre-rinsing to flush residual products out, (ii) caustic cleaning for removing deposits, and (iii) final-rinsing for washing out residual caustic. Both rinsing operations last 10 minutes. The alkaline solution can promote the solubility of lipid and enhance cleaning efficiency. The duration of caustic cleaning is selected based on the flow channel studies reported by Helbig *et al.* [208]. Wastewater collected from the cleaning stage is treated using a conventional chemical coagulation technique, in which ferric chloride and an anionic polymer are dosed to trap particles. Using this technique, more than 80% chemical oxygen demand (COD), biochemical oxygen demand (BOD), total suspended solids, phosphorus, organic nitrogen and oil, can be removed [209]. The treated water is alkaline due to the use of caustic, so its pH is adjusted by adding nitric acid, before being discharged to drain. The solid waste collected from the coagulation process is sent for incineration.

CIP2 is similar to CIP1 with three steps: (i) 1.5 minute pre-rinsing, (ii) caustic cleaning, and (iii) 1.5 minute final-rinsing. The caustic cleaning time is estimated using the pilot-scale data reported by Yang *et al.* [210]. In that study, a rotary spray head was employed for cleaning egg yolk deposits. Cleaning using continuous (Scenario 1C) and pulsed (Scenario 1P) flows (see Fig. A.3) were tested for different temperatures, T (20-55 °C), and concentrations of sodium hydroxide, C_{NaOH} (0-15 kg/m^3). Pulsed-flow cleaning featured 1 min caustic solution flow, followed by 1 min delay in a repeating cycle. CIP2 wastewater is treated the same as CIP1.
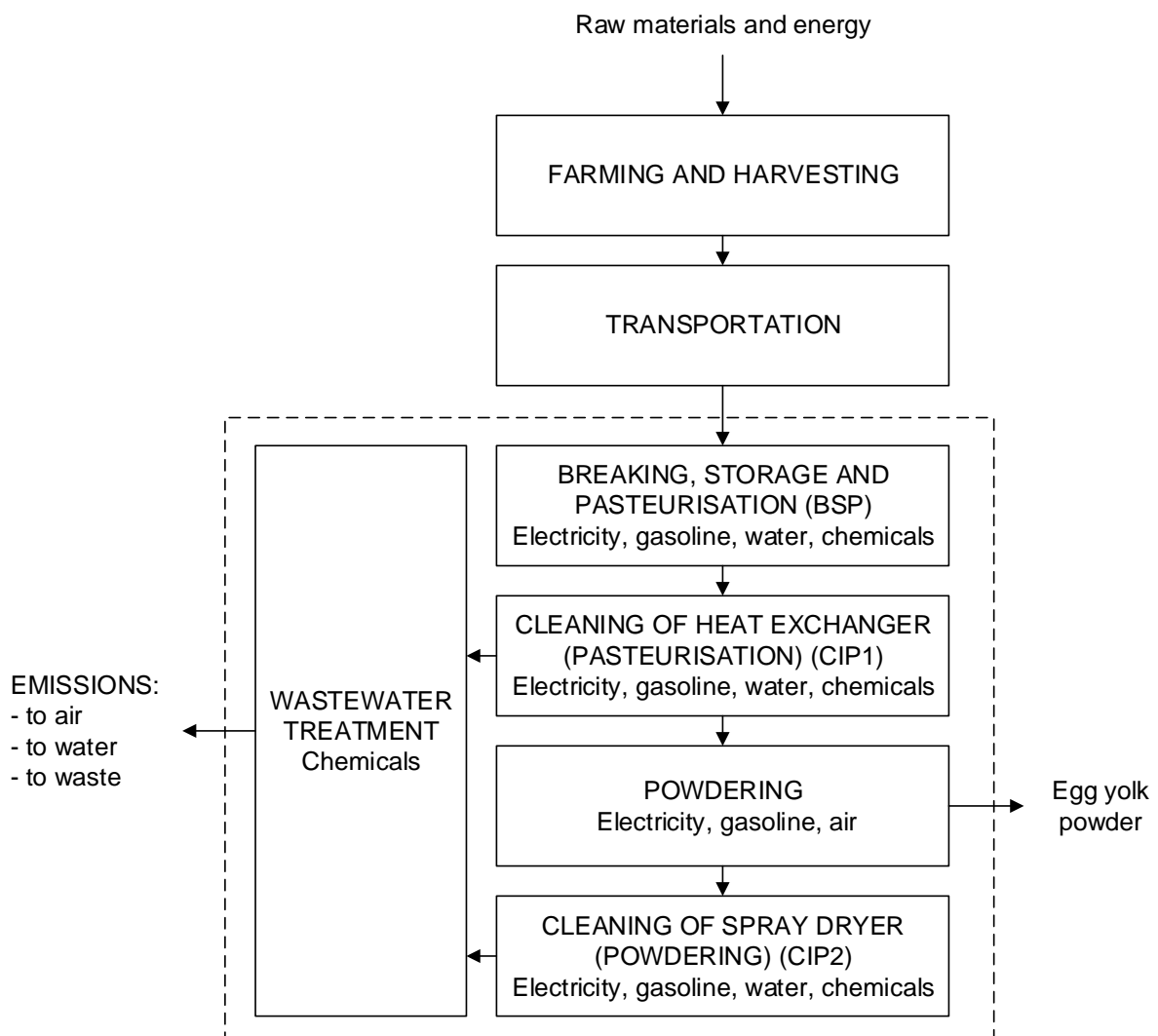
Fig. A.2. Process flow diagram of egg yolk powder manufacture.

Table A.1. Life cycle inventory (per functional unit) of egg yolk powder production for different scenarios

Input	Unit	Scenario 1C (continuous-flow CIP2)	Scenario 1P (pulsed-flow CIP2)	Scenario 2 Electricity	Scenario 3 Solar energy	Scenario 4 UFO-MBR
Breaking, storage and pasteurization (BSP)						
Input						
Transported eggs	kg	8.11		8.11	8.11	8.11
Water	m^3	2.44×10^{-2}		2.44×10^{-2}	2.44×10^{-2}	2.44×10^{-2}
Electricity	kWh	0.78		0.78	0.78	0.78
Natural gas	kWh	0.49		0.49	0.49	0.49
Diesel	kWh	2.05×10^{-3}		2.05×10^{-3}	2.05×10^{-3}	2.05×10^{-3}
Gasoline	kWh	4.51×10^{-6}		4.51×10^{-6}	4.51×10^{-6}	4.51×10^{-6}
Glycol	kg	4.38×10^{-3}		4.38×10^{-3}	4.38×10^{-3}	4.38×10^{-3}
Anhydrous ammonia	kg	0.10		0.10	0.10	0.10
R-22	kg	7.90×10^{-2}		7.90×10^{-2}	7.90×10^{-2}	7.90×10^{-2}
Output						
Liquid egg white	kg	4.43		4.43	4.43	4.43
Liquid egg yolk	kg	2.18		2.18	2.18	2.18
Discarded eggs	kg	0.57		0.57	0.57	0.57
Egg shells	kg	0.90		0.90	0.90	0.90
CIP1 (pasteurizing heat exchanger)						
Input						
Water	m^3	5.69×10^{-4}		5.69×10^{-4}	5.69×10^{-4}	5.69×10^{-4}
Electricity	kWh	1.73×10^{-4}		2.07×10^{-2}		1.73×10^{-4}
Natural gas	kWh	2.05×10^{-2}				2.05×10^{-2}
Solar energy	kWh	5.51×10^{-4}			2.07×10^{-2}	
NaOH	kg	8.68×10^{-4}		5.51×10^{-4}	5.51×10^{-4}	5.51×10^{-4}
HNO$_3$	kg	5.53×10^{-3}		8.68×10^{-4}	8.68×10^{-4}	8.68×10^{-4}
FeCl$_3$	kg	2.39×10^{-5}		5.53×10^{-3}	5.53×10^{-3}	5.53×10^{-3}
Anionic polymer	kg	4.12×10^{-3}		2.39×10^{-5}	2.39×10^{-5}	2.39×10^{-5}
Incinerated waste	kg	5.69×10^{-4}		4.12×10^{-3}	4.12×10^{-3}	4.12×10^{-3}
Emissions to water						
COD	kg	4.15×10^{-4}		4.15×10^{-4}	4.15×10^{-4}	4.15×10^{-4}
BOD	kg	2.11×10^{-4}		2.11×10^{-4}	2.11×10^{-4}	2.11×10^{-4}
Phosphorus	kg	2.28×10^{-6}		2.28×10^{-6}	2.28×10^{-6}	2.28×10^{-6}
Organic nitrogen	kg	1.42×10^{-5}		1.42×10^{-5}	1.42×10^{-5}	1.42×10^{-5}
Oil and grease	kg	1.13×10^{-6}		1.13×10^{-6}	1.13×10^{-6}	1.13×10^{-6}

Drying

Input

Liquid egg yolk	kg	4.15×10^{-4}	2.18	2.18	2.18
Electricity	kWh	2.11×10^{-4}	3.84×10^{-4}	3.84×10^{-4}	3.84×10^{-4}
Natural gas	kWh	2.28×10^{-6}	2.31	2.31	2.31

Output

Egg yolk powder	kg	1.0	1.0	1.0	1.0

Emissions to air

Waste heat	kWh	0.68	0.68	0.68	0.68
Evaporated water	kg	1.19	1.19	1.19	1.19

CIP2 (spray dryer)

Input

Water	m^3	2.39×10^{-3}	1.03×10^{-3}	2.39×10^{-3}	2.39×10^{-3}	7.85×10^{-4}
Electricity	kWh	3.32×10^{-4}	1.43×10^{-4}	8.61×10^{-2}		6.99×10^{-3}
Natural gas	kWh	8.58×10^{-2}	3.69×10^{-2}			8.58×10^{-2}
Solar energy					8.61×10^{-2}	
NaOH	kg	1.10×10^{-2}	4.70×10^{-3}	1.10×10^{-2}	1.10×10^{-2}	1.10×10^{-2}
HNO$_3$	kg	1.73×10^{-2}	7.46×10^{-3}	1.73×10^{-2}	1.73×10^{-2}	1.73×10^{-2}
FeCl$_3$	kg	5.52×10^{-3}	2.38×10^{-3}	5.52×10^{-3}	5.52×10^{-3}	5.52×10^{-3}
Anionic polymer	kg	2.39×10^{-5}	1.03×10^{-5}	2.39×10^{-5}	2.39×10^{-5}	2.39×10^{-5}
Incinerated waste	kg	4.12×10^{-3}	1.78×10^{-3}	4.12×10^{-3}	4.12×10^{-3}	4.12×10^{-3}
NaCl	kg					2.58×10^{-3}
NaHOCl	kg					2.39×10^{-7}
PVDF (membrane)	kg					9.91×10^{-9}
Polyamide (membrane)	kg					2.76×10^{-7}
Polypropylene (spacer)	kg					6.59×10^{-7}
Coated steel (housing)	kg					3.47×10^{-6}

Emissions to water

COD	kg	1.73×10^{-3}	1.73×10^{-3}	1.73×10^{-3}	1.73×10^{-3}	1.73×10^{-3}
BOD	kg	8.81×10^{-4}	8.81×10^{-4}	8.81×10^{-4}	8.81×10^{-4}	8.81×10^{-4}
Phosphorus	kg	9.53×10^{-6}	9.53×10^{-6}	9.53×10^{-6}	9.53×10^{-6}	9.53×10^{-6}
Organic nitrogen	kg	5.59×10^{-5}	5.59×10^{-5}	5.59×10^{-5}	5.59×10^{-5}	5.59×10^{-5}
Oil and grease	kg	4.76×10^{-6}	4.76×10^{-6}	4.76×10^{-6}	4.76×10^{-6}	4.76×10^{-6}
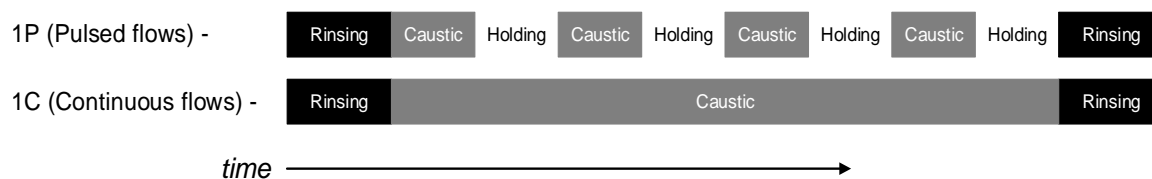
Fig. A.3. Schedule of cleaning operations in CIP2 [210].

A.2.3 Impact assessment

The midpoint environmental impacts resulted from egg yolk powder processing were simulated and analysed using the ReCiPe 2016 Midpoint (E) v1.02 method, which is to transform life cycle inventory results to 18 midpoint indicate scores [211]. Midpoint indicators focus on single environmental problems. In this study, 8 impact categories (IC) were considered, including global warming (GW, kg CO_2 eq), ionisation radiation (IR, kBq Co_{60} eq), terrestrial ecotoxicity (TE, kg 1,4-DCB), marine ecotoxicity (ME, kg 1,4-DCB), human carcinogenic toxicity (HCT, kg 1,4-DCB), human non-carcinogenic toxicity (HNCT, kg 1,4-DCB), fossil resource scarcity (FRS, kg oil eq) and water consumption (WC, m^3). Calculations were performed using the commercial LCA software, SimaPro version 8.0.

A.2.4 Scenario analysis

A scenario analysis is performed in terms of the processes consuming large amounts of energy and water in the model. Three different scenarios are investigated. The first scenario is to replace the original heating resource (natural gas) for heating the cleaning solutions by electricity, labelled Scenario 2 electricity. The second is to source all power, including heating and pumping, from solar sources, labelled Scenario 3 solar energy. A solar tank is assumed to produce hot water for cleaning. The pumps in the CIP units are powered by electricity generated from solar panels. The third scenario is to reuse about two-thirds of the CIP2 wastewater using a hybrid technique, UFO-MBR, reported by Holloway *et al.* [212] (Scenario 4 UFO-MBR). In this, a membrane bioreactor is employed for pre-treating the wastewater, and the treated water is filtered by forward osmosis and reverse osmosis to produce potable water for cleaning. The effluent from the membrane bioreactor is treated using ultrafiltration and then sent to drain.

A life time of 5 years is chosen for the membranes. The materials required to produce the membranes but not to construct the system are accounted for [213], and are summarised in Table A.1.

A.3 Results and discussion

A.3.1 Inventory analysis

Table A.1 lists LCI data for production of egg yolk powder for four different cases. The major inputs are eggs, water, electricity and natural gas. Around 8.11 kg transported fresh eggs can produce one FU of dried egg yolk product, which is close to the conversion ratio (9.21 kg eggs for 1 kg egg yolk powder) reported by Berggren [214]. The difference is owing to different moisture contents of the product. Berggren showed that about 0.0156 m^3 water, 0.61 kWh electricity, 0.22 kg fuel oil, 0.01 kg sodium hydroxide and 0.0042 kg sulfuric acid were utilised to manufacture 1 kg yolk powder. The dosage of NaOH in this case (0.011 kg) is similar, but electricity and water consumptions (0.783 kWh and 0.0284 m^3, respectively) are higher than Berggren's values. This is because a large volume of water is used in the process to wash the fresh eggs in the breaker facilities. This breaking, storage and pasteurisation (BSP) process makes up 89.2% of total water consumption (0.0244 m^3).

The stages of BSP and powdering can be considered as hotspots for energy consumption, with 1.27 kWh (34.4% of total) and 2.31 kWh (62.7%), respectively. In BSP, this is due to refrigeration before pasteurisation and heating liquid egg yolk to 67 °C in the pasteurisation stage. Refrigeration is an energy-intensive process. Energy is utilised to heat air to 180 °C for drying egg yolk [85].

A.3.2 Impact assessment

A.3.2.1 Environmental profile (Continuous-flow CIP2)

Fig. A.4 compares the relative contribution of each sub-process in terms of different impact categories. The environmental scores for different ICs are listed in Table A.2. In Fig. A.4, apart from TE and FRS, all environmental impacts for the BSP stage are significantly higher than other processes, followed by the powder step. The high ME, HCT and HNCT impacts are mainly contributed from the electrical consumption for refrigeration in the BSP stage (0.782 kWh). Many US power plants burn fossil fuel (coal and petroleum) to produce electricity, and the combustion emits pollutants such as NO_x, SO_2, Hg, *etc* [215], increasing the HCT and HNCT potentials. The total ME and HNCT impacts (133.6 and 110.18 kg 1,4-DCB, respectively) are higher than other categories, indicating that the production of dried egg yolk product will result in serious marine ecotoxicity and human non-carcinogenic toxicity potentials. In contrast, the contribution from CIP1 is negligible. For GW, the stages of pasteurisation, drying, CIP2 and CIP1 contribute approximately 54%, 38%, 7% and less than 1 %, respectively.

One of the major contributors of TE is heavy metals. Natural gas includes heavy metals, resulting in their emission during combustion [205]. The CIP2 process (42.2% of total) has higher impacts on TE than powdering. This is because heavy metals come not only from natural gas, but also from the addition of coagulants ($FeCl_3$). Furthermore, the nitric acid used for adjusting pH is decomposed by light or heat to produce nitric oxide, which is also the major contributor of TE and can be considered as a hotspot. Moreover, the ferric chloride used for coagulation and the metallic species in natural gas cause serious IR impacts, and around 57%, 19% and 18% are from BSP, CIP2 and powdering, respectively.

The processes of BSP and drying contribute most impacts on FRS, at around 32% and 60% of the total, respectively. This is owing to large natural gas consumption. Compared with the cleaning processes (CIP1 and CIP2), production of pasteurised liquid egg yolk and drying need more water (WC). This is attributed to not only washing fresh eggs, but also electricity generation and fossil fuel extraction (about 0.263 m^3 and 0.0523 m^3 water per 1 kWh of natural gas and electricity, respectively [205]).

These results are now compared with the LCA for the skimmed milk powder production reported by Krokida *et al.* [202]. The powder step is one of energy-intensive processes in the dairy plant. The total GW for CIP2 using continuous flows (1.71 kg CO_2 eq) is close to the value for drying milk without using reverse osmosis to concentrate milk (1.42 kg CO_2 eq). By contrast, the WC for processing egg yolk powder (0.627 m^3) is lower than that for skimmed milk powder (1.19 m^3). This is because more processing units are employed in the diary sector. A standard milk powder production line includes separation, standardisation, pasteurisation, evaporation, spray drying, fluidised bed dryer and air clean-up by cyclones. An evaporator is not used in egg yolk powder manufacturing owing to the high york viscosity upstream of the dryer.
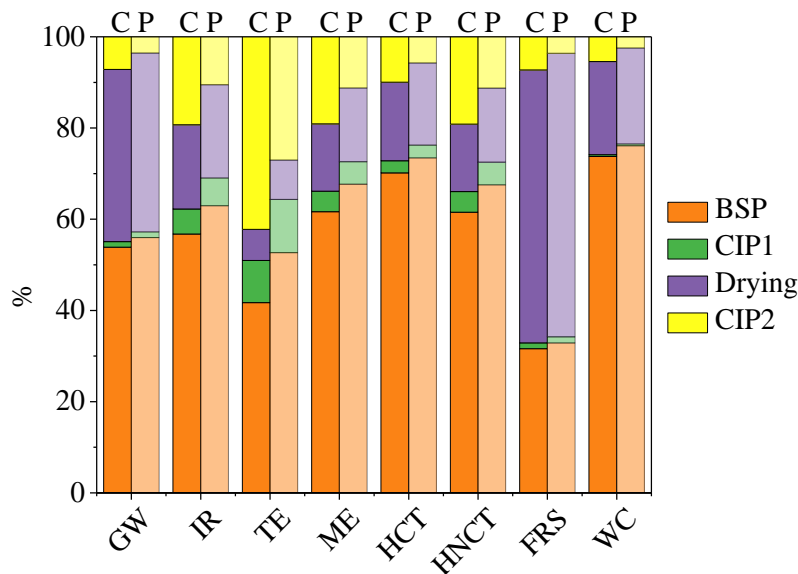
Fig. A.4. Environmental impact profiles of egg yolk powder manufacture with different methods for spray dryer cleaning; solid colour – continuous flow (C); light colour – pulsed flow (P). Impacts: GW – global warming; IR – ionizing radiation; TE – terrestrial ecotoxicity; ME – marine ecotoxicity; HCT – human carcinogenic toxicity; HNCT – human carcinogenic non-toxicity; FRS – fossil resource scarcity; WC – water consumption.

Table A.2. Environmental impacts of different stages in egg yolk powder manufacturing

Stage	GW (kg CO_2 eq)	IR (kBq Co_{60} eq)	TE (kg 1,4-DCB)	ME (kg 1,4-DCB)	HCT (kg 1,4-DCB)	HNCT (kg 1,4-DCB)	FRS (kg oil eq)	WC (m^3)
BSP	0.92	3.78×10^{-2}	0.38	82.4	1.04	67.8	0.13	0.437
CIP1	2.04×10^{-2}	3.66×10^{-3}	8.61×10^{-2}	6.0	3.97×10^{-2}	5.0	5.19×10^{-3}	2.25×10^{-3}
Drying	0.644	1.23×10^{-2}	6.34×10^{-2}	19.7	0.256	16.3	0.246	0.121
CIP2 continuous/pulsed	0.122 / 0.058	12.8×10^{-3} / 6.3×10^{-3}	0.39 / 0.20	25.5 / 13.7	0.148 / 0.082	21.1 / 11.3	2.98×10^{-2} / 1.43×10^{-2}	3.2×10^{-2} / 1.4×10^{-2}
Total continuous CIP2/pulse CIP2	1.71/1.64	6.66×10^{-2}/6.00×10^{-2}	0.92/0.73	134/122	1.48/1.42	110/100	0.411/0.395	0.592/0.574
% change in total for pulsing	-3.7%	-9.8%	-21%	-8.8%	-4.4%	-8.9%	-3.8%	-3.0%

A.3.2.2 Pulsed-flow CIP

Yang *et al.* [210] reported that applying the cleaning solution intermittently improved the water consumption of cleaning cooked egg yolk soil on the tank surface. Intermittent cleaning gave a better cleaning rate than continuous flows. The case for cooked deposits is similar to the deposit formed in a spray dryer. The period between each burst provides more time for alkali solution to diffuse into the soil matrix and enhance its dissolution. More deposit could then be cleaned with a given volume of cleaning solution [216]. How this affects the overall environmental performance of egg yolk powder manufacturing is assessed by comparing pulsed-flow cleaning of the dryer (CIP2) with Scenario 1C (*i.e.* continuous-flow CIP2). Fig. A.4 compares the environmental performances between continuous-flow (Scenario 1C) and pulsed-flow CIP2 (Scenario 1P). The pulsed-flow CIP2 improves the impacts of the continuous-flow case by more than 50%. The major difference is attributed to its shorter effective cleaning time (*e.g.* 15 min for pulsed flows compared to 34.8 min for continuous flows), meaning that less energy, water and NaOH are consumed.

A.3.2.3 Optimisation of pulsed CIP2

The temperature and NaOH concentration of cleaning solution are key factors determining the cleaning efficiency [217]. The effect on cleaning egg yolk soil of a range of temperatures, T (25-55 °C) and NaOH concentration, C_{NaOH} (1-5 kg/m^3) was studied by Yang *et al.* [35]. To highlight the influence of both temperature and alkali concentration, the contributions to GW, TE, ME and WC are shown in Fig. A.5. These results are normalised to the reference case: Scenario 1P ($C_{NaOH} = 5$ kg/m^3, $T = 55$ °C). Fig. A.5(a) to (d) show a similar trend. The alkaline solution at low concentration and high temperature gave the lowest impacts on the environment. This is due to the fact that cleaning using a low concentration alkaline solution with high temperature is more efficient. High temperature enhances dissolution and swelling of fouling soils, and increases the cleaning efficiency [218]. Although cleaning with a high temperature solution consumes more energy and causes more environmental impacts, the cleaning time is reduced, resulting in decrease of the total environmental scores. In contrast, at higher NaOH concentrations, the structure of deposits changes, increasing the difficulty of removal [219]. The effect of alkali concentration depends on the protein type, so experiments

are required to find the optimal concentration for cleaning [218, 220, 221]. In Fig. A.5(d), using low temperature water (without any NaOH dosage) results in less WC than cleaning with alkaline solution; however, Helbig *et al.* [208] reported that cleaning using low alkali concentration solution was the most efficient. The reason is that NaOH production also consumes water, which contributes to the total WC score. The lowest WC is thus the case of cleaning using hot water.
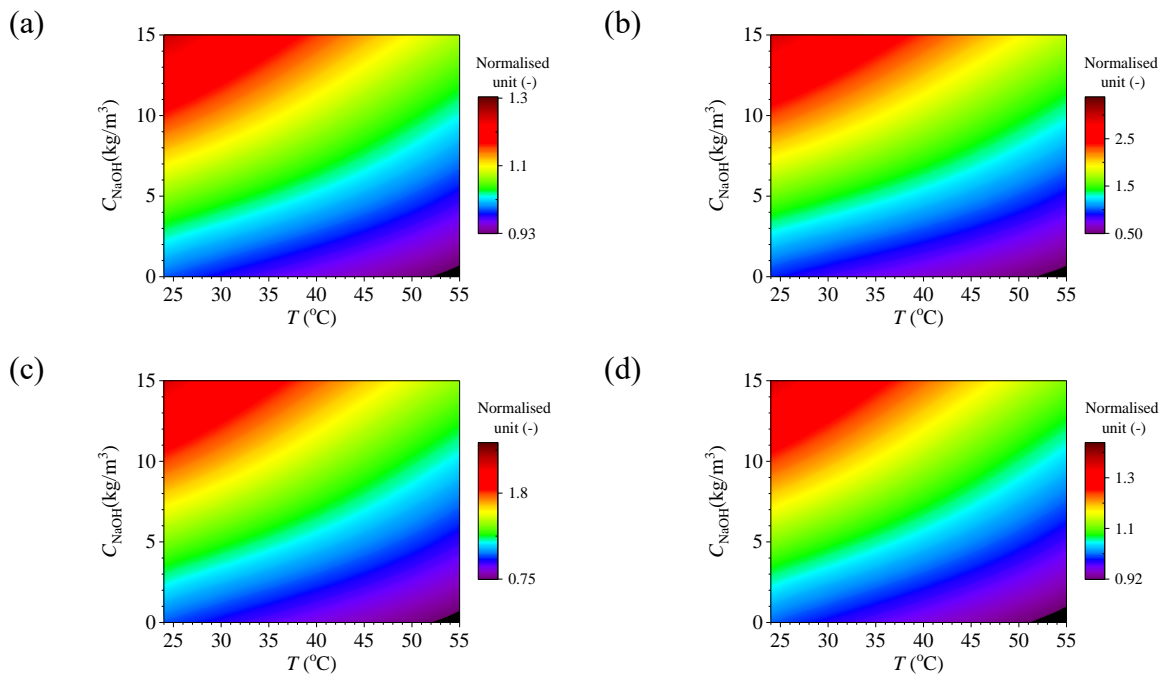
Fig. A.5. Effects of NaOH concentration and temperature on normalised (a) GW, (b) TE, (c) ME and (d) WC for pulsed-flow CIP2. Values normalised by Scenario 1P ($C_{NaOH} = 5$ kg/m^3, 55 °C).

A.3.3 Effect of production and cleaning times

In the food and biotech sectors, regular cleaning is necessary for mitigating hygiene issues; however, frequent cleaning can reduce the productivity and increase the operation cost. Excessive cleaning can also result in more energy, water and chemical consumptions, as well as more wastewater produced. To assess the effects of productivity and cleaning on the environment, a series of cases are simulated by fixing an 8 h cycle time, including production and shutdown for cleaning. Fig. A.6 compares the normalised environmental impacts in terms

of the ratio of cleaning time to production time, τ_{cp}. The case of pulsed-flow CIP2 (Scenario 1P) with an 8 h operating period is selected as the reference case, including 33 min for cleaning ($\tau_{cp} = 0.074$). The relative productivity, RP, is given by

$$RP = \frac{1.074}{(1 + \tau_{cp})} \tag{A.1}$$

A range of τ_{cp} values (0.039-0.24) was evaluated, and the RP values change from 1.03 to 0.86. All four impact categories show a nearly linear relationship with τ_{cp}, which is consistent with the previous discussion, namely longer cleaning times resulting in higher environmental impacts. TE is the most sensitive due to the natural gas and HNO_3 consumptions for cleaning and wastewater treatment, respectively. This indicates that the environmental footprint could be reduced effectively by decreasing the cleaning time; however, ME, GW and WC show small changes with the cleaning time.

Even though the results show that a shorter cleaning period (*i.e.* smaller τ_{cp}) can alleviate the environmental impacts and boost the productivity, the choice of τ_{cp} is constrained: insufficient cleaning can have serious consequences. For example, in the dairy sector, if the equipment is not cleaned completely, residual milk or fouling may enhance bacterial growth [17]. Moreover, a longer production time causes deposit ageing, increasing the difficulty of removing [222]. In order to find the optimal CIP cycle, hygiene, productivity and sustainability all need to be considered.
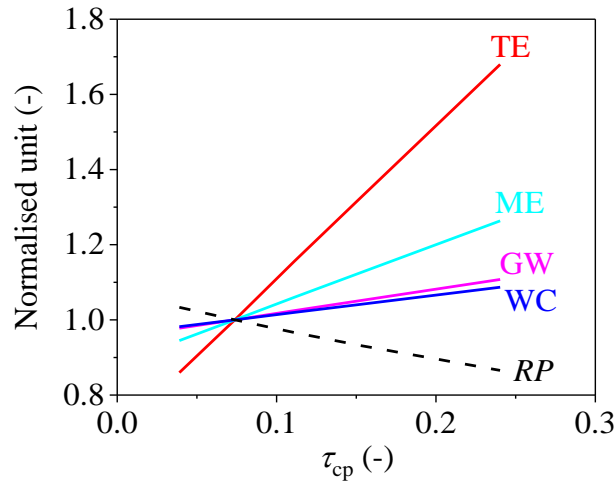
Fig. A.6. Effect of normalised cleaning time on normalised environmental impacts and productivity.

A.3.4 Scenario analysis

A.3.4.1 Impact of production scale

The spray dryer is the major unit in a powder manufacturing plant, and the production rate is determined by the dryer diameter, D, which was collected from a manufacturer [85]. The environmental footprints per FU for dryers with different diameters were evaluated. A 5.0-m diameter dryer was selected as the reference case, with a productivity of 5360 kg of egg yolk powder per batch. Another 3 spray dryers with different diameters were simulated and compared, including 5.5 m (6430 kg/batch), 4.5 m (4300 kg/batch), and 2.5 m (1300 kg/batch). Scenario cleaning 1P was considered. The flow rate of the rotating nozzle, $\dot{m}$, for the reference 5.0-m dryer is 20300 kg/h. The flow rates for other dryers were calculated using the wetting rate, which is the flow rate per unit width of falling film, given by $\dot{m}/\pi D$ (0.36 kg/m-sec) [210]. The effects of dryer diameter on ICs are plotted in Fig. A.7. The results for the 4.5-m and 5-m dryers are similar, but the smallest system shows significantly higher IR, TE, HCT and HNCT. Among these categories, the environmental footprints decrease with diameter, due to the fact that a larger spray dryer can create more egg yolk powder. The scores per FU are thus lower, even though more energy and materials are consumed. This indicates that from the production point of view, larger production equipment is more efficient.
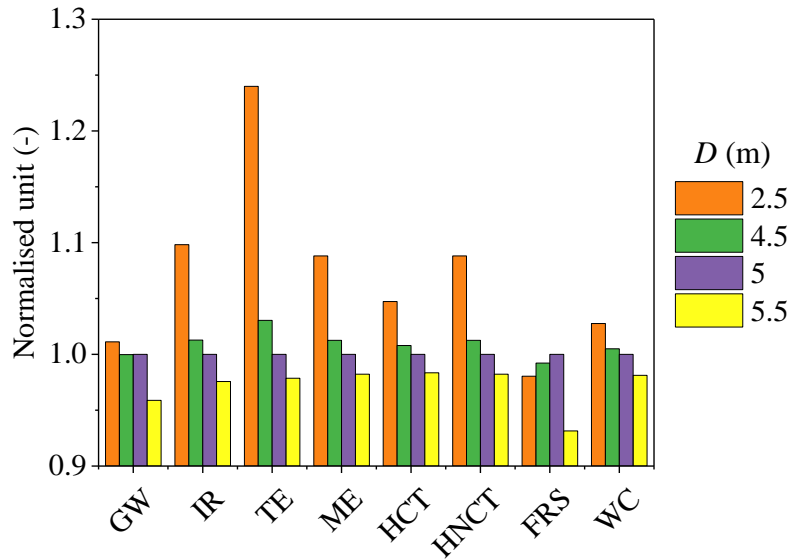
Fig. A.7. Effect of production scale on total environmental impacts of the process. Data normalised against results for 5-m diameter spray dryer.

A.3.4.2   *Process improvement*

Three potential improvements with some sustainable benefits are tested:

a) Scenario 2 – using electricity for warming cleaning solutions
b) Scenario 3 – using solar energy for heating and pumping cleaning solutions
c) Scenario 4 – using a UFO-MBR technique for recycling and reusing wastewater

These are normalised by the baseline case, Scenario 1P and the results are summarised in Fig. A.8. Only small changes in GW, IT, FRS and WC can be observed for Scenarios 2-4. While replacing natural gas by electricity for heating cleaning solutions (Scenario 2) decreases TE by approximately 11%, ME, HCT and HNCT are increased significantly due to coal burning. The impacts of ME, HCT and HNCT are able to be alleviated by alternative sources such as heat pumps, although the 180 °C air inlet temperature for powdering is beyond the current limit of heat pumps [223]. Replacing the original source by solar energy (Scenario 3) can lower the TE score by around 10% and decrease HCT slightly, but WC increases. This is because some materials as well as water are used for manufacturing solar panels. This is owing to chemicals such as silicon and cadmium telluride [224] and water are used for manufacturing solar panels.

Recycling and reusing wastewater using the UFO-MBR system (Scenario 4) can save around two thirds of the total water used in the factory, but the total WC remained the same. This is due to the fact that additional water is used for manufacturing the membranes and the chemicals utilised in the UFO-MBR process. This is an example where an alternative method can reduce the local environmental impact, but not globally.

The results indicate that there is no single alternative technique which can provide noticeable improvements for all impact categories apart from renewable energy for electricity. This LCA study provides valuable insights into the trade-offs between the local improvements and environmental impacts.
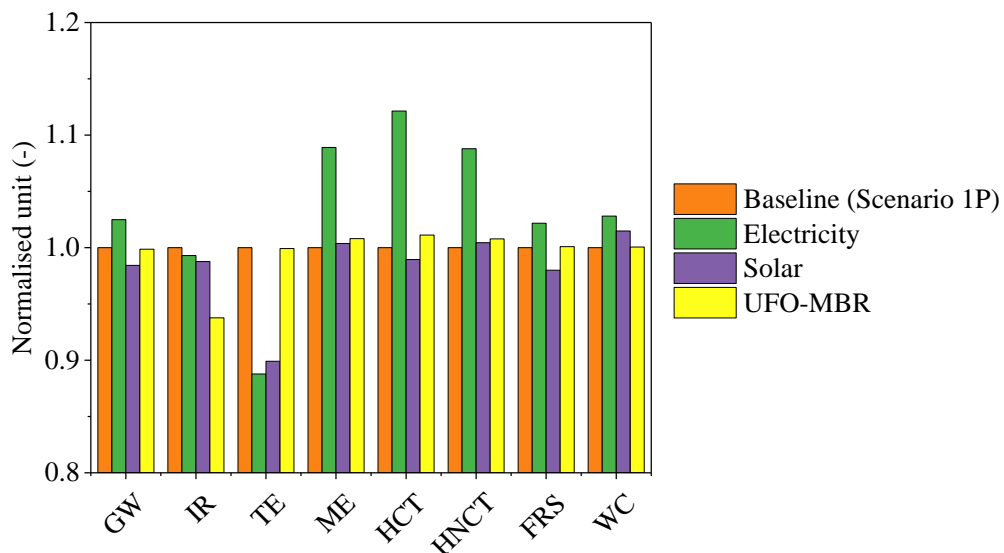
Fig. A.8. Effects of alternative processing scenarios on the environmental impacts of egg yolk powder manufacturing.

A.4 Conclusions

The LCA method has been employed to assess the environmental footprints for an egg yolk powder production process. The inventory analysis highlights both BSP and drying processes as the main energy consumers in the production. The BSP stage is a hotspot for all impact categories apart from FRS due to refrigeration. Pollutants emitted from coal combustion in

power plants cause human and ecological toxicity impacts. Compared to other sub-processes, the BSP process also consumes the most water. This is attributed to fresh egg washing before breaking. By contrast, the CIP2 process contributes more terrestrial ecotoxicity impacts than powdering due to the wastewater treatment (dosages of $FeCl_3$ and HNO_3).

The results demonstrate that compared to conventional continuous-flow cleaning, intermittent cleaning is more efficient and improves the environmental footprints for all impact categories by about 50%. Cleaning with high temperature and low NaOH concentration is more environmentally-friendly. Cleaning using water alone causes less WC than using low alkali concentration solution, because NaOH production also needs water. The sensitivity analysis for the cleaning to production ratio shows that over-cleaning not only decreases productivity, but also increases the environmental impact scores.

The investigation of production scale indicates that larger-scale equipment is more sustainable due to its larger production rate and less environmental impacts. Three potential improvements for egg yolk powder processing have been assessed. Replacing natural gas heating by electricity can reduce TE impacts significantly, but the other ICs increases. Although using solar energy can improve TE noticeable and reduce GW, HCT and FRS slightly, WC increases. This is owing to water use for manufacturing solar panels. In addition, recycling and reusing wastewater (UFO-MBR) does not provide significant improvements for all ICs. Among these scenarios, no one case can reduce impacts for all categories effectively, indicating that finding an acceptable trade-off between ICs is needed.

The study demonstrates how managing cleaning can improve the environmental sustainability of the food industry. The work of Yang *et al*. [210] is an example where cleaning performance was improved by understanding the mechanisms involved in cleaning. Cleaning mechanisms vary for different fouling layers, as deposits behave differently (*e.g.* egg and milk protein in alkali). Moreover, quantitative information about soils is needed for designing cleaning strategies. This dissertation aims to develop *in situ* measurement methods for soft solid layers in applications such as cleaning, and quantitative models for understanding these measurements. This will allow engineering approaches to be used to identify and enhance cleaning mechanisms and thereby improve the sustainability of food (and related) manufacturing operations

Appendix B Modelling of Two Immiscible Liquids in A Model Eye Subject to Saccadic Motion

B.1   Introduction

The vitreous humour is a gel-like substrate and fills the region between the lens and the retina of the humans' eyeball. The replacement of the vitreous humour by a viscous silicon oil is often used to manage complicated retinal detachment surgery [184]. One problem encountered with these silicone oil tamponades is emulsification of the oil in the aqueous solution generated by the eye as a result of the eye's saccadic movement [225]. This can cause cataracts, glaucoma and keratopathy [185, 186, 226]. Oil droplet formation is believed by some workers to be driven by the shear stress induced by saccadic motion at the interface between the phases [187]. Quantification of the shear stresses is needed to confirm this hypothesis, which in turn requires knowledge of the fluid motion.

In addition to experimental studies, some simulations of the flow pattern generated by the saccadic rotation of a single phase have been reported. Repetto *et al.* [227] presented an analytical solution of the flow in a spherical chamber subject to torsional oscillations, mimicking the saccadic motion of the eyeball. Steady streaming flows were observed in both theoretical and experimental results, with good quantitative agreement. Abouali *et al.* [228] employed 3-dimensional CFD simulations with an eye-shaped geometry to predict the flow of vitreous humour (see Fig. B.1) during saccadic motion. The numerical results showed that in the vitreous cavity (vitreous humour occupies in human eye), the streaming flow along the rotational axis was high. Boushehrian *et al.* [229] reported a CFD study of the effects of saccadic motion on the flow field and movement of pigment particles in the anterior chamber, which is in front of the lens (see Fig. B.1). They employed Lagrangian particle trajectory analysis to simulate the particle paths. They showed that natural convection caused by the

temperature difference between the cornea and iris surfaces enhanced the movement of the pigment. The deposition of pigment particles on the cornea was mainly due to the saccadic movement. This explained Krukenberg's spindle, where pigmented iris cells deposit on the inner surface of the cornea.
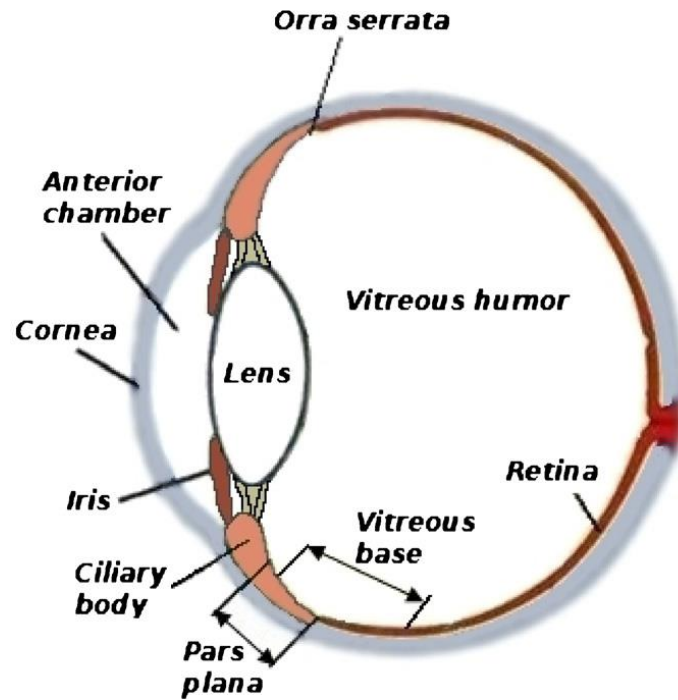

Fig. B.1. Anatomy of eye, reproduced from Abouali *et al.* [228].

The CFD tools generated in this dissertation were used to study the motion of tamponade and related fluids in the vitreous chamber of the eye during saccadic movement. A model system based on laboratory round bottom flasks, shown in Fig. B.2(a), was constructed and tests conducted by PhD student Ru Wang. The flask internal radius is 20 mm. The sphere is rotated around its vertical axis by a stepper motor. An example of a motion cycle is shown in Fig. B.2(b). The sphere rotates at a fixed angular velocity, ω (here, 600 °/s) for a set oscillation amplitude, A, followed by a rest period of the same duration (for this case). The sphere then rotates back to the original position at $-\omega$ for $-A$, followed by another rest to complete the cycle. Silicon oil, saline solutions and a two-phase mixture solution of saline and oil (9:91 vol:vol) (see inset in Fig. B.2(a)) were tested at different amplitudes. Particle image velocimetry (PIV), conducted by Ru Wang, was used to capture the distribution of velocities

once steady state had been established (at least 20 cycles). A 3-dimensional CFD model was created by the author, and the data are compared with the PIV results.
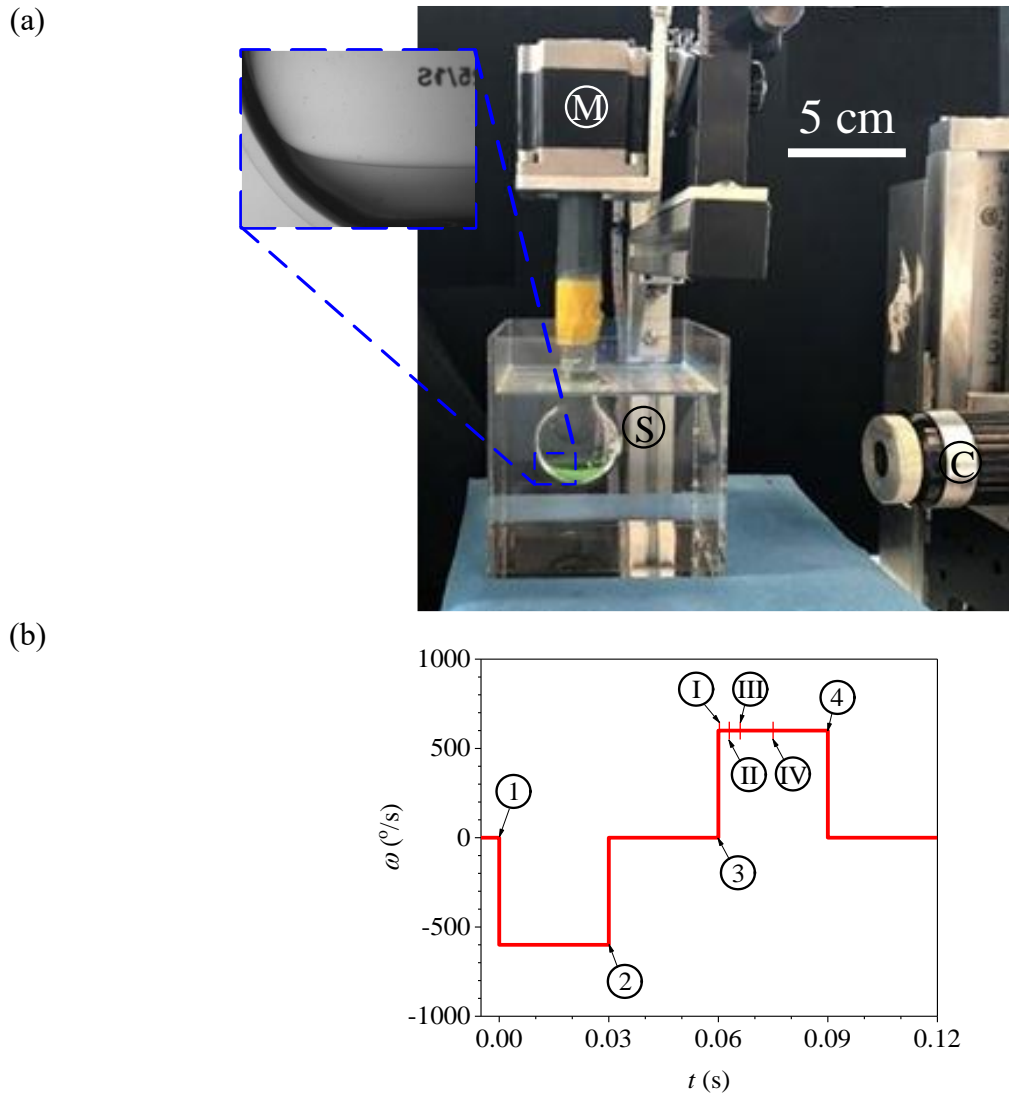
(a)

(b)

Fig. B.2. (a) Schematic of apparatus for mimicking saccadic motion. Inset shows a photograph of an oil-water (more dense) interface at rest. Labels: C – camera; M – stepper motor; S – spherical chamber. (b) Angular velocity cycle. Conditions: $\omega = 600$ °/s, $A = 18°$.

B.2 Model Formulation

The saccadic motion in the spherical chamber was simulated using the volume of fluid (VOF) approach to determine the distributions of fluid velocities. A 3-dimensional transient model was built using an open source software, OpenFOAM version 4.0 running on a SuperServer 1027R-WRF4+ server with 12 cores (Intel® Xeon® E5-2630V2 Processor 2.60 GHz). In VOF, the momentum equation for the calculated domain is described by

$$\rho \left(\frac{\partial \mathbf{v}}{\partial t} + \mathbf{v} \cdot \nabla \mathbf{v} \right) = -\nabla p + \mu \nabla^2 \mathbf{v} + \rho \mathbf{g} \qquad \text{(B.1)}$$

where $\mathbf{v}$ is the velocity vector and p is the pressure. ρ and μ are the average density and average viscosity, respectively. $\mathbf{g}$ is the gravity vector and was oriented in the $-z$ direction. In each computed grid cell, the volume fraction of the saline phase is α and the volume fraction of silicone oil is $(1 - \alpha)$, with $0 \le \alpha \le 1$. Both the average density and average viscosity in each cell are computed by the following linear laws of mixtures:

$$\rho = \rho_{\text{saline}}\alpha + \rho_{\text{oil}}(1 - \alpha) \qquad \text{(B.2)}$$

$$\mu = \mu_{\text{saline}}\alpha + \mu_{\text{oil}}(1 - \alpha) \qquad \text{(B.3)}$$

The mass continuity equation is written in terms of α:

$$\frac{\partial \alpha}{\partial t} + \nabla \cdot (\mathbf{v}\alpha) = 0 \qquad \text{(B.4)}$$

The properties of both fluids are summarised in Table B.1.

Table B.1. Fluid properties at 20 °C, provided by PhD student Ru Wang

Parameter	Value
μ_{oil}	920 mPa s
ρ_{oil}	973 kg/m^3
$\sigma_{oil\text{-}saline}$ [a]	0.0044 N/m
μ_{saline}	1.2 mPa s
ρ_{saline}	1007 kg/m^3

[a] σ is the interfacial tension.

A 2-D schematic of the model geometry is presented in Fig. B.3. Surfaces AB, BC and CD are the glass walls, and the coloured area denotes the fluids. All walls were set at the rotational wall velocity in OpenFOAM, and can be written as $\mathbf{v} = r\omega$, where r is the radial distance from the axis of rotation ($r = \sqrt{x^2 + y^2}$). OpenFOAM employs Cartesian co-oridinates: the origin $(0, 0, 0)$ was set to be the centre of the vessel and the z-axis was specified as the rotational axis. In OpenFOAM, the interaction between the fluid and the wall is described by the wall adhesion model proposed by Brackbill *et al.* [182], where the surface normal of the fluid in the grid cell close to the wall is adjusted based on the given contact angle, θ_w. The surface normal, $\hat{n}$, in this dynamic boundary condition is given by

$$\hat{n} = \hat{n}_w cos\theta_w + \hat{t}_w sin\theta_w \tag{B.5}$$

Here $\hat{n}_w$ is the unit vector normal to the wall and $\hat{t}_w$ is the unit vector tangential to the wall. A fixed contact angle of 17° was specified for all wall boundary conditions. This is the static value measured by Ru Wang. AD was set as an open boundary ($p = 0$).
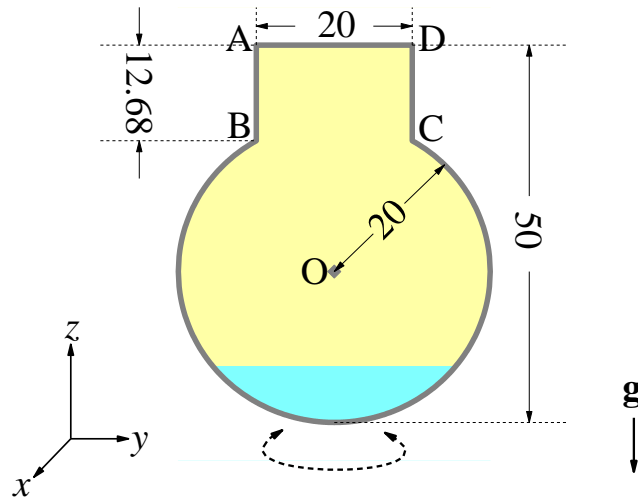
Fig. B.3. Geometry for saccadic motion simulation. Colours: yellow – oil; cyan – saline. All dimensions in mm. O denotes the origin of the Cartesian co-ordinates (0, 0, 0). **g** shows the direction of gravity.

A 3D geometry with a structured hexahedral mesh (153542 elements) was constructed using the commercial CFD software, ANSYS version 18.0. The mesh file was exported from workbench into OpenFOAM for the modelling using the 'fluent3DMeshToFoam' function. The OpenFOAM solver for incompressible two-phase case, interFoam, was employed. The model was run as a transient, with the secondary flow approaching a pseudo-steady state after several cycles. All cases were computed for at least 20 cycles. Fig. B.4 shows the evolution of the maximum V_z for pure oil and pure saline on the vertical plane. At $t > 0.5$ s (4 cycles), the maximum V_z in saline approaches an asymptote. By contrast, the maximum V_z for oil fluctuates, with a maximum value around 0.05 m/s and a value in the rest period about 0.0003 m/s.

The computational time depended on the cases. Simulations with saline alone were the most time-consuming, taking approximately 12 h for each cycle.
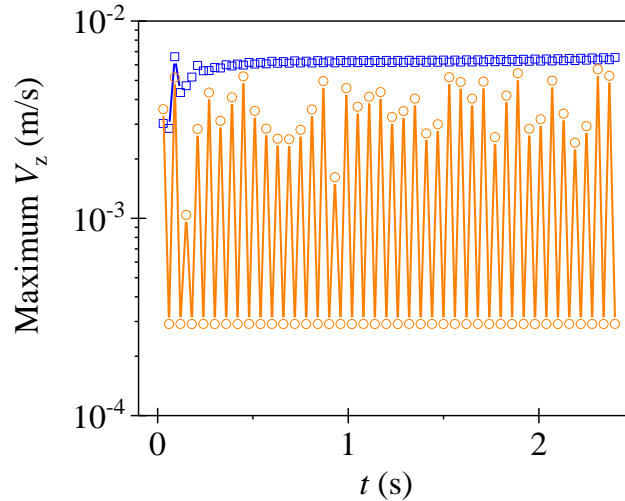
Fig. B.4. Evolution of the maximum V_z on the vertical plane through the axis of rotation. Test conditions: $\omega = 600$ °/s, $A = 18°$, liquids: 91/9 vol/vol silicon oil (orange)/saline (blue).

B.3   Results and Discussion

Fig. B.5(a) shows the oil velocity distributions obtained from PIV on the plane containing the rotational axis, *i.e.* the plane in Fig. B.3. All velocities are average values because only 4 images can be taken by the PIV camera, but the duration of each cycle under the test conditions is 0.12 s and is shorter than the PIV frame duration (0.25 s, the maximum frame rate: 4). Good agreement with the simulation results (see Fig. B.5(b,i) and (b,ii)) is obtained in terms of the velocity distributions. However, the simulations slightly overestimate the magnitude of the velocities. The predicted $\bar{V}_x$ distribution is presented in Fig. B.5(b,iii), but this quantity cannot be measured by the PIV system used due to its direction being normal to the measured plane, which is a restriction of the PIV setup. The predicted values are nearly zero due to periodic oscillation which averages to zero.

Fig. B.5(iv) compares the measured and predicted secondary flows. Both show that the flow in the vertical plane consists of four circulation cells. The simulation agrees with the experimental data well and indicates that the CFD model can be used to estimate the flow pattern induced by the saccadic movement with some confidence. The predicted shear stress is plotted in Fig. B.5(b,v). The maximum shear stress (about 10 Pa) occurs at the wall. The shear stress decays

249

with decreasing radius, and the minimum value is about 2 Pa at the centre, but it is not a linear function (see black line in Fig. B.5(b,v)).
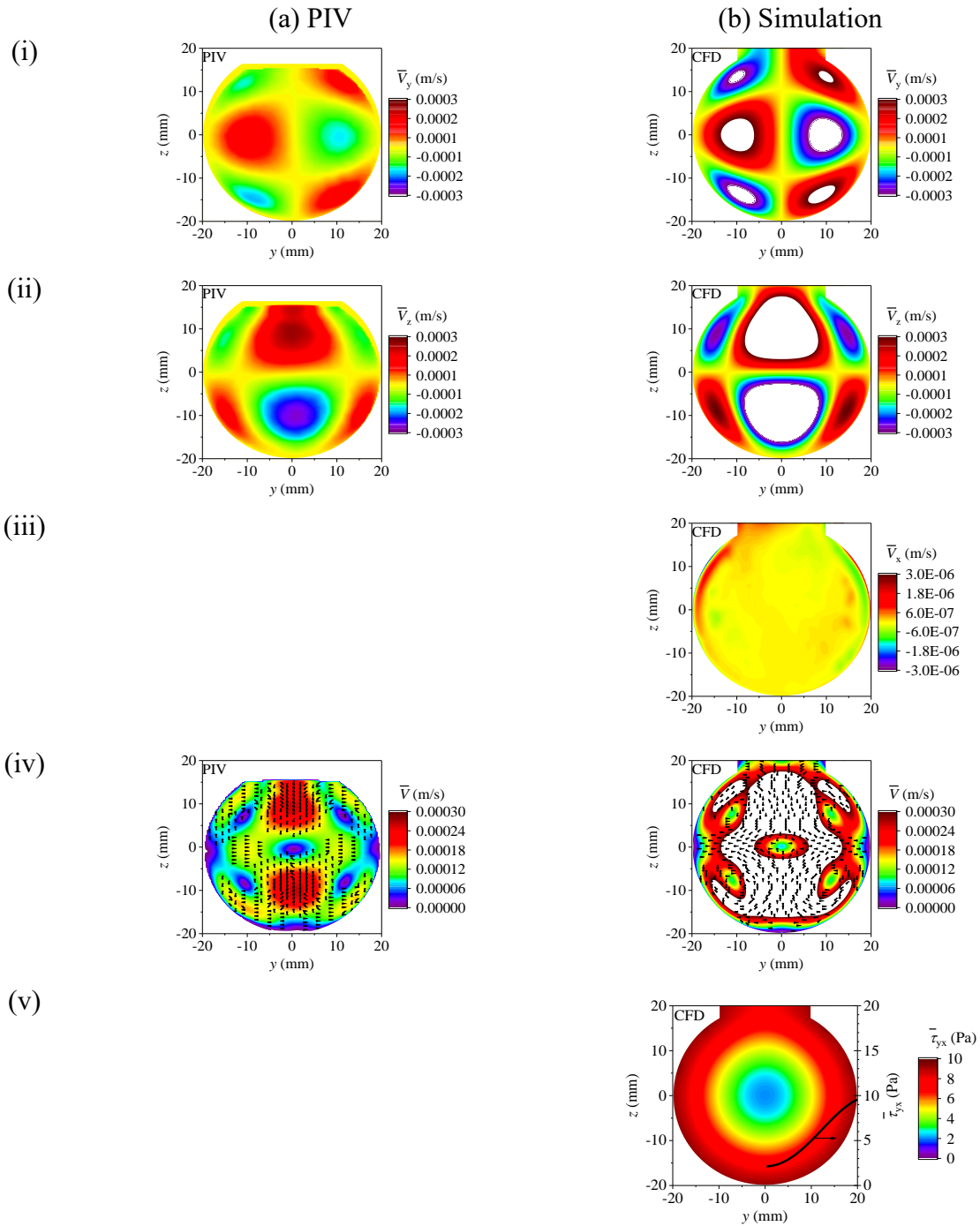
Fig. B.5. Comparison of (i) average *y*-axis velocity, (ii) average *z*-axis velocity, (iii) average *x*-axis velocity, (iv) flow pattern and (v) predicted shear stress obtained from (a) PIV and (b) simulation for oil on the *x*-plane (Fig. B.3). Test conditions: $\omega = 600$ °/s, $A = 18°$. In (iv), $\bar{V}$ is the average velocity of $\bar{V}_y$ and $\bar{V}_z$, and arrows denote the flow direction. Black line in (v) shows the profile of predicted shear stress along y.

The distribution of $\bar{V}_y$ (radial velocity with respect to the point O in Fig. B.3) in the PIV results for pure saline differs from the simulations (see Fig. B.6(i)). This is due to the fact that the measured plane was not at the centre. This is evident in Fig. B.6(a,iv), where the arrows are all in the same direction. The velocity distribution is expected to be asymmetric or symmetric due to the asymmetric setup and oscillation. Fig. B.6(ii) shows good agreement between the PIV and simulation results. In both cases there are some noisy values around the wall, which results from small vortices there. The $\bar{V}_x$ values are also very small for saline (Fig. B.6(b,iii)). The predicted flow pattern (see Fig. B.6(b,iv)) shows that only two circulations happened, which is different from the oil case. Comparing $\bar{V}$ for the oil with $\bar{V}$ for the saline, the maximum value (streaming intensity) for the oil is smaller. These are attributed to the differences in viscosity. Repetto *et al.* [230] reported that the $\bar{V}$ value depended strongly on the Womersley number, $Wo = \sqrt{R^2\omega/\nu}$, where R is the radius and ν is the kinematic viscosity of the fluid. Compared to the oil case, the maximum shear stress for saline also occurs at the wall but is noticeably smaller (around 0.01 Pa), and it decays faster with distance from the wall, reaching zero at $y = 19$ mm.
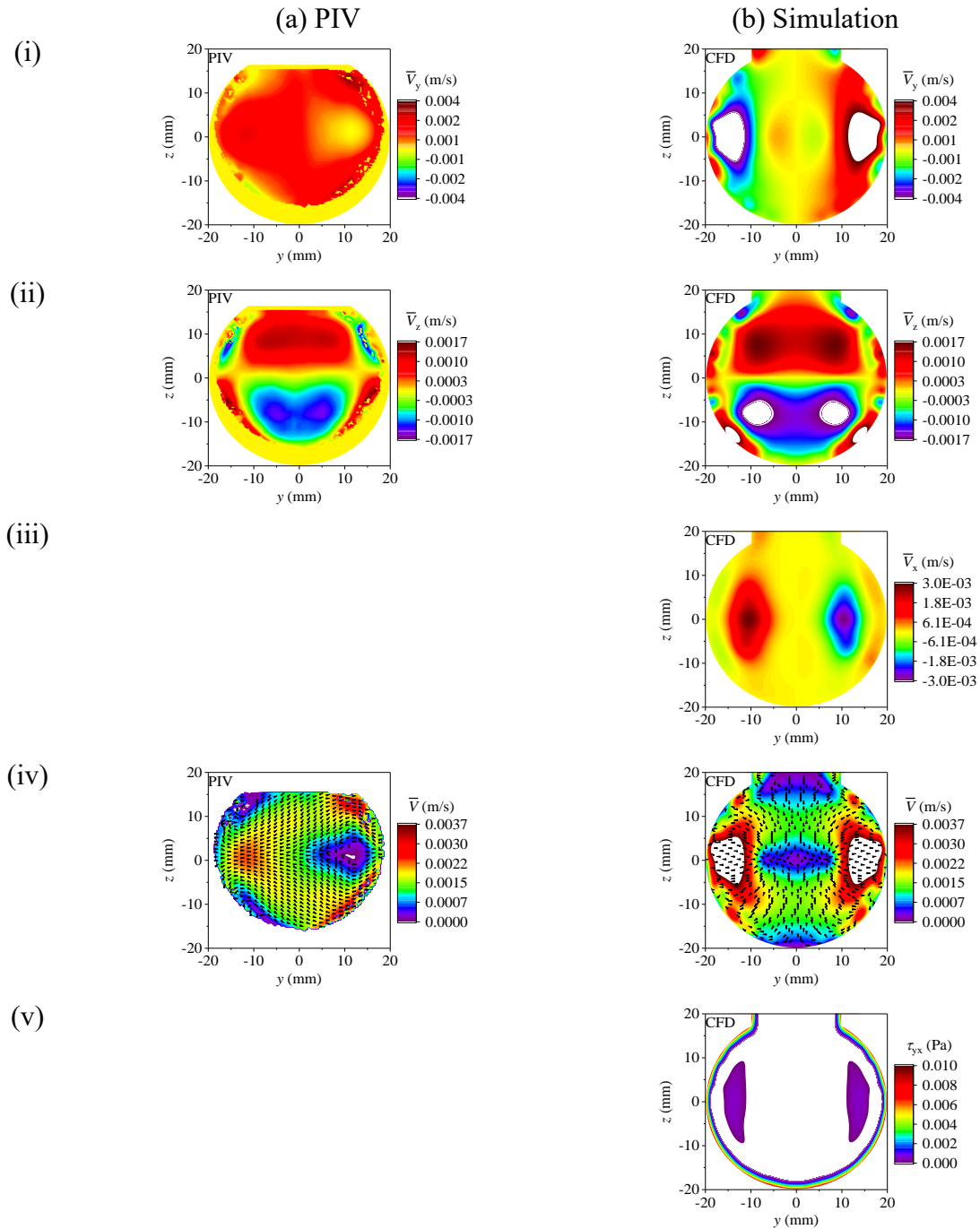
Fig. B.6. Comparison of (i) average *y*-axis velocity, (ii) average *z*-axis velocity, (iii) average *x*-axis velocity, (iv) flow pattern and (v) predicted shear stress obtained from (a) PIV and (b) simulation for saline on *x*-axis orbital plane. Test conditions: ω = 600 °/s, A = 18°. In (iv), $\overline{V}$ is the average velocity of $\overline{V}_y$ and $\overline{V}_z$, and arrows denote the flow direction.

Fig. B.7(a,i) shows the predicted V_x values for oil on the equatorial plane. The values at all four points are very small, and at times 1 and 3 they are nearly zero. V_z for oil (Fig. B.7(a,iii)) shows

a similar trend to V_x. By contrast, for saline in Fig. B.7(b,i), the V_x values are high at all four times with the maximum of about 0.005 m/s. The saline V_z values are also much higher than the oil velocities. This is because V_x and V_z involve the secondary flow. In the saline case, after the secondary flow was induced, the flow would not be affected by the periodic oscillations due to its lower viscosity, and vice versa. This phenomenon can be observed in Fig. B.7(ii). At points 2 and 4, V_y for both fluids shows absolute maximum at the wall, which is the same as the rotational velocity due to no-slip, and it declines with decreasing x. However, the V_y values for saline decrease much faster than for oil. This is attributed to the viscosity difference: momentum can transfer to a longer distance in a higher viscosity fluid, so in the oil momentum can be transferred to the centre of the chamber. The V_y values for a smaller time step are presented in Fig. B.7(iv). In saline, the momentum only can be transferred as far as $x = 19$ mm by the end of the rotation.

The absolute maximum τ_{yx} for oil in the cycle is about 20 Pa and occurs at the wall, which is twice the shear stress shown in Fig. B.5(b,v). This is because the latter value is the average of four data. However, the predicted maximum τ_{yx} for saline is more than 270 Pa. This unexpectedly high value is attributed to the mesh elements at the wall being too coarse for this case.
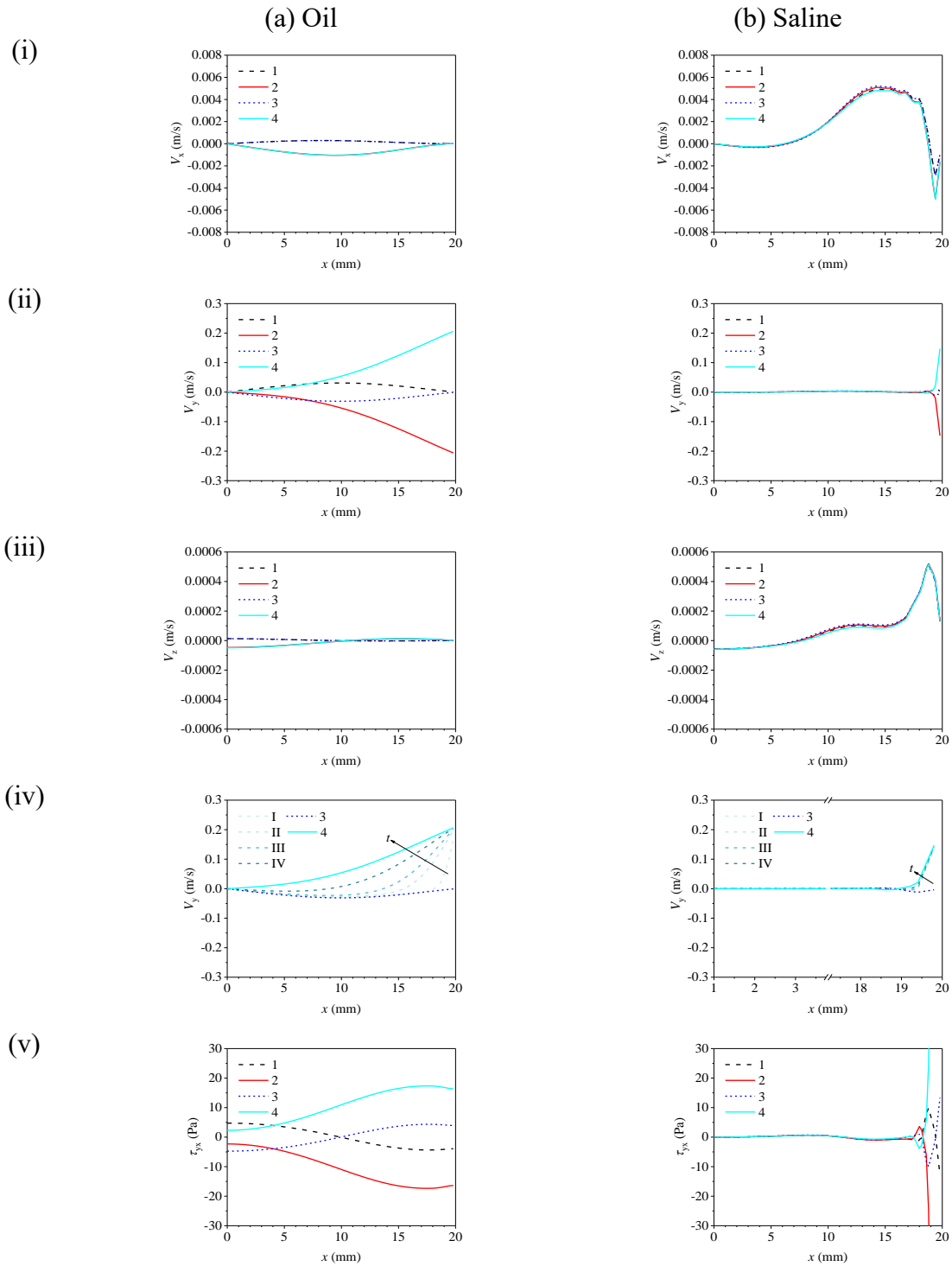
Fig. B.7. Profiles of predicted (i) V_x, (ii) V_y, (iii) V_z, (iv) momentum transfer and (v) shear stress for (a) oil and (b) saline on the equatorial (x-y) plane at different times (see Fig. B.2(b)). Test conditions: $\omega = 600$ °/s, $A = 18°$.

Fig. B.8 compares the predicted shapes of the interface between the silicone oil and saline with the experimental results for two values of A. With the smaller ampltitude, $A = 5.4°$, the solution

255

momentum is small and the interface does not differ much from the static case (determined by surface tension). The simulation gives a similar shape. The larger amplitude, 36°, gives a wavy interface (see Fig. B.8(b,i)) which is also predicted by the simulation. The largest absolute velocities occur around the interface. The reasonable agreement in shapes indicate that the model can be predict the effect of saccadic motion for the two-phase case. The induced shear stresses are shown in Fig. B.8(iii). With $A = 5.4°$, the maximum shear stress (about 10 Pa) occurred at the wall. By contrast, at $A = 36°$, the maximum τ_{yx} value (around 10 Pa) occurred not only at the wall, but also around the interface: the larger amplitude let the momentum transfer to the interface. This indicates that for this case, the location of the maximum shear stress depends on the applied amplitude.
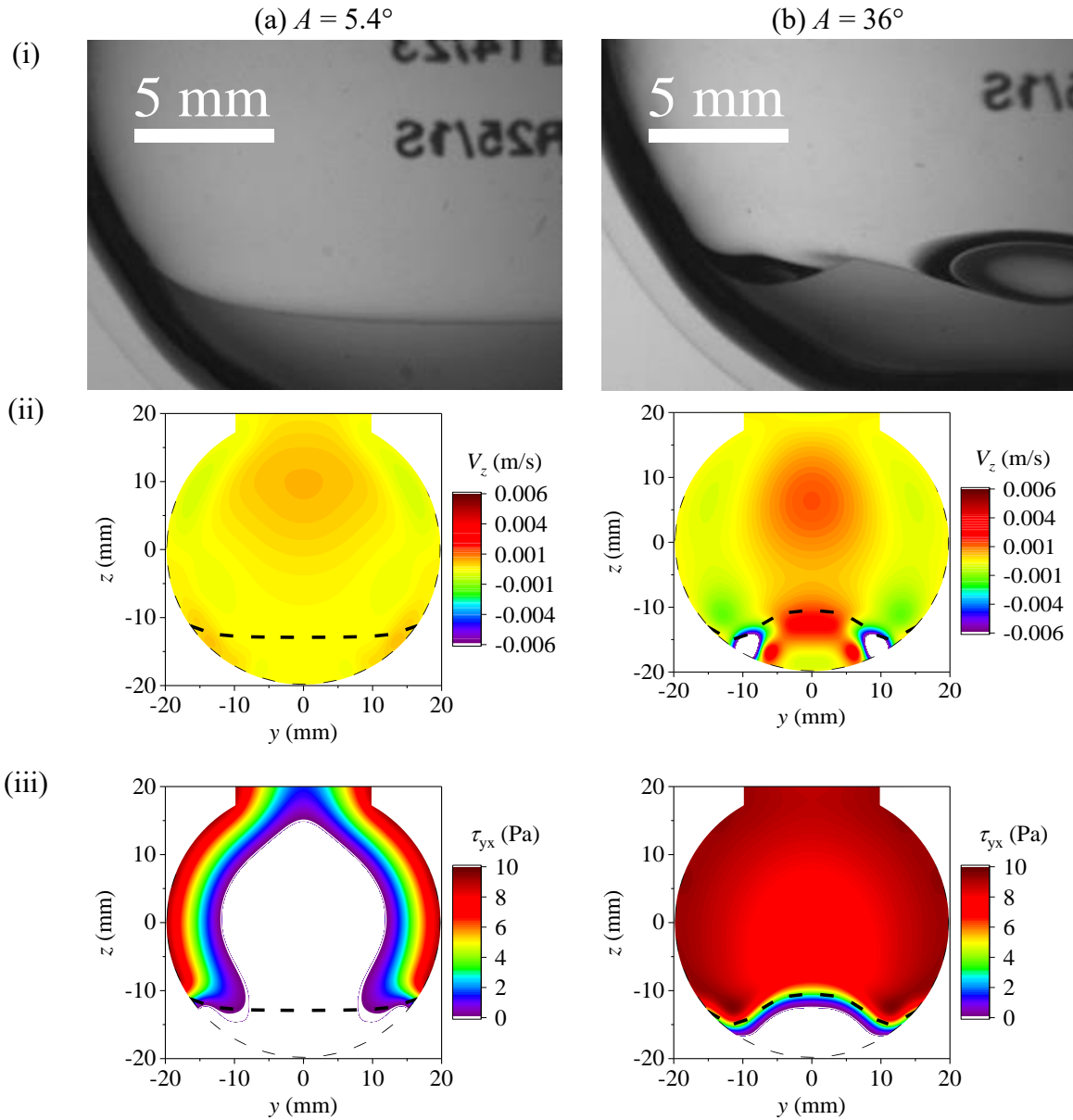
(a) $A = 5.4°$ (b) $A = 36°$

(i)

(ii)

(iii)

Fig. B.8. Comparison of (i) images, (ii) predicted z-axis velocity and (iii) predicted shear stress for A = (a) 5.4° and (b) 36°. On the vertical plane through the axis of rotation. Test conditions: 91% oil: 9% saline, ω = 600 °/s, at point 4 (refer to Fig. B.2(b)). Black dashed line indicates the interface between oil and saline.

B.4 Conclusions

The VOF modelling approach developed in the dissertation was successfully applied to a further case, the motion of viscous and less viscous liquids in a model eyeball. The simulation results for pure oil and pure saline were compared with the PIV results, and good agreement

between velocity distributions was obtained. The simulation of a two-phase case gave a good prediction of the interface shape. The predicted shear stresses showed that the large amplitude caused the maximum shear stress to occur around the interface. This numerical study allows regions of high shear stress to be identified. It was proven that the multi-phase CFD model can be extended to other cases with some confidence.